A NUMERICAL STUDY OF THE SLOW PYROLYSIS OF THERMALLY THICK WOOD SPHERES

A Thesis

Presented to the Faculty of the Graduate School

of Cornell University

In Partial Fulfillment of the Requirements for the Degree of

Master of Science

by

Krystle Smith

January 2014

ABSTRACT

Two one-dimensional numerical simulations were developed to model the pyrolysis of wood spheres, based on the proposed model developed by Park et al., 2010. Both of these models include physical processes coupled with a kinetic mechanism that describes the pyrolysis reactions, including heat transfer within the wood particle, chemical decomposition of wood into products, and the pressure-driven flow of gas-phase species through the porous media, described using Darcy's law. The Park model used the kinetic mechanism developed by Park et al., 2010, where wood decomposes through a few parallel reactions and secondary reactions to form gas, tar, and char. The Gauthier model implements a more detailed kinetic mechanism, presented by Gauthier et al., 2013, which describes the decomposition of the main constituents of wood – cellulose, hemicellulose, and three types of lignin – and characterizes gas and tar fractions with a limited number of components.

To accurately determine the ability of the model to predict the pyrolysis process, both models were configured to match the experimental conditions presented in this thesis. This included an in depth study into the external heat transfer, material properties, and some kinetic parameters from the Park model used in the simulation.

Model outputs were compared to thermogravimetric analysis mass loss profiles and time-resolved temperature and species profiles of permanent gases and several light volatiles from the slow pyrolysis of dry poplar wood spheres. Model predictions from both the Park and Gauthier kinetic mechanisms matched reasonably well with experimental data, although the Gauthier model predicted a very large production of species from the desorption of chemisorbed species at higher temperatures that was not seen experimentally. Additionally,

both models were generally able to predict the trends in yields of species with particle size and temperature. From this study, the following were determined: (1) The main release of gaseous products occurred before the exothermic peak seen in the temperature profiles, which supports the view that this peak is caused by the decomposition of an intermediate solid. (2) Both the Park and Gauthier models predicted a higher yield for tar and a lower yield for char than seen experimentally, which could be caused by secondary char being formed from the decomposition of tar as it moves through the biomass particle. (3) Two peaks were observed in the species profiles for CH_4 at low temperatures, supporting the notion of the release of chemisorbed species that is implemented in the Gauthier model; however, this release is much smaller than predicted by the model.

The development of the Gauthier model contributes considerably to numerical modeling of the pyrolysis process. This model provides detailed information on the composition of volatiles being produced through the slow pyrolysis of thermally thick particles, as well as the timing of the release of specific species. While there are many advantages to using this model to predict pyrolysis on a larger scale, there are also some disadvantages, including the difficulty in defining accurate initial and boundary conditions for the system. However, most of these difficulties are present in any detailed numerical model.

BIOGRAPHICAL SKETCH

Krystle Smith earned her Bachelor of Science degree in Mechanical Engineering from Brigham Young University in April of 2008, where she graduated magna cum laude. After graduating, Krystle worked at Raytheon Missile Systems in Tucson, Arizona, before joining the graduate program in Mechanical Engineering at Cornell University in August of 2010.

Krystle has been the recipient of numerous honors and awards, including earning placement on the Dean's List for four semesters and being awarded a full tuition scholarship for three consecutive years. She is also a member of Tau Beta Pi, an engineering honors society.

Krystle Smith has had her work presented at the Fall Technical Meeting of the Eastern States Section of the Combustion Institute. Additionally, her research has been published in the international journal, Energy & Fuels.

To my family.

ACKNOWLEDGMENTS

I would like to express my gratitude to my advisor, Dr. Elizabeth Fisher, for her exceptional guidance in my research. This work would not have been possible without her enthusiasm, encouragement, and insightful suggestions. I would also like to thank Dr. Ashim K Datta for his advice and assistance in developing numerical models, as well as using COMSOL Multiphysics. I am deeply grateful to my colleague, Hayat Bennadji, for her extensive collaboration in my research. I would also like to thank Dr. Eliseo Ranzi, Emma Barker Hemings, and Michele Corbetta for sharing their kinetic mechanism pre-publication, as well as for their many helpful comments and discussions.

I would like to acknowledge the financial support provided by Yossie Hollander and the Fondation des Fondateurs. I would also like to thank the David R. Atkinson Center for a Sustainable Future (ACSF) at Cornell University for their support.

I want to express my deepest appreciation to my husband, Paul, and my son, Peyton, for their love, encouragement, and support. I will be forever grateful for their love and sacrifice. I am also exceedingly grateful to my parents for their endless love and support.

TABLE OF CONTENTS

LIST OF FIGURES

LIST OF TABLES

LIST OF SYMBOLS

A	pre-exponential factor (s^{-1}), surface area (m^2)
b_h	blowing correction factor
B	permeability (m^2)
Bi	Biot number
c	specific heat capacity (J/kg K)
c_p	constant pressure specific heat capacity (J/kg K)
d	pore size (m)
D	diameter (m)
e	emissivity
E	activation energy (J/mol K)
F	view factor
h	heat transfer coefficient (W/m^2 K)
Δh	heat of reaction (J/kg)
k	reaction rate (s^{-1})
M	molecular weight (kg/mol)
Nu	Nusselt number
P	pressure (Pa)
Pr	Prandtl number
Q	heat generation (W/m^3)
$\dot{Q}$	heat per unit time
r	radius (m)
R	universal gas constant (8.314 J/mol K)
Re	Reynolds number
S	mass generation (kg/m^3 s)
St	Stanton number
T	temperature (K)
u	velocity (m/s)
V	velocity (m/s), volume (m^3)

Greek Letters

α	thermal diffusivity (m^2/s)
β	fit parameter for temperature profiles up to 450 K
γ	fit parameter for overall temperature profiles
δ	fit parameter for TGA mass loss profiles
ε	porosity
ζ	sensitivity variable
η	degree of pyrolysis
λ	thermal conductivity (W/m K)
μ	viscosity (kg/m s)
ρ	density (kg/m^3)
σ	Stefan-Boltzmann constant (5.67×10^{-8} W/m^2 K)
ψ	goodness of fit parameter

Subscripts

a	virgin wood
c	char, primary char generation
c2	secondary char generation
g	gas, primary gas generation
g2	secondary gas generation
is	intermediate solid
s	solid
t	tar
v	total volatiles
w	initial virgin wood
0	initial condition
∞	free stream

CHAPTER 1

INTRODUCTION

With the depletion of fossil fuels and rising concerns of the environmental impact of conventional sources of energy, technological research has begun focusing on the development of alternative fuels. A sustainable energy source that is receiving increasing attention is biomass, which could provide a transition from traditional carbon-based fuels such as coal, petroleum, and natural gas to a carbon-neutral fuel (Park et al., 2010).

Biomass is a renewable resource, with feedstocks ranging from agricultural or forest residues to municipal waste. In Greece, plant biomass in the form of agricultural residues was found to be equivalent to 40-50% of the gross energy consumption (Vamvuka et al., 2003), while in China, the yield of agricultural residues is up to 0.81 billion tons, supplying about 32.1% of the primary energy in 1998 (Li et al., 2004).

Several thermochemical conversion processes exist for converting biomass into more usable forms of energy, including combustion, gasification, and pyrolysis. While direct electrical or thermal energy can be recovered from biomass through combustion, other thermal processes like pyrolysis or gasification allow the conversion of woody biomasses into more valuable gaseous or liquid combustibles (Janse et al., 2000). Currently, biomass-derived biofuels are the only current sustainable source of liquid fuels required for transportation (Huber, 2008).

Biomass pyrolysis involves the thermal degradation of raw organic materials in the absence of an oxidizer in order to extract products for later applications. While this

conversion route results in a vast number of chemical compounds, its products are often lumped into three groups: gas, tar, and char.

Gas products comprise CO, H_2, CO_2, CH_4, and other light hydrocarbons (Fagbemi et al., 2001; Sharypov et al., 2002; Boroson et al., 1989; Williams and Besler, 1996). Gases can be used as a combustible material for heating power (Mok et al., 1980; Soltes and Elder, 1981), or can be converted into liquid fuels through additional conversion processes.

Tars are composed of hydrocarbons of higher C content and other organic compounds which are volatile at pyrolysis temperatures and condense at lower temperatures (Grieco and Baldi, 2011). These compounds can be used as a renewable fuel, which can be easily stored and transported, and can also be used for the production of chemicals (Czernik and Bridgwater, 2004).

The solid residue left after the pyrolysis of biomass is considered char. Because of its low sulfur and phosphorus contents and textural reactivity properties, it is widely used in the chemical, pharmaceutical, and food industries (Encinar et al., 1996). Recently, char has attracted considerable interest as a solid amendment to improve the water retention and productivity of poor agricultural soils (Lehmann and Joseph, 2009; Manya, 2012). Char can also be used as a fuel, a feedstock for activated carbon, or as a reducing agent in the metallurgical industry (Bennadji et al., 2013).

Numerous factors influence the yields, composition, and properties of the products produced from the pyrolysis of biomass. Chief among these are the temperature, pressure, and heating rate of the process (Di Blasi, 2008). Also important are the properties of the raw biomass, including chemical composition, density, moisture content, and particle size and shape (Di Blasi, 2008). The operating conditions can maximize the yields of char or gas and

tar (Bridgwater, 1999, 2003; Antal et al., 2003). The current study focuses on the conditions favoring char production, with relatively mild thermal processing of large biomass particles, generally known as slow pyrolysis.

In order to understand and optimize the pyrolysis process for large-scale development, a mathematical model is needed which can quantitatively represent the various physical phenomena involved in the decomposition of biomass. Models provide powerful tools which can be used for process design, prediction of reactor performances, understanding of pollutants evolution, analysis of process transients, and examination of strategies for effective control (Di Blasi, 2008). The thermochemical conversion of biomass in practical systems results from a strong interaction between chemical and physical processes. These include heat transfer, decomposition kinetics, flow of gaseous products through the porous media, changes in material properties with the extent of pyrolysis and temperature, and anisotropic property behavior, among others. Therefore, models need an appropriate description in relation to both the chemical kinetics and to transport phenomena (Ranzi et al., 2008).

There are many different kinetic models that have been developed for the pyrolysis of wood. A good review is given by Di Blasi, 2008. The simplest models use a single decomposition reaction, using a first-order Arrhenius reaction (Di Blasi, 1998a; Aiman and Stubington, 1993; Tabatabaie-Raissi et al., 1989). Other models approximate the pyrolysis process with two (Tang, 1967) or three (Thurner and Mann, 1981; Chan et al., 1985; Font et al., 1990) parallel first-order reactions to predict the production of gas, tar, and char. More complex kinetic mechanisms include a further decomposition of tar in the gas phase (Liden et al., 1988; Di Blasi, 1993a, Di Blasi, 2002) or the formation of an intermediate product

through the primary decomposition of biomass, which gives rise to gas, tar, and char (Koufopanos et al., 1989; Shafizadeh and Bradbury, 1979; Bradbury et al., 1979).

Detailed models exist in the literature which couple mechanisms of pyrolysis reactions with the conservation equations of mass, momentum, and energy for the pyrolysis of single wood particles (Larfeldt et al., 2000; Janse et al., 2000; Bryden et al., 2002; Di Blasi, 2002). The most advanced models take into account the following physical processes: heat transfer by convection, conduction and radiation, convective transport of volatile species, and gas pressure and velocity variations, with the latter variables being described by means of the Darcy law (Di Blasi, 2008). A review of models which couple chemical kinetics with mathematical descriptions of physical processes is given in Gronli, 1996 and Di Blasi, 1993b.

In this study, two numerical models of the slow pyrolysis of poplar wood are investigated. In Chapter 2 of this thesis, experimental data used for comparison to the numerical models is presented. This data includes mass loss profiles from thermogravimetric analysis of poplar wood samples, along with time-resolved temperature and species profiles from the slow pyrolysis of dry poplar wood spheres under well-defined conditions. Measured species include permanent gases and several light volatile species. Chapter 3 presents the development of two one-dimensional numerical models based on the proposed model developed by Park et al., 2010. Both of these models include physical processes coupled with a kinetic mechanism that describes the pyrolysis reactions, including heat transfer within the wood particle, chemical decomposition of wood into products, and pressure-driven flow of gas-phase species through the porous media, described using Darcy's law. The Park model uses the kinetic mechanism developed by Park et al., 2010, where wood decomposes through a few parallel reactions and secondary reactions to form gas, tar, and char, while the Gauthier

model uses a more detailed kinetic mechanism to describe the decomposition of the main constituents of wood – cellulose, hemicellulose, and three types of lignin – and characterizes gas and tar fractions with a limited number of components. Both of these models are modified to match the experimental conditions presented in Chapter 2. In Chapter 4, predictions from the model developed in Chapter 3 are compared to the experimental data. Comparisons include temperature profiles, species profiles, yields of specific species, and final yields of gas, tar, and char. Conclusions of this work are presented in Chapter 5. Figure 1 gives a visual representation of the organization of this thesis.

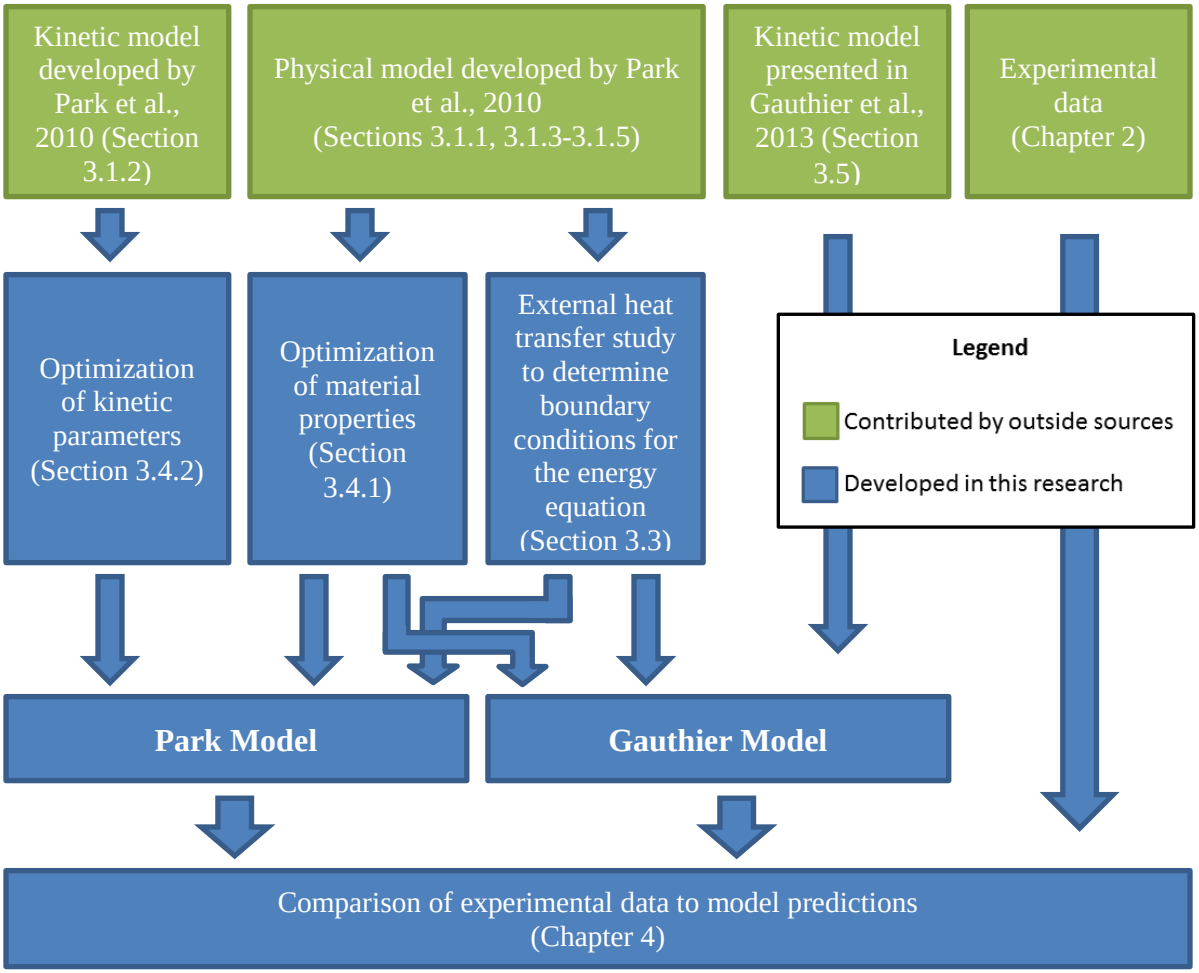

Figure 1. Visual representation of the organization of this thesis

CHAPTER 2

EXPERIMENTAL ANALYSIS OF WOOD PYROLYSIS

The numerical simulation developed for this research was compared to experimental data obtained from thermogravimetric analysis and the slow pyrolysis of single wood spheres. The setup used for these experiments provided very well-defined operating conditions which could easily be implemented into the numerical model. This section provides details about the wood used in these experiments, followed by the methods and key data from both the TGA and pyrolysis experiments. TGA mass loss profiles were provided by Michelle Serapiglia, Department of Horticulture, Cornell University (unpublished work, 2012). Experimental temperature profiles and time-resolved species data for permanent gases and several light volatile species from the slow pyrolysis of dry poplar spheres was provided by Hayat Bennadji, Sibley School of Mechanical and Aerospace Engineering, Cornell University (unpublished work, 2013).

2.1 Materials

Wood spheres were fashioned out of untreated poplar dowels purchased from California Dowel & Turnings. Two diameters were studied: 2.54 ± 0.11 cm and 3.8 ± 0.03 cm. The composition of the wood was estimated based on elemental composition, as described by

Calonaci et al., 2010. Results for both the ultimate analysis and the component analysis are presented in Tables 1 and 2, respectively.

Table 1. Ultimate analysis of poplar wood[a]

Ultimate Analysis (wt %)	COIL[b]
C	47.72 ± 2.09
H	6.35 ± 0.03
O	45.93 ± 0.13

[a]All numbers are presented on a dry, ash-free (DAF) basis.
[b]COIL: Cornell Isotope laboratory

Table 2. Component analysis of poplar wood[a]

Component	Wt %
CELL (cellulose)	46.98%
HCE (hemicellulose)	25.52%
LIG-C (lignin richer in carbon)	0.87%
LIC-H (lignin richer in hydrogen)	26.3%
LIG-O (lignin richer in oxygen)	0.34%

[a]All numbers are presented on a dry, ash-free (DAF) basis

The wood spheres were dried at 105°C and stored in desiccant jars. Smaller spheres were dried for six hours and larger sphere for eight hours. The mass of the wood sphere was measured immediately before the beginning of each experiment and compared to the value immediately after drying. This comparison indicated that negligible amounts of water were absorbed subsequent to drying (<0.7%).

2.2 Thermogravimetric Analysis of Poplar Wood Samples

The poplar wood was studied in a series of thermogravimetric experiments run in a nitrogen environment (M. Serapiglia, Department of Horticulture, Cornell University, unpublished work, 2012). Prior to TGA analysis, the wood was ground to a fine powder and sieved

through a 0.25 mm mesh. Biomass samples (10 ± 0.4 mg) were heated at 20°C/min from room temperature up to 105°C and held for 10 minutes to dry out the sample. After drying, the wood was heated at a rate of 5°C/min up to a temperature of 500°C. Experimental conditions are given in Table 3.

Table 3. TGA experimental conditions

Run Number	Initial Sample Mass (g)	Dried Sample Mass (g)	Particle Size (mm)	Heating Rate (°C/min)	Final Temperature (°C)	Char Mass at 500°C (g)
1	9.863	9.279	0.25	5	500	1.362
2	10.09	9.508	0.25	5	500	1.388
3	9.639	9.074	0.25	5	500	1.317

Figure 2 shows the mass loss profiles from the three TGA runs. Weight percent values were calculated using the mass of the sample after drying as the initial mass.

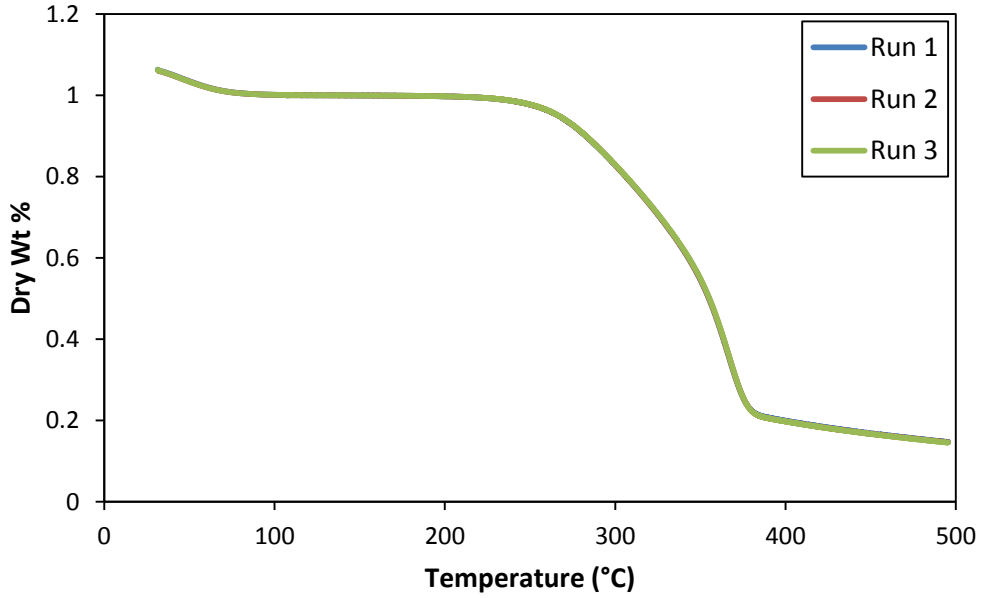

Figure 2. Mass loss profiles from the TGA runs with poplar wood. Weight percent values are calculated based on dried mass.

Because the TGA experimental data was used to analyze the kinetic mechanisms used in the simulation, it was important to verify that they were kinetically controlled. Data from previous TGA experiments using white pine samples were used for this verification. Three runs were performed for each combination of the sample masses (5 and 10 mg), particle sizes (0.25 and 0.5 mm), and heating rates (5 and 10°C/min) that were studied. The temperature program followed the same procedure as that used for the poplar analysis, except that the second heating rate was adjusted to 10°C/min in some cases. Figures 3 and 4 show the mass loss profiles for 5°C/min and 10°C/min heating rates, respectively. Weight percent values were calculated using the mass of the sample after drying as the initial mass.

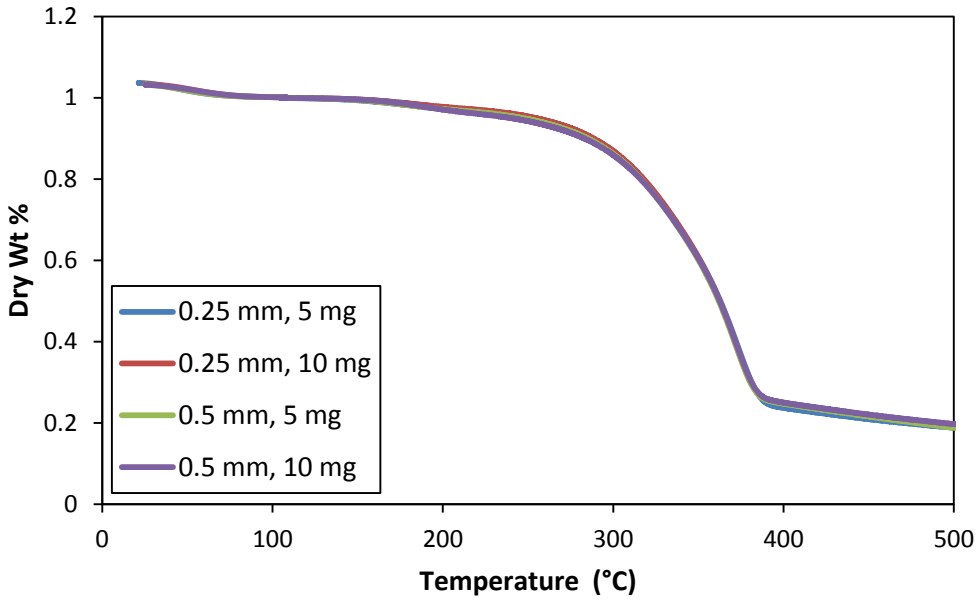

Figure 3. Mass loss profiles for white pine samples at a 5°C/min heating rate. Weight percent values were calculated based on dried mass.

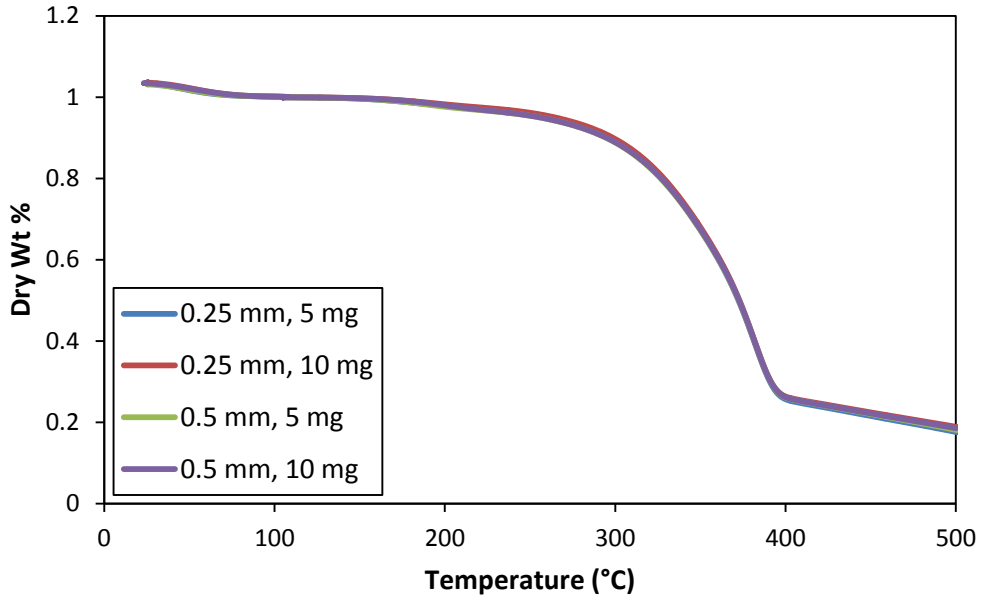

Figure 4. Mass loss profiles for white pine samples at a 10°C/min heating rate. Weight percent values were calculated based on dried mass.

White pine mass loss profiles verified that the mass and size of the sample had no effect on the profiles for either heating rate studied, and thus that the experimental setup used for the poplar runs was kinetically controlled.

2.3 Slow Pyrolysis of Poplar Wood Spheres

Wood spheres were pyrolyzed in a bench-scale tubular reactor, heated by a flow of hot nitrogen (H. Bennadji, Mechanical and Aerospace Engineering, Cornell University unpublished work, 2013). After steady state conditions were reached with the nitrogen flow, wood spheres were rapidly inserted into the center of the reactor, with the wood grain direction oriented the same as the flow direction. The particle was allowed to pyrolyze for 30-

40 minutes, after which it was removed into a side-arm of the reactor that was cooled with a 20 SLPM flow of room-temperature nitrogen and allowed to cool to 110°C or lower. Following this, the particle was either removed from the reactor and allowed to cool in room air, or was reinserted into the heated nitrogen flow and again allowed to heat up to the set temperature, after which it was moved back into the side-arm, allowed to cool, then removed completely from the reactor. A detailed explanation of the experimental setup is described in Bennadji et al., 2013.

Temperature profiles were measured at the center of the wood spheres using a 0.5-mm ID sheathed and grounded, K-type thermocouple inserted through holes drilled into the particle. Holes were drilled by hand with a drill press using a 0.508 mm drill bit with an uncertainty of ± 0.7 mm. The volatiles released during the pyrolysis process were sampled downstream of the wood particle through an open-ended quartz sampling tube. Sampled gases flowed through ice-water cooled traps for tar removal, and then into a Fourier Transform Infrared (FTIR) analyzer for time-resolved profiles of volatile species. Additional measurements were taken for carbon monoxide with an NDIR analyzer for better time resolution of species profiles.

The operating conditions for the experimental data used in this research are summarized in Tables 4 and 5. For each condition, the pyrolysis was repeated a minimum of two times.

Table 4. Experimental conditions for the slow pyrolysis of poplar wood spheres with a 2.54 cm diameter.

Run number	Particle Size (cm)	Final Particle T, ^{0}C	Pyrolysis Time (min)	Re_D [a]	Run	m dry wood (g)	Char (%)
P1-L1	2.54	368.8	30	4561	1	4.105	29.17
P1-L2	2.535	367.3	30		2	4.32	28.84
P1-L3	2.535	374.2	30	4530	3	4.535	28.02
P1-L4	2.54	374.4	30		4	4.23	28.47
P1-M1	2.54	423	30	4302	1	4.3	22.79
P1-M2	2.53	418.9	30		2	4.065	22.89
P1-H1	2.54	470.3	30	4124	1	4.54	- [b]
P1-H2	2.54	477.6	30		2	4.286	- [b]

[a]Re_D: Reynolds number based on the reactor internal diameter (ID - 5.25 cm) and final particle temperature.
[b]Char split in half and pieces were missing

Table 5. Experimental conditions for the slow pyrolysis of poplar wood spheres with a 3.8 cm diameter.

Run number	Particle Size (cm)	Final Particle T, ^{0}C	Pyrolysis Time (min)	Re_D [a]	Run	m dry wood (g)	Char (%)
P2-L1	3.8	374.4	40	4530	1	14.9	28.8
P2-L2	3.81	372.9	40		2	14.28	28.15
P2-L3	3.785	373	40		3	15.13	28.9
P2-M1	3.8	417.2	40	4320	1	15.117	24.47
P2-M2	3.785	419.2	40		2	14.12	24.08
P2-M3	3.81	417.4	40		3	15.24	24.52
P2-H1	3.795	486.5[c]	40	4086	1	14.93	- [b]
P2-H2	3.79	488.5	40		2	14.965	- [b]
P2-H3	3.81	480.1	40		3	14.11	- [b]

[a]Re_D: Reynolds number based on the reactor internal diameter (ID - 5.25 cm) and final particle temperature.
[b]Char split in half and pieces were missing
[c]Thermocouple was not working properly.

Temperature profiles from the center of the particle and time-resolved species plots for permanent gases and several light volatile species for each of the experimental setups given in Tables 4 and 5 are given in Appendix A.

CHAPTER 3

NUMERICAL SIMULATION OF WOOD PYROLYSIS

Two one-dimensional numerical simulations were developed to model the pyrolysis of wood spheres. Physical processes incorporated in the both models include heat transfer within the wood particle, chemical decomposition of the wood into products, and the pressure-driven flow of gaseous species through the porous media. While these models do not capture every aspect of the pyrolysis process (see Section 5.3), they do provide useful insights into the pyrolysis process and support the development of higher fidelity models.

Both of the models used in this research are based on the proposed model developed by Park et al., 2010. Details of this model are presented in Section 3.1. Both the Park and Gauthier models incorporate the differential equations given in this paper to describe physical processes, including heat transfer within the particle and pressure-driven flow of gas-phase species. The Park model also includes the kinetic mechanism developed by Park et al., 2010, while the Gauthier model implements a more detailed kinetic mechanism that is presented later. Following the presentation of the base model from Park et al., 2010, a discussion on the method for determining the significance of adaptations made to the numerical model is presented in Section 3.2. In Section 3.3, the effects of various modes of external heat transfer are investigated. Following this, the optimization of parameters from the model developed by Park et al., 2010 for the experimental setup used in this research are discussed in Section 3.4.

Lastly, the detailed kinetic mechanism given by Gauthier et al., 2013 is presented in Section 3.5.

3.1 Base Model

A model of single-particle pyrolysis was developed based on a numerical model proposed by Park et al., 2010. This model was implemented in one-dimensional, spherical coordinates and models the interior of a pyrolyzing wood sphere, as shown in
Figure 5. Evaporation of moisture in the virgin wood, diffusion of species in the vapor phase, and shrinkage of the wood particle as it pyrolyzes are not included in the model. A complete set of the differential equations used to describe this model is given in Appendix B.

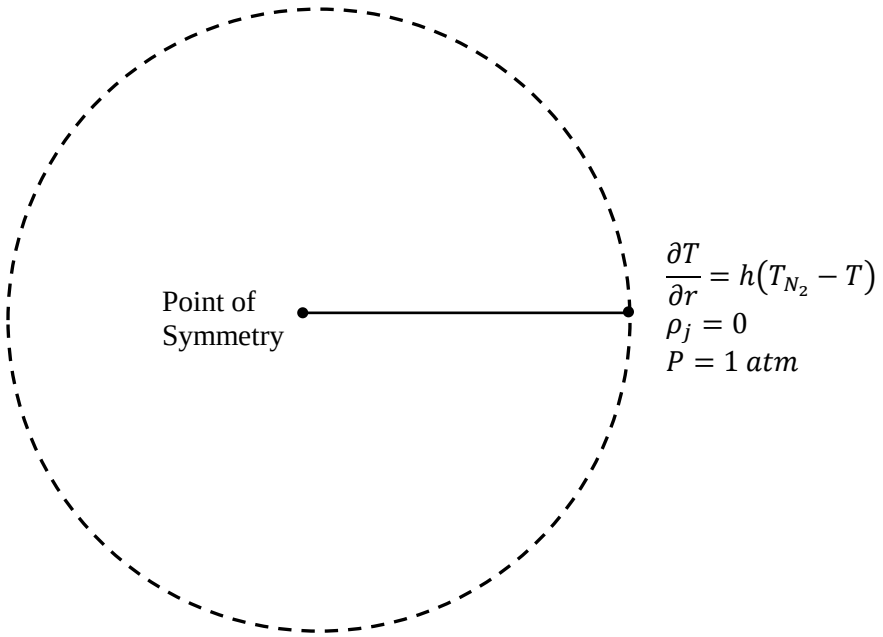

Figure 5. Schematic of the one-dimensional numerical model with boundary conditions

The model presented in Park et al., 2010 was chosen as a base model because of the similarities in the experimental setup to those used in this research. Also, the paper gives a very detailed explanation of the physics, chemical kinetics, and material properties that were used, which made it simple to implement.

In this section, the material properties from the base model are first presented, after which the kinetic mechanism is discussed. Following this, the physics of the model are presented, including mass conservation, pressure-driven flow, and conservation of energy. Last, the implementation of the model is discussed.

3.1.1 Material Properties

Material properties used in the Park model (Park et al., 2010) are presented in Table 6. This simulation was built to model the pyrolysis of a maple sphere; however, as described by Park et al., 2010, many property values were obtained from the literature and are not specific to maple wood. A more in depth discussion of the material properties used in this research is presented in Section 3.4.1.

Table 6. Material properties for the base model from Park et al., 2010

Property	Definition	Value	Units
ρ_w	Wood density	630[a]	kg/m^3
c_w	Wood specific heat	1500 + 1.0T	J/kg K
c_c	Char specific heat	$420 + 2.09T + 6.85 \times 10^{-4}T^2$	J/kg K
c_{pt}	Tar specific heat	$-100 + 4.4T - 1.57 \times 10^{-3}T^2$	J/kg K
c_{pg}	Gas specific heat	$770 + 0.629T - 1.91 \times 10^{-4}T^2$	J/kg K
d	Pore diameter	$5 \times 10^{-5}(1-\eta) + 1 \times 10^{-4}\eta$	m
e	Pore emissivity	1	-
σ	Stefan-Boltzmann constant	5.67×10^{-8}	$W/m^2 K^4$
ε	Virgin wood porosity	0.4	-
$\lambda_{w,radial}$	Wood thermal conductivity, radial direction	0.1046	W/m K
$\lambda_{w,grain}$	Wood thermal conductivity, grain direction	0.255	W/m K
$\lambda_{w,tangential}$	Wood thermal conductivity, tangential direction	0.255[b]	W/m K
$\lambda_{c,radial}$	Char thermal conductivity, radial direction	0.071	W/m K
$\lambda_{c,grain}$	Char thermal conductivity, grain direction	0.105	W/m K
$\lambda_{c,tangential}$	Char thermal conductivity, tangential direction	0.105[b]	W/m K
λ_v	Thermal conductivity of volatiles	0.0258	W/m K
B_w	Wood permeability	5×10^{-16}	m^2
B_c	Char permeability	1×10^{-13}	m^2
e_w	Wood emissivity	0.7	-
e_c	Char emissivity	0.92	-
μ	Viscosity of volatiles	3.0×10^{-5}	kg/m s
M_g	Gas molecular weight	0.038	kg/mol
M_t	Tar molecular weight	0.11	kg/mol
R	Gas constant	8.314	J/mol K

[a]Values measured by Park et al., 2010
[b]Values estimated by Park et al., 2010

3.1.2 Kinetic Mechanism

Park's kinetic mechanism (Park et al., 2010) assumes that virgin wood is pyrolyzed through three parallel paths to form gas, tar, and an intermediate solid. The tar reacts further to form gas and char through secondary reactions, while the intermediate solid decomposes further to produce char. The kinetic mechanism is shown in Figure 6. All reaction rates are modeled as first-order, Arrhenius-type reactions.

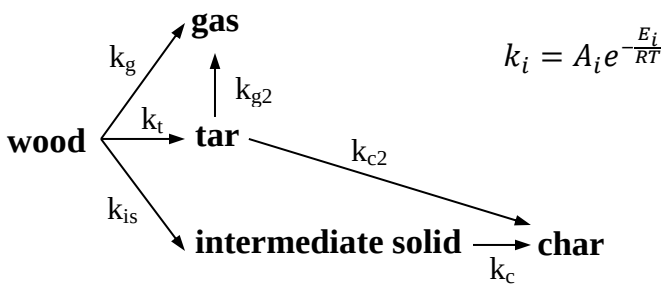

Figure 6. Kinetic mechanism for the base model from Park et al., 2010

Kinetic parameters and thermochemistry for these reactions are chosen by Park, in part from prior literature and in part to match Park's experimental data. Values are listed in Table 7.

Table 7. Base model kinetic parameters and Δh from Park et al., 2010

Reaction	t	g	is	c	c2	g2
A_i (s^{-1})	1.08 x 10^{10}	4.38 x 10^{9}	3.75 x 10^{6a}	1.38 x 10^{10a}	1.0 x 10^{5}	4.28 x 10^{6}
E_i (J/mol)	148,000	152,700	111,700	161,000[a]	108,000	108,000
Δh_i (kJ/kg)	80	80	80	-300[a]	-42	-42

[a]Parameters determined by curve fitting to Park's experimental results

3.1.3 Species Conservation

The conservation of each component in the baseline Park model (Park et al., 2010) is governed by the production and destruction from chemical reactions, as well as convective mass flux for gaseous species. Material properties used in these equations are provided in Table 6 and reaction parameters are given in Table 7.

The densities of solid and gaseous species are defined separately, given by the two equations below.

$$\rho_{solid} = \frac{m_{solid}}{V_{sphere}}$$

$$\rho_{volatiles} = \frac{m_{volatiles}}{\varepsilon V_{sphere}}$$

The change in mass per unit volume for each solid component is solely determined by the pyrolysis reactions.

$$Virgin\ Wood\text{:}\ \frac{\partial \rho_a}{\partial t} = S_a = -\left(k_t + k_g + k_{is}\right)\rho_a$$

$$Intermediate\ Solid\text{:}\ \frac{\partial \rho_{is}}{\partial t} = S_{is} = k_{is}\rho_a - k_c\rho_{is}$$

$$Char^{1}\text{:}\ \frac{\partial \rho_c}{\partial t} = S_c = k_c\rho_{is} + k_{c2}\varepsilon\rho_t$$

Mass conservation of volatiles is dependent on the production of species due to chemical reactions as well as the mass flux through the control volume boundaries. The mass flux of

[1] Equation has been modified from Park et al., 2010 due to errors. Original equation: $\frac{\partial \rho_c}{\partial t} = S_c = k_c\rho_{is} + k_{c2}\rho_t$

each of the gaseous species is based on diffusion and convection; however, in this model, it is assumed that diffusion is very small compared to the convection, and thus is neglected.

$$Tar^{2}: \frac{\partial(\varepsilon\rho_t)}{\partial t} + \frac{1}{r^2}\frac{\partial}{\partial r}(r^2 V\rho_t) = S_t = k_t\rho_a - \left(k_{c2} + k_{g2}\right)\varepsilon\rho_t$$

$$Gas^{3}: \frac{\partial\left(\varepsilon\rho_g\right)}{\partial t} + \frac{1}{r^2}\frac{\partial}{\partial r}\left(r^2 V\rho_g\right) = S_g = k_g\rho_a + k_{g2}\varepsilon\rho_t$$

where ε is the porosity and is calculated by the following:

$$\varepsilon = 1 - \frac{\rho_s}{\rho_w}(1 - \varepsilon_w)$$

Here, ρ_s and ρ_w are the total solid and initial virgin wood masses per unit volume, respectively.

3.1.4 Pressure-Driven Flow

Due to the porous nature of both wood and char, pressure-driven flow within the wood particle is modeled following Darcy's law and is used to calculate the velocity of gaseous species.

$$V = -\frac{B}{\mu}\frac{\partial P}{\partial r}$$

[2] Equation has been modified from Park et al., 2010 due to errors. Original equation: $\frac{\partial(\varepsilon\rho_t)}{\partial t} + \frac{1}{r^2}\frac{\partial}{\partial r}(r^2 V\rho_t) = S_t = k_t\rho_a - \left(k_{c2} + k_{g2}\right)\rho_t$

[3] Equation has been modified from Park et al., 2010 due to errors. Original equation: $\frac{\partial(\varepsilon\rho_g)}{\partial t} + \frac{1}{r^2}\frac{\partial}{\partial r}\left(r^2 V\rho_g\right) = S_g = k_g\rho_a + k_{g2}\rho_t$

where μ is the viscosity and B is the permeability. The permeability is linearly interpolated between virgin wood and char values (Park et al., 2010).

$$B = (1 - \eta)B_w + \eta B_c$$

The degree of pyrolysis, η, is calculated as

$$\eta = 1 - \frac{\rho_a + \rho_{is}}{\rho_w}$$

Tar and gas species are assumed to behave as ideal gases at the temperatures and pressures used in this study.

$$P = P_t + P_g; \;\; P = \frac{\rho RT}{M}$$

where M and R are the molecular weight and the universal gas constant, respectively. The total pressure equation is given by the following (Park et al., 2010):

$$Total\ Pressure: \frac{\partial}{\partial t}\left(\frac{\varepsilon P}{T}\right) - \frac{1}{r^2}\frac{\partial}{\partial r}\left(r^2 \frac{BP}{\mu T}\frac{\partial P}{\partial r}\right) = \left(\frac{R}{M_t}S_t - \frac{R}{M_g}S_g\right)$$

3.1.5 Energy Conservation

As presented in Park et al., 2010, energy conservation within the particle is a balance of thermal conduction, convection of the gaseous species, and the generation of heat from the chemical reactions. Local thermal equilibrium is assumed between the volatiles and solids.

$$\left(c_w\rho_a + c_w\rho_{is} + c_c\rho_c + \varepsilon c_{pt}\rho_t + \varepsilon c_{pg}\rho_g\right)\frac{\partial T}{\partial t} + \left(c_{pt}\rho_t + c_{pg}\rho_g\right)V\frac{\partial T}{\partial r}$$

$$= \frac{1}{r^2}\frac{\partial T}{\partial r}\left(r^2\lambda\frac{\partial T}{\partial r}\right) + Q$$

where

$$Q = -\left(k_t\Delta h_t + k_g\Delta h_g + k_{is}\Delta h_{is}\right)\rho_a - k_c\Delta h_c\rho_{is} - \left(k_{c2}\Delta h_{c2} + k_{g2}\Delta h_{g2}\right)\rho_t$$

Conduction within the particle is represented by an effective conductivity value that represents radiative heat transfer through the pores as well as a weighted average of conductivity properties of volatiles, wood, and char (Park et al., 2010).

$$\lambda = (1-\eta)\lambda_w + \eta\lambda_c + \varepsilon\lambda_v + \frac{13.5\sigma T^3 d}{e}$$

where σ, *e*, and d are the Stefan-Boltzmann constant, emissivity, and pore size, respectively. Thermal conductivities for the wood and char are calculated using the following equations:

$$\lambda_w = \left(\lambda_{w,radial} + \lambda_{w,tangential} + \lambda_{w,grain}\right)/3$$

$$\lambda_c = \left(\lambda_{c,radial} + \lambda_{c,tangential} + \lambda_{c,grain}\right)/3$$

Thermal boundary conditions are determined by external heat transfer, which are discussed in Section 3.3.

3.1.6 Implementation of the Numerical Model

The numerical model was implemented in COMSOL Multiphysics Version 4.3, a commercial software package for multi-physics applications. COMSOL offers a flexible environment that

can numerically solve systems of differential equations using a finite element method. Physical-based equations can easily be implemented into the software to be solved simultaneously, which provides a platform compatible with modeling the complex physics involved in pyrolysis, which includes heat transfer, fluid flow in porous media, and chemical reactions.

COMSOL itself was chosen because of its ability to model all of the different types of physics involved in the pyrolysis process with the ability to specify the equations exactly as presented in Park et al., 2010. In addition, COMSOL provided simple methods to modify mesh size, time steps, and tolerances to verify that the solutions being presented were not dependent on these values. There are many other additional benefits to using COMSOL, including the following:

1. Ease of implementation of physics
2. Flexibility of the software to handle differential equations and boundary conditions
    a. Additional terms can be added to equations through source terms
    b. Any variable can be defined as an equation
    c. General mathematical equations can be used to specify unique physics
3. User-friendly software interface
4. Interface with Excel and Matlab for easy post-processing of results

While there were many advantages to using COMSOL, there were also some drawbacks. Because species conservation equations are written for each individual component, kinetics had to be defined as a source term for each individual species instead of specifying a set of chemical reactions. This is not a major concern for a simple kinetic

mechanism, but becomes very complicated when trying to implement a complex set of reactions that involve a large number of species. Another difficulty in using COMSOL was a lack of spherical coordinates within the software. Input parameters thus had to be adjusted in order to supply COMSOL with the correct form of the differential equations. Additionally, some of the differential equations in the software were defined differently than those presented by Park et al., 2010. This also required adjustments of input parameters in COMSOL to provide the appropriate equations to be solved. Details about the implementation of equations in COMSOL can be found in Appendix E.

Despite the disadvantages of COMSOL, the software provided a suitable platform for modeling the physical and chemical processes involved with the pyrolysis of a wood sphere.

3.2 Method for Determining the Significance of Adaptations Made to the Numerical Model

Modifications were made to the numerical model to improve its compatibility with the experimental setup used in this research. However, a parameter needed to be defined to be able to ascertain the significance of these alterations on the system, as well as determining how well the simulation matched experimental data. In this section, a goodness of fit parameter, ψ, is first presented and defined. Following this, the run-to-run variability between experimental data was calculated using this definition. Lastly, this run-to-run variability was used to select values for ψ that would be used to determine the significance of the effects of modifications to the simulation.

3.2.1 Goodness of Fit Parameter

To compare two sets of data, a method to determine the goodness of fit was specified. This could be used to compare simulation results to experimental data, or to compare two different simulations to each other. The goodness of fit was calculated using the least squares method and defined as ψ.

$$\psi = \sum_{i=0}^{n} (y_i - z_i)^2$$

$$y_i = value\ for\ case\ 1$$

$$z_i = value\ for\ case\ 2$$

3.2.2 Run-To-Run Variability

Three sets of data were used to quantify the variability between experimental runs. The first set considered was temperature profiles up to 450 K. This data set captured the variability in experimental data before the wood really begins to react, minimizing the influence of the chemical reactions. The second data set was the overall temperature profiles. This information provided the differences produced over the entire pyrolysis run. The last set of data analyzed was the mass loss profiles from the TGA data.

Goodness of fit values (ψ) were calculated between similar experimental runs for each of the three data sets specified previously. Values for temperature profiles up to 450 K and overall temperature profiles are presented in Tables 8 through 19, while those for TGA mass loss profiles are given in Table 20.

Sphere Diameter: 2.54 cm, Low Final Particle Temperature (P1-L)

Table 8. ψ calculated between P1-L experimental runs for temperature profiles up to 450 K

	Run 1	Run 2	Run 3	Run 4
Run 1	x	27700	36700	4900
Run 2	-	x	2800	15000
Run 3	-	-	x	19500
Run 4	-	-	-	x

Table 9. ψ calculated between P1-L experimental runs for overall temperature profiles

	Run 1	Run 2	Run 3	Run 4
Run 1	x	81200	126600	56500
Run 2	-	x	47800	108200
Run 3	-	-	x	62800
Run 4	-	-	-	x

Sphere Diameter: 2.54 cm, Medium Final Particle Temperature (P1-M)

Table 10. ψ calculated between P1-M experimental runs for temperature profiles up to 450 K

	Run 1	Run 2
Run 1	x	1300
Run 2	-	x

Table 11. ψ calculated between P1-M experimental runs for overall temperature profiles

	Run 1	Run 2
Run 1	x	57300
Run 2	-	x

Sphere Diameter: 2.54 cm, High Final Particle Temperature (P1-H)

Table 12. ψ calculated between P1-H experimental runs for temperature profiles up to 450 K

	Run 1	Run 2
Run 1	x	2300
Run 2	-	x

Table 13. ψ calculated between P1-H experimental runs for overall temperature profiles

	Run 1	Run 2
Run 1	x	156900
Run 2	-	x

Sphere Diameter: 3.8 cm, Low Final Particle Temperature (P2-L)

Table 14. ψ calculated between P2-L experimental runs for temperature profiles up to 450 K

	Run 1	Run 2	Run 3
Run 1	x	2900	1400
Run 2	-	x	6900
Run 3	-	-	x

Table 15. ψ calculated between P2-L experimental runs for overall temperature profiles

	Run 1	Run 2	Run 3
Run 1	x	55300	28900
Run 2	-	x	158400
Run 3	-	-	x

Sphere Diameter: 3.8 cm, Medium Final Particle Temperature (P2-M)

Table 16. ψ calculated between P2-M experimental runs for temperature profiles up to 450 K

	Run 1	Run 2	Run 3
Run 1	x	22800	15900
Run 2	-	x	3100
Run 3	-	-	x

Table 17. ψ calculated between P2-M experimental runs for overall temperature profiles

	Run 1	Run 2	Run 3
Run 1	x	123600	170500
Run 2	-	x	231600
Run 3	-	-	x

Sphere Diameter: 3.8 cm, High Final Particle Temperature (P2-H)

Table 18. ψ calculated between P2-H experimental runs for temperature profiles up to 450 K

	Run 1	Run 2	Run 3
Run 1	x	~~33900~~[a]	~~61300~~[a]
Run 2	-	x	8500
Run 3	-	-	x

[a]Values were neglected because of thermocouple errors for Run 1. See Section 2.3.

Table 19. ψ calculated between P2-H experimental runs for overall temperature profiles

	Run 1	Run 2	Run 3
Run 1	x	~~195700~~[a]	~~1007200~~[a]
Run 2	-	x	399400
Run 3	-	-	x

[a]Values were neglected because of thermocouple errors for Run 1. See Section 2.3.

TGA Mass Loss Profiles

Table 20. ψ calculated between TGA mass loss profiles

	Run 1	Run 2	Run 3
Run 1	x	0.0073	0.0228
Run 2	-	x	0.0098
Run 3	-	-	x

3.2.3 Definition of Fit Parameters

The goodness of fit values calculated to determine run-to-run variability were used to define fit parameter for the three different data sets studied. First, the average of the ψ values was taken over all of the data in a given data set. The fit parameters were then defined to be half of this average value. Fit parameters are given in Table 21.

Table 21. Fit parameters used to determine the significance of modifications to the numerical model

Validity Range	Fit Parameter	Value
Temperature Profile up to 450 K	β	5700
Overall Temperature Profile	γ	62000
TGA Mass Loss Profile	δ	0.0066

When studying the effects of a modification to the simulation, the fit parameters were used to determine its significance. If the value calculated for ψ was less than the appropriate fit parameter presented in Table 21, then the modification was determined to be insignificant and the effect could be neglected.

3.3 Examination of the External Heat Transfer

Heat transfer to the wood sphere is a critical component of the pyrolysis simulation. The heating of the particle triggers all the physical processes involved in the decomposition of wood into products, and so must be modeled accurately in order to be able to predict the experimental data. The external heat transfer in this research mainly provided by a heated, turbulent nitrogen flow through a tubular reactor which convectively heats the wood sphere as it flows over it. Radiative heat transfer is also a contributor, transferring heat from the reactor walls to the wood particle. However, all of these processes must be approximated by simplified versions which can be applied to a one-dimensional model.

In this section, the convection heat transfer based on geometry and temperature is presented first. Following this, the effect on the convection from blowing cause by gas-phase species leaving the wood particle is discussed. Lastly, the contribution of radiation to the external heat transfer is examined.

3.3.1 Convection Heat Transfer Based on Geometry and Temperature

External convective heat transfer coefficients based on the temperature and geometry of the experimental setup were calculated from the correlation presented in Whitaker, 1972 for flow past a single sphere.

$$Nu = 2 + \left(0.4Re_D^{1/2} + 0.06Re_D^{2/3}\right)Pr^{0.4}\left(\frac{\mu}{\mu_s}\right)^{1/4}$$

However, the convection heat transfer from the heated nitrogen in the reactor to the wood sphere is much more complex than this simple correlation, as the flow combines turbulent pipe flow with external flow over a sphere.

To determine how well the correlation matches the experimental conditions, experiments were performed with aluminum spheres using the same procedure as that for the wood pyrolysis experiments. Seven runs were done covering three different diameters and three different gas temperatures. Temperature profiles were measured at the center of the aluminum spheres. These temperature profiles were then compared to a one-dimensional lumped capacitance analytical model, which is valid for $Bi < 0.1$, corresponding to a convection coefficient less than 465 W/m^2K. The heat transfer coefficient in the analytical model was modified until the goodness of fit, ψ, between the aluminum sphere experimental and analytical profiles was minimized. This value was then taken to be the experimental heat transfer coefficient.

A comparison between the heat transfer coefficients determined experimentally and the value calculated from Whitaker's correlation (1972) are presented in Table 22, along with the difference between the two.

Table 22. Convection heat transfer coefficients determined experimentally and using the correlation presented by Whitaker, 1972 for flow past a single sphere

Run #	Sphere Diameter (cm)	Initial Temperature (°C)	Final Temperature (°C)	$h_{experimental}$ (W/m^2K)	$h_{correlation}$ (W/m^2K)	Difference (%)
1	3.81	23	470	57.57	50.93	12%
2	2.54	30.5	371.45	67.68	56.08	17%
3	1.27	31.75	382.5	86.66	79.42	8%
4	1.27	31.65	420.9	96.95	82.01	15%
5	2.54	36.44	425.39	66.63	58.54	12%
6	1.27	33.83	431.3	87.15	82.60	5%
7	2.54	30	431	68.37	58.86	14%

While the error between the experimental and correlation heat transfer coefficients is as high as 17%, this lies within the error presented by Whitaker, 1972 for the correlation for flow past a single sphere, which is given as ±30%. A plot of the experimental versus correlation heat transfer coefficients is shown in Figure 7.

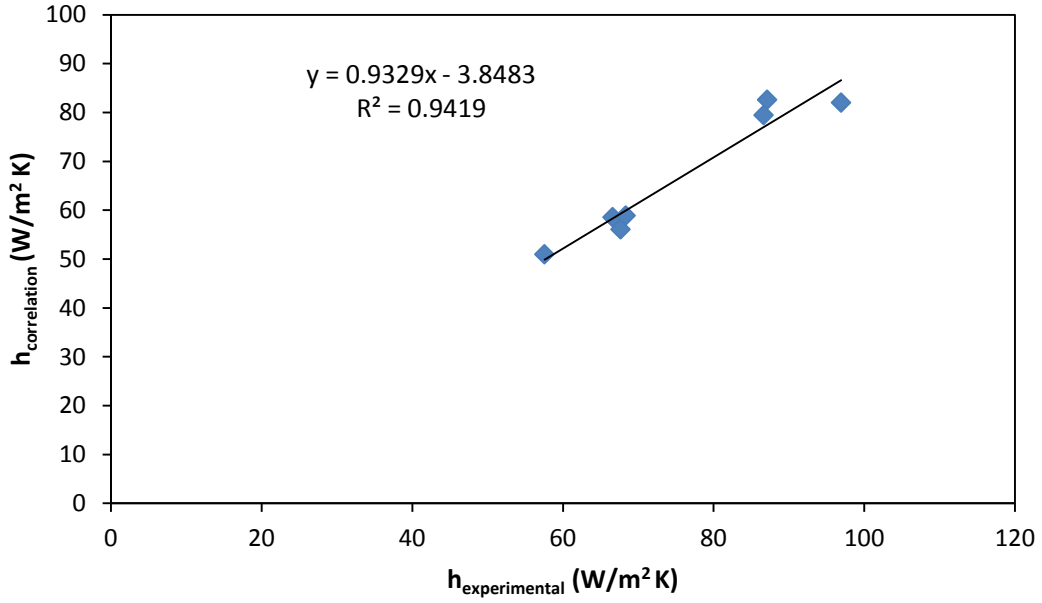

Figure 7. Comparison of correlation and experimental convection heat transfer coefficients

From this plot, it can be seen that the correlation values match the experimental values fairly well without much scatter.

The effect of the discrepancies in heat transfer coefficients between experimental and correlation values was studied in the wood sphere pyrolysis simulation to determine the extent of the change in temperature profiles. To compare these two, the wood pyrolysis model was set up for each of the aluminum sphere experimental conditions and run with the experimentally determined heat transfer coefficient as well as the coefficient calculated from Whitaker's correlation (1972). Material properties used in the models are discussed in Section 3.4.1. A goodness of fit, ψ, was then calculated by comparing the temperature profiles from each of the two simulations. The results are presented in Table 23. Differences in the heat transfer coefficients are insignificant if ψ is less than γ, the fit parameter calculated from the run-to-run variability between experimental temperature profiles.

Table 23. Goodness of fit comparing simulations using heat transfer coefficients determined experimentally and with the correlation presented by Whitaker, 1972 for flow past a single sphere

Run #	Sphere Diameter (cm)	Initial Temperature (°C)	Final Temperature (°C)	$h_{experimental}$ (W/m^2K)	$h_{correlation}$ (W/m^2K)	Goodness of Fit
1	3.81	23	470	57.57	50.93	435000
2	2.54	30.5	371.45	67.68	56.08	56000
3	1.27	31.75	382.5	86.66	79.42	5000
4	1.27	31.65	420.9	96.95	82.01	37000
5	2.54	36.44	425.39	66.63	58.54	184000
6	1.27	33.83	431.3	87.15	82.60	4000
7	2.54	30	431	68.37	58.86	262000

From the goodness of fit values, it can be seen that the discrepancy in convective heat transfer coefficients is significant for three of the seven runs, which correspond to the runs with higher temperatures and larger wood diameters.

Four of the seven runs done with conditions from the aluminum sphere experiments had a similar setup to experimental runs done with wood spheres. Because the purpose of this modeling is to match experimental outputs, these runs were compared to an average experimental temperature profile with the appropriated experimental conditions. Table 24 gives the details of average experimental conditions that match each of the four runs.

Table 24. Parameters for model runs done for analysis of convective heat transfer coefficients that were similar to wood sphere pyrolysis experiments

Run #	Sphere Diameter (cm)	Final Temperature (°C)	Comparable Experimental Setup	Experimental Sphere Diameter (cm)	Average Experimental Final Temperature (°C)
1	3.81	470	P2-H	3.81	480.4
2	2.54	371.45	P1-L	2.54	370.4
5	2.54	425.39	P1-M	2.54	425.6
7	2.54	431	P1-M	2.54	425.6

The simulation was run with the same initial and final temperatures as the average wood experimental temperature profiles, but with the same correlation and experimental heat transfer coefficients as described in Table 22. This provided a way to study the effect of the heat transfer coefficient in relation to the experimental data without the additional uncertainty introduced by differences in initial and final temperatures. Material properties used in the models are discussed in Section 3.4.1. Plots comparing average experimental temperatures to the simulation runs with the heat transfer coefficient determined with experimentally or through Whitaker's correlation (1972) are given in Figures 8 through 11. In these plots, temperature data after the center had reached steady-state conditions was removed to provide more detail in the noteworthy sections of the profiles.

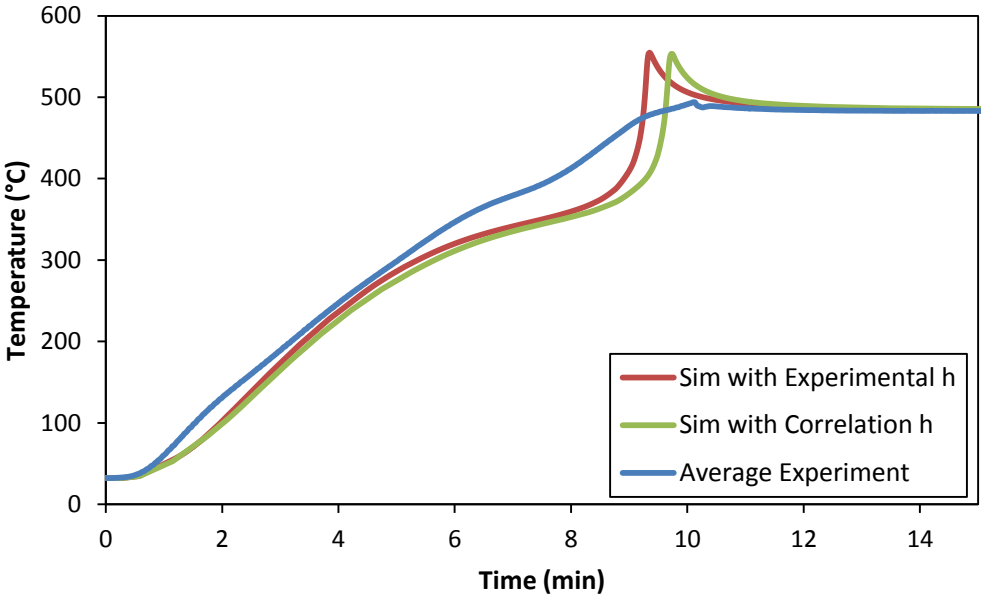

Figure 8. Temperature profiles comparing experiments to the simulation run with experimental and correlation convection heat transfer coefficients for Run 1

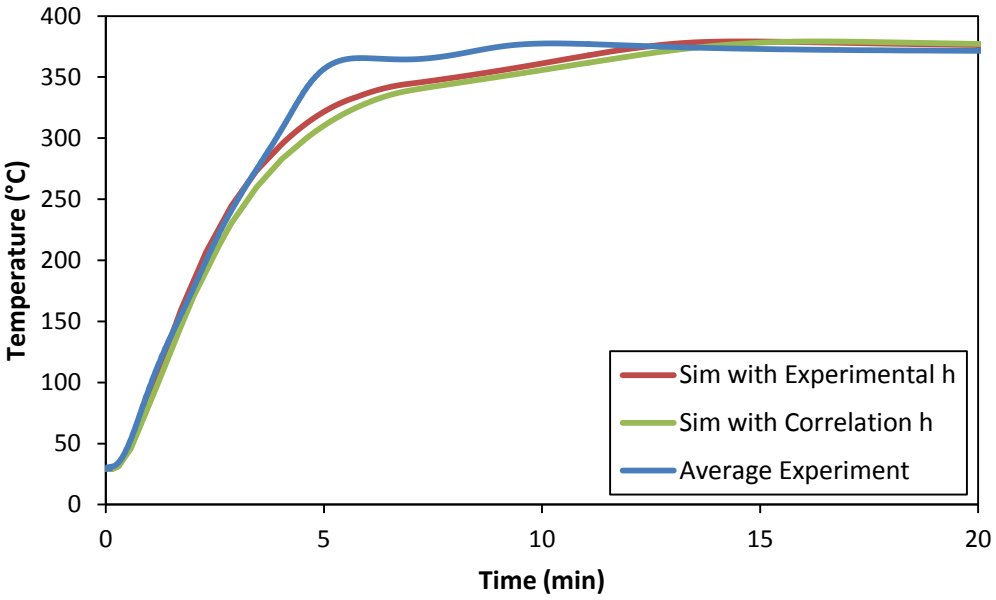

Figure 9. Temperature profiles comparing experiments to the simulation run with experimental and correlation convection heat transfer coefficients for Run 2

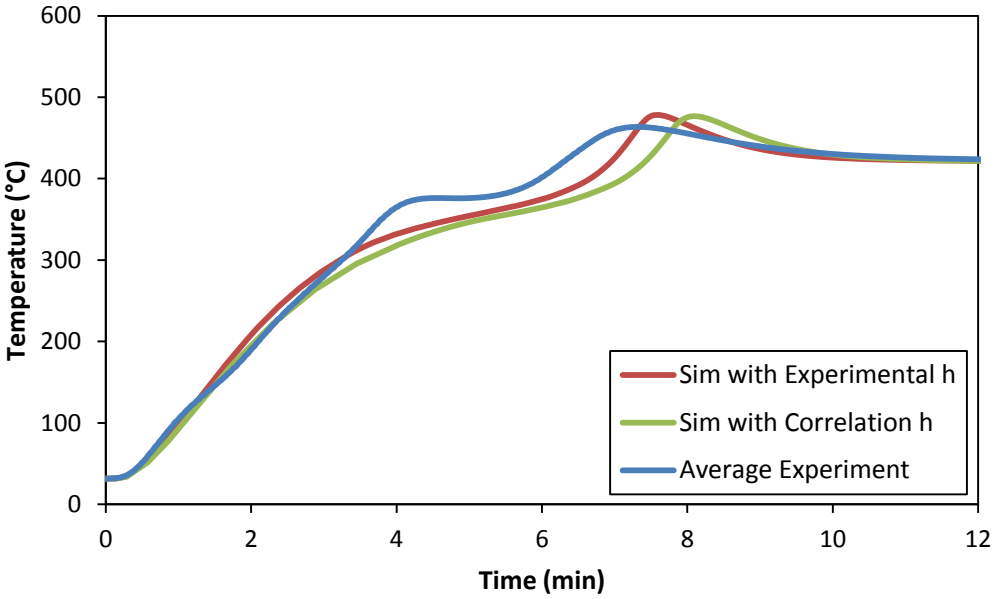

Figure 10. Temperature profiles comparing experiments to the simulation run with experimental and correlation convection heat transfer coefficients for Run 5

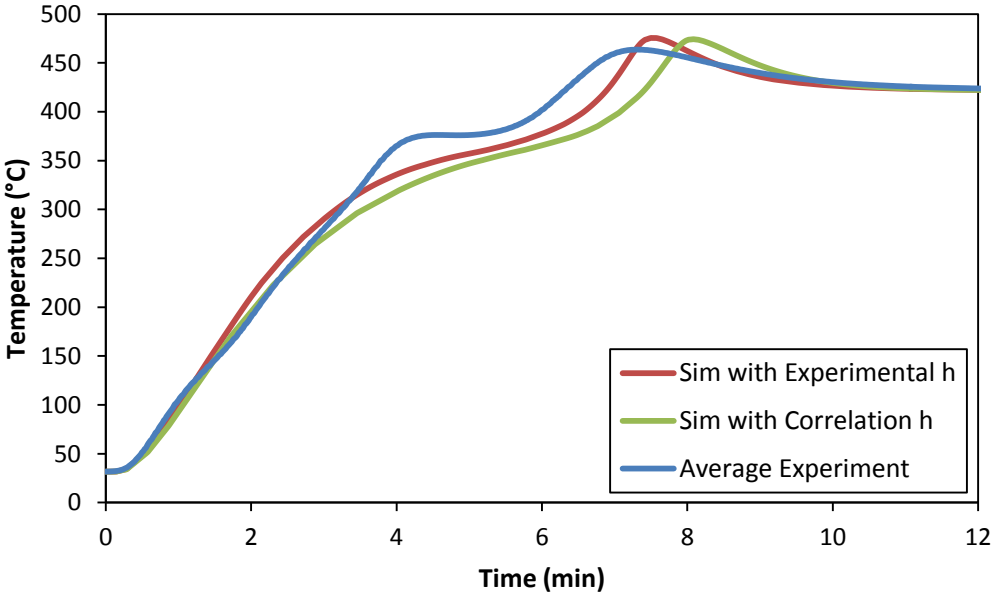

Figure 11. Temperature profiles comparing experiments to the simulation run with experimental and correlation convection heat transfer coefficients for Run 7

From these figures, it can be seen that the temperature profiles with the heat transfer coefficient determined with the correlation slightly trail those from the experimentally determined heat transfer coefficient. This is reasonable because the correlation heat transfer coefficients are smaller than the experimental values, which would cause the wood particle to heat up slower. Also, while the discrepancy in heat transfer coefficients causes a delay in the temperature profile, it does not alter the basic shape predicted by the simulation.

To quantitatively compare the two simulation temperature profiles to the experimental temperature profiles, a goodness of fit, ψ, was calculated between the simulation and experiments for both the experimentally determined heat transfer coefficient as well as the one determined with the correlation. Results of this study are listed in Table 25. Temperature profiles were only compared up to 450 K so that values were not strongly affected by the kinetic mechanism implemented in the simulation.

Table 25. Goodness of fit comparing simulation temperature profiles with heat transfer coefficients determined both experimentally and with Whitaker's correlation (1972) to experimental temperature profiles

Run #	Sphere Diameter (cm)	Final Temperature (°C)	Comparable Experimental Setup	Goodness of Fit for $h_{experimental}$	Goodness of Fit for $h_{correlation}$
1	3.81	470	P2-H	67000	85000
2	2.54	371.45	P1-L	3000	12000
5	2.54	425.39	P1-M	7000	6000
7	2.54	431	P1-M	8000	6000

From the goodness of fit values calculated for these few cases, the experimentally determined heat transfer coefficient gives an overall better fit to the wood pyrolysis temperature data than the coefficients determined using Whitaker's correlation (1972). A more thorough study in the future would be useful to determine whether these findings are

consistent over a larger data set than the few runs analyzed here. Approximate experimental heat transfer coefficients for this future investigation could be calculated by first determining the heat transfer coefficient from Whitaker's correlation (1972), after which an approximate experimental value could be calculated using the correlation presented in Figure 7. While Whitaker's correlation (1972) was used to determine heat transfer coefficients in this research, further exploration might suggest that an approximate experimental heat transfer coefficient would better represent the convective heat transfer transpiring between the heated nitrogen flow and wood sphere.

3.3.2 Modification of Convection Heat Transfer Due to Blowing

While the aluminum spheres used experimentally were able to predict the impact of geometry and temperature on the convection heat transfer, they were not able to capture the effect of gases leaving the surface of the particle. To estimate this effect, blowing was added to the model following the effect of transpiration on the turbulent thermal boundary layer from Kays and Crawford, 1980. While these effects were developed for flow over a flat plate, they give an estimate of the magnitude of the effect to determine its significance. The following equations are presented in Kays and Crawford, 1980 and represent the modification due to blowing.

$$\frac{St}{St_0} = \frac{b_h}{e^{b_h} - 1}$$

where

$$b_h = \frac{V_0/u_\infty}{St_0}$$

$St_0 = Stanton\ number\ for\ no\ transpiration\ at\ the\ same\ Reynolds\ number$

$V_0 = velocity\ perpendicular\ to\ the\ surface$

$u_\infty = free\ stream\ velocity$

The ratio of the Stanton number is equal to the ratio of h, the heat transfer coefficient. Because of this, the heat transfer coefficient with modification due to blowing is defined as the following.

$$h = h_0 \left(\frac{b_h}{e^{b_h} - 1}\right)$$

where b_h has been expressed in terms of different variables

$$b_h = \frac{V_0 D}{\alpha N u_0}$$

$D = sphere\ diameter$

$\alpha = thermal\ diffusivity$

$Nu_0 = Nusselt\ number\ for\ no\ transpiration$

In this equation, V_0 was expressed as the instantaneous velocity of total volatiles at the surface of the particle as provided by the model.

After modification to the convection heat transfer coefficient from blowing was added to the model, the significance of this effect was studied. To determine this, the temperature profiles from the model run with and without blowing were compared. If the difference in the

goodness of fit, ψ, between the two runs was less than γ, the fit parameter calculated from the run-to-run variability between experimental temperature profiles, than the effect of blowing can be neglected. Table 26 gives the goodness of fit for each of the conditions used for comparison to experimental data. Material properties used in these models are discussed in Section 3.4.1.

Table 26. Goodness of fit comparing simulation temperature profiles with and without blowing

Run #	Sphere Diameter (cm)	Initial Temperature (°C)	Final Temperature (°C)	Goodness of Fit
P1-L	2.54	29.1	371.2	10
P1-M	2.54	31.7	421.4	490
P1-H	2.54	33.4	474.1	7900
P2-L	3.8	29.2	373.4	70
P2-M	3.8	31.0	417.8	2000
P2-H	3.8	32.3	484.3	1200

From the goodness of fit values, it can be seen that blowing is insignificant and can be neglected.

3.3.3 Radiation Heat Transfer

Convection is the major mode of heat transfer to the wood particle; however, radiation could also provide a significant contribution. Although the experimentally determined heat transfer coefficients for the aluminum spheres included radiative heat fluxes as part of the effective heat transfer coefficient, the impact of radiative heat transfer would be larger in wood experiments because of the higher emissivity of wood and char (0.7 and 0.92 for wood and char emissivities, respectively, versus 0.05 for the emissivity of aluminum). To determine if

this effect is important, radiative heat transfer was added to the model and the temperature profiles with and without radiation were compared. If the difference in goodness of fit values was less than that from the variability between experimental runs, than the radiative heat transfer can be neglected.

In the experimental setup, the wood sphere is located in a T-section of the reactor that is insulated, but not heated. A short distance both upstream and downstream from the sphere, the walls of the reactor are heated to ensure a constant temperature of the nitrogen flow as it reaches the sphere. The temperature of the reactor walls in this heated section is known to be the same temperature as the nitrogen; however, the temperature is unknown for the walls in the insulated section. This section reports on the radiative heat transfer due to (1) the heated sections adjacent to the section containing the wood and (2) the insulated section into which the wood was inserted.

To determine the radiative heat transfer from the reactor walls to the wood sphere, the view factors were first calculated. The wood sphere is assumed to be enclosed by a cylinder, where the side walls are the insulated section of the reactor, and the two ends are substituted for the heated section of the reactor. The impact of lower temperature in the T-section of the reactor is not considered. Figure 12 shows the simplified geometry used to calculate the view factors. In this image, R_1 is the radius of the reactor, represented by the cylinder, R_2 is the radius of the wood sphere, and H is the distance from the wood sphere to the heated section of the reactor.

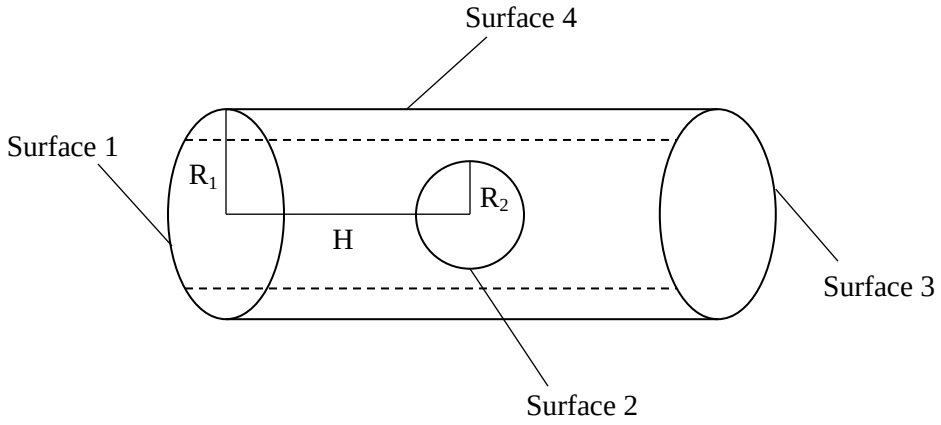

Figure 12. Simplified geometry of the reactor and wood sphere used to calculate radiative view factors from the sphere to the reactor walls

Calculations for the view factor of the heated section were done based on an equation presented by Howell, 1982 for radiation from a disc to a sphere. Surface 1 is the disc at the end of the cylinder, while Surface 2 is the wood sphere.

$$F_{1\to 2} = 2r_2^2\left(1 - \frac{1}{\sqrt{1+\frac{1}{h^2}}}\right) \qquad h = \frac{H}{R_1}, r_2 = \frac{R_2}{R_1}$$

Measurements from the reactor needed for the view factor calculation are given in Table 27.

Table 27. Measurements of the wood sphere and reactor for view factor calculations.

Variable	Definition	Value	Units
R_1	Radius of the reactor	2.625	cm
R_2	Radius of the wood sphere	1.27, 1.905	cm
H	Distance from the heated section of the reactor to the center of the wood sphere	7.5	cm

While the equation above evaluates the view factor from the disc to the sphere, the view factors presented here are from the sphere to the disc. The equation to convert between these two values is presented below.

$$F_{2\to1} = \frac{A_1}{A_2} F_{1\to2}$$

Because the geometry is identical for Surface 1 and Surface 3, view factor for the heated section of the reactor is twice that from the wood sphere to a single disc.

The view factor from the wood sphere to the insulated walls must also be calculated. Since the view factor from the sphere to itself is zero, the view factor from the sphere to the insulated walls is unity minus the view factor to Surfaces 1 and 3, as shown in the equation below.

$$F_{2\to4} = 1 - F_{2\to1\&3} = 1 - 2F_{2\to1}$$

Table 28 gives the view factors calculated for the two different sphere sizes. Note that R_2^2 appears in both r_2 and A_2, making the view factors independent of sphere size.

Table 28. Calculated view factors from the wood sphere to the heated and insulated reactor walls

Wood Sphere Radius	$F_{2\to1\&3}$	$F_{2\to4}$
1.27 cm	0.056	0.944
1.905 cm	0.056	0.944

Contribution of Adjacent Heated Walls

The view factors from the wood sphere to the heated walls are very small and their impact on the temperature profiles should be trivial. To verify this, the view factors were used to add radiative heat transfer from the heated walls to the model. The surface emissivity for the particle was calculated according to Park et al., 2010. Values for e_s and e_w are presented in Table 6 in Section 3.1.1.

$$\begin{cases} e_s = e_w & T_s < 450\ K \\ e_s = e_w + \dfrac{T_s - 450}{550 - 450}(e_c - e_w) & 450\ K \leq T_s \leq 550\ K \\ e_s = e_c & 550\ K\ <\ T_s \end{cases}$$

The simulation was run with and without radiation from the heated reactor walls for each of the conditions ran experimentally. A goodness of fit, ψ was then evaluated by comparing the temperature profiles from each of the simulations. Table 29 gives the goodness of fit for each of the conditions studied.

Table 29. Goodness of fit comparing the simulation with and without radiation from the heated section of the reactor walls

Run #	Sphere Diameter (cm)	Initial Temperature (°C)	Final Temperature (°C)	Goodness of Fit
P1-L	2.54	29.1	371.2	0.001
P1-M	2.54	31.7	421.4	0.01
P1-H	2.54	33.4	474.1	0.05
P2-L	3.81	29.2	373.4	0.005
P2-M	3.81	31.0	417.8	0.06
P2-H	3.81	32.3	484.3	0.2

From the goodness of fit values, which are much less than γ, it can be seen that the radiative heat transfer from the heated walls of the reactor has a negligible effect on the temperature profiles and can be neglected in the numerical model.

Contribution of Insulated Walls

The radiative heat transfer to the wood particle from the insulated walls could not be directly evaluated and implemented in the model to determine its significance due to the complex shape of the T-section of the reactor and because the temperature could not be measured over the entire insulated surface. However, the initial rate of heat transfer could be estimated at various wall temperatures and compared to the initial convection heat transfer to estimate its relevance.

Table 30 presents initial values of the convective heat transfer from the heated nitrogen and radiative heat transfer from the insulated walls for the six different cases studied experimentally. Radiation is presented for two different wall temperatures to encompass the maximum and minimum values anticipated from the experimental setup.

Table 30. Comparison of initial heat transfer due to radiation from insulated reactor walls to initial convection heat transfer

Run #	T_{final} (°C)	Initial $\dot{Q}_{conv}$ (W)	Initial $\dot{Q}_{rad,insulated\ walls}$ (W)	
			T_{walls} = 250°C	T_{walls} = 450°C
P1-L	371.2	38.93	5.78	21.10
P1-M	421.4	46.18	5.78	21.10
P1-H	474.1	54.39	5.78	21.10
P2-L	373.4	72.59	12.93	47.23
P2-M	417.8	84.54	12.93	47.23
P2-H	484.3	103.98	12.93	47.23

Comparing the radiative heat transfer to the convection, it can be seen that even at the low wall temperatures, the heat transfer due to radiation is at least 10% of the convective heat transfer. Since the temperature profiles have been shown to be sensitive to the convective heat transfer coefficient, and thus to the convection, this indicates that the radiation from the insulated walls is a significant factor.

Wall temperature measurements were done at discrete locations along the insulated section of the reactor for two different temperature settings to provide some information on the temperature of the reactor walls. Table 31 gives the minimum, maximum, and average wall temperatures measured for the two experimental setups.

Table 31. Maximum, minimum, and average wall temperatures taken at discrete locations of the insulated section of the reactor

Operating Temperature	Minimum Wall Temperature (°C)	Maximum Wall Temperature (°C)	Average Wall Temperature (°C)
Medium (~420°C)	285	324	298
High (~480°C)	270	372	334

From these values, it can be seen that the two temperatures used in Table 30 contain the wall temperatures measured experimentally and provide adequate bounds for the estimation of the effect of radiation from the insulated section of the reactor.

While a few measurements were done on the wall temperatures of the insulated section of the reactor, there was not enough information to implement the effect of radiation in the current model. Future research is needed to more thoroughly investigate the effect of the radiative heat transfer from the insulated walls and to include its effect in the model for a more accurate simulation.

3.4 Optimization of Parameters in the Numerical Model

In order to accurately determine the ability of a numerical model to predict the pyrolysis of a wood sphere, select parameters must be modified to match the experimental setup. After the model has been adapted, it can be evaluated against experimental data to determine how well it is able to predict the outputs from the experimental pyrolysis of wood.

In this section, the procedure for optimizing the material properties presented by Park et al., 2010, is first presented. Following this, the optimization of a few select parameters in the kinetic mechanism is discussed.

3.4.1 Material Properties

Material properties play a vital role in the physical phenomena that occur during the pyrolysis of a wood particle. Unfortunately, due to the variability of wood and the many additional factors that affect the properties of char, including the final temperature, heating rate, and particle size, it was impractical to directly measure material properties; sufficient material properties were also not available in the literature.

A sensitivity analysis was done on all the material properties that were used in the model developed by Park et al., 2010 to determine which ones were significant. Following this, experimental temperature profiles were used to first determine the relevant char properties, and then the wood properties.

3.4.1.1 Sensitivity Analysis

In order to determine which material properties had a significant impact on the simulation, and therefore which properties needed to be determined for this experimental setup, a sensitivity analysis was done on all of the wood and char properties used in the model presented by Park et al., 2010. Two parameters were chosen to determine the significance of each of the material properties. The first parameter was the time for the temperature at the center of the wood sphere to reach 450 K. This value illustrated the impact of a material property on the timing of the temperature profile, and since the temperature cutoff is fairly low, was not strongly affected by the kinetics used in the model. The second parameter that was used was the peak temperature reached in the simulation. This parameter showed the impact of a material property on the overall temperature profile. The following were used as sensitivity variables to determine which material parameters were significant. Nominal values in these equations were obtained using the properties as they are presented in the Park paper.

$$\zeta_{450K} = \frac{\Delta\, time}{nominal\ time}$$

$$\zeta_{peak\ T} = \frac{\Delta\, peak\ temperature}{nominal\ peak\ temperature}$$

After the sensitivity parameters were established, a literature search was done to determine the range of acceptable values for the parameters to be studied. If little or no data existed for a specific variable without extensive research, the range of values was taken from an order of magnitude below the original value from Park et al., 2010, to an order of

magnitude above. Minimum and maximum values for each of the material properties in the sensitivity analysis are given in Table 32.

Table 32. Minimum and maximum values of the material properties used for the sensitivity analysis

Property	Original Value	Min Value	Max Value	Units
ρ_w	630	300	945	kg/m^3
c_w	1500 + 1.0*T	670	4214	J/kg K
c_c	$420 + 2.09*T + 6.85 \times 10^{-4}*T^2$	670	2520	J/kg K
c_{pt}	$-100 + 4.4*T - 1.57 \times 10^{-3}*T^2$	$0.5*c_{pt}$	$1.5*c_{pt}$	J/kg K
c_{pg}	$770 + 0.629*T - 1.91 \times 10^{-4}*T^2$	$0.5*c_{pg}$	$1.5*c_{pg}$	J/kg K
d_w	5×10^{-5}	5×10^{-6}	5×10^{-4}	m
d_c	1×10^{-4}	1×10^{-5}	1×10^{-3}	m
λ_w	0.204	0.074	0.4	W/m K
λ_c	0.094	0.0412	0.1156	W/m K
k_v	0.0258	0.015	0.0387	W/m K
B_w	5×10^{-16}	5×10^{-17}	5×10^{-15}	m^2
B_c	1×10^{-13}	1×10^{-14}	1×10^{-12}	m^2
μ	3×10^{-5}	3×10^{-6}	3×10^{-4}	kg/m s
ε_w	0.4	0.25	0.6	-

Once the range of values was decided for each of the material properties, the simulation was run holding all but one of the parameters constant, and then setting that value to first the minimum, and then the maximum value. After all of the material properties were run, the sensitivity variables were compared to determine which parameters were important. The results of this sensitivity analysis are given in Figures 13 and 14 for ζ_{450K} and $\zeta_{peak\ T}$, respectively.

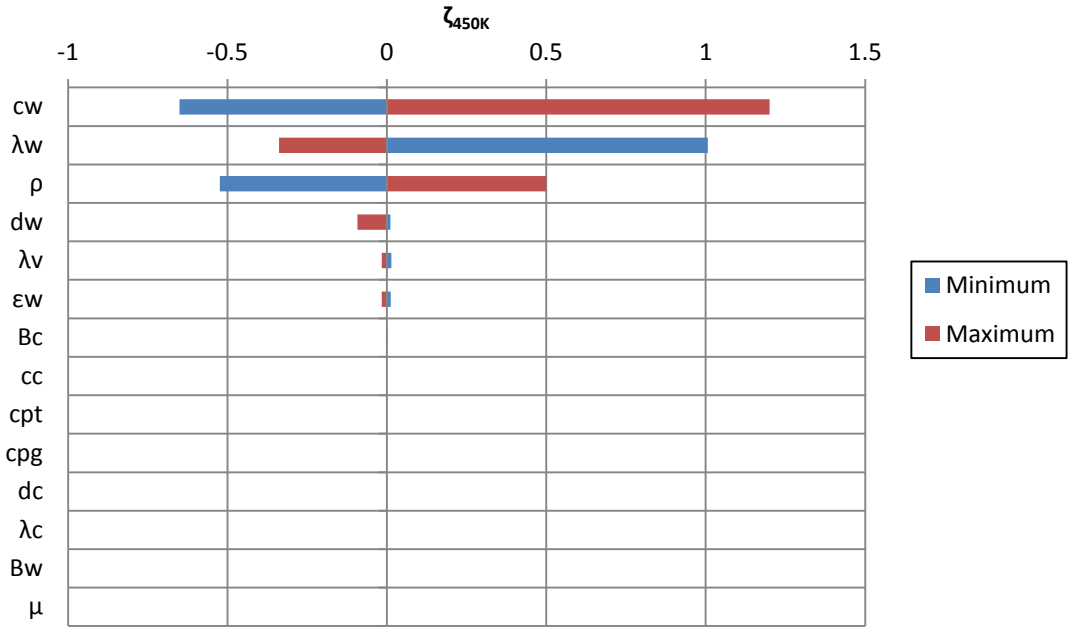

Figure 13. Sensitivity of ζ_{450K} to material properties. Minimum and maximum values are given in Table 32.

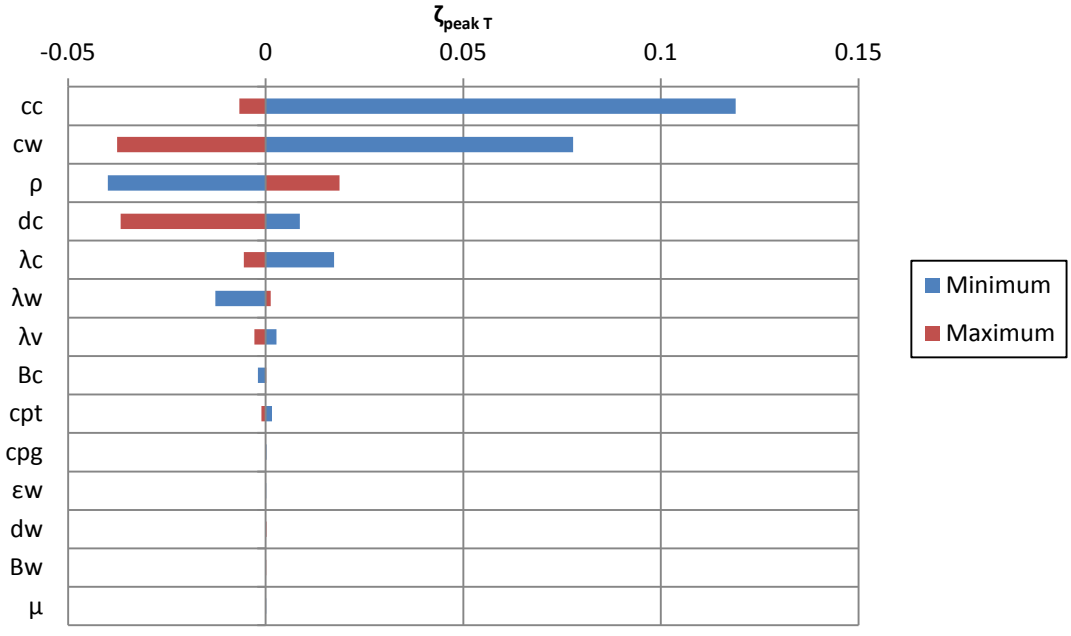

Figure 14. Sensitivity of ζ_{peak} T to material properties. Minimum and maximum values are given in Table 32.

From this study, the significant material properties are presented in Table 33.

Table 33. Significant material properties determined from the sensitivity analysis

Parameter	Definition
ρ_w	Wood density
λ_w	Wood thermal conductivity
c_w	Wood specific heat
λ_c	Char thermal conductivity
c_c	Char specific heat
d_c	Char pore size

The only value from these parameters that could be directly measured was the wood density. This parameter was determined by calculating the density of each of the 17 wood spheres used experimentally from mass and volume measurements, and then taking the average value. The wood density used in the model is given in Table 34.

Table 34. Measured density of poplar wood averaged over 17 samples

Parameter	Definition	Value	Units
ρ_w	Density of poplar wood	509.2	kg/m^3

The other parameters were determined by finding the parameter values that gave a best fit to experimental temperature data, as described in Section 3.4.1.2.

3.4.1.2 Experimental Data used for Material Parameter Optimization

Wood properties were optimized against the two experimental runs performed with a wood sphere diameter of 2.54 cm at a medium final particle temperature. However, there was not

enough experimental data of the reinsertion of the char in this data set to use for the optimization of the char properties. For this reason, a previous set of temperature data from the pyrolysis of poplar wood spheres purchased from Lowes was used to evaluate char properties. While the poplar was not identical to the wood used for the experimental data used in the rest of this research, it provided enough data from the reinsertion of char particles to determine the char properties.

Experimental procedures for the older data set followed those described in Section 2.3. For these runs, wood spheres with a diameter of 2.54 cm were pyrolyzed at a medium final particle temperature. Experimental conditions are provided in Table 35.

Table 35. Experimental conditions for char reinsertion runs done with Lowes poplar

Run	Initial Char Temperature (°C)	Final Char Temperature (°C)
1	93.8	413.4
2	103.5	416.1

3.4.1.3 Optimization of Char Properties

From the five remaining unknown material properties, the three char values were determined first. Ideally, the wood properties could be determined independently of the kinetics or char properties; however, experimentally, the surface of the wood begins to react too quickly to get useful information from the temperature data before other factors begin to influence the results. Therefore, the char properties were determined first and then added to the model that was used to determine the wood properties.

The model used for comparison to the char temperature data was identical to the Park wood model with initial conditions modified to match the experimental conditions for reheating the char. This included modifying the initial and final temperatures, particle size, convective heat transfer coefficient, and char density. Although a kinetic mechanism was included in this model, the initial conditions used for the char runs do not meet the conditions needed to initiate the chemical reactions, providing an inert system that matches the char experiments while removing the possibility of introducing additional errors through the creation of a new model. Both the Park model and the model implementing Gauthier kinetics (see Section 3.5) gave identical results, as expected, so the Park model was used for these calculations because of its shorter computational time.

The density of char, presented in Table 36, was first calculated using mass and volume measurements of the char particles formed during the two experimental char runs.

Table 36. Measured density of char formed from Lowes poplar spheres with a 2.54 cm diameter pyrolyzed at a medium temperature

Parameter	Definition	Value	Units
ρ_c	Density of char	268	kg/m^3

Due to the fact that the final shape of the char particle was an ellipsoid, an equivalent diameter was calculated to approximate the ellipsoid as a sphere for use in the one-dimensional spherical model. While the char had three different diameter dimensions, the two smaller diameters were close to the same value, so the ellipsoid was approximated as having one larger diameter and two smaller diameters of the same size to simplify the calculations. The small diameter was taken as an average of the measured values for the two smaller diameter sizes. The following equations were used to calculate the equivalent diameter.

$$\frac{Volume_{equivalent\ sphere}}{Surface\ Area_{equivalent\ sphere}} = \frac{Volume_{ellipsoid}}{Surface\ Area_{ellipsoid}}$$

$$\frac{1}{6}D_{eq} = \frac{Volume_{ellipsoid}}{Surface\ Area_{ellipsoid}}$$

$$V_{ellipsoid} = \frac{4}{3}\pi a^2 b, \qquad a = a < b$$

$$Surface\ Area_{ellipsoid} = 2\pi a^2\left(1 + \frac{b}{ae}sin^{-1}e\right), \qquad e^2 = 1 - \frac{a^2}{b^2}$$

Table 37 gives values used to calculate the char equivalent diameter, both the measured quantities and those calculated using the above equations. Also included is the calculated equivalent diameter.

Table 37. Measured and calculated values used to calculate the char equivalent diameter used to approximate the char ellipsoid as a sphere for use in the one-dimensional numerical model

Parameter	Definition	Value	Units
a	Smaller radius of ellipsoid (a = a < b)	8.5	mm
b	Larger radius of ellipsoid (a = a < b)	10.75	mm
$V_{ellipsoid}$	Volume of ellipsoid	3253	mm^3
Surface $Area_{ellipsoid}$	Surface area of ellipsoid	1072	mm^2
D_{eq}	Equivalent diameter	18.2	mm

The equivalent diameter calculated above was also used to compute an approximate convective heat transfer coefficient using the correlation for flow past a single sphere presented in Whitaker, 1972. The heat transfer coefficient is given in Table 38.

Table 38. Convective heat transfer coefficient calculated for char using the equivalent diameter in the correlation for flow past a single sphere presented in Whitaker, 1972

Parameter	Value	Units
h	66.72	W/m K

Once the parameters used to describe the setup of the char experiments were determined, a range of values for the char properties to be studied needed to be established. The range of values for λ_c, c_c, and d_c were chosen to match that used in the sensitivity analysis and are shown in Table 39, along with the initial step sizes taken in this study.

Table 39. Range and step size of values used to optimize the char material properties

Parameter	Value Range	Initial Step Size	Units
λ_c	0.04-0.12	0.01	W/mK
c_c	650-2250	100	J/kg K
d_c	$1x10^{-5}$-$1x10^{-3}$	variable	m

The Park char model was run for every combination of λ_c, c_c, and d_c values in their given ranges. A goodness of fit, ψ, was evaluated for each of the simulation runs by comparing the temperature profiles to the experimental data from the two char experiments. Only values up to the maximum temperature were used for this calculation. The average of these two ψ values was taken and the material properties that corresponded to the minimum average ψ were taken as the best fit parameters.

During this study, the best fit parameters reached the imposed maximum for λ_c, 0.12 W/mK. This range was expanded to determine properties that were not artificially determined based on the imposed limits; however, char thermal conductivity reached values that were far-removed from the range used for this optimization, which was determined from values found in the literature (Kung and Kalelkar, 1973; Hankalin et al., 2009). There are many reasons for

these large discrepancies, including modeling a three-dimensional experimental setup with anisotropic properties as a one-dimensional geometry with isotropic properties, approximating an ellipsoid with an equivalent sphere, a non-homogeneous initial temperature within the char particle, or the fact that the thermocouple may not fit as well in the char due to shrinkage during the pyrolysis process. Also, there may be some residual reactivity of the char during the reinsertion and successive heating that could affect the temperature profile. Due to these unrealistic values and the many sources for error, the ranges for the char thermal conductivity was regulated to its initial values and the best fit parameters were determined within these bounds. The final char properties used in this research are given in Table 40.

Table 40. Optimized char material properties

Parameter	Value	Units
λ_c	0.12	W/m K
c_c	2050	J/kg K
d_c	1×10^{-5}	m

The comparison of temperature profiles between the experiments and simulation using the best fit parameters are given in Figures 15 and 16 for experimental runs 1 and 2, respectively.

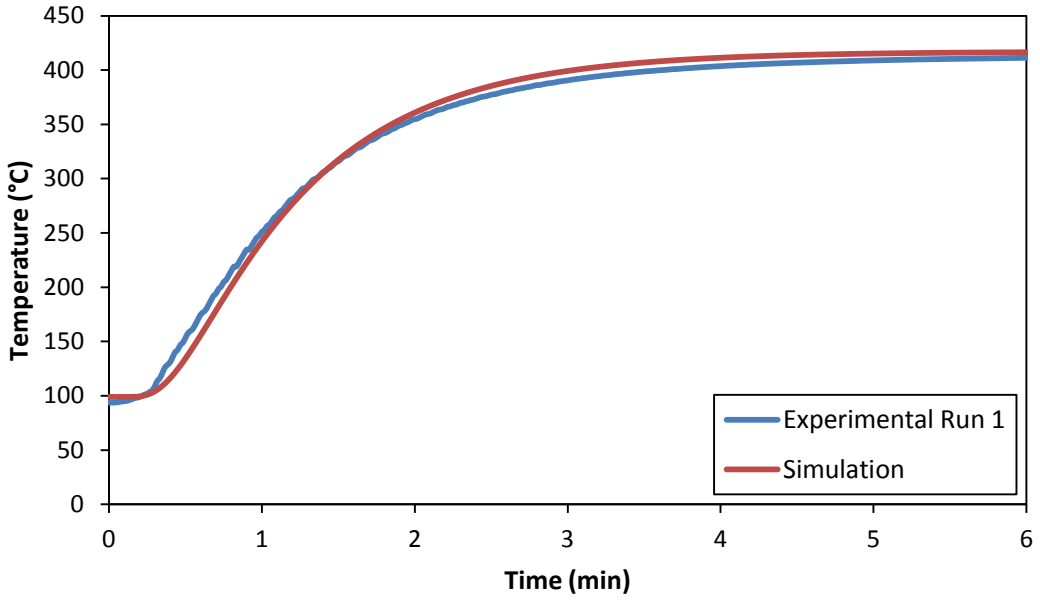

Figure 15. Temperature profiles comparing simulation with optimized char properties to char experimental run 1

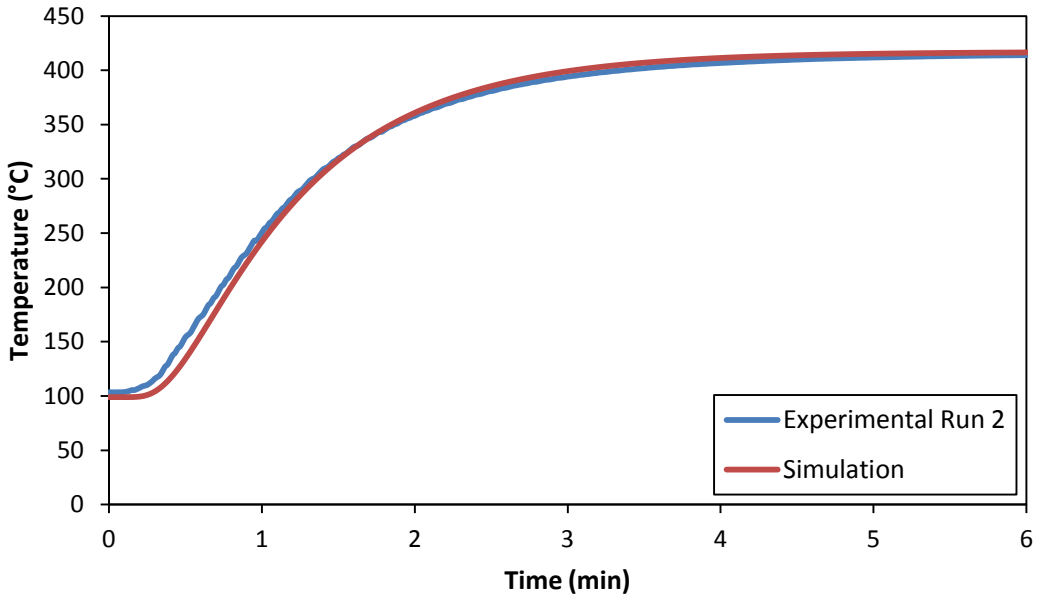

Figure 16. Temperature profiles comparing simulation with optimized char properties to char experimental run 2

The temperature profiles using the best fit parameters in the simulation fit well to the experimental profiles. There is some discrepancy between the temperature profiles due to the artificially imposed boundaries on the material properties. Table 41 gives the goodness of fit comparing the temperature profiles from the char experimental data to the outputs from the char model with optimized char properties.

Table 41. Goodness of fit comparing the char model with optimized char properties to the temperature profiles from the char experimental data

Run #	Goodness of Fit
Char Run 1	26000
Char Run 2	15000

From the goodness of fit values, it can be seen that the model predictions fit well with experimental values because the goodness of fit, ψ, is much lower for both runs than γ.

3.4.1.4 Optimization of Wood Properties

Once the char properties were established, the wood properties were determined. The simulation was run with both the Park and Gauthier kinetic models (see Section 3.5 for details about Gauthier kinetics) to separately determine wood properties. Because the outside of the wood begins to react very quickly, the kinetics used in the model could potentially have an effect on the calculated wood properties. For this reason, both models were used and the results were compared at the conclusion of the study. The following steps were completed with both the Park and Gauthier wood models.

The initial conditions that corresponded to the experimental setup were input into the one-dimensional spherical wood model. The char properties and wood density were also added. Once the model was established, a set of runs were done to determine the material parameters that gave a temperature profile that best fit the experimental data, analogous to the process of obtaining the char properties. The overall range and initial step size for λ_w and c_w used in this study are given in Table 42.

Table 42. Range and step size of values used to optimize the wood material properties

Parameter	Value Range	Initial Step Size	Units
λ_w	0.05-0.4	0.05	W/mK
c_w	700-4200	100	J/kg K

The wood model was run for every combination of λ_w and c_w values. A goodness of fit, ψ, was calculated for each of the simulation runs by comparing the temperature profiles to the experimental data from the two experimental temperature profiles. Only values up to 450 K (177°C) were used for this calculation to minimize the impact of the chemical reactions. The average of the two ψ values was taken and the material properties that corresponded to the minimum average ψ were taken as the best fit parameters.

During this study, the best fit value for λ_w reached the imposed maximum, 0.4 W/mK, similar to the findings for char properties. When the range of the thermal conductivity was expanded, the best fit parameters reached much higher than the range used for this optimization, which was determined from literature values (Hankalin et al., 2009). There are many possible reasons for these inconsistencies, including modeling a three-dimensional experimental setup with anisotropic properties as a one-dimensional geometry with isotropic properties, and the effect of the implemented kinetic model, which cannot predict all of the

chemical reactions occurring within the wood particle. Due to these improbable values, the range for the wood thermal conductivity was restricted to its initial values and the best fit parameters were determined within these bounds.

While the wood pore size was not a significant material parameter, and so was not optimized in this study, its value was modified from that given in Park et al., 2010. The char pore size determined in this study was smaller than the original value for the wood pore size. Because this is physically unrealistic, and since the value of the wood pore size does not significantly impact the temperature profiles, the wood pore size was changed to a more reasonable value. Given that the char pore size was found to be an order of magnitude lower than the Park value, the wood pore size was chosen to also be an order of magnitude below the original value.

The final wood properties from both the Park and Gauthier models are given in Table 43.

Table 43. Optimized wood material properties

Parameter	Park Model Value	Gauthier Model Value	Units
λ_w	0.4	0.4	W/m K
c_w	2375	2375	J/kg K
d_w	5×10^{-6}	5×10^{-6}	m

Figures 17 and 18 plot the comparison of the temperature profiles for experimental runs 1 and 2, respectively, to the temperature profile from the Park model using its associated best fit parameters. Figures 19 and 20 contrast the temperature profiles from the Gauthier model with its corresponding best fit parameters for experimental runs 1 and 2, respectively.

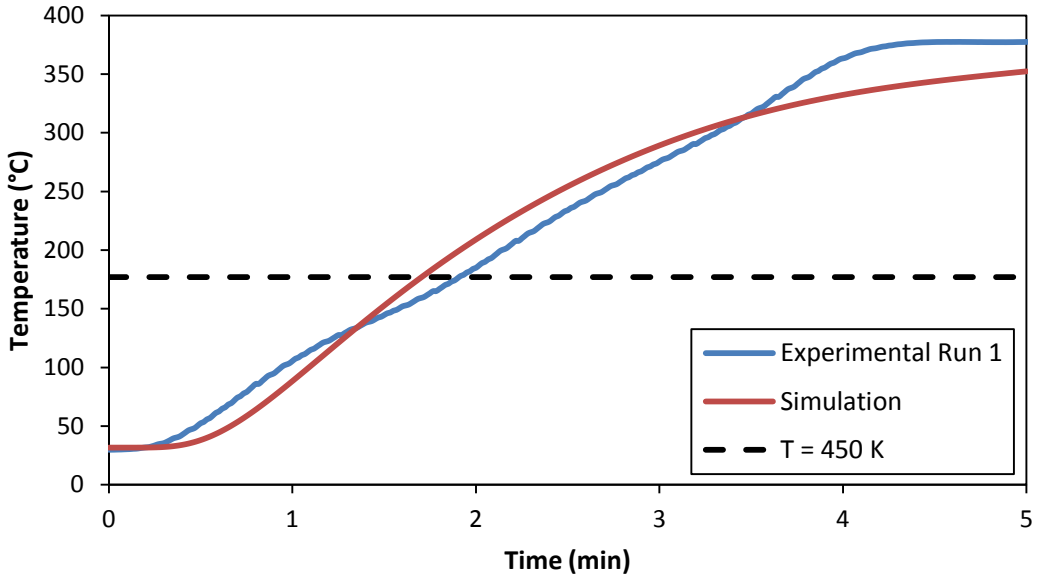

Figure 17. Comparison of the temperature profiles from experimental run 1 of the small diameter (2.54 cm), medium temperature case (P1-M1) to the Park model with optimized wood properties

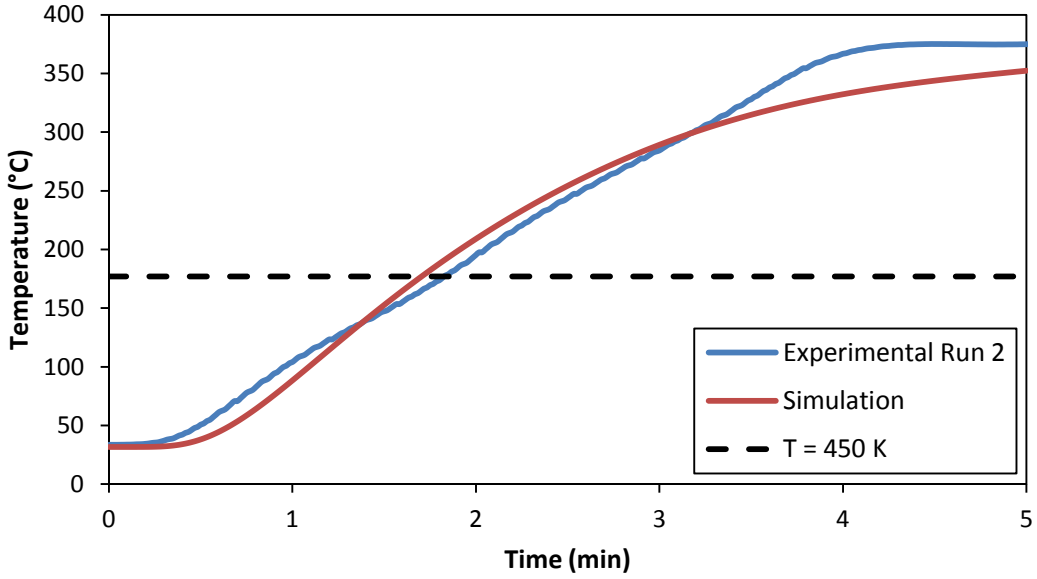

Figure 18. Comparison of the temperature profiles from experimental run 2 of the small diameter (2.54 cm), medium temperature case (P1-M2) to the Park model with optimized wood properties

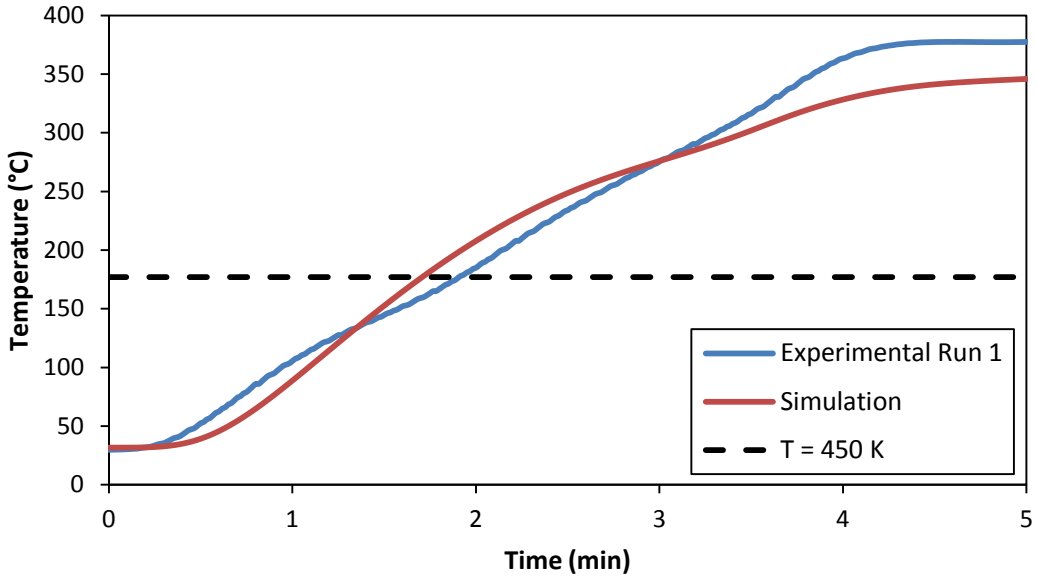

Figure 19. Comparison of the temperature profiles from experimental run 1 of the small diameter (2.54 cm), medium temperature case (P1-M1) to the Gauthier model with optimized wood properties

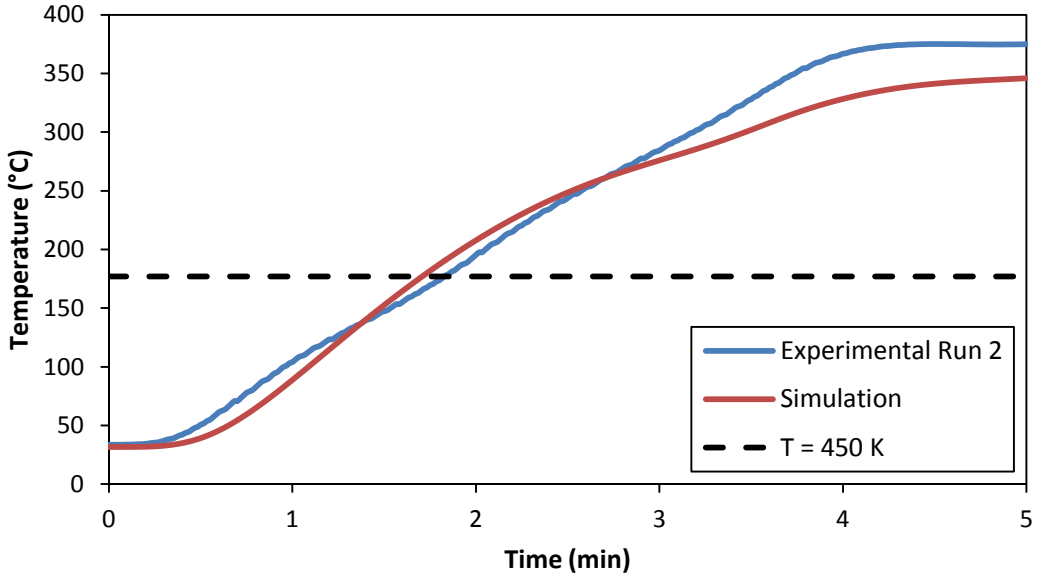

Figure 20. Comparison of the temperature profiles from experimental run 2 of the small diameter (2.54 cm), medium temperature case (P1-M2) to the Gauthier model with optimized wood properties

The temperature profiles using the best fit parameters in the simulation fit fairly well to the experimental profiles up to the fitting point, 450 K (177°C). There is some discrepancy between the temperature profiles from experiments and those from the two different models due to the artificially imposed boundaries on the material properties. Table 44 gives the goodness of fit, ψ, between the experimental temperature profiles and the Park and Gauthier models with optimized wood parameters.

Table 44. Goodness of fit comparing both the Park and Gauthier wood models with optimized wood properties to the two temperature profiles for 2.54 cm sphere diameter at a medium final particle temperature (P1-M)

Run #	Goodness of Fit for Park Model	Goodness of Fit for Gauthier Model
P1-M1	22000	21000
P1-M2	15000	13000

From Table 44, it can be seen that the goodness of fit values are much worse than β. More research into the material properties of poplar wood used in the experimental data of this study is needed to more accurately model the pyrolysis process.

It is interesting to note that the wood properties determined through the optimization process described above were the same for both the Park and Gauthier models. From this, it can be seen that the two kinetic mechanisms implemented in the model do not have a significant effect on the temperature profile as the wood particle heats up to 450 K and verifies that the material properties are independent of these two kinetic mechanisms.

3.4.2 Optimization of Kinetic and Thermochemical Parameters from the Kinetic Mechanism Presented in Park et al., 2010

While most of the parameters which define the first-order, Arrhenius-type reactions used in the proposed model developed by Park et al., 2010 were taken from the literature, four values were curve fit to the experimental data presented in the Park paper (2010). These include the pre-exponential factor for the wood to intermediate solid reaction, A_{is}, and the pre-exponential factor, activation energy, and heat of reaction for the decomposition of intermediate solid to char, given by A_c, E_c, and Δh_c, respectively. Values for these parameters in Park et al., 2010 are presented in Table 45.

Table 45. Kinetic parameters and thermochemistry values that were curve fit to experimental data from Park et al., 2010

Parameter	Definition	Value	Units
A_{is}	Pre-exponential factor for wood to intermediate solid reaction	3.75×10^6	s^{-1}
A_c	Pre-exponential factor for intermediate solid to char reaction	1.38×10^{10}	s^{-1}
E_c	Activation energy for intermediate solid to char reaction	161,000	J/mol
Δh_c	Heat of reaction for intermediate solid to char reaction	-300	kJ/kg

In order to match the kinetic mechanism to the pyrolysis of poplar wood, these parameters were curve fit to experimental data from both the TGA and slow pyrolysis of poplar wood spheres. TGA mass loss profiles were used to optimize A_{is}; however, because the decomposition of intermediate solid to char does not affect the change in mass of solids, the three parameters for the intermediate solid to char reaction – A_c, E_c, and Δh_c – had to be optimized using data from the slow pyrolysis of wood spheres.

Mass loss data from the thermogravimetric analysis of poplar wood was used to optimize the pre-exponential factor for the wood to intermediate solid reaction, A_{is}. For comparison, a model was created to mimic the TGA experimental setup, based on the Park model. The model was run for a range of A_{is} values and the mass loss outputs were compared to the experimental data. A goodness of fit, ψ, was calculated between the simulation outputs and each of the three experimental profiles, which use the mass after drying as the initial mass. From these three ψ values, an average was calculated and minimized to determine the curve fit pre-exponential factor, A_{is}. The optimization range and the final curve fit value are presented in Table 46.

Table 46. Optimization range and curve fit value for A_{is} in the Park kinetic mechanism

A_{is} Parameter	Value(s)	Units
Optimization Range	$2 \times 10^6 - 4 \times 10^6$	s^{-1}
Curve fit Value	2.26×10^6	s^{-1}

Figure 21 compares the mass loss profiles of the simulation using the original value for A_{is} to the curve fit value. Also included in this plot is an average experimental mass loss profile, which was calculated using the data from the three TGA runs.

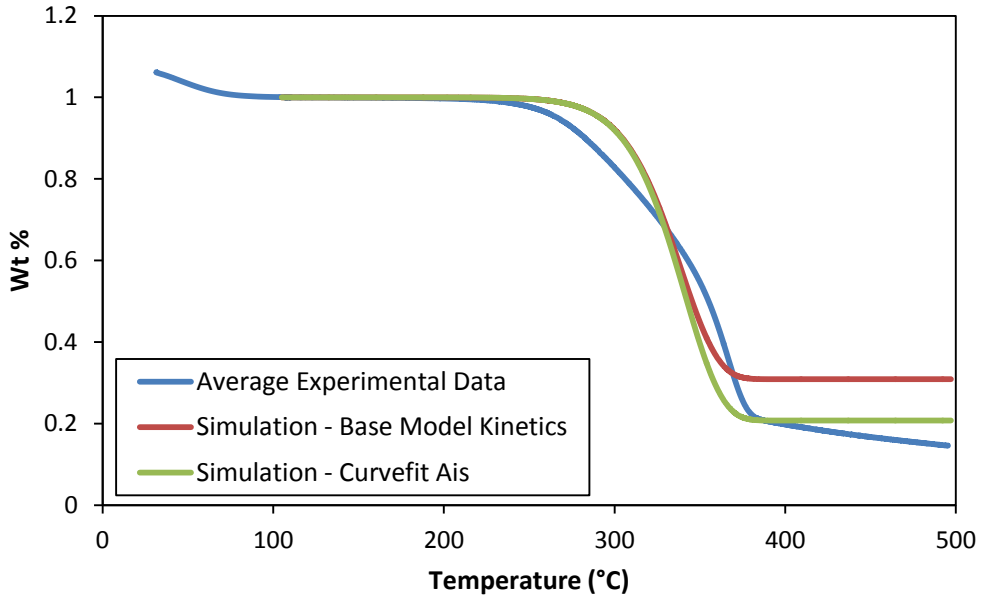

Figure 21. Mass loss profiles from average experimental TGA data along with simulation runs using either original value for A_{is} from Park et al., 2010 or the value curve fit to the experimental data used in this research

While the shape and timing of the mass loss profiles from the simulation were not affected by the pre-exponential factor A_{is}, the final mass of char predicted by the model was modified by this parameter, as expected. The overall shape and timing of the profiles is mainly determined by the conversion of wood to tar, which occurs in parallel with the wood to intermediate solid reaction, but has a much higher reaction rate. Since the kinetic parameters associated with this reaction were not modified, the basic shape and timing remains the same. However, the wood to intermediate solid reaction does have an effect on the final amount of char predicted by the kinetics. Changing the pre-exponential factor A_{is} varies how quickly wood is transformed into intermediate solid, and thus how much of the wood goes to form the intermediate solid, which then decomposes further to form char. The

optimization of A_{is} thus affects how much of the initial mass stays in the solid phase and alters the end weight percent of solids presented in the mass loss profiles.

Since the parameters specifying the decomposition of intermediate solid to char were not captured in the TGA mass loss profiles, they were determined by comparing the simulation to temperature profiles from the slow pyrolysis of wood spheres. Experimental runs were used for four different experimental setups for the optimization of A_c, E_c, and Δh_c: 2.54 cm wood sphere diameter at a medium final particle temperature (P1-M), 2.54 cm wood sphere diameter at a high final particle temperature (P1-H), 3.8 cm wood sphere diameter at a medium final particle temperature (P2-M), and 3.8 cm wood sphere diameter at a high final particle temperature (P2-H). Low temperature experimental temperature profiles were not used in this optimization. The range of values studied for these three parameters are given in Table 47.

Table 47. Ranges used for the optimization of kinetic variables for the intermediate solid to char reaction from the Park model

Parameter	Value Range	Units
A_c	$8.0 \times 10^9 - 2.4 \times 10^{10}$	s^{-1}
E_c	145,000 – 185,000	J/mol
Δh_c	(-500) – (-250)	kJ/kg

The simulation was run for every combination of A_c, E_c, and Δh_c values and the temperature profiles were compared to the experimental data. Errors from reaction parameters not optimized in this study caused the temperature profile from the simulation to be offset from the experimental values. Therefore, using a goodness of fit, ψ, to determine optimum values would try and minimize the error from the other reaction parameters, instead of matching the size and shape of the exothermic peak caused by the intermediate solid to char

reaction. For this reason, two values were used to compare the simulation outputs to the experimental temperature profiles and determine the optimum values for A_c, E_c, and Δh_c. The first value was the maximum temperature reached in the profile. The second was the width of the exothermic peak, determined by the difference in time for the temperature to go from $0.98*T_{max}$ through the maximum temperature, and then back to the same value on the other side of the temperature peak. Using these two values, the optimum values for the intermediate solid to char parameters were determined and are presented in Table 48.

Table 48. Optimized kinetic parameters for the intermediate solid to char reaction from the Park model

Parameter	Final Value	Units
A_c	9.0×10^9	s^{-1}
E_c	155,000	J/mol
Δh_c	-300	kJ/kg

Figures 22 through 25 compare the temperature profiles of the simulation using the original values for A_c, E_c, and Δh_c to the optimized values for the four different setups used in the optimization process. Also included in these plots are the average experimental temperature profiles. For the low temperature cases, model outputs with and without optimized kinetic parameters were almost identical. For a comparison of the model with optimized kinetic parameters to the experimental data at low temperatures, see Section 4.2.

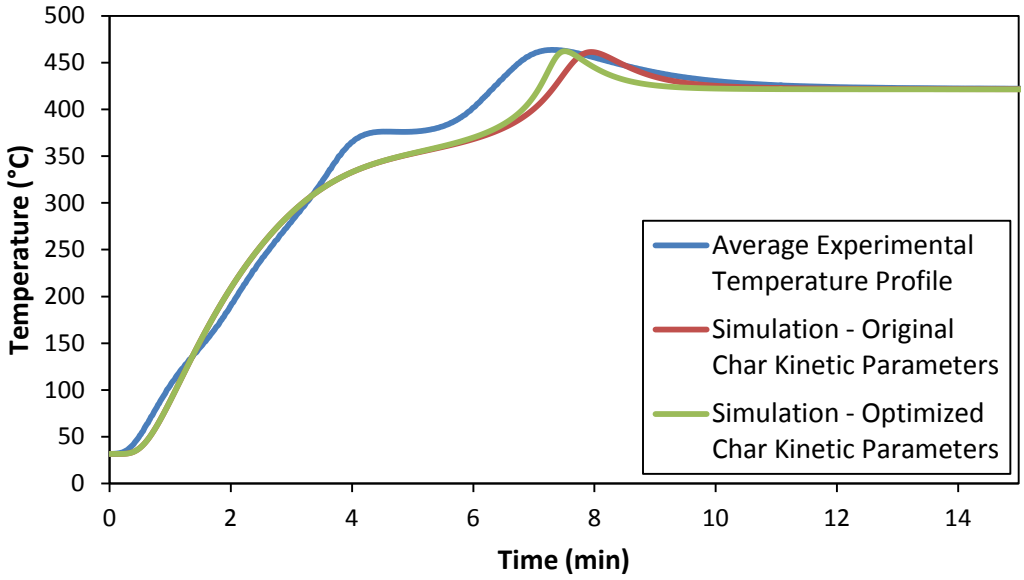

Figure 22. Temperature profiles from average experimental data for 2.54 cm sphere diameter with a medium final particle temperature (P1-M) along with simulation runs using either original values for A_c, E_c, or Δh_c from Park et al., 2010 or those that were curve fit to the experimental data used in this research

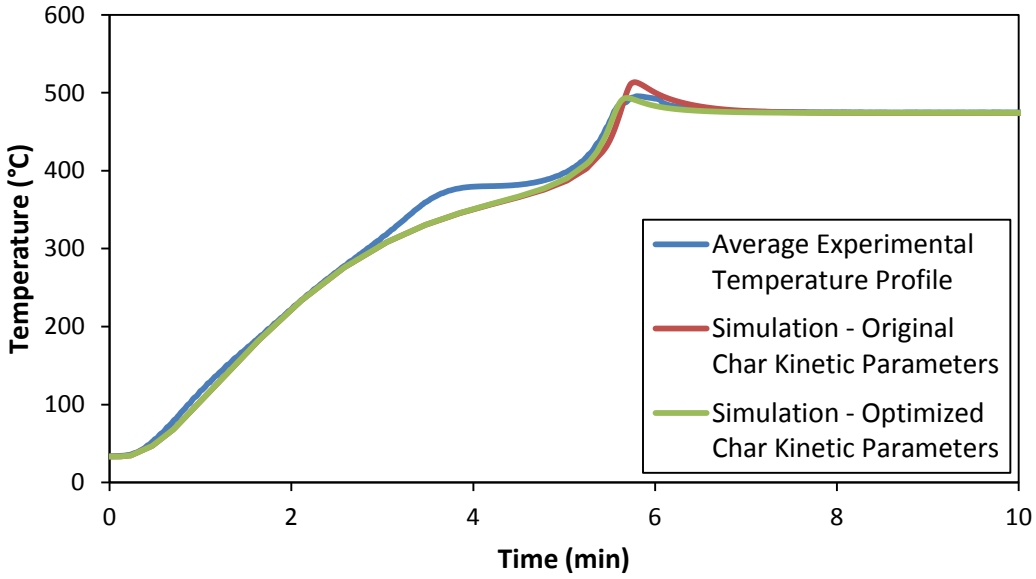

Figure 23. Temperature profiles from average experimental data for 2.54 cm sphere diameter with a high final particle temperature (P1-H) along with simulation runs using either original values for A_c, E_c, or Δh_c from Park et al., 2010 or those that were curve fit to the experimental data used in this research

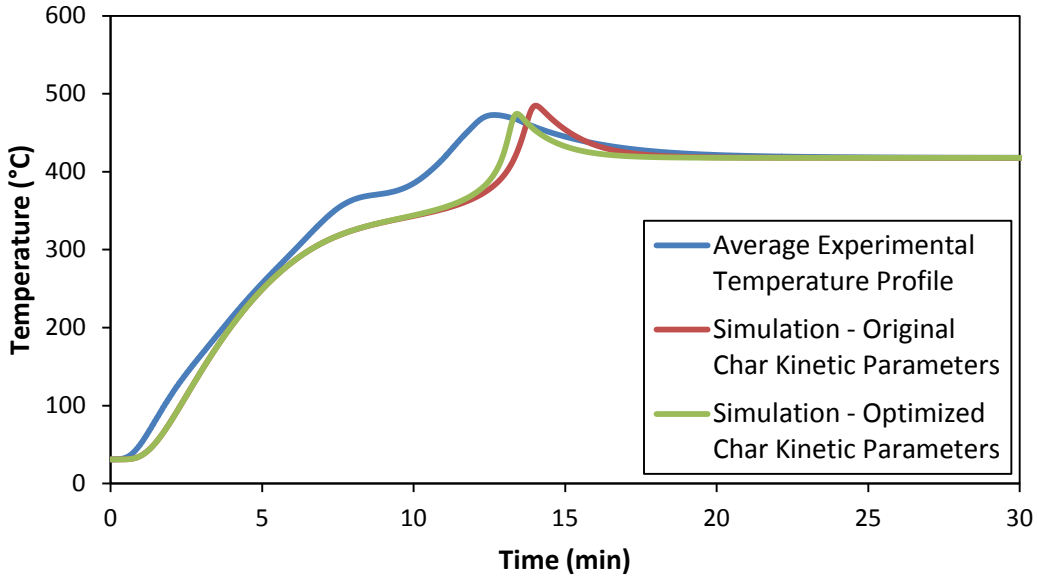

Figure 24. Temperature profiles from average experimental data for 3.8 cm sphere diameter with a medium final particle temperature (P2-M) along with simulation runs using either original values for A_c, E_c, or Δh_c from Park et al., 2010 or those that were curve fit to the experimental data used in this research

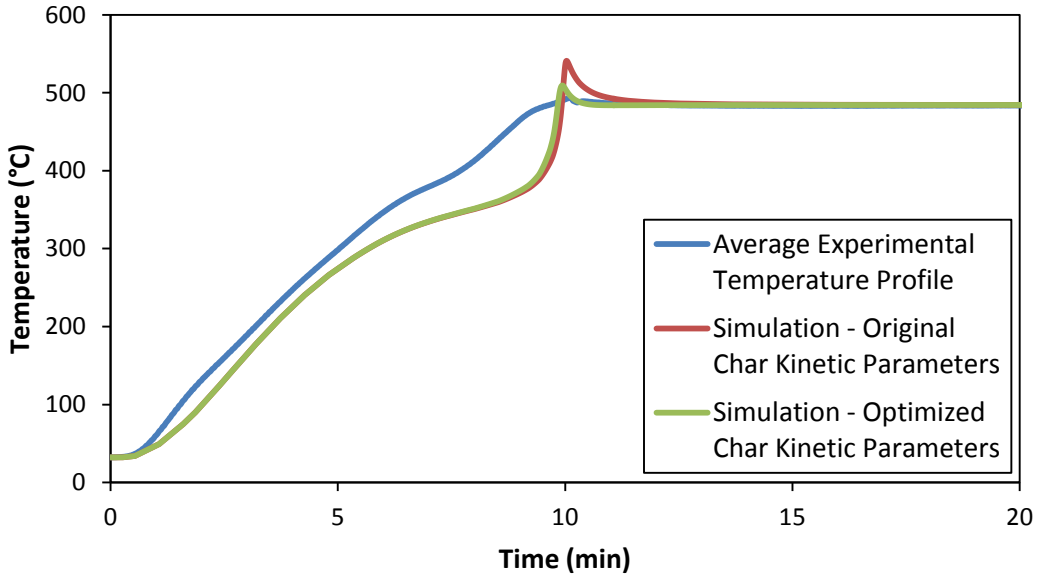

Figure 25. Temperature profiles from average experimental data for 3.8 cm sphere diameter with a high final particle temperature (P2-H) along with simulation runs using either original values for A_c, E_c, and Δh_c from Park et al., 2010 or those that were curve fit to the experimental data used in this research

From these figures, it can be seen that the maximum temperatures reached with the optimized char kinetic parameters are closer to the experimental values than the original parameters from Park et al., 2010. However, because the parameters were optimized against four sets of data, the width of the exothermic peaks are much smaller than both the experimental values and the simulation using the original char kinetic parameters.

3.5 Implementation of the Gauthier Kinetic Mechanism

The chemical reactions involved with the pyrolysis of biomass are very complex and challenging to determine. Many factors contribute to the difficulty of determining the kinetics and their associated thermochemistry. These factors include the variability and non-uniformity of biomass samples, the complexity of identifying and quantifying the species involved, as well as the coupling of kinetics with other physical processes such as heat transfer and flow of gaseous products through the porous media. In addition to this, it is desirable to have a general kinetic mechanism that can be applied to a variety of biomass types and pyrolysis conditions, yet specific enough to gain useful and relevant results.

Various kinetic mechanisms exist where wood decomposes through a few reactions to form three main products: gas, tar, and char (Di Blasi, 1993a; Liden et al., 1988; Ghabi et al., 2008). While these methods are generally able to predict the final distribution of products and temperature within the biomass sample, a more comprehensive mechanism is desired that can provide additional information about the composition of these products.

A detailed, multistep kinetic mechanism presented in Gauthier et al., 2013, was implemented in the numerical model. This mechanism defines a lumped stoichiometry of the

devolatilization of the three main components of biomass – cellulose, hemicellulose, and three types of lignin – and characterizes gas and tar fractions with a limited number of components. The chemical reactions for the decomposition of cellulose, hemicellulose, and the three types of lignin are shown in Figures 26, 27, and 28, respectively.

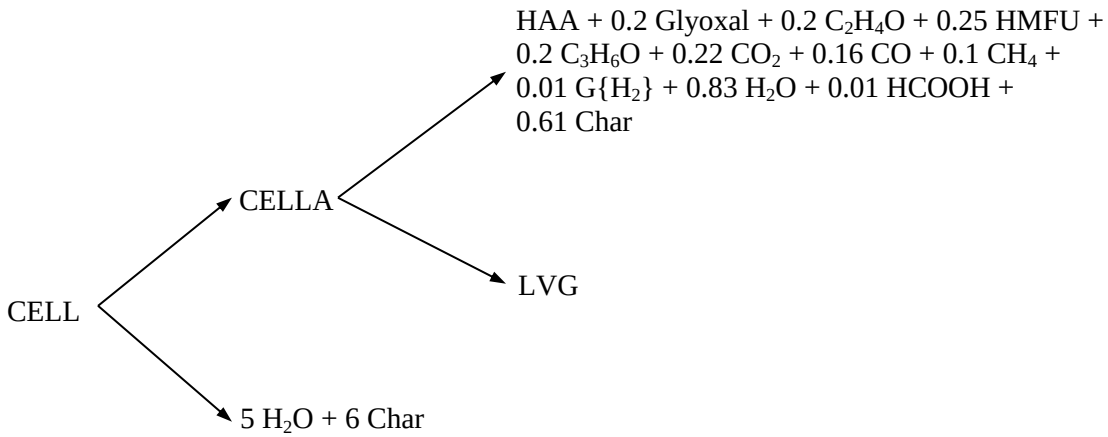

Figure 26. Decomposition of cellulose from Gauthier et al., 2013

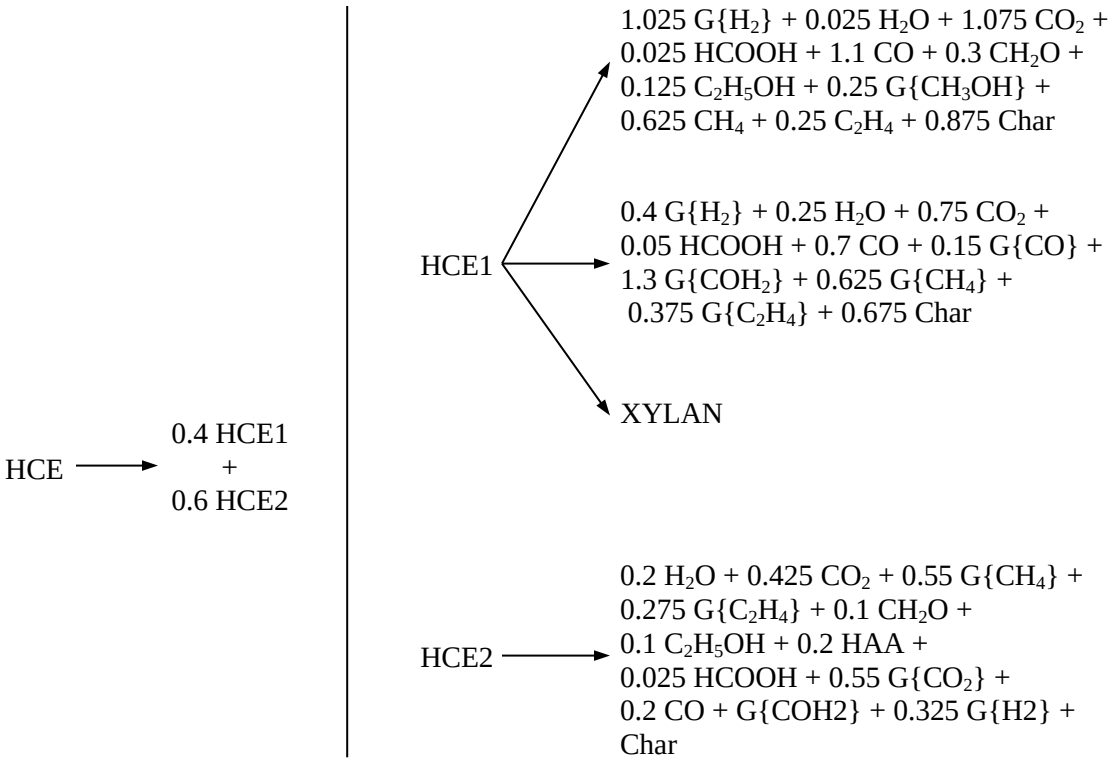

Figure 27. Decomposition of hemicellulose from Gauthier et al., 2013

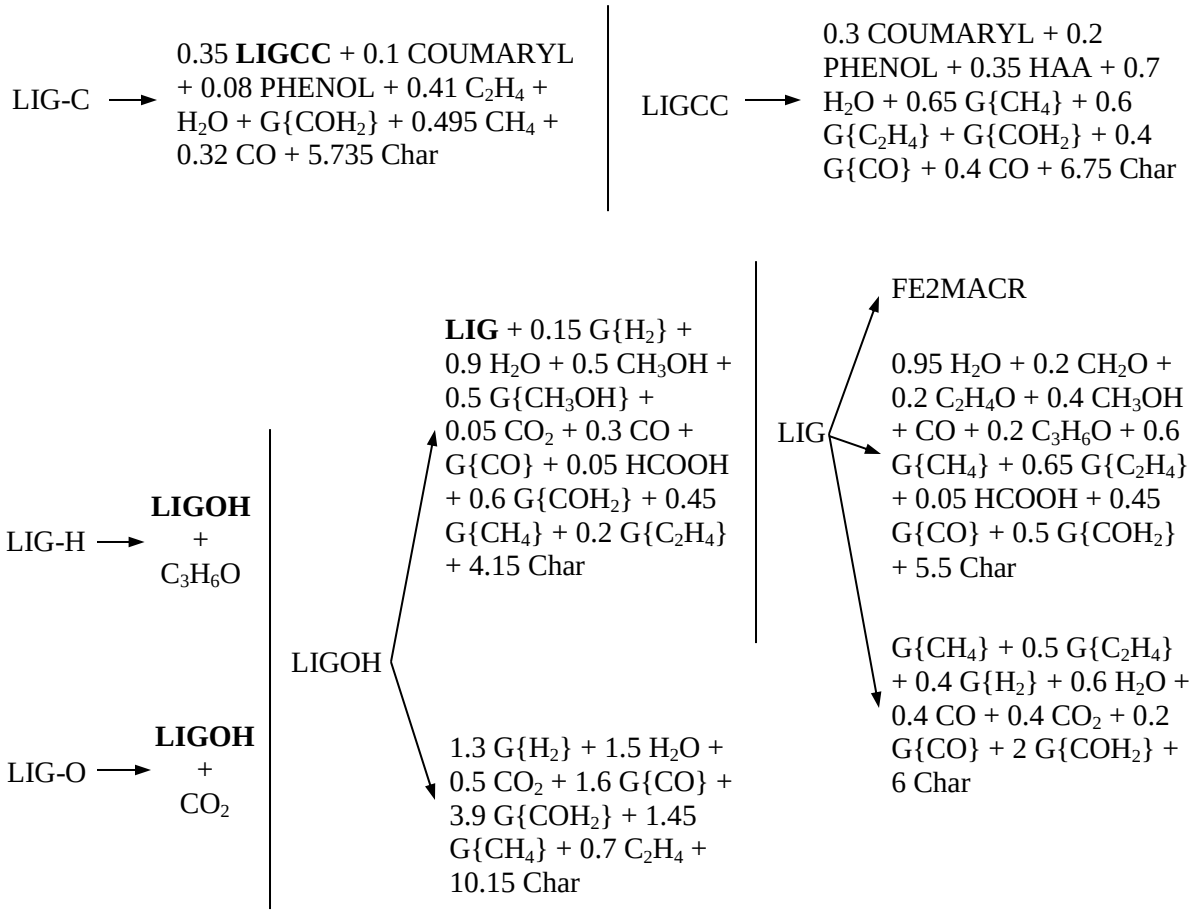

Figure 28. Decomposition of three types of lignin from Gauthier et al., 2013

Rate constants and heats of reaction corresponding to the reactions presented in Figures 26 through 28 are given in Table 49.

Table 49. Parameters for the kinetic mechanism presented by Gauthier et al., 2013

Reaction	**Kinetic constant[a] [s^{-1}]**	**Reaction Heat [$kJ.kg^{-1}$]**
CELL → CELLA	8×10^{13} exp (-45000/RT)	0
CELLA → HAA + 0.2 Glyoxal + 0.2 C_2H_4O + 0.25 HMFU + 0.2 C_3H_6O + 0.22 CO_2 + 0.16 CO + 0.1 CH_4 + 0.01G{H_2} + 0.83 H_2O + 0.01 HCOOH + 0.61 Char	1×10^{9} exp (-30000/RT)	650

CELLA → LVG	$4\times T \exp(-10000/RT)$	490
CELL → 5 H_2O + 6 Char	$8\times10^{7} \exp(-31000/RT)$	-1800
HCE → 0.4 HCE1 + 0.6 HCE2	$1\times10^{10} \exp(-31000/RT)$	100
HCE1 → 1.025 G{H_2} + 0.025 H_2O + 1.075 CO_2 + 0.025 HCOOH + 1.1 CO + 0.3 CH_2O + 0.125 C_2H_5OH + 0.25 G{CH_3OH} + 0.625 CH_4 + 0.25 C_2H_4 + 0.875 Char	$3\times10^{9} \exp(-32000/RT)$	22
HCE1 → 0.4 G{H_2} + 0.25 H_2O + 0.75 CO_2 + 0.05 HCOOH + 0.7 CO + 0.15 G{CO} + 1.3 G{COH_2} + 0.625G{CH_4} + 0.375G{C_2H_4} + 0.675 Char	$0.15\times T \exp(-8000/RT)$	-1400
HCE1 → XYLAN	$3\times T \exp(-11000/RT)$	590
HCE2 → 0.2 H_2O + 0.425 CO_2 + 0.55 G{CH_4} + 0.275 G{C_2H_4} + 0.1 CH_2O + 0.1 C_2H_5OH + 0.2 HAA + 0.025 HCOOH + 0.55 G{CO_2} + 0.2 CO + G{COH_2} + 0.325G{H_2} + Char	$1\times10^{10} \exp(-33000/RT)$	-330
LIG-C → 0.35 LIGCC + 0.1 COUMARYL + 0.08 PHENOL + 0.41 C_2H_4 + H_2O + G{COH_2} + 0.495 CH_4 + 0.32 CO + 5.735 Char	$4\times10^{15} \exp(-48500/RT)$	-100
LIG-H → LIGOH + C_3H_6O	$2\times10^{13} \exp(-37500/RT)$	130
LIG-O → LIGOH + CO_2	$1\times10^{9} \exp(-25500/RT)$	260
LIGCC → 0.3 COUMARYL + 0.2 PHENOL + 0.35 HAA + 0.7 H_2O + 0.65 G{CH_4} + 0.6 G{C_2H_4} + G{COH_2} + 0.4 G{CO} + 0.4 CO + 6.75 Char	$5\times10^{6} \exp(-31500/RT)$	-450
LIGOH → LIG + 0.15 G{H_2} + 0.9 H_2O + 0.5 CH_3OH + 0.5 G{CH_3OH} + 0.05 CO_2 + 0.3 CO + G{CO} + 0.05 HCOOH + 0.6 G{COH_2} + 0.45 G{CH_4} + 0.2 G{C_2H_4} + 4.15 Char	$3\times10^{8} \exp(-30000/RT)$	70
LIGOH → 1.3 G{H_2} + 1.5 H_2O + 0.5 CO_2 + 1.6 G{CO} + 3.9 G{COH_2} + 1.45G{CH_4} + 0.7 C_2H_4 + 10.15 Char	$1\times10^{2} \exp(-15000/RT)$	-1300
LIG → FE2MACR	$8\times T \exp(-12000/RT)$	890
LIG → 0.95 H_2O + 0.2 CH_2O + 0.2 C_2H_4O + 0.4 CH_3OH + CO + 0.2 C_3H_6O + 0.6 G{CH_4} + 0.65 G{C_2H_4} + 0.05 HCOOH + 0.45 G{CO} + 0.5 G{COH_2} + 5.5 Char	$1.2\times10^{9} \exp(-30000/RT)$	-300
LIG → G{CH_4} + 0.5 G{C_2H_4} + 0.4 G{H_2} + 0.6 H_2O + 0.4 CO + 0.4 CO_2 + 0.2 G{CO} + 2 G{COH_2} + 6 Char	$0.25\times T\times\exp(-8000/RT)$	-1770

$G\{CO_2\} \rightarrow CO_2$	6×10^5 exp(-24000/RT)	-860
$G\{CO\} \rightarrow CO$	5×10^{11} exp(-50000/RT)	-1500
$G\{COH_2\} \rightarrow CO + H_2$	5×10^{11} exp(-71000/RT)	6800
$G\{H_2\} \rightarrow H_2$	5×10^{11} exp(-75000/RT)	0
$G\{CH_4\} \rightarrow CH_4$ $G\{C_2H_4\} \rightarrow C_2H_4$ $G\{CH_3OH\} \rightarrow CH_3OH$	0.5×10^{13} exp(-50000/RT)	0

[a]Activation energy expressed in kcal/kmol

A more detailed explanation of the kinetic mechanism is given in Gauthier et al., 2013. Additional information about the species used in the kinetic mechanism can be found in Appendix D. A complete set of the differential equations used to describe both the Gauthier model is given in Appendix B. Results using this kinetic model as well as a comparison to the kinetic mechanism used in the Park model are presented in Chapter 4.

CHAPTER 4

RESULTS AND DISCUSSION

The results obtained from the one-dimensional numerical simulations using both the kinetic mechanism presented by Park et al., 2010 and Gauthier et al., 2013, were compared to the mass loss, center temperature, and species data acquired experimentally. Both of these models include the modifications presented in Sections 3.2 through 3.5. Experimental profiles presented in this chapter are averaged values calculated over all the runs performed for a given run setup. To see all of the experimental results, see Appendix A. A complete set of the inputs and runs parameters for both of the numerical models used for comparison to experimental profiles in this chapter are given in Appendix C. A full model report from COMSOL Multiphysics is available in Appendix F for the final Park model implemented in the software, along with a report for the Gauthier model which only includes deviations from the Park model.

while that for the Gauthier model only includes deviations from the Park model report.

In this chapter, the TGA mass loss profiles obtained experimentally are first compared to those from both the Park and Gauthier models. Following this, temperature profiles from both of the models are compared to those obtained experimentally from the slow pyrolysis of poplar wood spheres. After this, the production of gas, tar, and char from the experimental data is compared to that predicted by both the Park and Gauthier models. Last, species profiles and yields from the Gauthier model are compared to experimental data.

4.1 Comparison of Thermogravimetric Analysis Data to TGA Model Outputs

Experimental TGA mass loss profiles were compared to both the Park and Gauthier numerical models. The experimental profile presented here is an average of all the TGA runs performed. Mass loss profiles for the models and experiments are given in Figure 29.

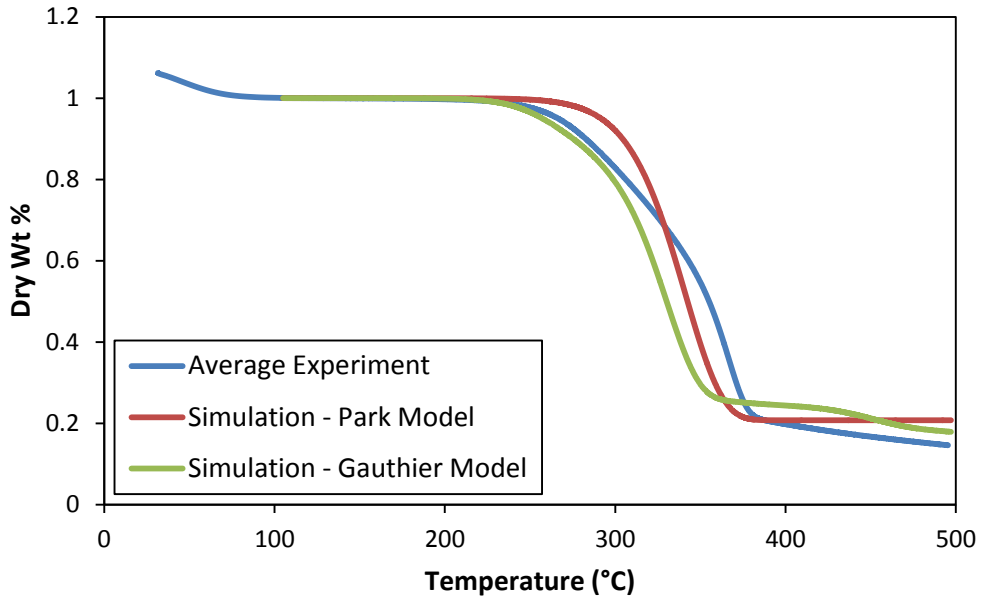

Figure 29. Comparison of TGA mass loss profiles from the Park and Gauthier models to the average experimental profile

From these mass loss profiles, it can be seen that the solid mass loss predicted by both the Park and Gauthier models match the experimental profiles fairly well. For the Park model, the half-destruction point predicted by the model matches reasonably well with the

experimental value. Also, the final elbow of the plot observed around 370°C matches well with the experimental profile, as expected from the optimization of the pre-exponential factor for the wood to intermediate solid reaction (see Section 3.4.2). However, the model does not predict the slow mass losses seen in the initial and final sections of the experimental TGA mass loss profile. These same discrepancies were observed in Park et al., 2010, where it was noted that the kinetic scheme better represented the decomposition of cellulose, the primary constituent of wood, which decomposes between 315-400°C (Yang et al., 2007). The model does not adequately capture the effects of the decomposition of hemicellulose at low temperatures (between 220°C and 315°C, Yang et al., 2007) and lignin over the entire temperature range (from ambient to 900°C, Yang et al., 2007).

For the Gauthier model, the initial mass loss matches very well with the experimental profile. Also, the slow mass loss seen at high temperature is also captured in this model. However, the model predicts a much faster mass loss between 300-375°C, during the decomposition of cellulose. While the mass loss profile predicted by the Gauthier model does not match extremely well, it has been developed to be a general kinetic mechanism that can be used to describe the pyrolysis process in a variety of applications, and so has been developed to match many different data sets reasonably well.

To determine how well each of the models predicted the mass loss curves from experimental TGA data, a goodness of fit, ψ, was calculated comparing experimental and model profiles. Table 50 presents the goodness of fit for the mass loss profiles for both the Park and Gauthier models.

Table 50. Goodness of fit comparing experimental TGA mass loss profiles to the outputs from the Park and Gauthier models

Model	Goodness of Fit
Park Model	29
Gauthier Model	57

From the goodness of fit parameters, it can be seen that overall, the Park model is able to predict the mass loss profiles from experimental data more accurately.

4.2 Comparison of Experimental Temperature Profiles from the Slow Pyrolysis of Poplar Wood Spheres to Pyrolysis Model Outputs

Temperature profiles obtained experimentally at the center of wood sphere particles were compared to those predicted with both the Park and Gauthier models. Experimental profiles presented here are averaged over all the runs performed for a given setup. Temperature profiles for the models and experiments are presented in Figures 30 and 31.

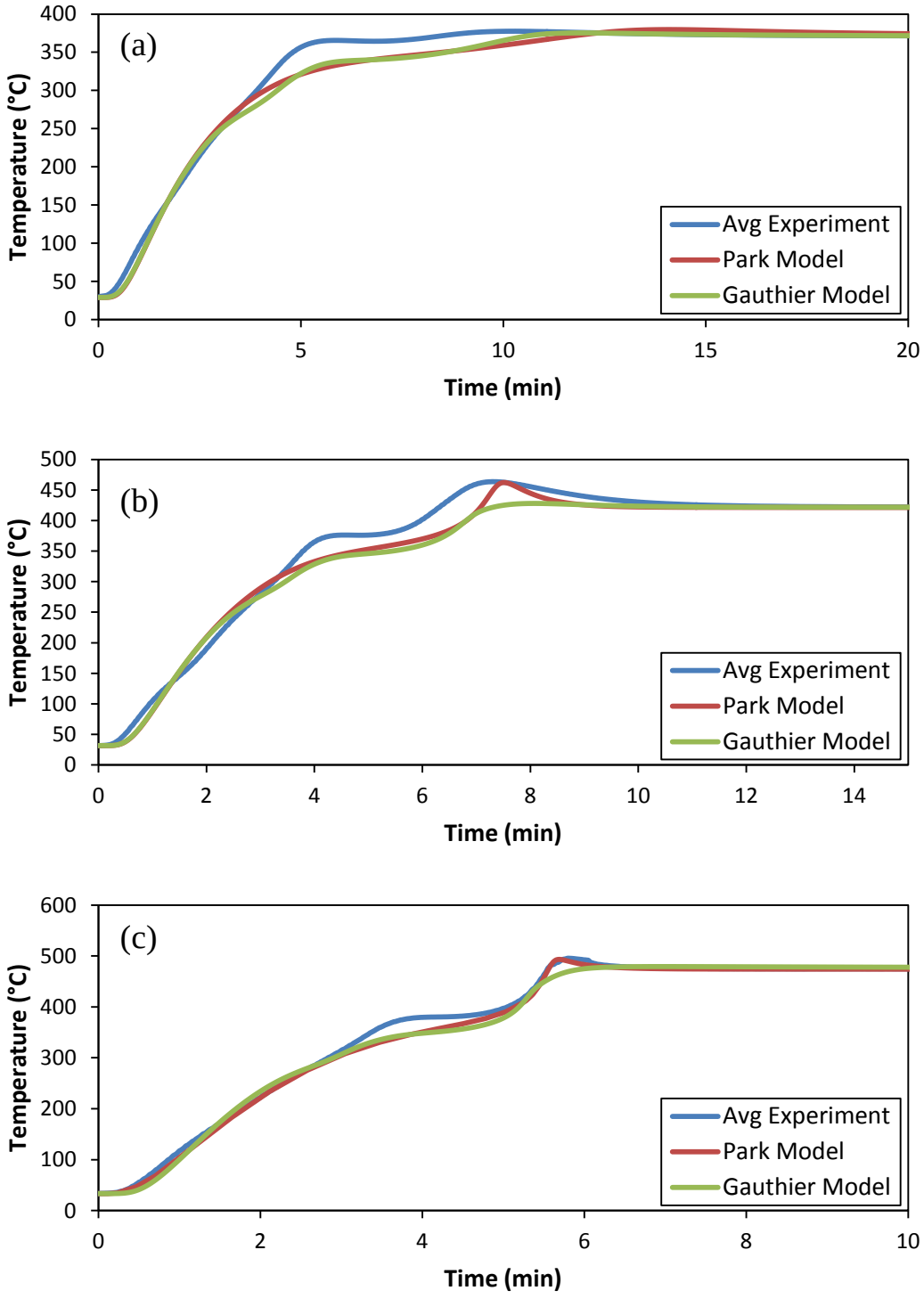

Figure 30. Comparison of average experimental temperature profile to those from the Park and Gauthier models for 2.54 cm sphere diameter with (a) a low final particle temperature (P1-L), (b) a medium final particle temperature (P1-M), and (c) a high final particle temperature (P1-H)

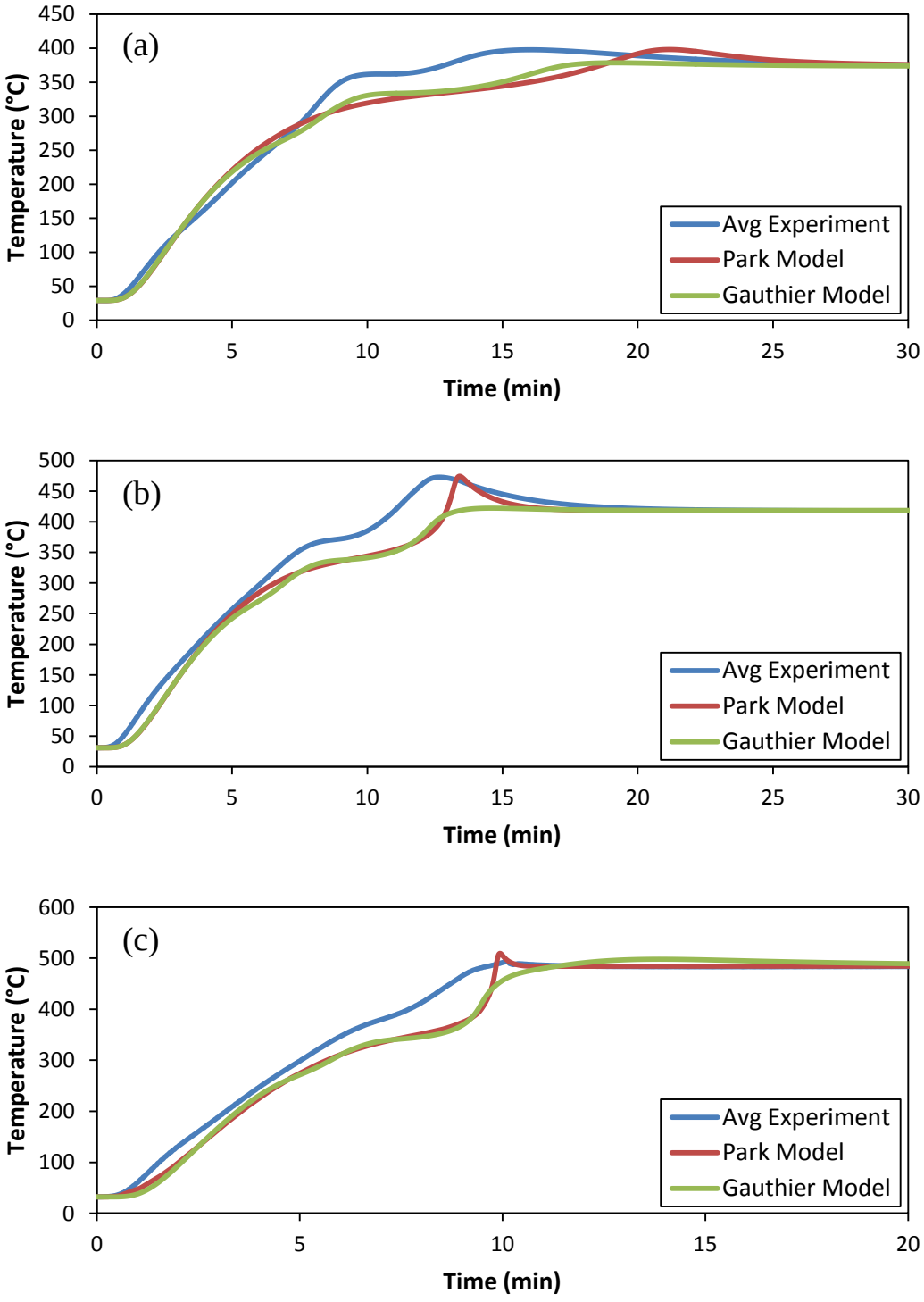

Figure 31. Comparison of average experimental temperature profile to those from the Park and Gauthier models for 3.8 cm sphere diameter with (a) a low final particle temperature (P2-L), (b) a medium final particle temperature (P2-M), and (c) a high final particle temperature (P2-H)

The temperature profiles predicted by both models capture the basic features of the experimental temperature profile: a plateau caused by endothermic reactions, followed by a temperature peak from exothermic reactions. For both models, however, the endothermic reactions begin too soon, causing the plateau in the profile to be lower than the experimental value. Also, the endothermic plateaus are not as distinct in the model predictions as seen in the experiments.

The maximum temperature of the exothermic peak predicted by the Park model matches fairly well with the experimental profiles, due to the optimization of kinetic parameters (see Section 3.4.2), but the width of the peak is generally smaller than the experiments. Also, the peaks occur later than experiments for the lower and medium final particle temperatures. For the Gauthier model, the peak values are generally lower than those seen experimentally, but the width and timing of the peaks are comparable to the experimental values, with the peak predicted by the model occurring slightly later than the experimental peak for the larger wood spheres.

To determine how good each of the models predicted the temperature profiles found experimentally, a goodness of fit, ψ, was calculated for each of the runs comparing the model outputs to the average experimental temperature data. Table 51 presents the goodness of fit for the temperature profiles of both the Park and Gauthier models.

Table 51. Goodness of fit comparing outputs from the Park and Gauthier models to experimental temperature profiles

Run #	Park Model	Gauthier Model
P1-L	280000	260000
P1-M	320000	470000
P1-H	70000	120000
P2-L	1160000	820000
P2-M	1330000	1520000
P2-H	1140000	1330000

From the goodness of fit parameters, it can be seen that the Gauthier model more accurately predicts the temperature profiles for lower final particle temperatures, while the Park model performs better for the medium and higher temperature cases. It is interesting to note that both models have the most difficulty predicting the medium operating temperature cases, while the Park model is best able to model the high temperature cases and the Gauthier model evaluates the low temperature cases most accurately.

4.3 Comparison of Experimental Production of Gas, Tar, and Char from the Slow Pyrolysis of Poplar Wood Spheres to Pyrolysis Model Outputs

This section compares the formation of gas, tar, and char from both the Park and Gauthier models to those obtained experimentally. Time-resolved plots of the production of gas are given in Figures 32 and 33. Experimental profiles presented here are averaged over all of the runs performed for a given setup. Final yields of gas, tar, and char from both models, as well as experimental yields, are presented in Figure 34. For the experiments and the Gauthier

model, gas is considered to be the sum of C_2H_4, CH_4, CO, CO_2, and H_2. Ethylene (C_2H_4) was not observed experimentally and hydrogen was only found in trace amounts experimentally for the 3.8 cm sphere diameter at a high final particle temperature (P2-H). Experimental tar yields were determined by taking the difference between the initial wood mass and the mass accounted for the production of gas of char.

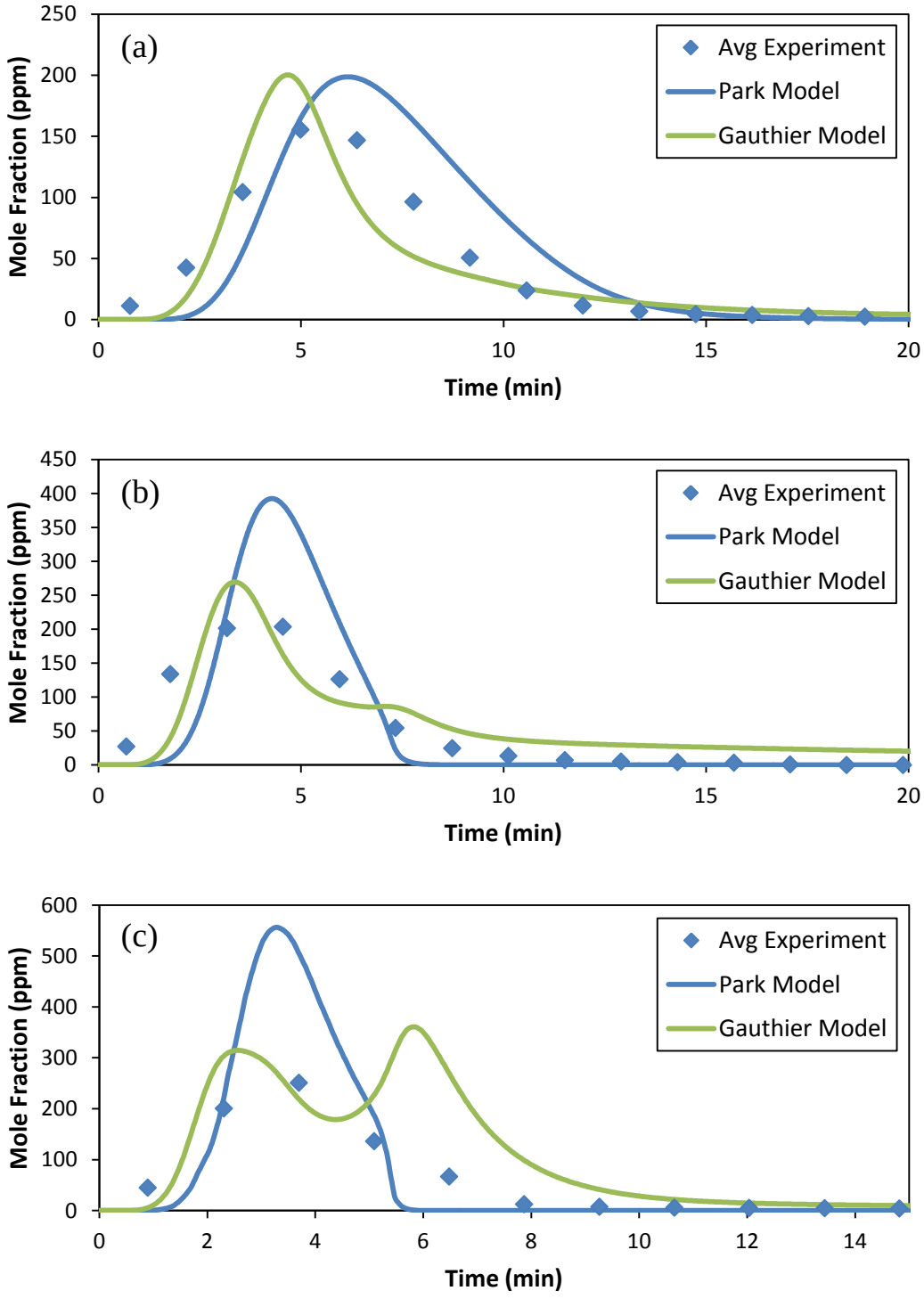

Figure 32. Comparison of average experimental gas profile to those from the Park and Gauthier models for 2.54 cm sphere diameter with (a) a low final particle temperature (P1-L), (b) a medium final particle temperature (P1-M), and (c) a high final particle temperature (P1-H)

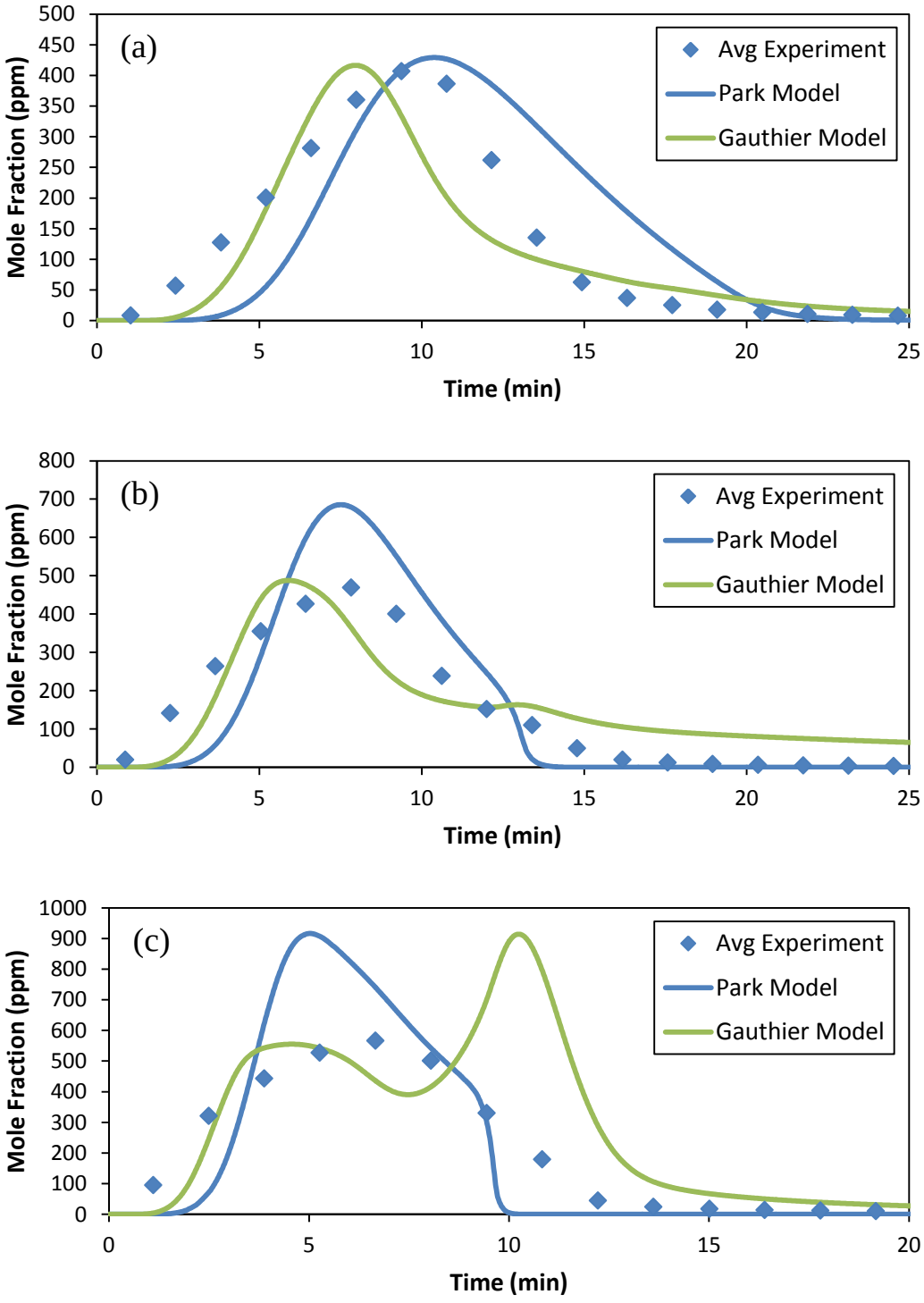

Figure 33. Comparison of average experimental gas profile to those from the Park and Gauthier models for 3.8 cm sphere diameter with (a) a low final particle temperature (P2-L), (b) a medium final particle temperature (P2-M), and (c) a high final particle temperature (P2-H)

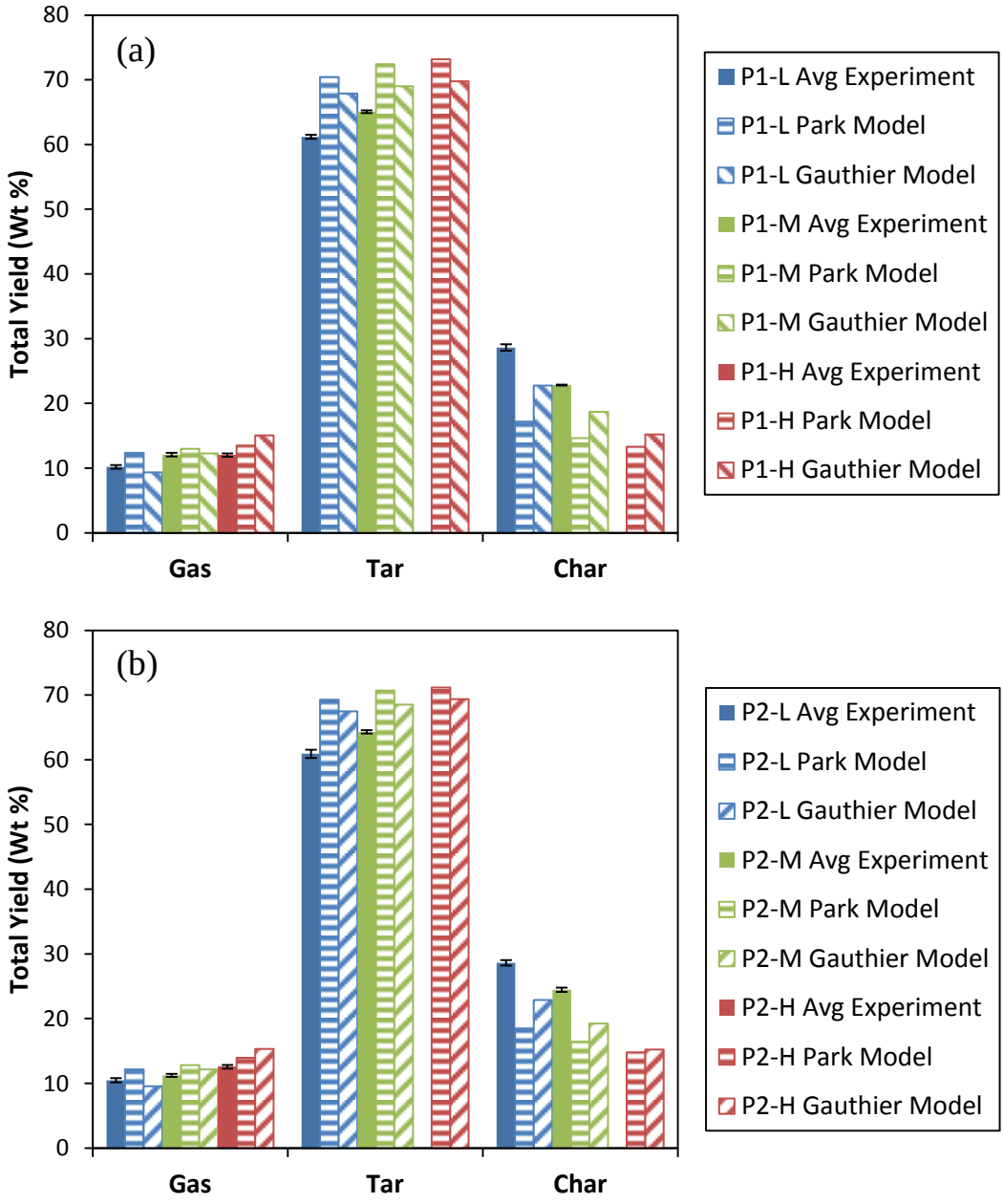

Figure 34. Average experimental yields of gas, tar, and char as compared to the predictions from the Park and Gauthier models for (a) 2.54 cm sphere diameter and (b) 3.8 cm sphere diameter. For the high temperature cases, the char split and could not be measured experimentally, and so the char and tar percentages could not be determined.

The Park model predicts the time-resolved production of gas fairly well, with better predictions for lower temperatures and larger sphere diameters. Comparing the gas production to the temperature profiles, it can be seen that the majority of the gas is produced during the endothermic plateau, before the exothermic temperature peak occurs. This supports the view that the exothermic process is caused by the decomposition of an intermediate solid, after the release of the main volatiles. While the total yield of gas is over-predicted by the Park model for all cases, it is very close to the experimental values and predicts the same trends as seen experimentally: an increase in production with increasing temperature and very little difference in output between the small and large wood sphere diameters.

For the Gauthier model, the prediction of time-resolved release of gas is reasonably accurate for the low temperature cases, especially for the large sphere diameter. However, at higher temperatures, a secondary peak appears that is not seen experimentally, and the value of this peak increases with increasing operating temperatures. This secondary release of gases corresponds to the release of chemisorbed species in the kinetic mechanism, which occurs during the exothermic temperature peak. Overall, the Gauthier model under-predicts the total production of gas at low temperatures, but over-predicts the yield of gas at higher final particle temperatures because of these secondary peaks. However, the model is able to capture the basic trends of gas production with increasing operating temperature and particle size.

For both models, the prediction of char produced through the pyrolysis process is much smaller than that seen experimentally. Because both models slightly over-predicted the final solid mass produced from the TGA runs, the production of char is affected by the physical processes which occur during the pyrolysis of a thermally thick particle. This discrepancy could be caused by secondary charring reactions of the volatiles as they travel

through the pores to the surface of the particle. Zaror et al., 1985 and Mazumdar and Chatterjee, 1973 found that increased residence times caused by greater thicknesses of particles or reactor beds, respectively, enhance the formation of secondary char from tar species. This phenomenon would also explain the considerably lower yields of tars seen experimentally than were predicted by either model. While the Park model does implement a secondary decomposition of tar to char, these reactions are not significant for the low temperatures studied here (Park et al., 2010). Despite these discrepancies, however, both models are able to predict the general trends of the experimental yields of gas, tar (increase with increasing temperature and decrease with increasing particle size), and char (decrease with increasing temperature and increase with increasing particle size) with temperature and particle size.

4.4 Comparison of Experimental Species Data from the Slow Pyrolysis of Poplar Wood Spheres to Pyrolysis Model Outputs

This section compares the formation of specific gaseous species measured experimentally to those predicted with the Gauthier model. Time-resolved species profiles from the model and experimental data are first presented in Figures 35 through 40. Following a discussion of these results, plots comparing the model results with and without desorption kinetics to experimental data are presented in Figures 41 through 46, after which a discussion of these results is presented. Total yields of each of the species for both the simulation and the experiments are then given in Figure 47, followed by a discussion of the results. Experimental profiles presented here are averaged over all of the runs performed for a given setup.

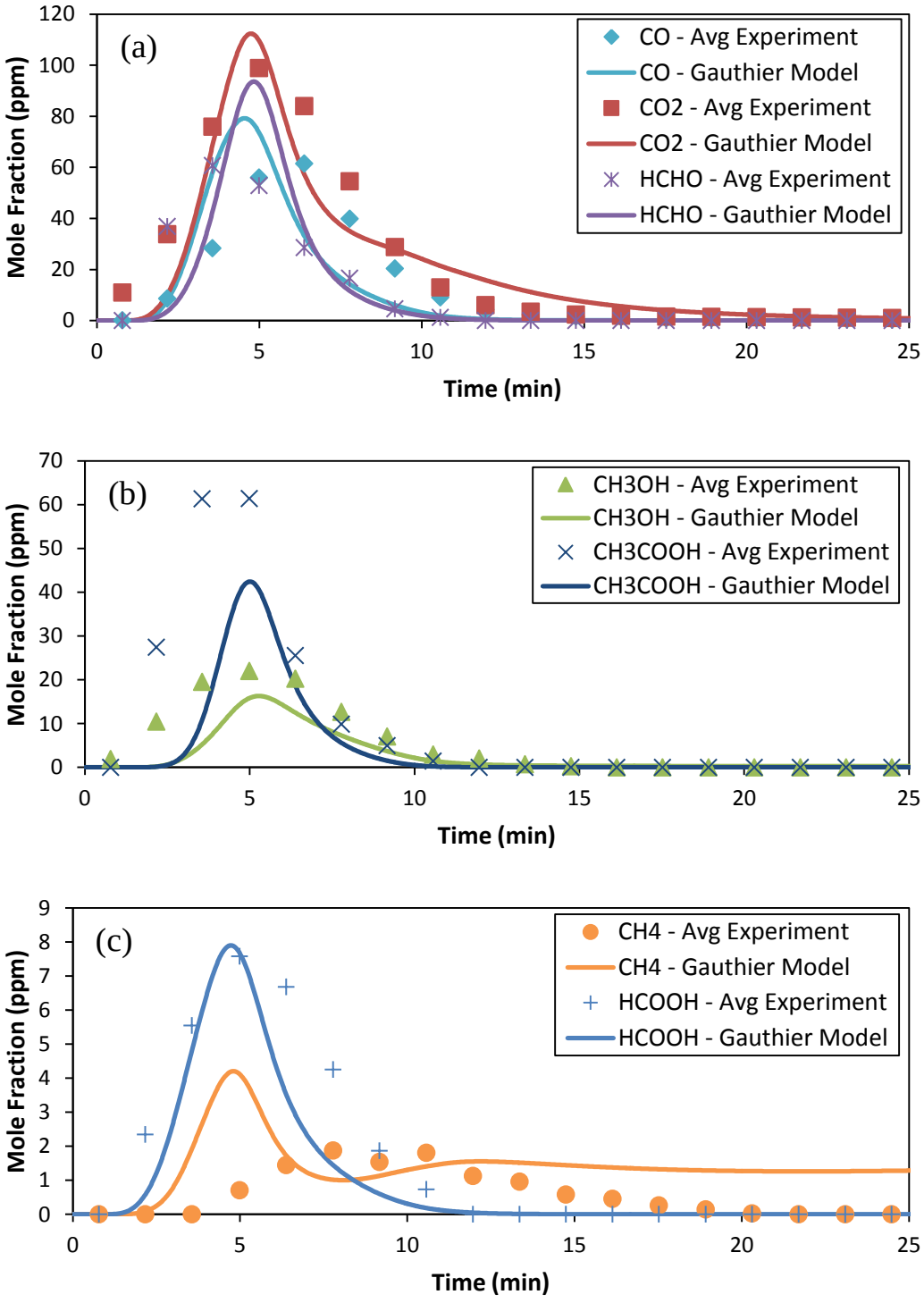

Figure 35. Comparison of average experimental species profiles to those from the Gauthier model for 2.54 cm sphere diameter with a low final particle temperature (P1-L) for (a) CO, CO_2, & HCHO, (b) CH_3OH & CH_3COOH, and (c) CH_4 & HCOOH

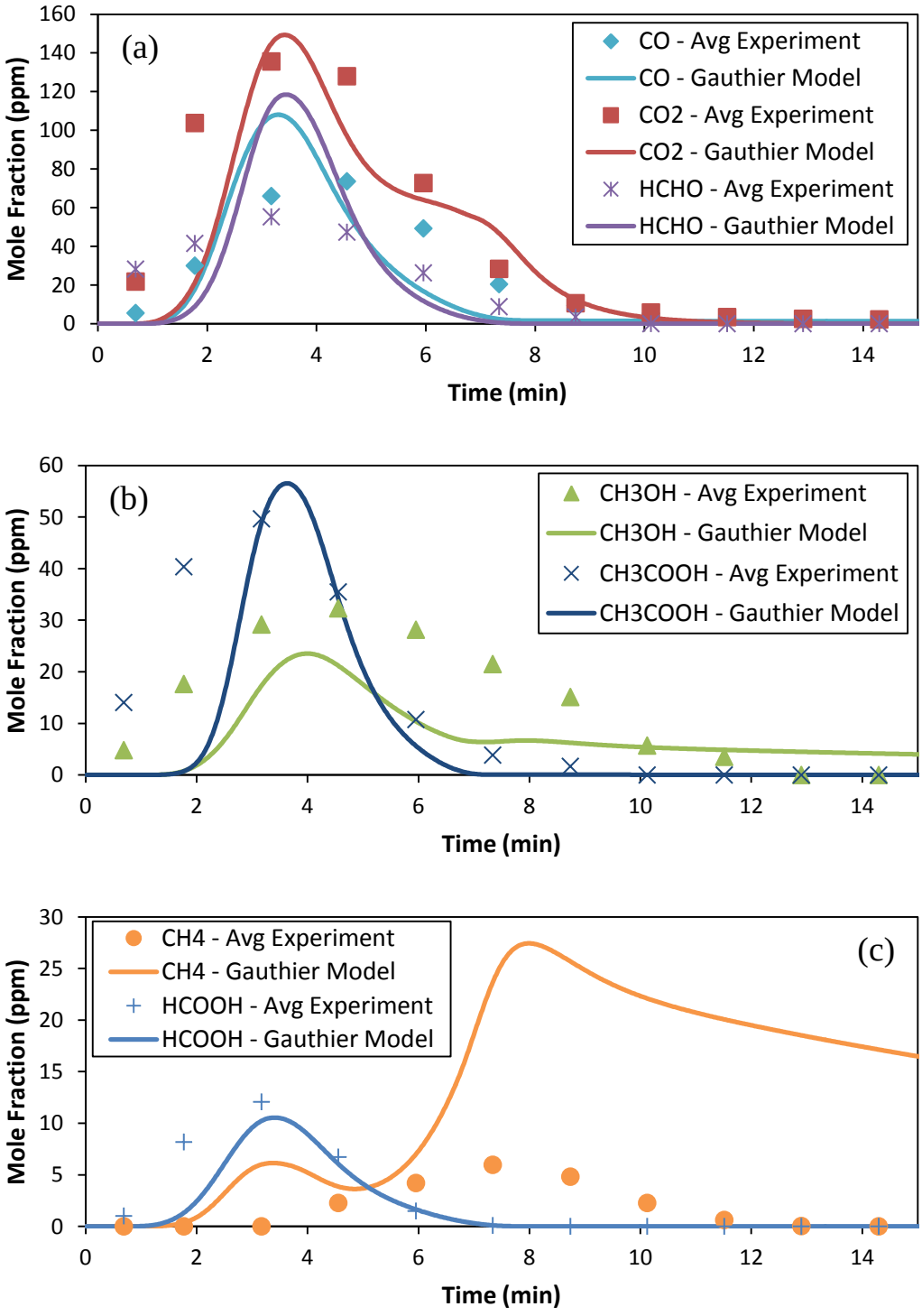

Figure 36. Comparison of average experimental species profiles to those from the Gauthier model for 2.54 cm sphere diameter with a medium final particle temperature (P1-M) for (a) CO, CO_2, & HCHO, (b) CH_3OH & CH_3COOH, and (c) CH_4 & HCOOH

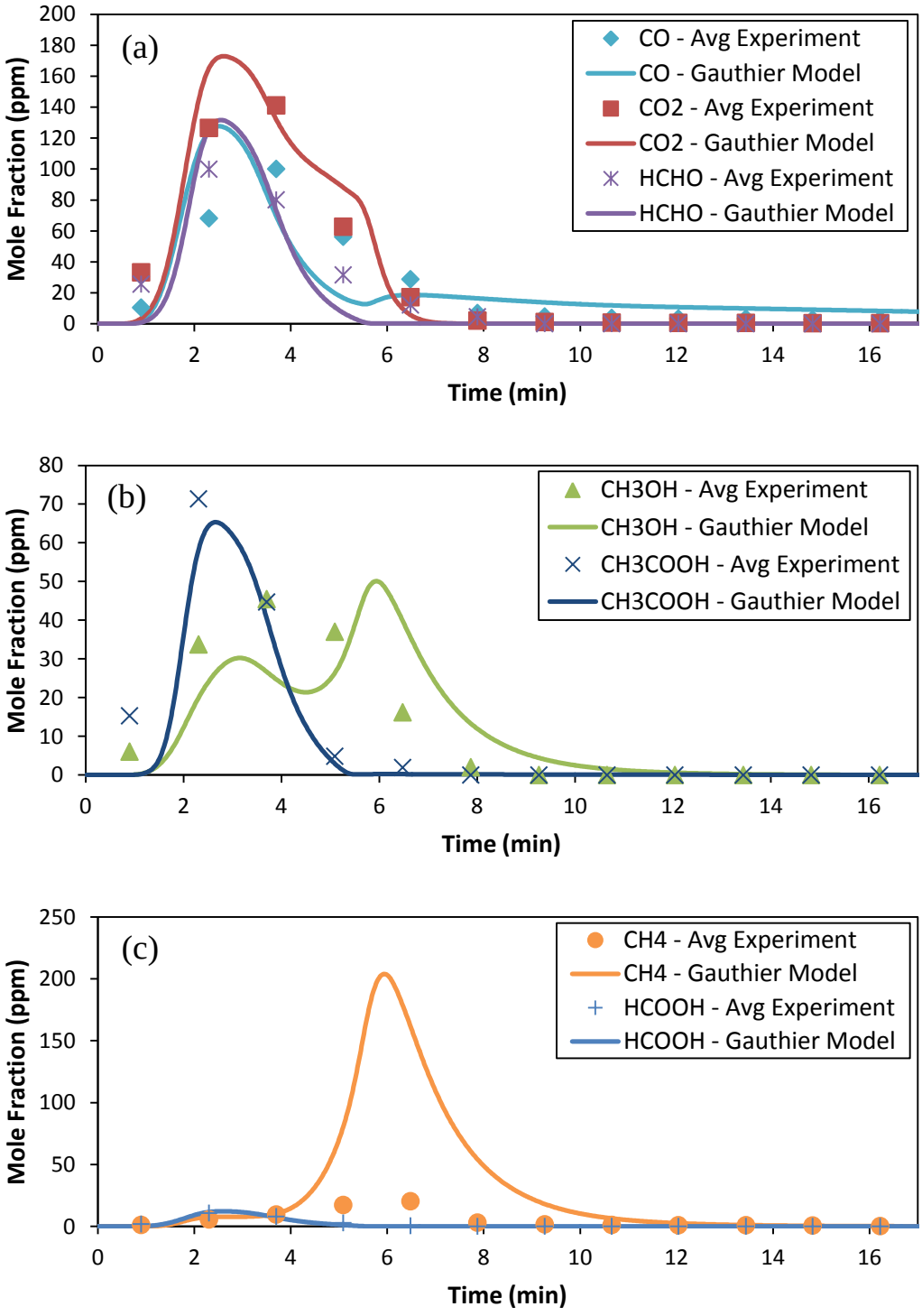

Figure 37. Comparison of average experimental species profiles to those from the Gauthier model for 2.54 cm sphere diameter with a high final particle temperature (P1-H) for (a) CO, CO_2, & HCHO, (b) CH_3OH & CH_3COOH, and (c) CH_4 & HCOOH

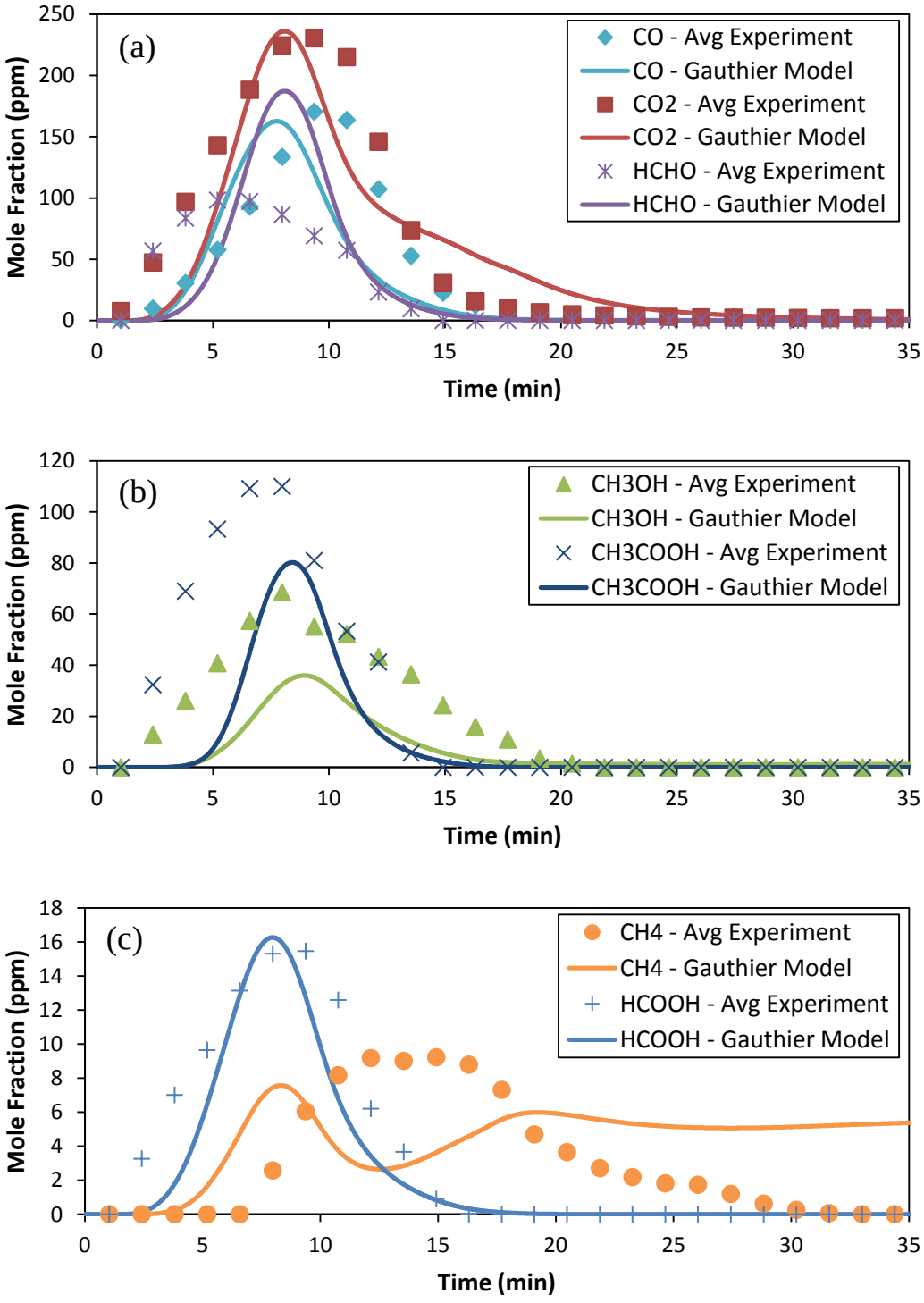

Figure 38. Comparison of average experimental species profiles to those from the Gauthier model for 3.8 cm sphere diameter with a low final particle temperature (P2-L) for (a) CO, CO_2, &HCHO, (b) CH_3OH & CH_3COOH, and (c) CH_4 & HCOOH

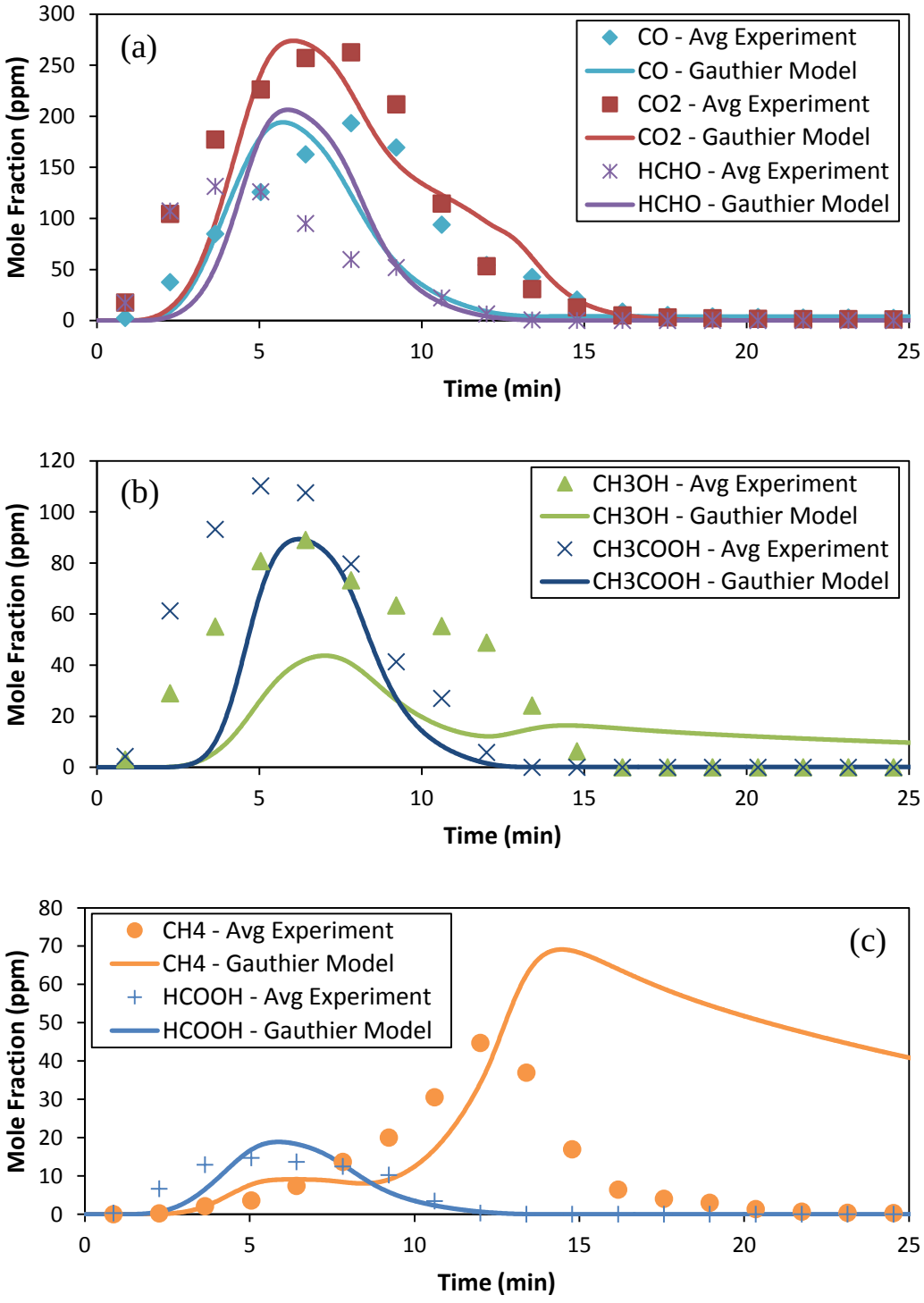

Figure 39. Comparison of average experimental species profiles to those from the Gauthier model for 3.8 cm sphere diameter with a medium final particle temperature (P2-M) for (a) CO, CO_2, & HCHO, (b) CH_3OH & CH_3COOH, and (c) CH_4 & HCOOH

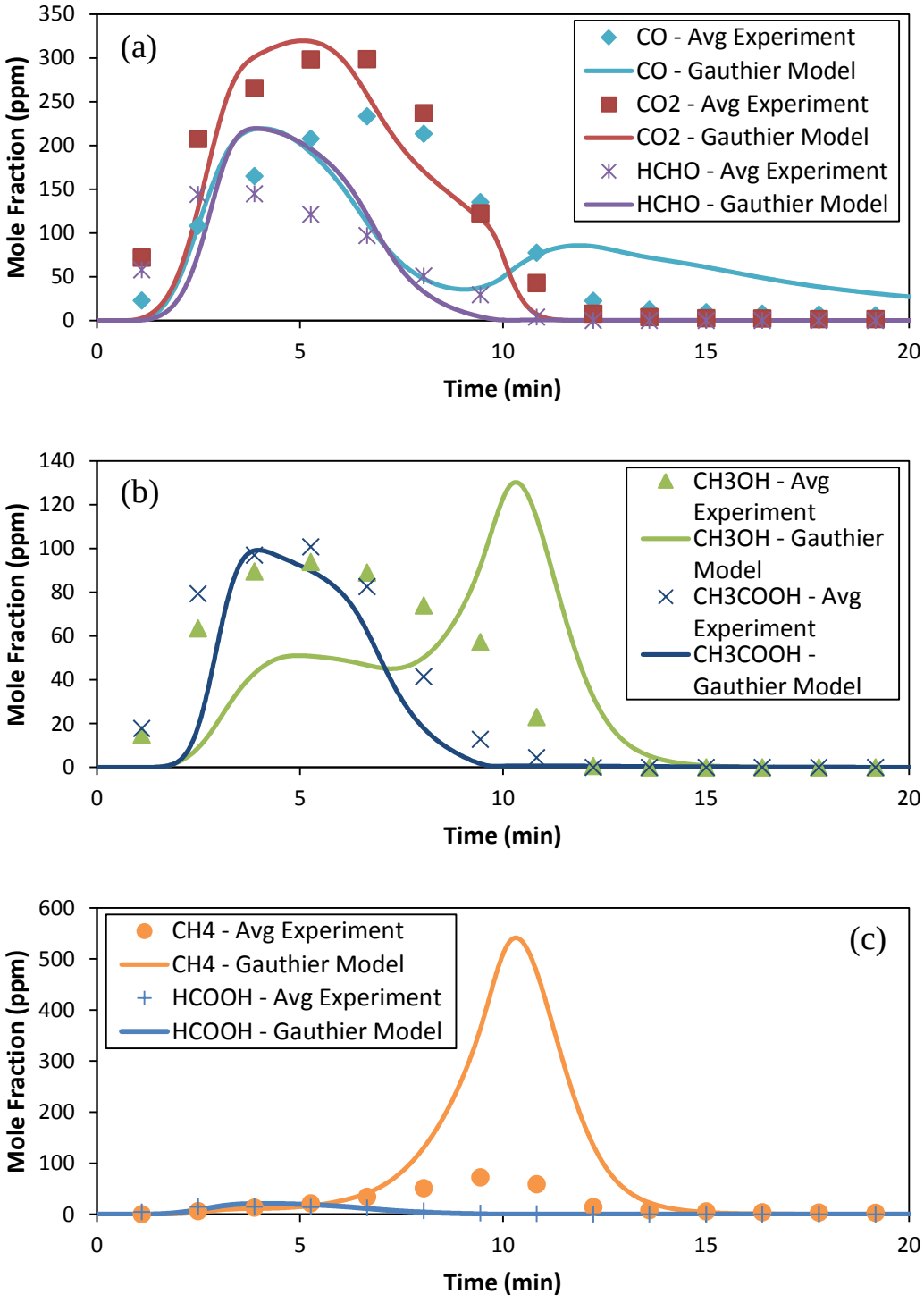

Figure 40. Comparison of average experimental species profiles to those from the Gauthier model for 3.8 cm sphere diameter with a high final particle temperature (P2-H) for (a) CO, CO_2, & HCHO, (b) CH_3OH & CH_3COOH, and (c) CH_4 & HCOOH

The shape of the species profiles agrees well with experiments for the production of HCHO, CH_3COOH, and HCOOH with the Gauthier model. In general for these species, the width of the peak predicted by the model is smaller than the experimental profile and the peak values are offset in time.

For carbon monoxide and methanol, a secondary peak begins to form as the operating temperature increases, with the maximum value of the second peak exceeding that of the first peak for CH_3OH at the high final particle temperature cases. This second peak is not seen experimentally for these two species and is caused by the release of chemisorbed species in the Gauthier kinetic mechanism, and corresponds to the exothermic peak in the temperature profiles.

While there is not a distinct second peak caused by the release of chemisorbed species for carbon dioxide predicted by the Gauthier model, the effect of their release can be seen in the shape of the CO_2 profile predicted by the model. This effect becomes more pronounced as the operating temperature increases, but is not seen in the experimental data.

The species profiles for methane predicted by the Gauthier model are very different from those seen experimentally. Similar to carbon monoxide and methanol, there are two distinct peaks predicted by the model. As the operating temperature increases, however, the second peak reaches extremely high values. For the high temperature cases, this secondary peak is so large that it completely envelops the initial peak. While this distinctive behavior predicted by the Gauthier model is not seen in the experimental profiles, the CH_4 experimental species profiles appear to show two separate peaks for the low temperature cases. In addition, this second peak occurs at the same time as the exothermic peak in the exothermic peak in the experimental temperature profile, which has previously been noted to

be caused by the decomposition of an intermediate solid. The combination of both of these features seen experimentally supports the notion of the release of chemisorbed species; however, the magnitude of this release is too high in the Gauthier model and causes distinct difference in the profiles of the species released through the decomposition of chemisorbed species.

To determine the effects of the release of chemisorbed species, the Gauthier model was run without these desorption kinetics. Four of the seven species studied previously were affected by these alterations: CO, CO_2, CH_4, and CH_3OH. Figures 41 through 46 plot the time-resolved profiles of these species from the Gauthier model with and without desorption kinetics, along with the average experimental species profiles.

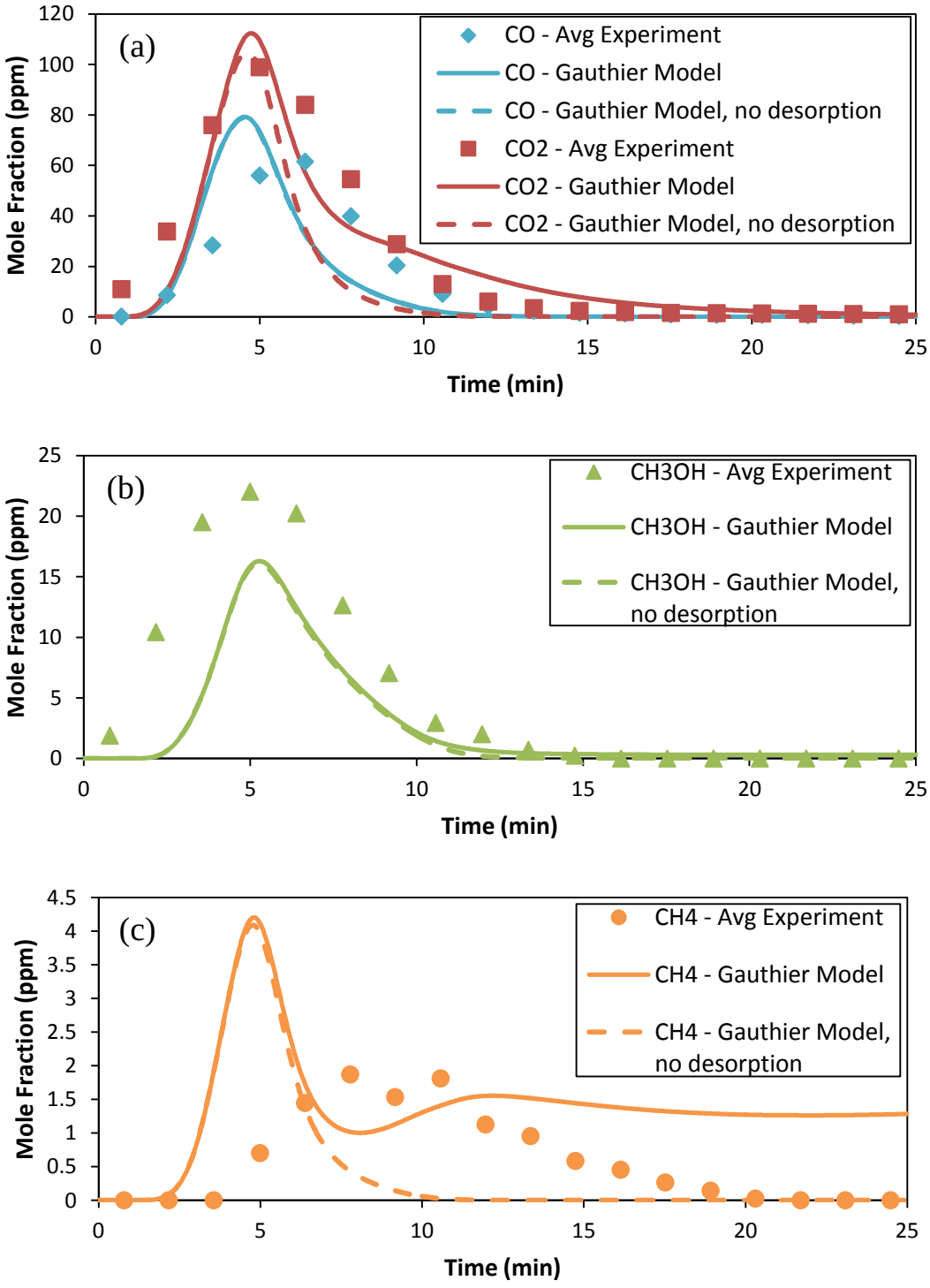

Figure 41. Comparison of average experimental species profiles to those from the Gauthier model with and without desorption kinetics for 2.54 cm sphere diameter with a low final particle temperature (P1-L) for (a) CO & CO_2, (b) CH_3OH, and (c) CH_4

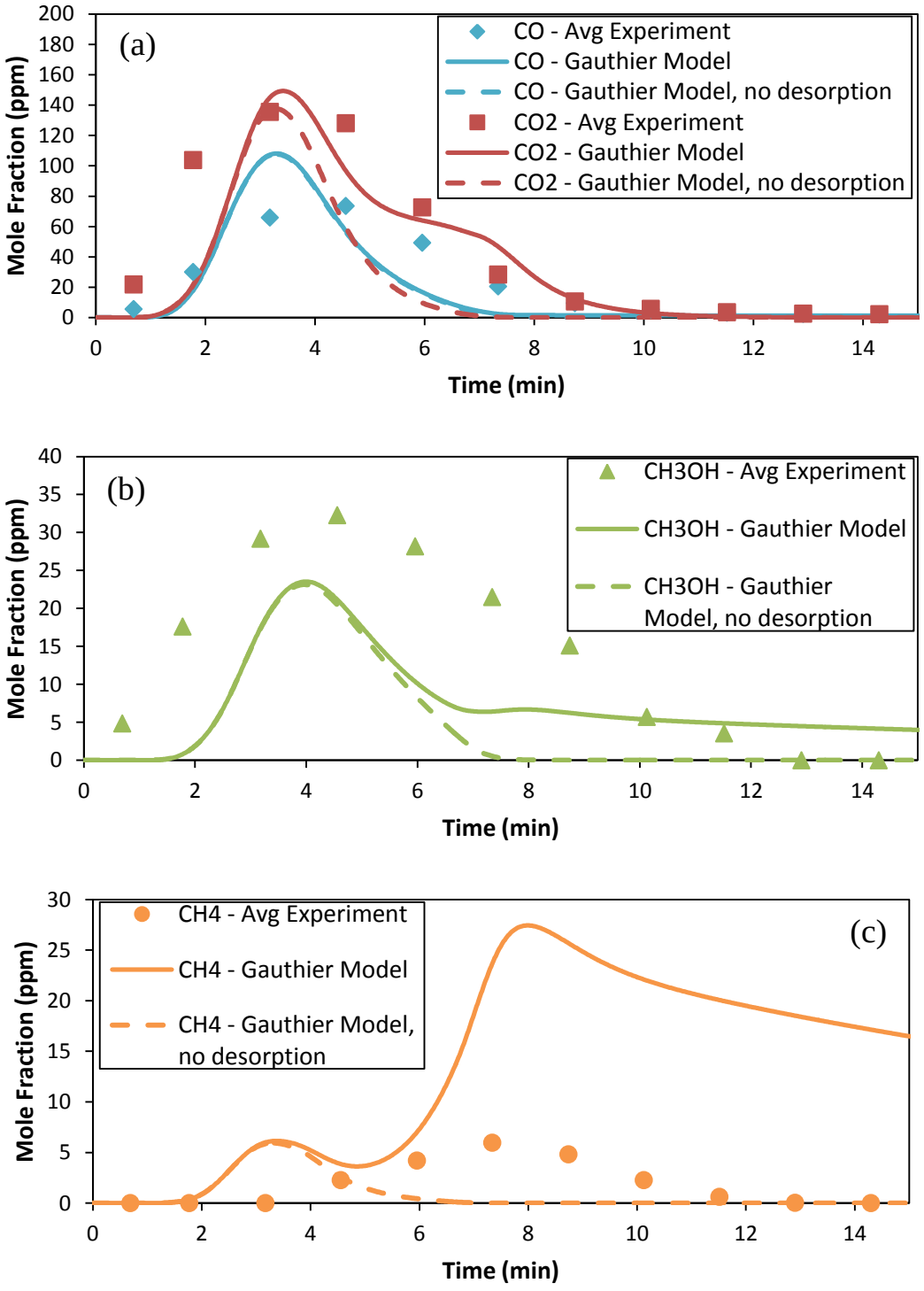

Figure 42. Comparison of average experimental species profiles to those from the Gauthier model with and without desorption kinetics for 2.54 cm sphere diameter with a medium final particle temperature (P1-M) for (a) CO & CO_2, (b) CH_3OH, and (c) CH_4

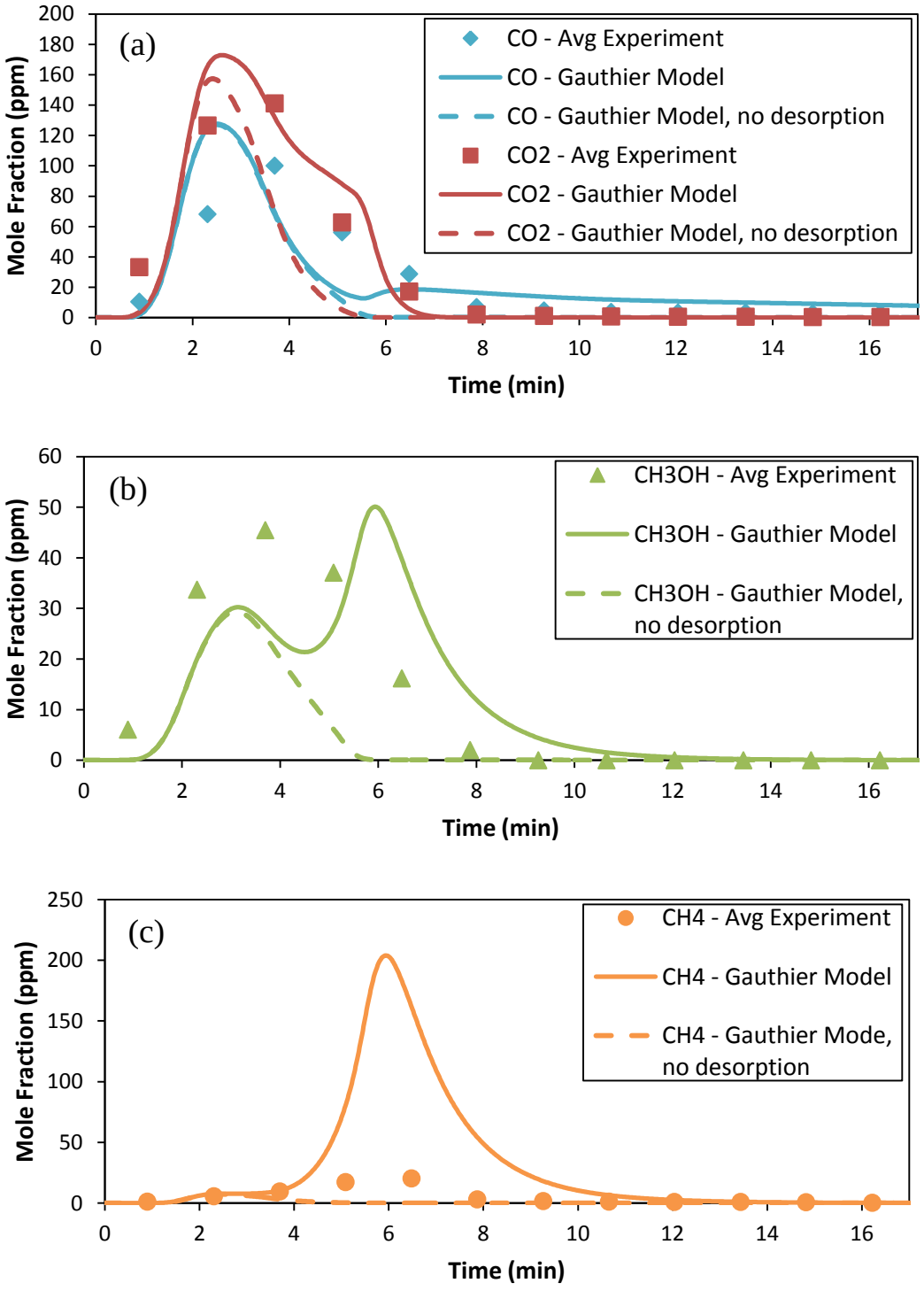

Figure 43. Comparison of average experimental species profiles to those from the Gauthier model with and without desorption kinetics for 2.54 cm sphere diameter with a high final particle temperature (P1-H) for (a) CO & CO_2, (b) CH_3OH, and (c) CH_4

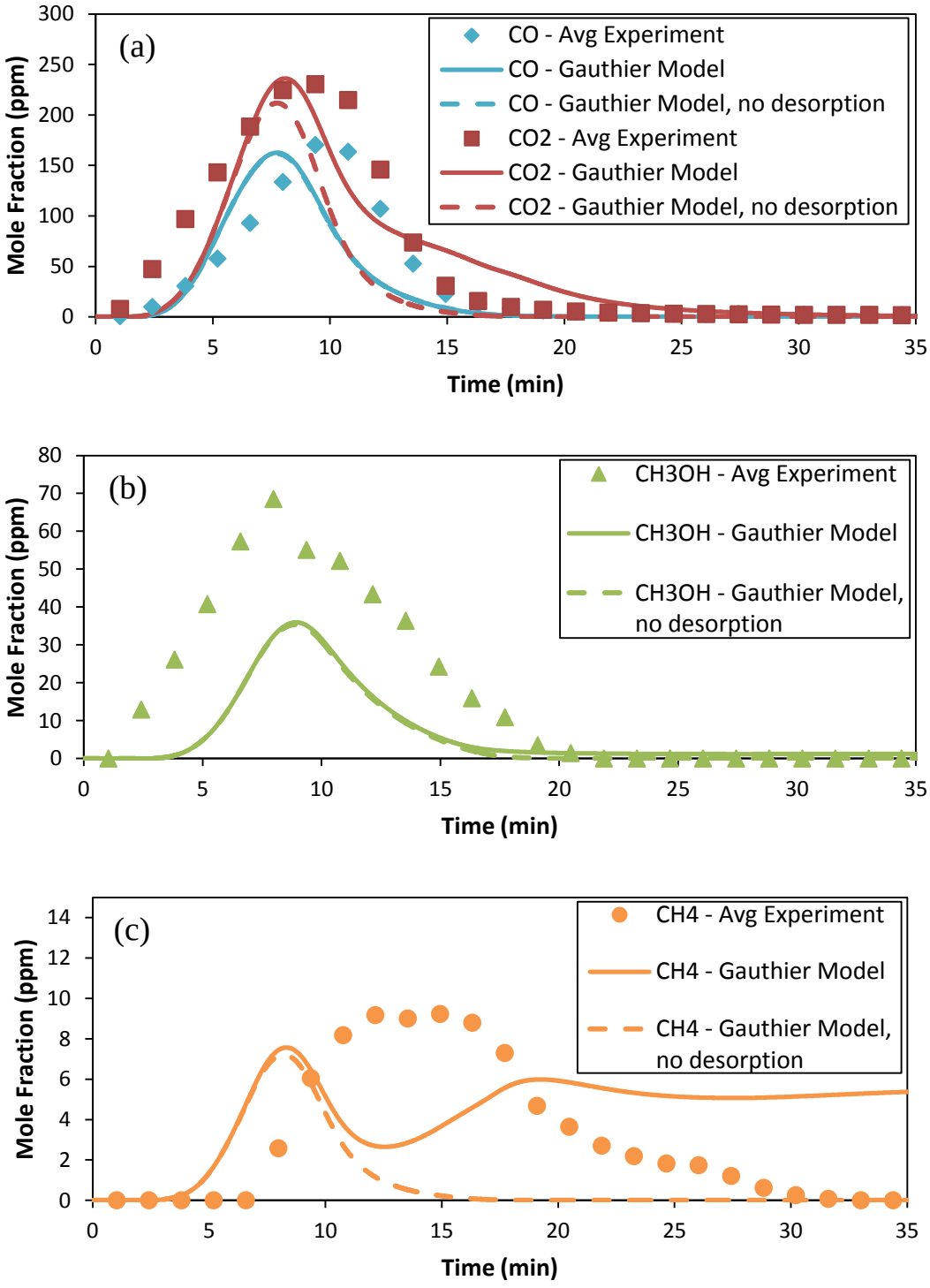

Figure 44. Comparison of average experimental species profiles to those from the Gauthier model with and without desorption kinetics for 3.8 cm sphere diameter with a low final particle temperature (P2-L) for (a) CO & CO_2, (b) CH_3OH, and (c) CH_4

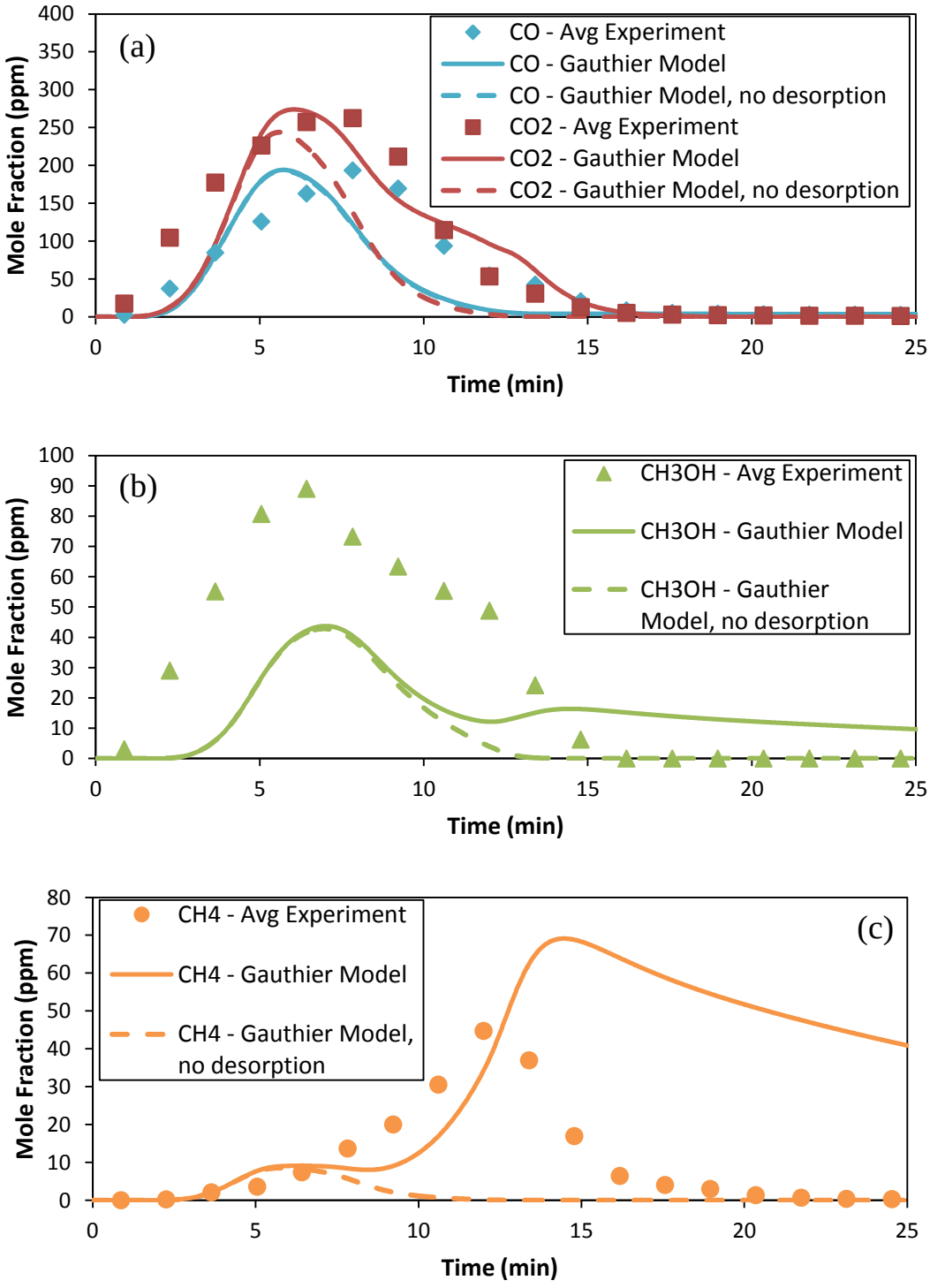

Figure 45. Comparison of average experimental species profiles to those from the Gauthier model with and without desorption kinetics for 3.8 cm sphere diameter with a medium final particle temperature (P2-M) for (a) CO & CO_2, (b) CH_3OH, and (c) CH_4

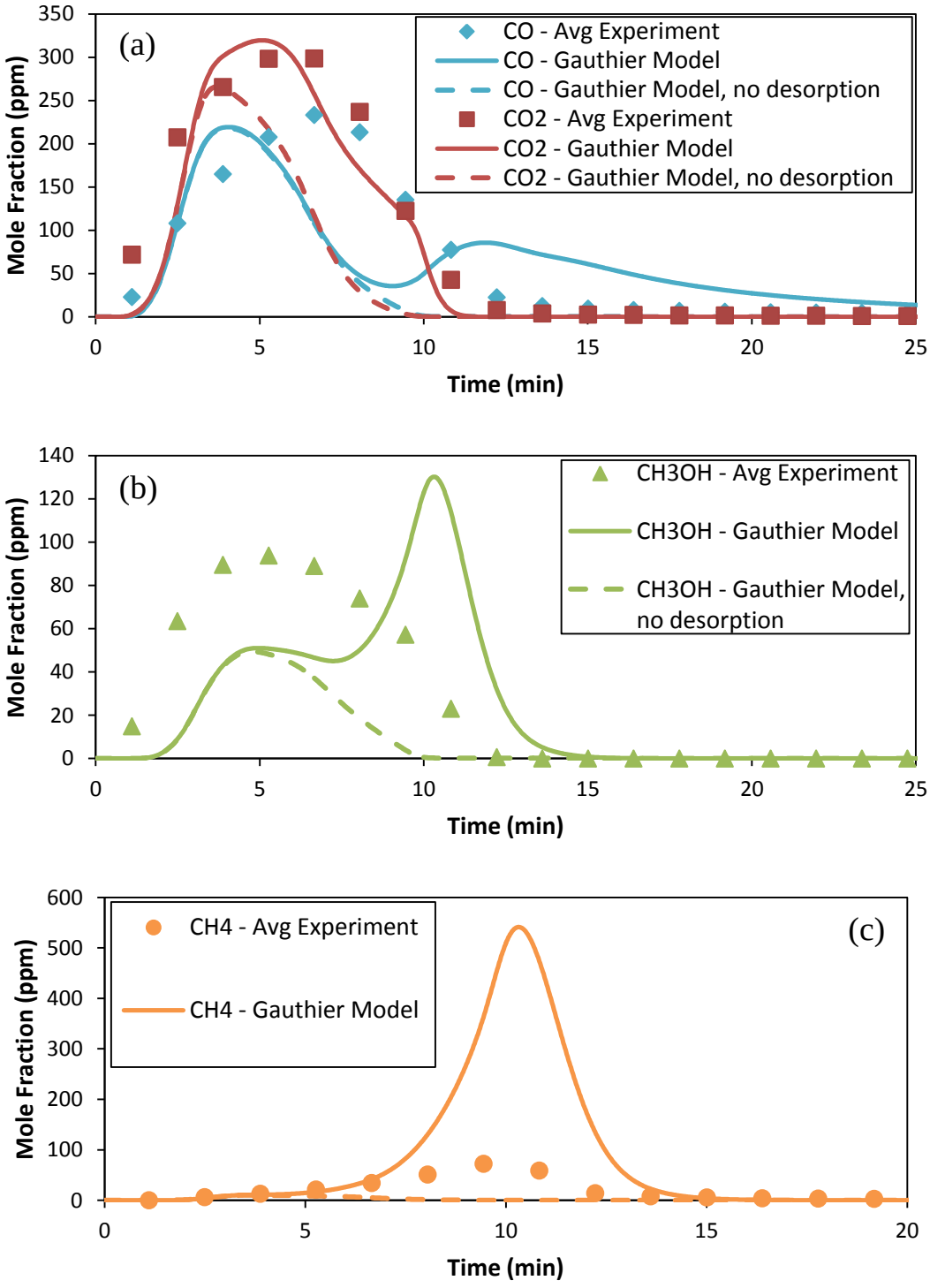

Figure 46. Comparison of average experimental species profiles to those from the Gauthier model with and without desorption kinetics for 3.8 cm sphere diameter with a high final particle temperature (P2-H) for (a) CO & CO_2, (b) CH_3OH, and (c) CH_4

From these figures, it can be seen that for most of the species, the release of chemisorbed species in the Gauthier model only affects the formation of a second peak in the time-resolved species profiles, where they exist with the desorption kinetics. However, for carbon dioxide, these reactions have an effect on the main production peak, as CO_2 never has a distinct second peak in the species profiles. The desorption of chemisorbed species causes a higher predicted peak and wider peak width than those predicted without these reactions.

For a quantitative representation of how well the Gauthier model predicts the experimental species profiles, errors were calculated between the model and experimental profiles for maximum values of the first peak reached in the profiles and the time to reach those peak values. Values are presented in Tables 52 and 53, respectively.

Table 52. Error between experimental data and Gauthier model predictions for the maximum value reached in species profiles. Positive values denote a higher maximum value predicted by the model than seen experimentally, while negative values signify a lower maximum value from the model than experiments. If more than one peak exists in the profile, values presented here correspond the peak which occurs first.

	P1-L	P1-M	P1-H	P2-L	P2-M	P2-H
CO	29%	47%	28%	-4%	0.5%	-6%
CO_2	14%	10%	23%	3%	4%	7%
CH_4	125%	3%	903%	-17%	-79%	650%
CH_3OH	-26%	-27%	-33%	-48%	-51%	-46%
HCHO	54%	114%	32%	91%	57%	52%
HCOOH	4%	-13%	15%	5%	29%	44%
CH_3COOH	-31%	14%	-8%	-27%	-19%	-1%

	> +50%
	+25% to +50%
	+10% to +25%
	-10% to +10%
	-25% to -10%
	-50% to -25%
	< -50%

Table 53. Error between experimental data and Gauthier model predictions for the time to reach peak values in the species profiles. Positive values denote the maximum value predicted by the model occurred later than the maximum in the experimental profile, while negative values signify that the model reached its peak value before experiments. If more than one peak exists in the profile, values presented here correspond to the peak which occurs first.

	P1-L	P1-M	P1-H	P2-L	P2-M	P2-H
CO	-29%	-28%	-32%	-17%	-27%	-39%
CO_2	-5%	8%	-30%	-14%	-23%	-24%
CH_4	-38%	-54%	-8%	-32%	-47%	9%
CH_3OH	6%	-12%	-15%	12%	9%	-6%
HCHO	36%	8%	10%	55%	61%	1%
HCOOH	-6%	7%	12%	-15%	17%	7%
CH_3COOH	0.1%	14%	15%	5%	23%	-25%

> +50%
+25% to +50%
+10% to +25%
-10% to +10%
-25% to -10%
-50% to -25%
< -50%

From Table 52, it can be seen that in general, the Gauthier model predicts higher values for the first peak achieved by the species than the peak values seen experimentally. The peak values predicted by the model for HCHO were a significant amount higher than experiments. The peak values for CH_4 at high temperatures were also much higher than the experimental values, which is caused by the high secondary peak formed from the release of chemisorbed CH_4 completely enveloping the first peak. Also of note, the model predictions for first peak values of CH_3OH are a considerably lower than the experimental values for every temperature and particle size case, as well as CH_4 and CH_3COOH for the larger wood diameter at low and medium temperatures. Despite these differences, there were also many cases where the model predictions matched very well with the experimental values. These include CO and CO_2 for the larger wood spheres, HCOOH at low operating temperatures, and CH_3COOH at higher operating temperatures.

The timing of these peak values predicted by the Gauthier model is very good for most of the species profiles, as can be seen in Table 53. For those that did not fit as well, the majority of the profiles from the model reached their peak values before the experiments. The

peak values of the release of species occur during the endothermic plateau in the temperature profiles, which correspond to the highest mass loss region of the experimental TGA data. In this region, the Gauthier model predicts a faster mass loss rate than seen experimentally, which would correspond to a faster release of species predicted by the model than seen in the experimental data. Especially of note, it can be seen that CO is always produced too soon in the model. Also, the model predicts the first peak values occurring sooner than experiments for CO_2 for the larger wood sphere cases and CH_4 at low and medium operating temperatures. In addition, the timing of the HCHO peak predicted by the model is very late for the larger wood sphere cases at low and medium temperatures.

Experimentally, CO and CO_2 are measured right away and end very late in the run, spreading the production over a long time. The production for CH_3OH, HCHO, HCOOH, and CH_3COOH occurs over a short time, beginning shortly after CO and CO_2, and ending much earlier in the run. For CH_4, production begins much later than the other species and ends shortly before CO and CO_2, with an overall production time in between that for CO and CO_2 and the other species.

For the Gauthier model, production of CO and CO_2 matches well with experiments, beginning early in the run and finishing towards the end, if at all in the case of CO at medium and high temperatures. Again, similar to the experimental results, HCHO and HCOOH begin to be produced after CO and CO_2, followed by CH_3OH and CH_3COOH. The model also predicts a short production time for these species, analogous to the experiments, except for CH_3OH, which is still produced at the end of some runs due to the release of chemisorbed species. CH_4 is the last of the species to start being produced and continues to be formed through the end of the run, except for the high temperature cases where the production of CH_4

ends after the other species. While the trend in timing of the production of species predicted by the Gauthier model generally matches with experiments, the release of chemisorbed CH_4 and CH_3OH cause their production in the model to last much longer than seen experimentally.

The timing of the peak values was also compared between the measured values and the model predictions. The comparison of the timing of peaks between experiments and model predictions are only discussed for the peak values that occur first, if two peaks exist for the profile. Experimentally, HCHO peaks first, followed by HCOOH, CH_3OH, and CH_3COOH. The peak of CO then occurs, after which CH_4 peaks. The peak for CO_2 occurs early (around CH_3OH) at lower temperatures and smaller wood sphere diameters, but moves later (around CO) at higher temperatures and larger particle sizes. From the model, CO peaks first, followed by HCHO, HCOOH, and CO_2. After this, the peaks for CH_3COOH and CH_3OH occur. For CH_4, the species peaks around CO_2 for low and medium temperatures, but peaks last for the high temperature cases due to the large second peak that encompasses the earlier peak. The trend of timing of the species peaks predicted by the Gauthier model matches fairly well with experiments for HCHO, HCOOH, CH_3COOH, and CO_2 at low temperatures and small particle sizes. However, the peaks for CO, CH_4, and CO_2 at high temperatures and larger particle sizes occur earlier than seen experimentally.

Total yields of each of the species measured experimentally are presented in Figure 47 for both the experiments and the Gauthier model predictions.

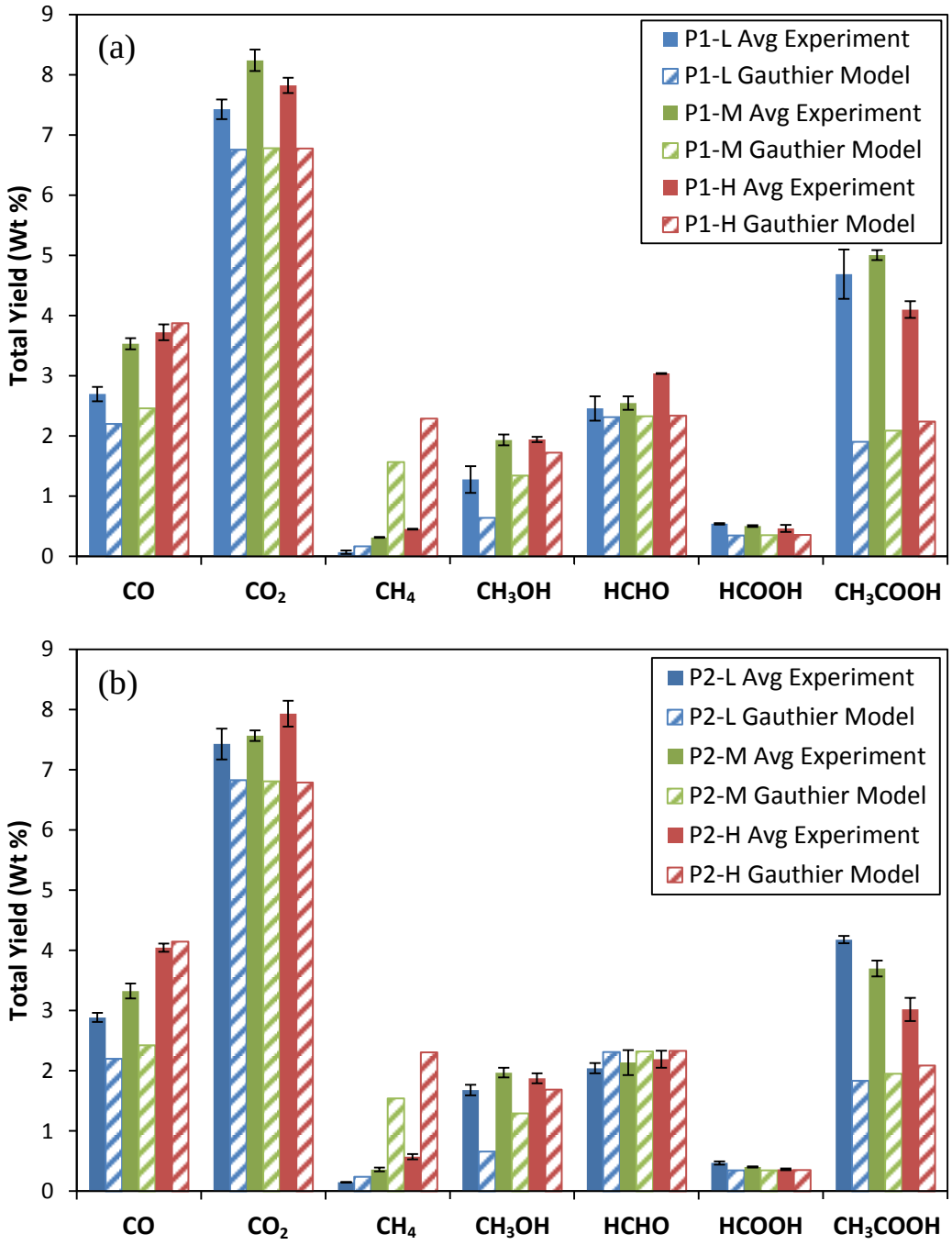

Figure 47. Average experimental species yields as compared to the predictions from the Gauthier model for (a) 2.54 cm sphere diameter and (b) 3.8 cm sphere diameter

For a quantitative representation of how well the Gauthier model predicted the experimental yield of species, errors were calculated between the experimental values and model predictions and are presented in Table 54.

Table 54. Error between experimental data and Gauthier model predictions for the total yields of species. Positive values denote a higher yield predicted by the model than seen experimentally, while negative values signify a lower yield from the model than experiments.

	P1-L	P1-M	P1-H	P2-L	P2-M	P2-H
CO	-18%	-30%	4%	-24%	-27%	3%
CO_2	-9%	-18%	-13%	-8%	-10%	-14%
CH_4	140%	397%	405%	62%	330%	305%
CH_3OH	-50%	-31%	-11%	-61%	-34%	-10%
HCHO	-6%	-9%	-23%	13%	9%	7%
HCOOH	-36%	-30%	-23%	-26%	-13%	-2%
CH_3COOH	-59%	-58%	-45%	-56%	-47%	-31%

	> +50%
	+25% to +50%
	+10% to +25%
	-10% to +10%
	-25% to -10%
	-50% to -25%
	< -50%

From this table, it can be seen that a majority of the species yields are under-predicted by the model. The main exception to this is the production of CH_4, which is significantly higher than the experimental values, especially at higher temperatures where the release of chemisorbed species causes an unrealistically high second peak in the species profile. In general, the model predictions are better for larger wood sphere diameters and higher temperatures.

Looking at the experimental trends of species yields with particle size, it can be seen that for CO and CO_2, production of both species is about the same for both the small and large wood sphere diameters. The yield of CH_4 increases with increasing particle size, while the production of HCHO, HCOOH, and CH_3COOH decrease with increasing particle size. The yield for CH_3OH increases with increasing particle size, except at high temperatures, where production decreases with increasing size. The Gauthier model is able to capture the trends

with particle size for all of these species except for HCHO, where the model predicts about the same yield for both the small and large wood sphere diameters. However, these trends with particle size are very small when compared to the trends with temperature.

For experimental trends of species yields with temperature, the production of CO, CH_4, and HCHO increase with increasing temperature. This trend also occurs for CO_2 produced from the large wood sphere diameter and CH_3OH for the small wood sphere diameter. For HCOOH, the experimental yield decreases with increasing temperature. CH_3COOH for the large wood sphere diameter cases also follows this trend. The remaining cases – CO_2 and CH_3COOH for the small particle size and CH_3OH for the large particle size – follow an increase in yield, then a decrease with increasing temperature.

The Gauthier model is able to predict the yield trends with temperature for CO, CH_4, and HCHO. However, it is not able to capture the trends for HCOOH or CH_3COOH, both of which the model predicts as having increasing yields with increasing temperature. This may be caused by the decomposition of these more complex molecules through secondary reactions at higher temperatures, which are not modeled in the simulation. For CO_2 and CH_3OH, the model is able to predict the trends with temperature for the smaller wood diameter cases, but fails to predict the trends for the larger particle size. With CH_3OH, the model predicts the same trend with temperature for the large diameter cases as for the small diameter cases, while experimentally the trend changes with particle size. However, for CO_2, the model predicts a decrease in yield with increasing temperature for the larger wood sphere diameter, which is not seen experimentally for either particle size.

CHAPTER 5

SUMMARY, CONCLUSIONS, AND FUTURE WORK

A numerical study of the pyrolysis of biomass is presented in this thesis. In this chapter, a summary of this work is first presented, along with major conclusions. Following this, suggestions for future work are discussed.

5.1 Summary and Conclusions

Two one-dimensional numerical simulations were developed to model the pyrolysis of wood spheres. These models were based on the proposed model developed by Park et al., 2010, and include physical processes coupled with a kinetic mechanism that describes the pyrolysis reactions. These phenomena include heat transfer within the wood particle, chemical decomposition of wood into products, and the pressure-driven flow of gas-phase species through the porous media, described using Darcy's law. The Park model included a kinetic mechanism developed by Park et al., 2010, where wood decomposes through a few parallel reactions and secondary reactions to form gas, tar, and char. The Gauthier model implements a more detailed kinetic mechanism, presented by Gauthier et al., 2013, which describes the decomposition of the main constituents of wood – cellulose, hemicellulose, and three types of lignin – and characterizes gas and tar fractions with a limited number of components.

Outputs from both the Park and Gauthier models were compared to the experimental

data. The kinetic mechanisms were evaluated by comparing model outputs to TGA mass loss curves. The predictions of both models matched the experimental profiles decently. The Park model matched the half-destruction point well, but was not able to capture the slow mass loss seen towards the beginning and end of the profile. These discrepancies were also observed in Park et al., 2010, where it was noted that the kinetic scheme better represented the decomposition of cellulose and did not adequately capture the effects of the decomposition of hemicellulose and lignin. The Gauthier model was able to predict the slow mass losses seen in the initial and final sections of the experimental TGA mass loss profile, but predicted a faster mass loss between 300-375°C, during the decomposition of cellulose. While the mass loss predictions did not match experimental values extremely well, this kinetic mechanism has be developed to match several sets of experimental data reasonably well.

For temperature profiles measured at the center of the wood particle, both models were able to predict the general aspects seen experimentally: an endothermic plateau, followed by an exothermic peak. For both models, the endothermic plateau began sooner than experiments and were not as distinct as the experimental plateaus. The Park model was able to predict the value of the exothermic peak very well, but the width was much smaller and the peak occurred later than seen experimentally. For the Gauthier model, the exothermic peak was lower than the experimental value, but the width and timing of the peaks were comparable to the experimental profiles, although the peaks occurred slightly later for larger wood spheres.

The production of gas predicted by both models was compared to experimental profiles. The Park model predicted the release of gases reasonably well. The Gauthier model predictions were also similar to the experimental profiles at lower temperatures, but predicted

a very high release of chemisorbed species at higher temperatures that produced a distinct second peak in the gas profile that was not seen experimentally. In both of the models and in the experimental profiles, the main release of gas occurred before the exothermic peak in the temperature profiles, supporting the view that the exothermic peak is caused by the decomposition of an intermediate solid.

Both the Park and Gauthier models were able to predict the yield of gas relatively well, as well as the trend in gas production with particle size and operating temperature. However, both models predicted higher tar yields and lower yields of char than seen experimentally. This could be caused by secondary char being formed from the decomposition of tar as it moves through and leaves the biomass particle. Despite these discrepancies, both models were able to predict the trends of tar and char yields with particle size and operating temperature.

Because the Gauthier model predicts the production of specific species, the release of individual species in the gas phase was compared to time-resolved experimental profiles. The model was able to predict the release of individual species fairly well, except for the release of chemisorbed species, which causes a distinct secondary peak in the species profiles. This secondary peak was especially considerably in the production of CH_4, where the secondary peak reaches extremely high values. While these significant secondary peaks caused by desorption kinetics in the model were not seen experimentally, measured profiles for CH_4 at low temperatures show two distinct peaks, supporting the notion of the release of chemisorbed species.

Discounting the secondary peaks caused by the desorption kinetics in the model, the peak values achieved in the species profiles predicted by the Gauthier model are generally

higher than experimental values. The timing of these peak values, however, matches reasonably well with experimental values. Also, trends in the timing of the release of species predicted by the model matches well with experiments for most cases. The exceptions to this are the release of CH_4 and CH_3OH, which are produced over a longer period in the model than seen experimentally, and the peaks of CO, CH_4, and occasionally CO_2, which occur earlier in the model than in the measured profiles.

The yields of individual species predicted by the Gauthier model were compared to experimental values. Total yields predicted by the model were generally lower than the experiments, except for CH_4, which has a much higher yield than the experimental value because of the extremely high secondary peaks caused by the release of chemisorbed species. However, despite these differences, the model was able to capture the trends of yields with particle size for all species except for HCHO. For the trends of species yields with temperature, the model predictions match well with experiments for CO, CH_4, and HCHO, as well as CO_2 and CH_3OH for the smaller particle size. The model fails to capture the trends of yields with temperature for HCOOH and CH_3COOH, along with CO_2 and CH_3OH for the larger particle sizes.

Both the Park and Gauthier models performed reasonably well when compared to experimental data. Either model would do well for predicting the amount of gas produced during the slow pyrolysis of thermally thick wood particles, as well as the trends in tar and char yields with particle size and temperature. The Gauthier model would also be useful for predicting the trends in yields of specific species with temperature and particle size. However, the release of chemisorbed species should be adjusted in the Gauthier kinetic mechanism before this model is used to predict the time-resolved release of volatiles.

The development of the Gauthier model contributes considerably to numerical modeling of the slow pyrolysis process. This model provides detailed information on the composition of volatiles being produced through the slow pyrolysis of thermally thick particles, as well as the timing of the release of specific species. Using this model on an industrial scale, these predictions could be used to more accurately make decisions concerning the post-processing of gases and/or tars, dependent on the composition of these products, as well as the ability to optimize the composition of gas-phase products through the collection of volatiles at specified times in the pyrolysis process.

However, while there are many advantages to using this model for slow pyrolysis on a larger scale, there are also some disadvantages, primarily with the specification of initial and boundary conditions that are appropriate for the reactor being used. As has been shown in this research, the heat transfer external to the biomass particle has a significant impact on the model outputs, and so need to be reasonably accurate. These boundary conditions, however, may not been easily determined for a reactor with many biomass particles without well-defined conditions for each one. Also, select material properties have also been shown to affect the model considerably, but properties could be difficult to determine for a large number of particles for which the variability is much larger than the few samples studied in this research.

5.2 Future Research

There are many areas for improvement for the numerical model developed in this research. First, the convection heat transfer coefficient and radiation from the insulated

reactor walls need additional analysis. The parameters defining these two processes need to be determined more accurately due to the substantial effect they have on model outputs. Also, select material properties were found to have a significant impact on model predictions. While effective material properties were determined in this research, model outputs did not match as well with experimental data as desired. In addition to these modifications to the model, alterations to the Gauthier kinetic mechanism are needed, including an adjustment to the release of chemisorbed species and the addition of secondary reactions describing the decomposition of tar into char.

After these adjustments are made to the model, additional effects that were not studied in this research should be investigated. These effects can have a significant impact on the ability of the simulation to predict experimental results. First, the significance of a multi-dimensional model and anisotropic material properties is discussed. After this, the impact of the diffusion of volatiles through the porous wood is presented. Lastly, the effect of shrinkage of wood particles as they pyrolyze is discussed. While these factors were not examined in this research, they provide areas for future research to build on the current model and improve the ability of a numerical simulation to predict the pyrolysis process.

Multi-dimensional Model and Anisotropic Material Properties

Even though a one-dimensional simulation provided basic information about the pyrolysis of wood spheres, many approximations were made to simplify the complexity of both the wood material and the experimental setup. To capture these effects, a multi-dimensional model is needed.

One significant approximation made in the numerical model used for this research was assuming wood properties were isotropic. Material properties are highly anisotropic due to the grain structure of the wood. Thermal conductivity across and tangential to the grain direction has been found to be approximately one-third that along the grain, while the permeability of the biomass matrix to gaseous species across the wood grain is much lower than that in the other two directions (Di Blasi, 2008). Because of this large variation, the dynamics of particle degradation are strongly affected by the grain structure of the solid (Di Blasi, 1998b).

Despite the benefits of a multi-dimensional model, the complexity and significant increase in computational time make is a less desirable solution to study the effects of anisotropic properties. An alternate method is presented by Ozisik, 1980, where the effect of anisotropic properties in the energy equation can be captured by transforming the heat-conduction equation into one dimension with a reference thermal conductivity. While this method captures the effect of the grain structure on the energy equation, it does not modify the effect of anisotropic properties in other conservation equations used to model the pyrolysis of wood. However, it does provide a first step for studying the effects of anisotropic material properties caused by the grain structure of wood.

Another factor impacted by the use of a one-dimensional simulations is the convective heat transfer. From fluid flow analysis, it is known that the velocity of a fluid around a solid sphere depends on the angular position from the free stream velocity (Incropera and DeWitt 2001). This correlates to a variable convective heat transfer coefficient that is dependent on the position in the flow. Consequently, certain angular positions along the surface of the wood sphere have higher heating rates than others. This leads to variation in the reaction front that cannot be predicted by a one-dimensional simulation. While the experimental setup could be

altered to simplify the boundary conditions for the conservation of energy, and thus make a one-dimensional model more suitable, a multi-dimensional model is needed to accurately predict the experimental data presented in this research.

A numerical model which incorporates more than one dimension would greatly enhance the ability of a numerical model to predict the physical processes which occur during the pyrolysis of woody biomass. While a one-dimensional simulation provided an initial step, future research would benefit considerably from a multi-dimensional model.

Diffusion of Gaseous Species

In the numerical model used in this research, diffusion of gaseous species produced from the pyrolysis process is assumed to be much smaller than the pressure-driven flow, and is thus neglected. Chan et al., 1985 found that at all temperatures, mass transfer by hydrodynamic flow for gaseous products is much faster than by diffusion, making the inclusion of diffusion unnecessary for non-oxidative pyrolysis. Many wood pyrolysis models exist in the literature that also neglect the effect of diffusion (Di Blasi, 2008). While this assumption is considered to be acceptable for this research, future studies could be done to verify its validity for these experimental conditions.

Particle Shrinkage During Pyrolysis

The wood particle is known to shrink as it undergoes pyrolysis. Also, for the experimental setup presented here, the shrinkage is not uniform, causing a change in the shape as the wood pyrolyzes. Initial wood sphere diameters and the three diameters describing the final char ellipsoids from the experimental data used in this research are presented in Tables 55 and 56.

Data was provided by Hayat Bennadji, Sibley School of Mechanical and Aerospace Engineering, Cornell University.

Table 55. Final char particle dimensions for wood spheres with a 2.54 cm initial diameter. For char diameters, a > b > c

Run #	Final Particle Temperature (°C)	Wood Diameter (cm)	Char Diameters (cm)		
			a	b	c
P1-L1	368.8	2.54	2.352	1.872	1.631
P1-L2	367.3	2.535	2.327	1.859	1.656
P1-L3	374.2	2.535	2.319	1.885	1.623
P1-L4	374.4	2.54	2.319	1.844	1.669
P1-M1	423	2.54	2.235	1.819	1.712
P1-M2	418.9	2.53	2.228	1.877	1.763
P1-H1	470.3	2.54	- [a]	- [a]	- [a]
P1-H2	477.6	2.54	- [a]	- [a]	- [a]

[a]Char split

Table 56. Final char particle dimensions for wood spheres with a 3.8 cm initial diameter. For char diameters, a > b > c

Run #	Final Particle Temperature (°C)	Wood Diameter (cm)	Char Diameters (cm)		
			a	b	c
P2-L1	374.4	3.8	3.477	2.837	2.642
P2-L2	372.9	3.81	- [a]	- [a]	- [a]
P2-L3	373	3.785	3.457	2.875	2.654
P2-M1	417.2	3.8	3.404	2.883	2.738
P2-M2	419.2	3.785	3.368	2.934	2.751
P2-M3	417.4	3.81	3.360	3.030	2.903
P2-H1	486.5	3.795	- [a]	- [a]	- [a]
P2-H2	488.5	3.79	- [a]	- [a]	- [a]
P2-H3	480.1	3.81	- [a]	- [a]	- [a]

[a]Char split

Shrinkage has been shown to affect the heat transfer rate through the solid, as well as the volatile residence times, which have an effect on the reaction rates and the product yield distribution (Di Blasi, 1996a). Also, for the experimental setup used in this research, convection is the primary form of heat transfer to the wood, which is dependent on the size

and shape of the particle. Because of this, the shrinkage is expected to be a significant factor and should be examined in future research.

APPENDIX A

Experimental temperature profiles from the center of the particle and time-resolved species plots for permanent gases and several light volatile species are given for each of the experimental setups (H. Bennadji, Mechanical and Aerospace Engineering, Cornell University unpublished work, 2013). While data exists for the entire run time, these plots are limited to a reduced time scale to provide more detail in noteworthy sections of the experimental profiles.

Experimental Data for 2.54 cm Wood Sphere Diameter with a Low Final Particle Temperature (P1-L)

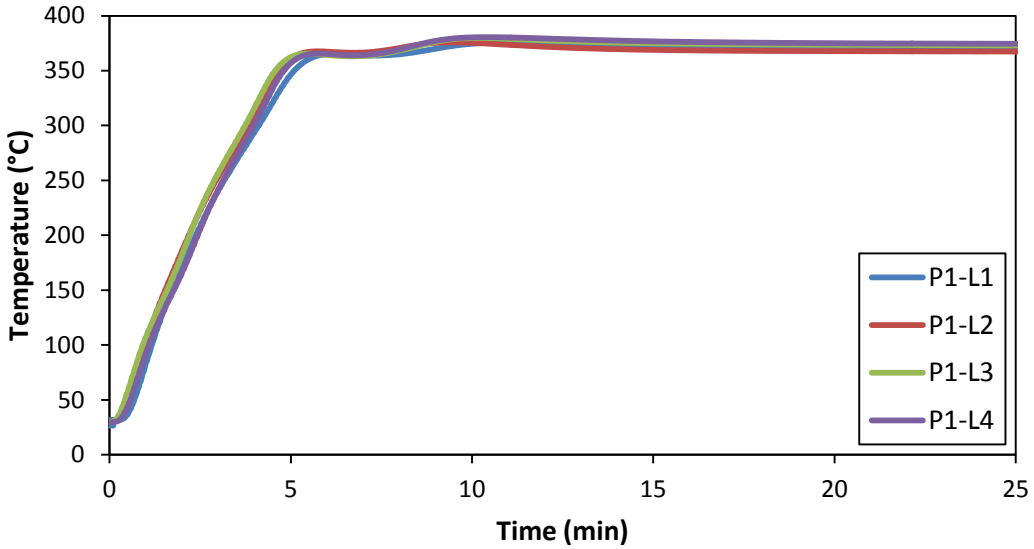

Figure 48. Experimental temperature profiles from the particle center for 2.54 cm wood sphere diameter with a low final particle temperature (P1-L)

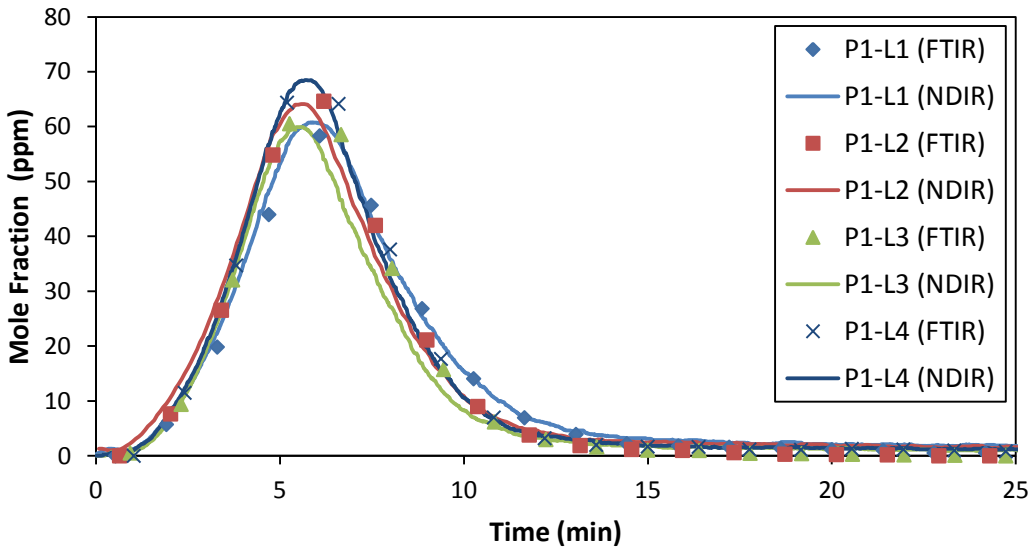

Figure 49. Experimental carbon monoxide (CO) profiles for 2.54 cm wood sphere diameter with a low final particle temperature (P1-L)

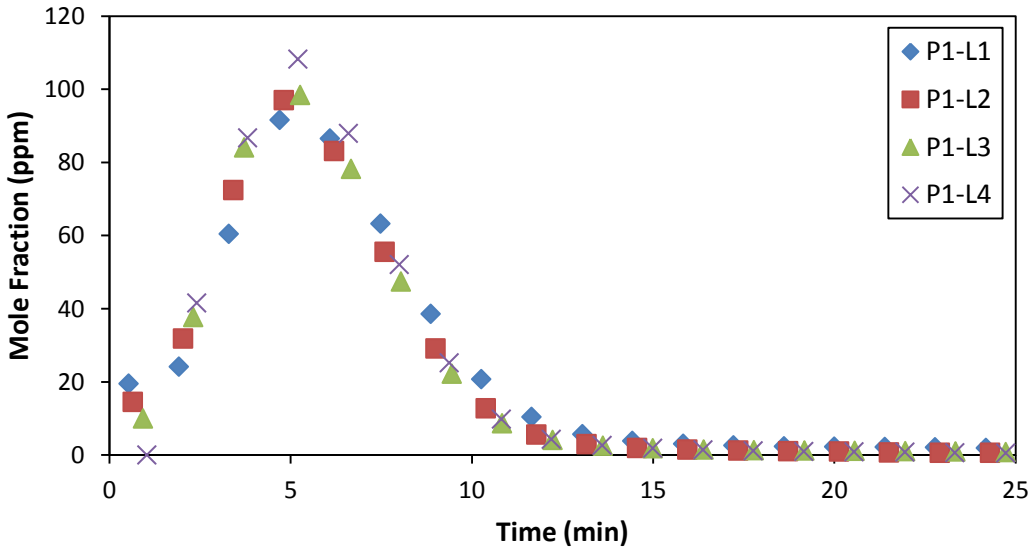

Figure 50. Experimental carbon dioxide (CO_2) profiles for 2.54 cm wood sphere diameter with a low final particle temperature (P1-L)

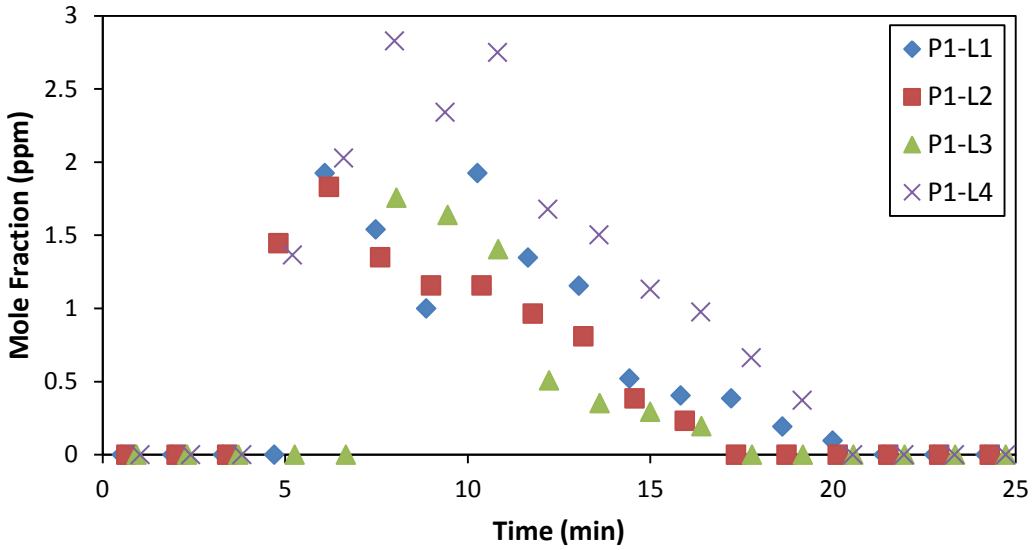

Figure 51. Experimental methane (CH_4) profiles for 2.54 cm wood sphere diameter with a low final particle temperature (P1-L)

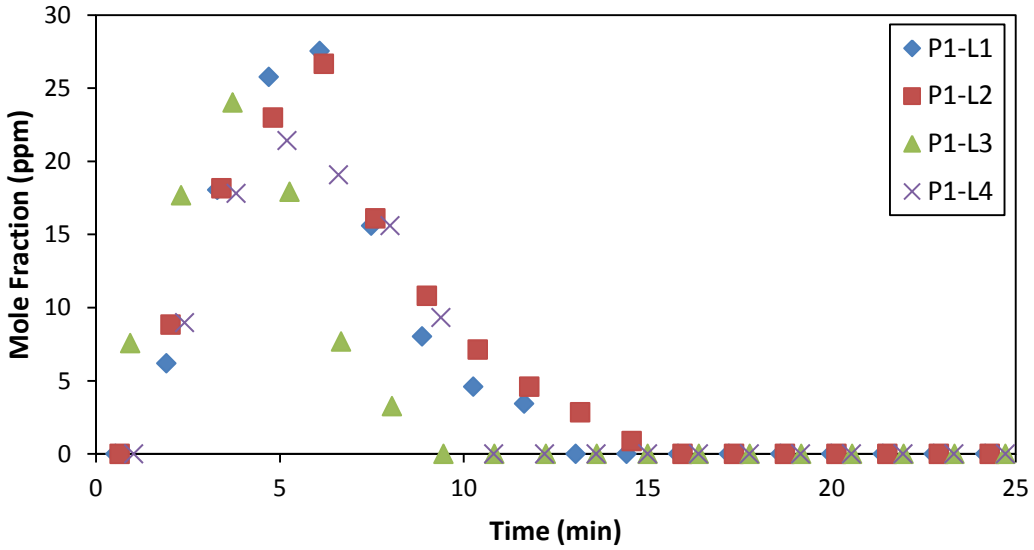

Figure 52. Experimental methanol (CH_3OH) profiles for 2.54 cm wood sphere diameter with a low final particle temperature (P1-L)

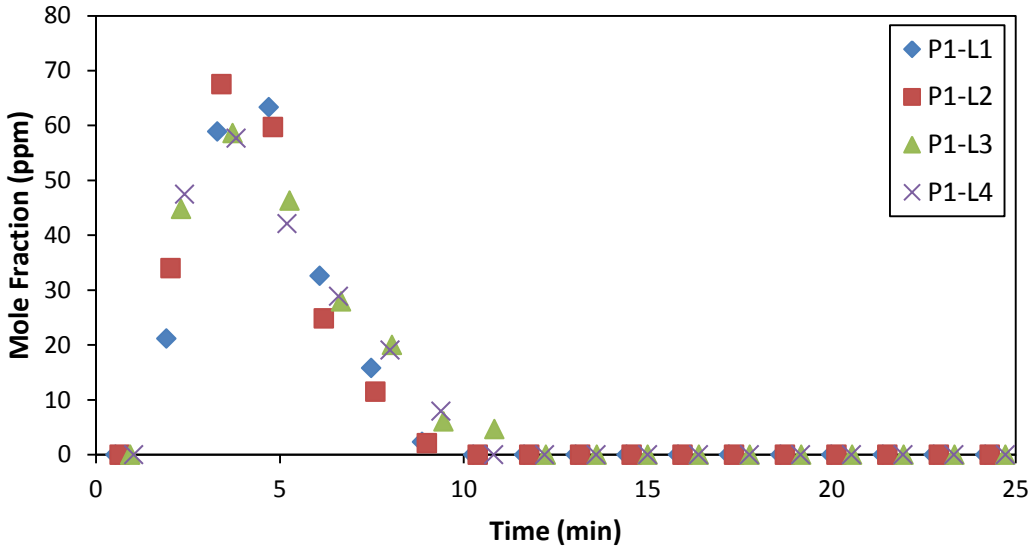

Figure 53. Experimental formaldehyde (HCHO) profiles for 2.54 cm wood sphere diameter with a low final particle temperature (P1-L)

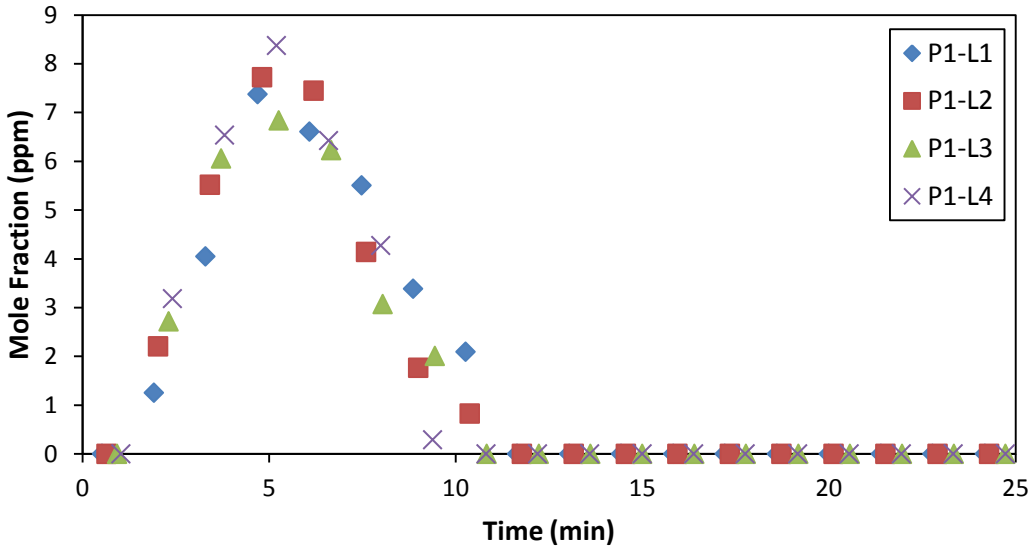

Figure 54. Experimental formic acid (HCOOH) profiles for 2.54 cm wood sphere diameter with a low final particle temperature (P1-L)

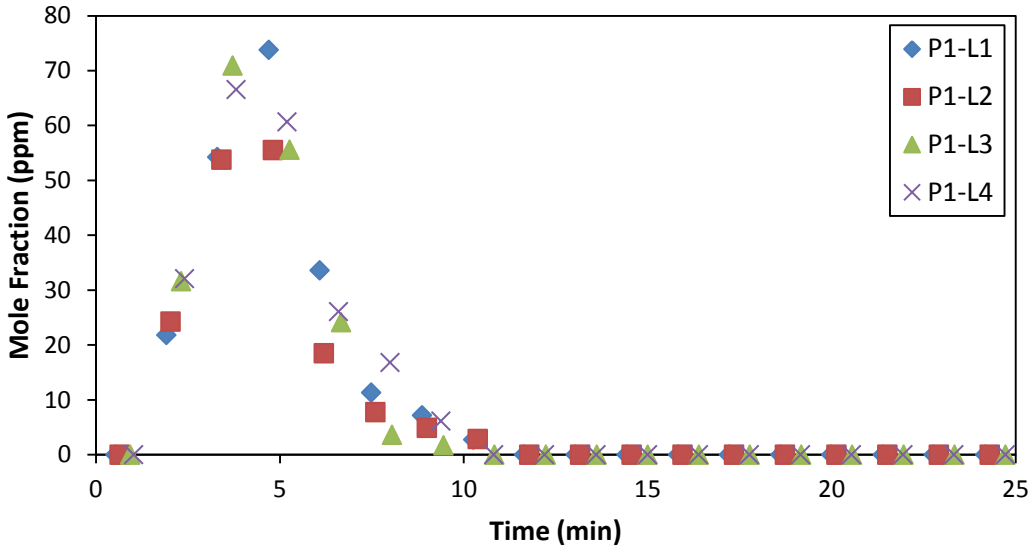

Figure 55. Experimental acetic acid profiles (CH_3COOH) for 2.54 cm wood sphere diameter with a low final particle temperature (P1-L)

Experimental Data for 2.54 Wood Sphere Diameter with a Medium Final Particle Temperature (P1-M)

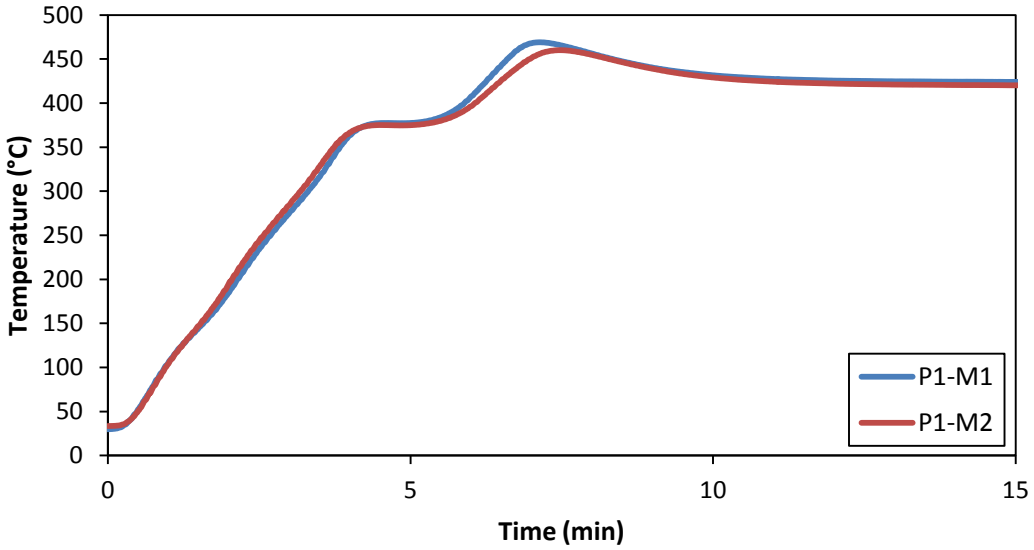

Figure 56. Experimental temperature profiles from the particle center for 2.54 cm wood sphere diameter with a medium final particle temperature (P1-M)

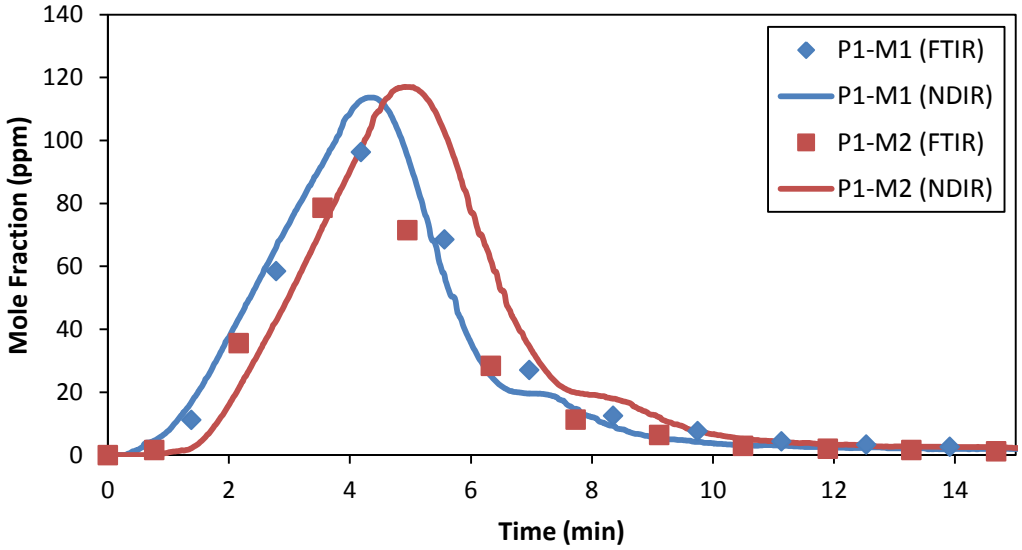

Figure 57. Experimental carbon monoxide (CO) profiles for 2.54 cm wood sphere diameter with a medium final particle temperature (P1-M)

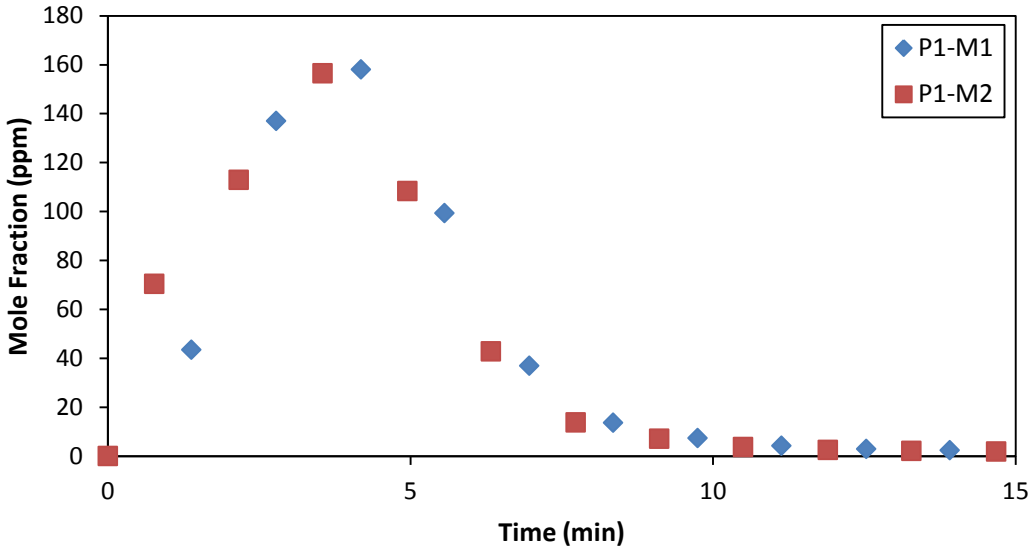

Figure 58. Experimental carbon dioxide (CO_2) profiles for 2.54 cm wood sphere diameter with a medium final particle temperature (P1-M)

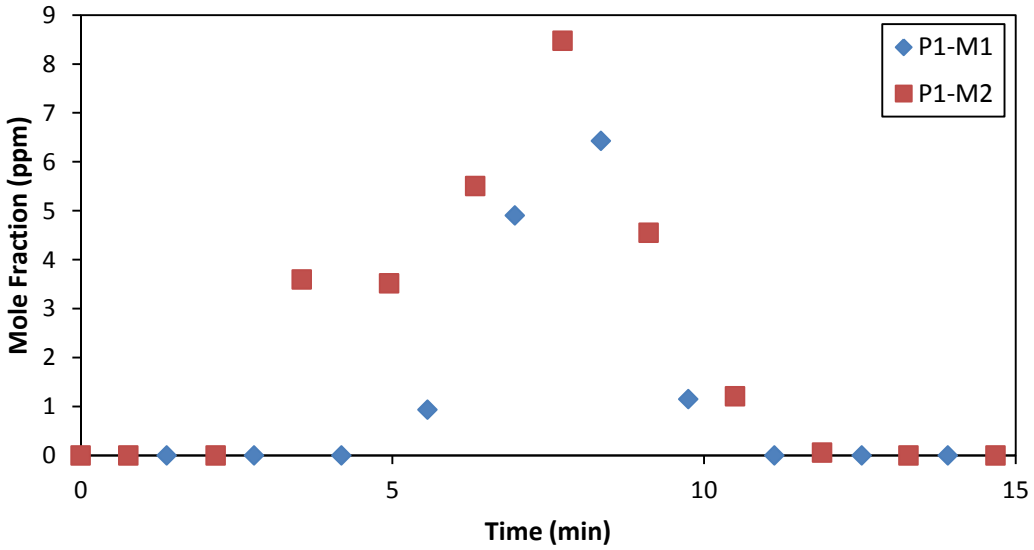

Figure 59. Experimental methane (CH_4) profiles for 2.54 cm wood sphere diameter with a medium final particle temperature (P1-M)

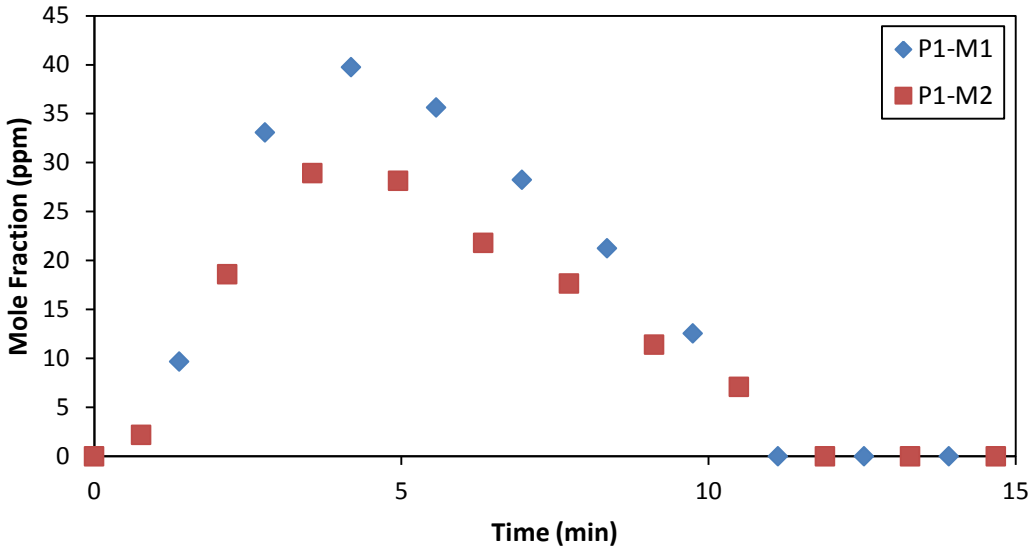

Figure 60. Experimental methanol (CH_3OH) profiles for 2.54 cm wood sphere diameter with a medium final particle temperature (P1-M)

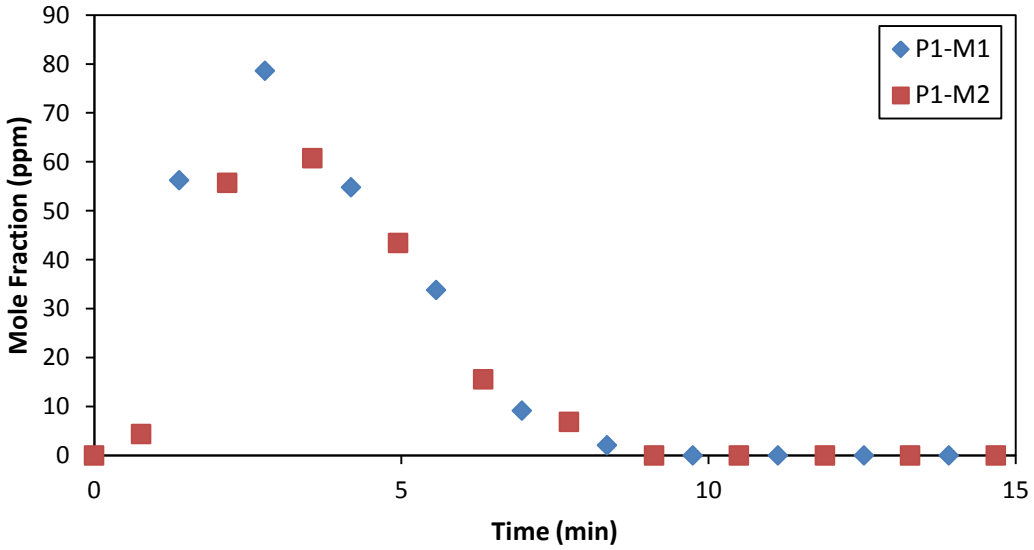

Figure 61. Experimental formaldehyde (HCHO) profiles for 2.54 cm wood sphere diameter with a medium final particle temperature (P1-M)

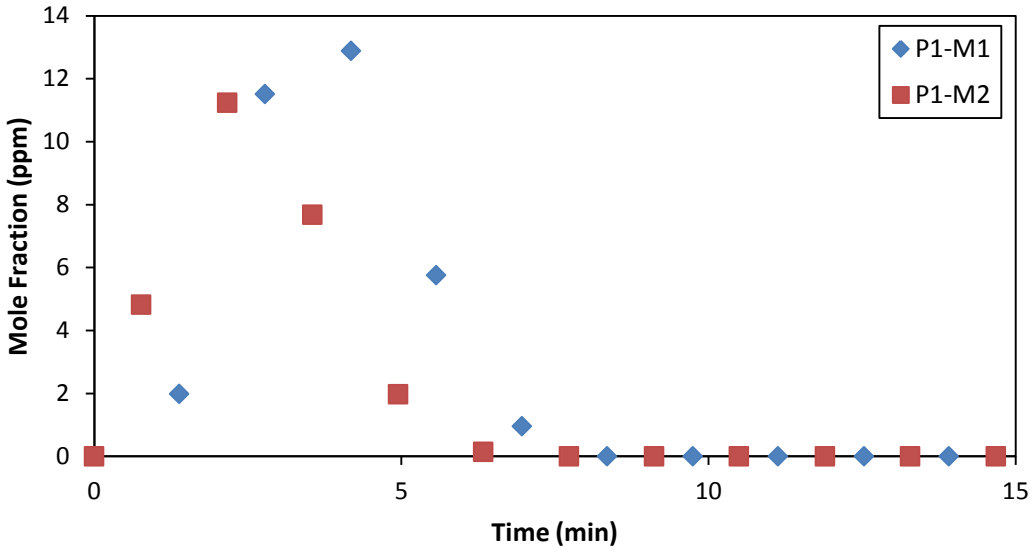

Figure 62. Experimental formic acid (HCOOH) profiles for 2.54 cm wood sphere diameter with a medium final particle temperature (P1-M)

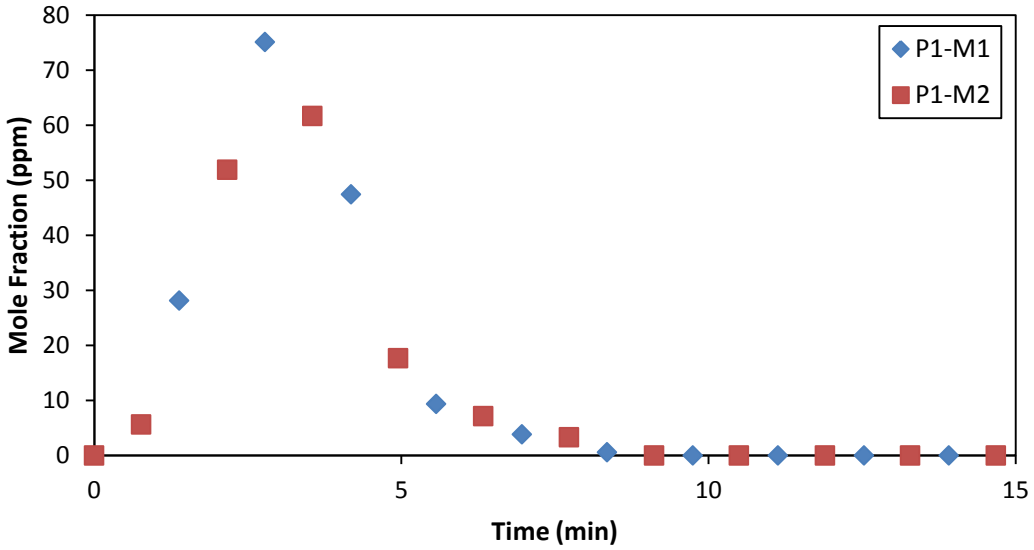

Figure 63. Experimental acetic acid (CH_3COOH) profiles for 2.54 cm wood sphere diameter with a medium final particle temperature (P1-M)

Experimental Data for 2.54 cm Wood Sphere Diameter with a High Final Particle Temperature (P1-H)

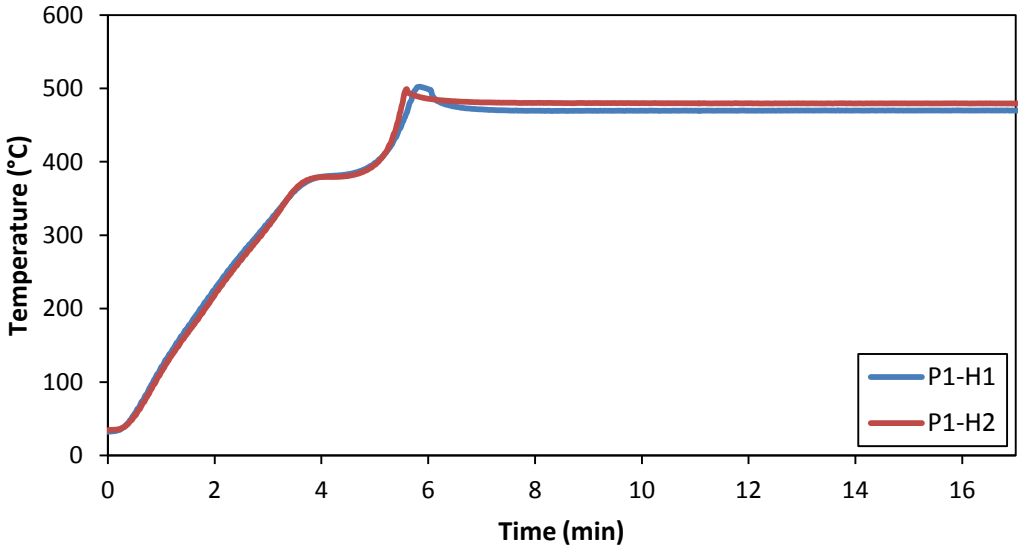

Figure 64. Experimental temperature profiles from the particle center for 2.54 cm wood sphere diameter with a high final particle temperature (P1-H)

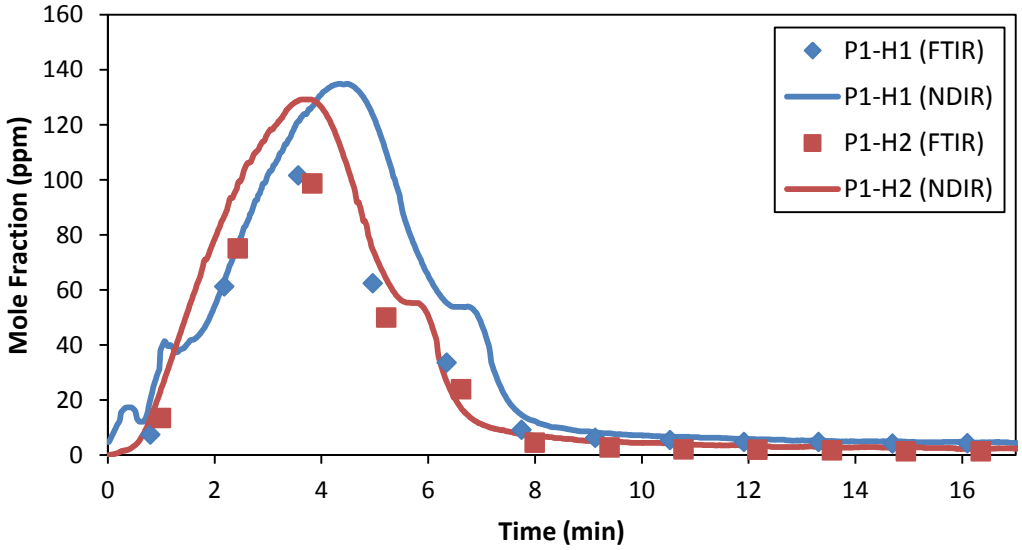

Figure 65. Experimental carbon monoxide (CO) profiles for 2.54 cm wood sphere diameter with a high final particle temperature (P1-H)

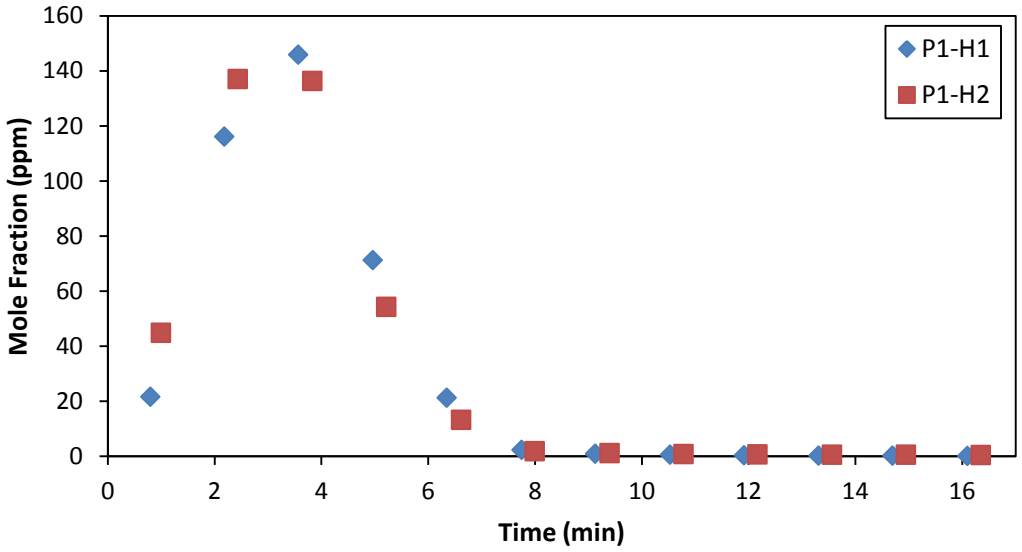

Figure 66. Experimental carbon dioxide (CO_2) profiles for 2.54 cm wood sphere diameter with a high final particle temperature (P1-H)

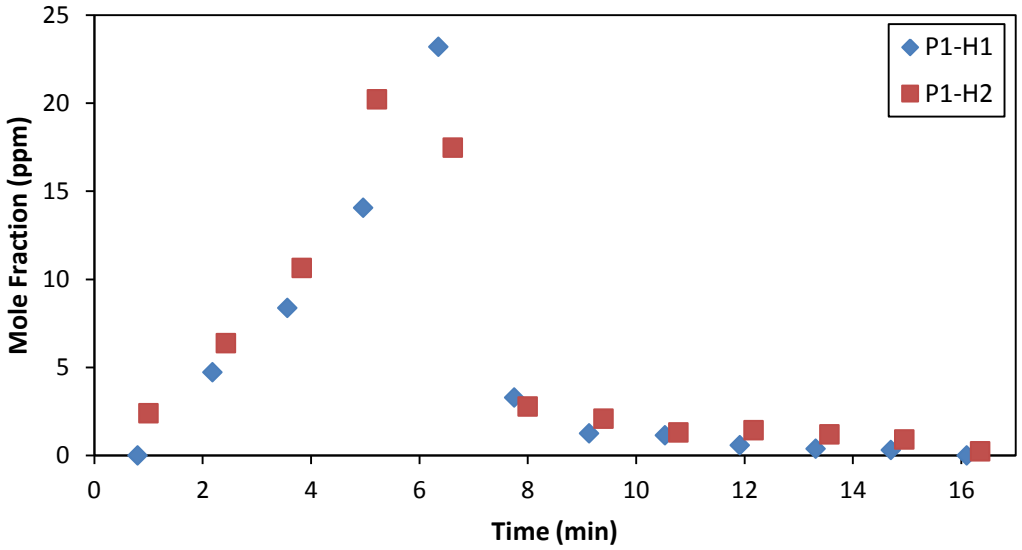

Figure 67. Experimental methane (CH_4) profiles for 2.54 cm wood sphere diameter with a high final particle temperature (P1-H)

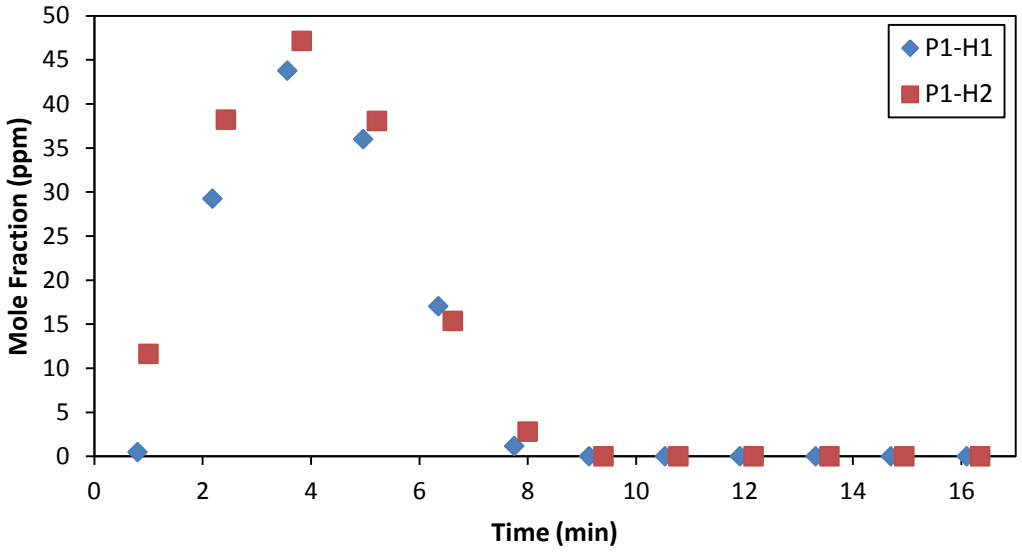

Figure 68. Experimental methanol (CH_3OH) profiles for 2.54 cm wood sphere diameter with a high final particle temperature (P1-H)

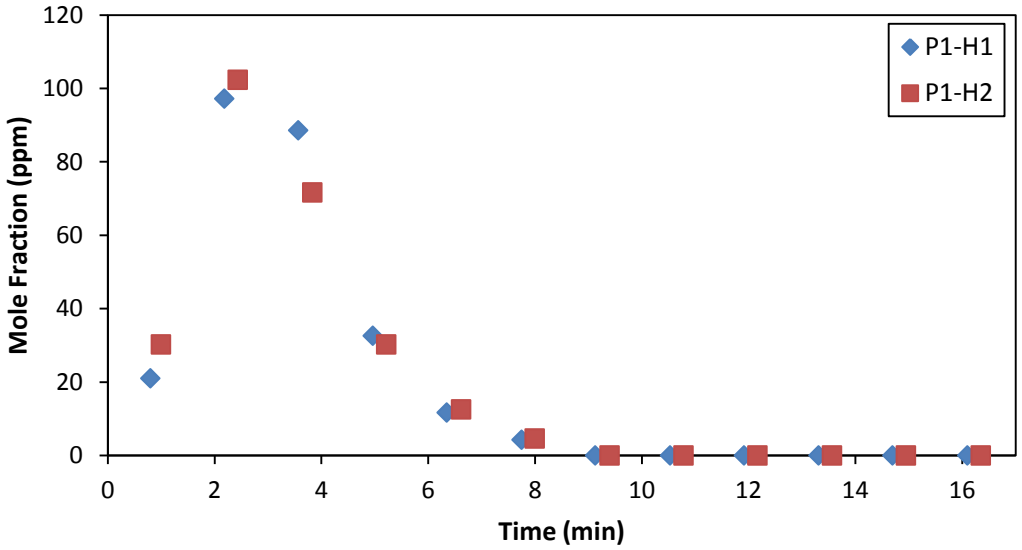

Figure 69. Experimental formaldehyde (HCHO) profiles for 2.54 cm wood sphere diameter with a high final particle temperature (P1-H)

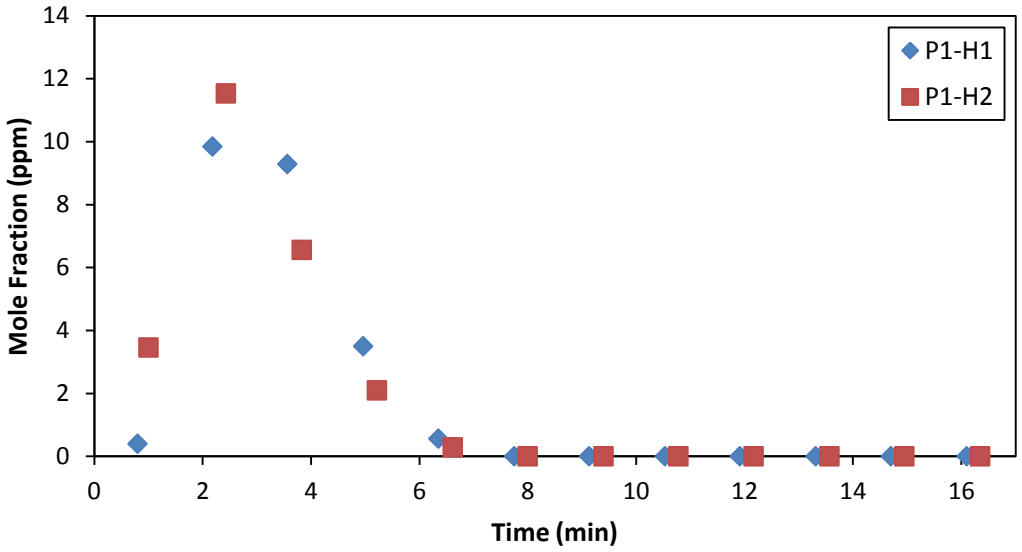

Figure 70. Experimental formic acid (HCOOH) profiles for 2.54 cm wood sphere diameter with a high final particle temperature (P1-H)

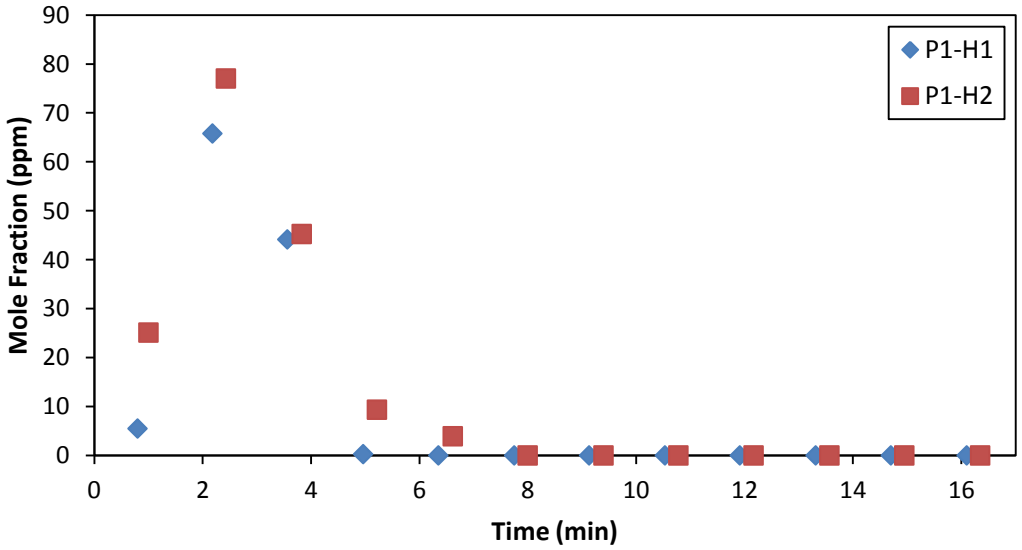

Figure 71. Experimental acetic acid (CH_3COOH) profiles for 2.54 cm wood sphere diameter with a high final particle temperature (P1-H)

Experimental Data for 3.8 cm Wood Sphere Diameter with a Low Final Particle Temperature (P2-L)

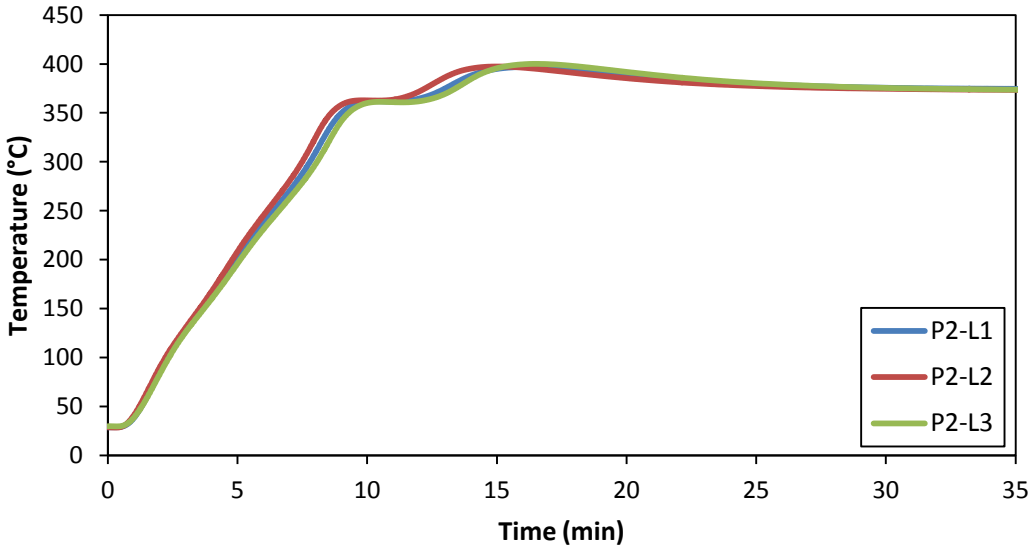

Figure 72. Experimental temperature profiles from the particle center for 3.8 cm wood sphere diameter with a low final particle temperature (P2-L)

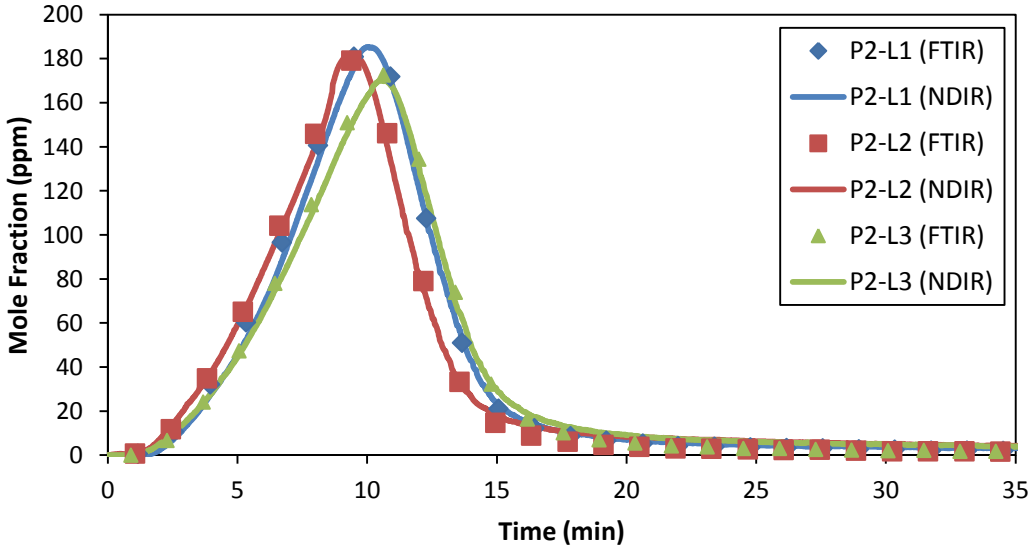

Figure 73. Experimental carbon monoxide (CO) profiles for 3.8 cm wood sphere diameter with a low final particle temperature (P2-L)

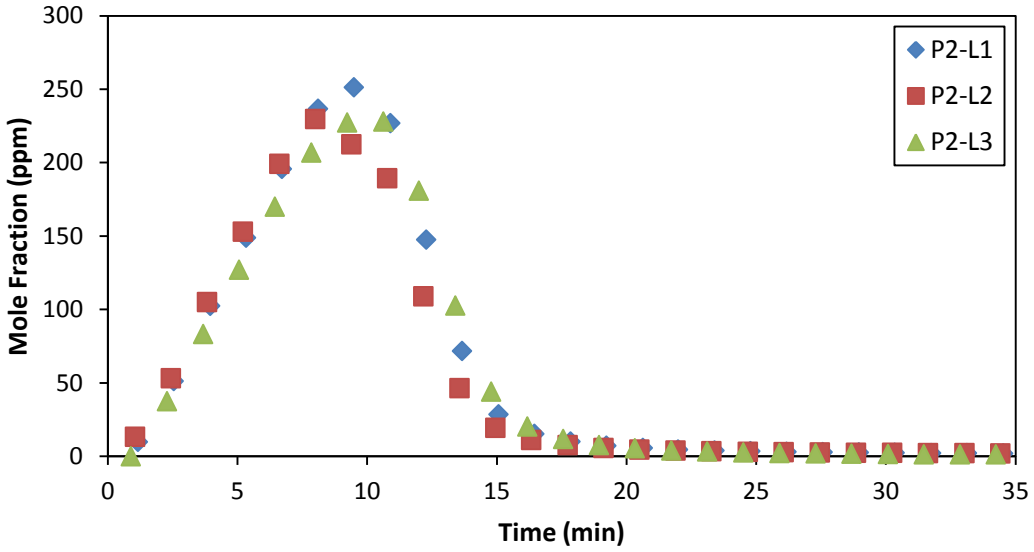

Figure 74. Experimental carbon dioxide (CO_2) profiles for 3.8 cm wood sphere diameter with a low final particle temperature (P2-L)

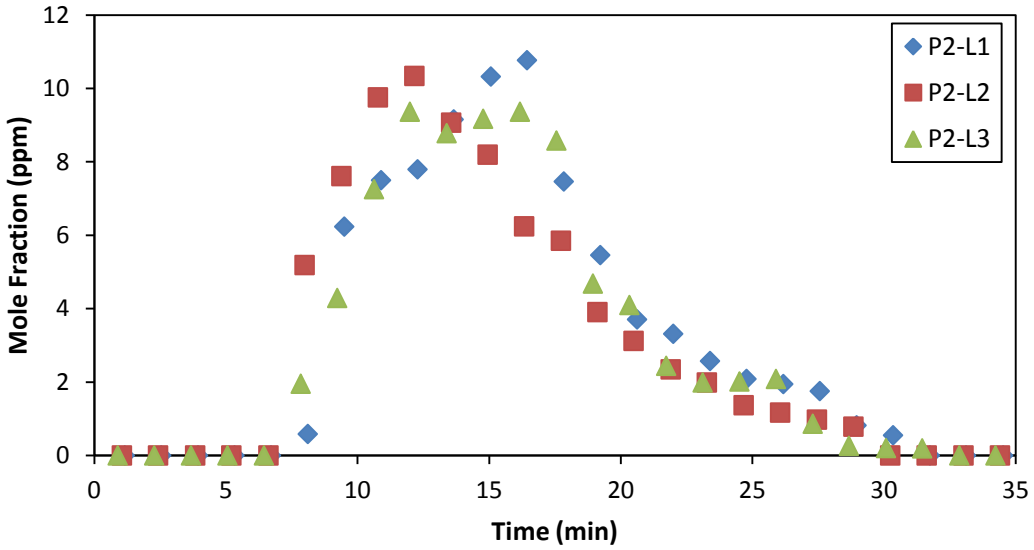

Figure 75. Experimental methane (CH_4) profiles for 3.8 cm wood sphere diameter with a low final particle temperature (P2-L)

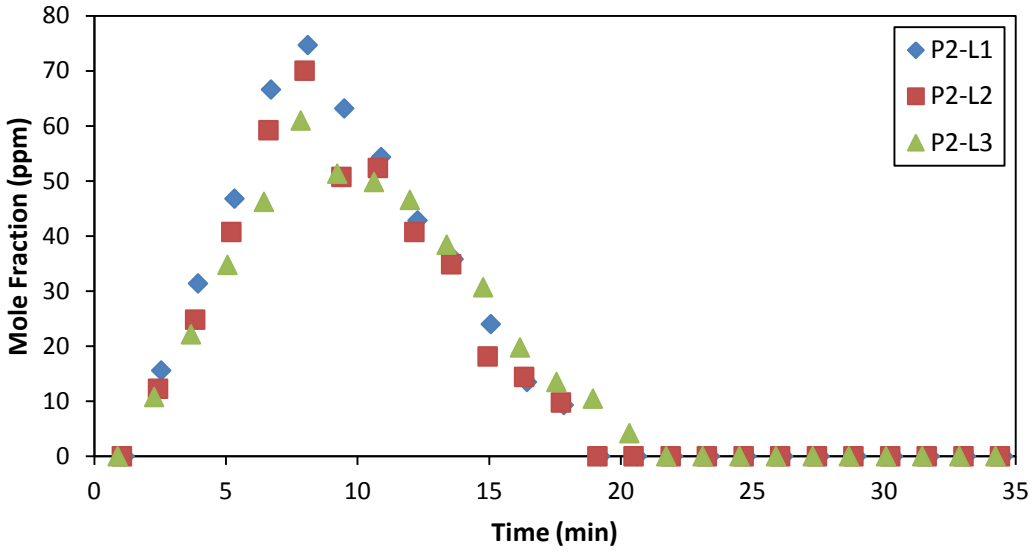

Figure 76. Experimental methanol (CH_3OH) profiles for 3.8 cm wood sphere diameter with a low final particle temperature (P2-L)

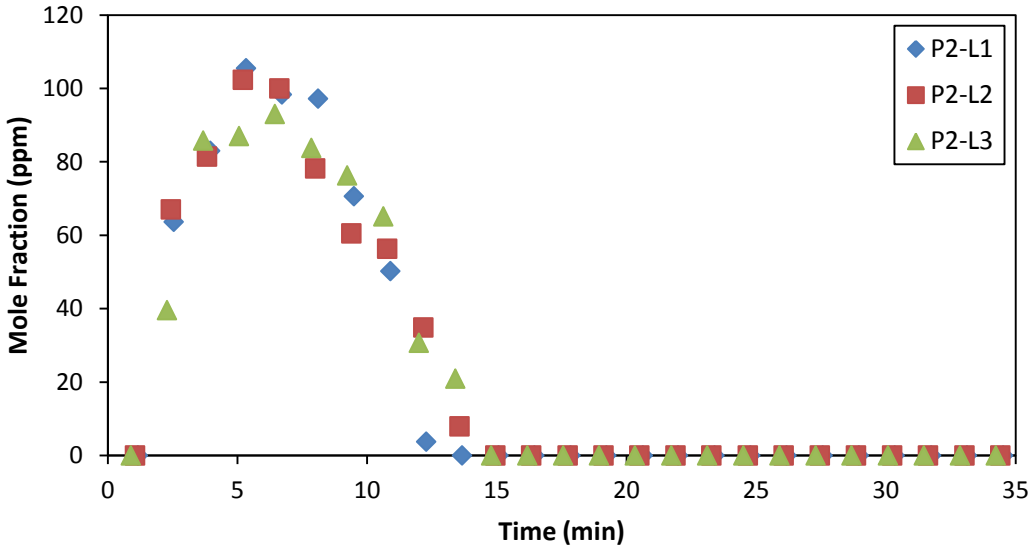

Figure 77. Experimental formaldehyde (HCHO) profiles for 3.8 cm wood sphere diameter with a low final particle temperature (P2-L)

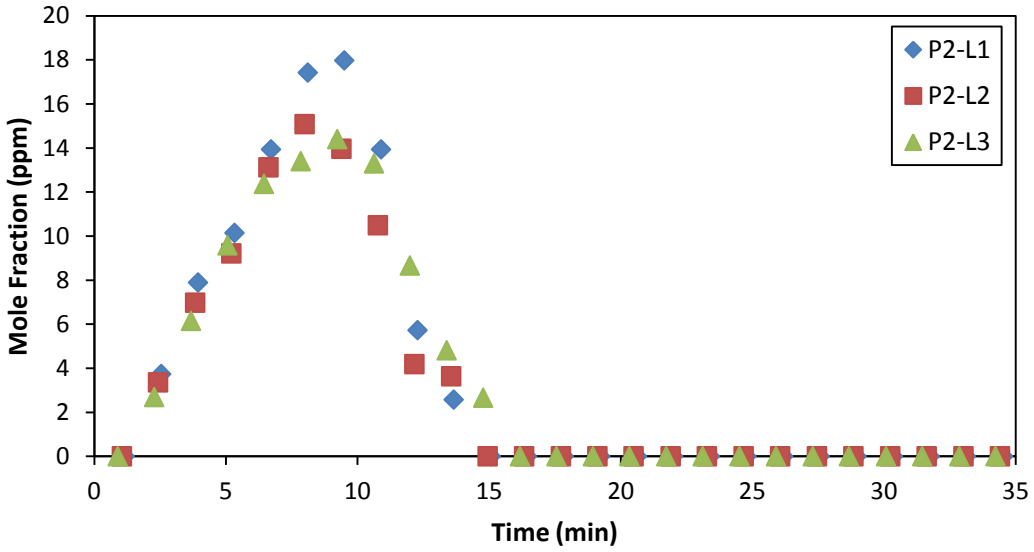

Figure 78. Experimental formic acid (HCOOH) profiles for 3.8 cm wood sphere diameter with a low final particle temperature (P2-L)

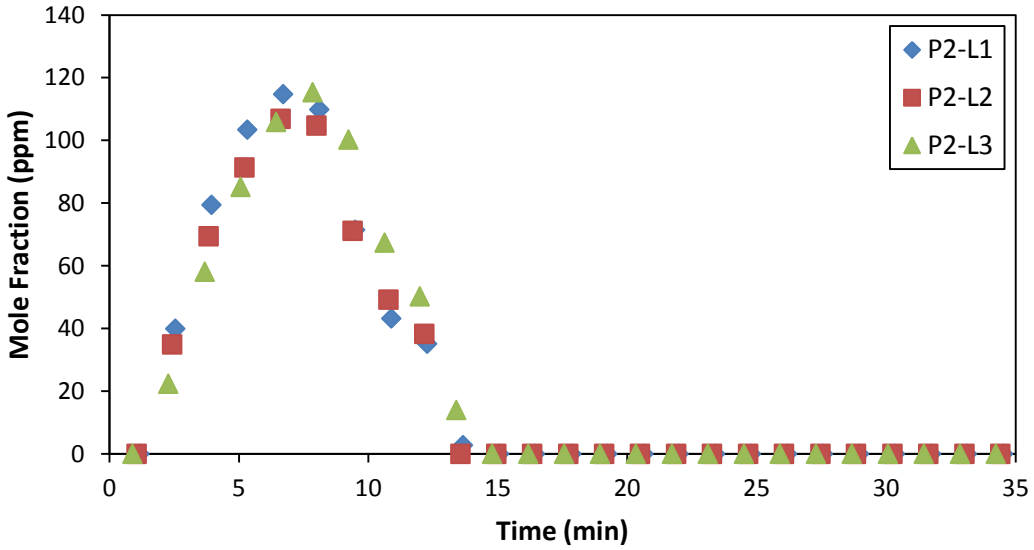

Figure 79. Experimental acetic acid (CH_3COOH) profiles for 3.8 cm wood sphere diameter with a low final particle temperature (P2-L)

Experimental Data for 3.8 cm Wood Sphere Diameter with a Medium Final Particle Temperature (P2-M)

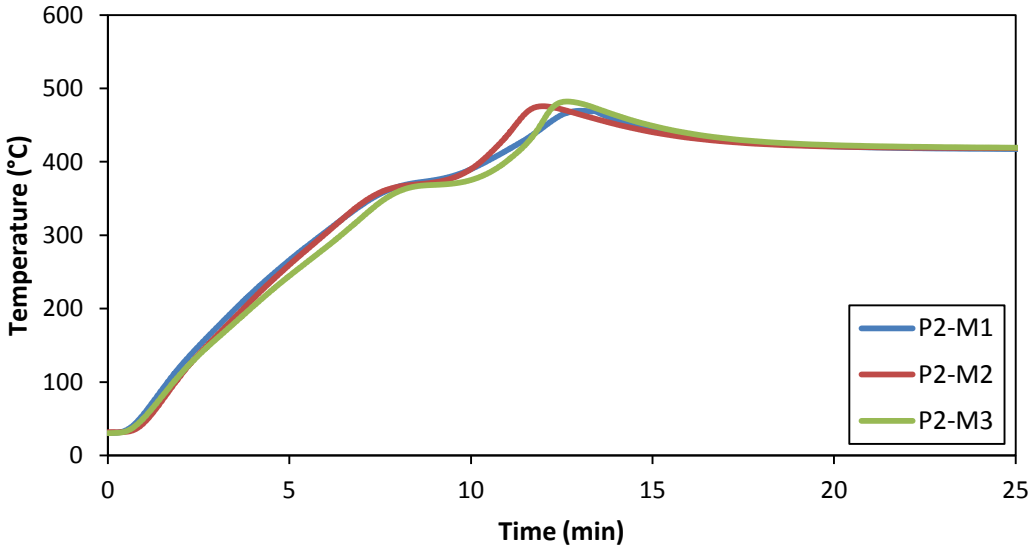

Figure 80. Experimental temperature profiles from the particle center for 3.8 cm wood sphere diameter with a medium final particle temperature (P2-M)

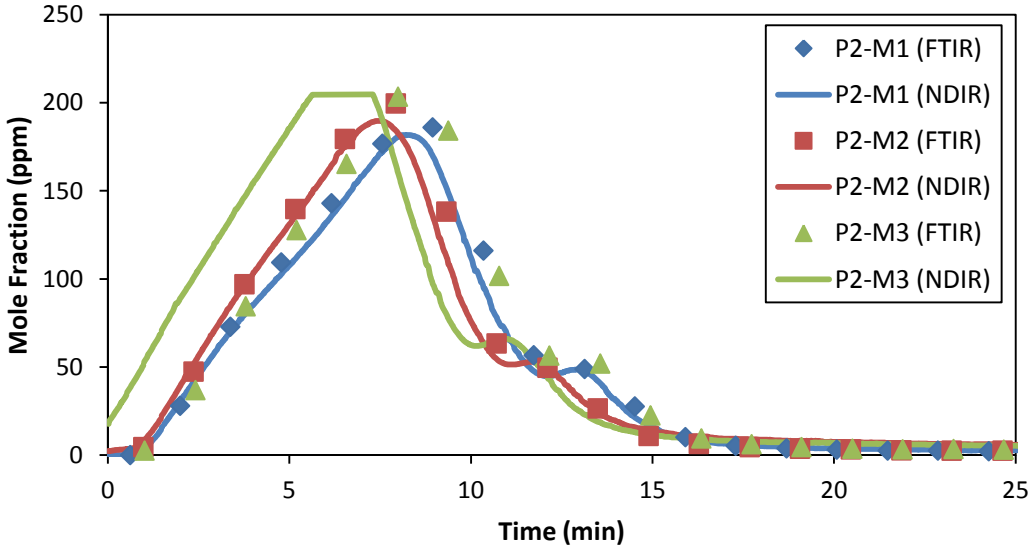

Figure 81. Experimental carbon monoxide (CO) profiles for 3.8 cm wood sphere diameter with a medium final particle temperature (P2-M)

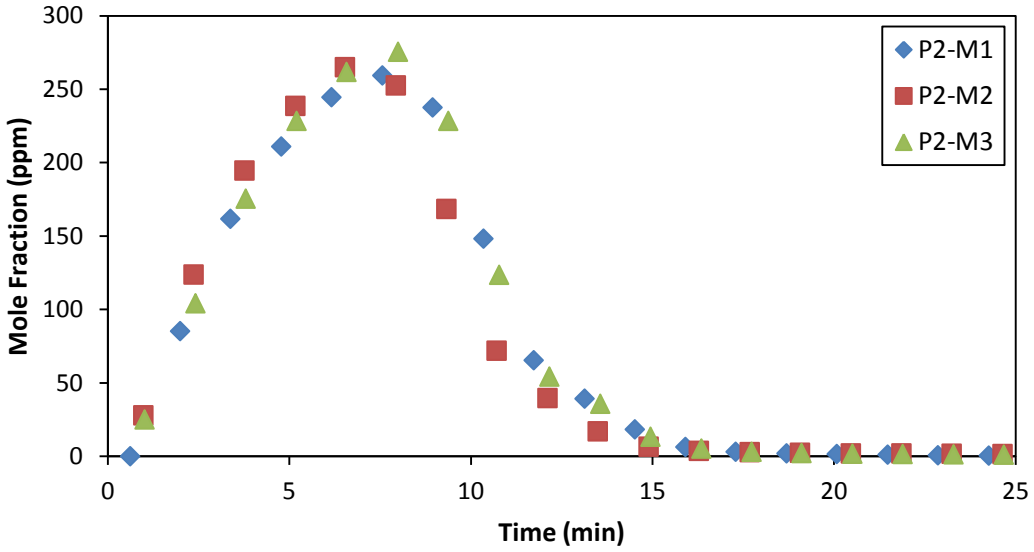

Figure 82. Experimental carbon dioxide (CO_2) profiles for 3.8 cm wood sphere diameter with a medium final particle temperature (P2-M)

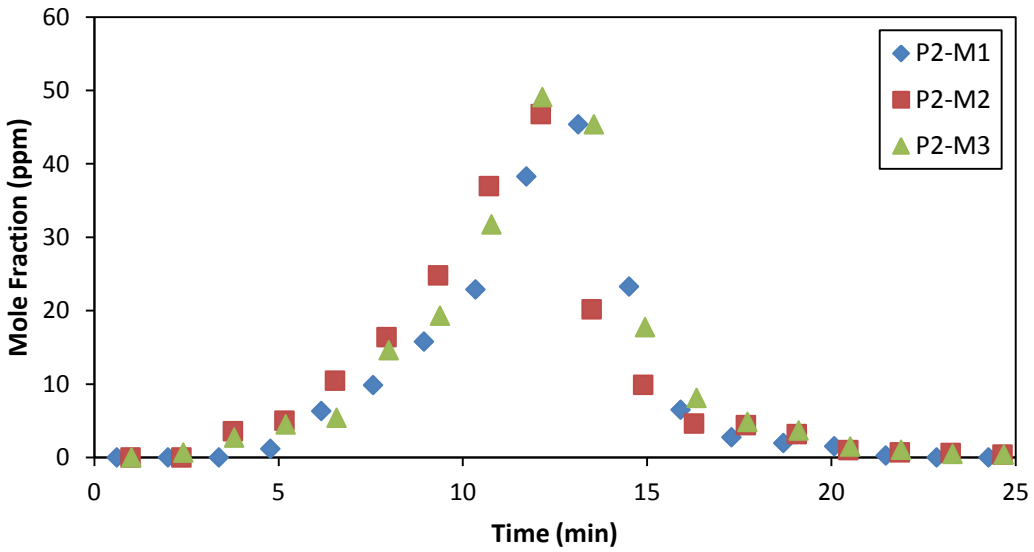

Figure 83. Experimental methane (CH_4) profiles for 3.8 cm wood sphere diameter with a medium final particle temperature (P2-M)

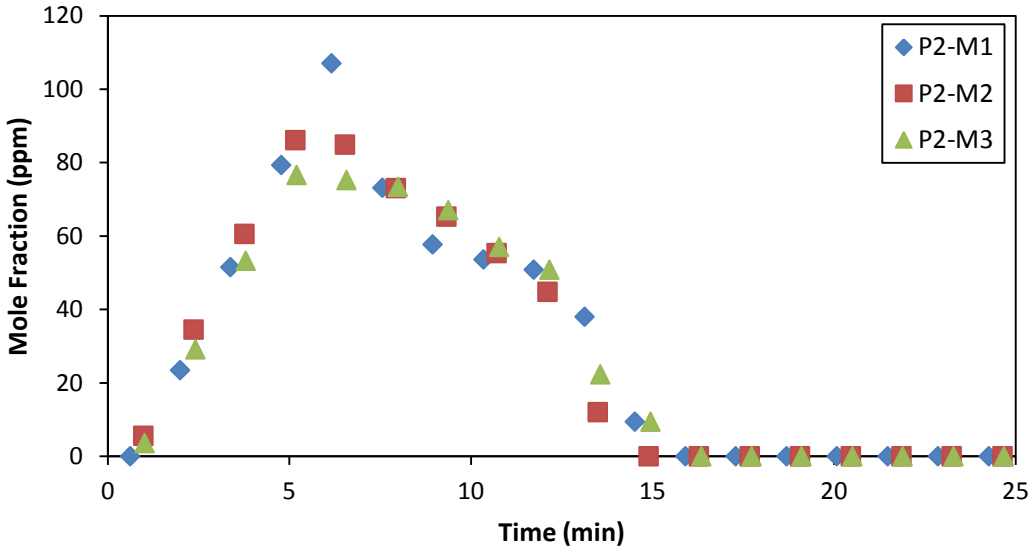

Figure 84. Experimental methanol (CH_3OH) profiles for 3.8 cm wood sphere diameter with a medium final particle temperature (P2-M)

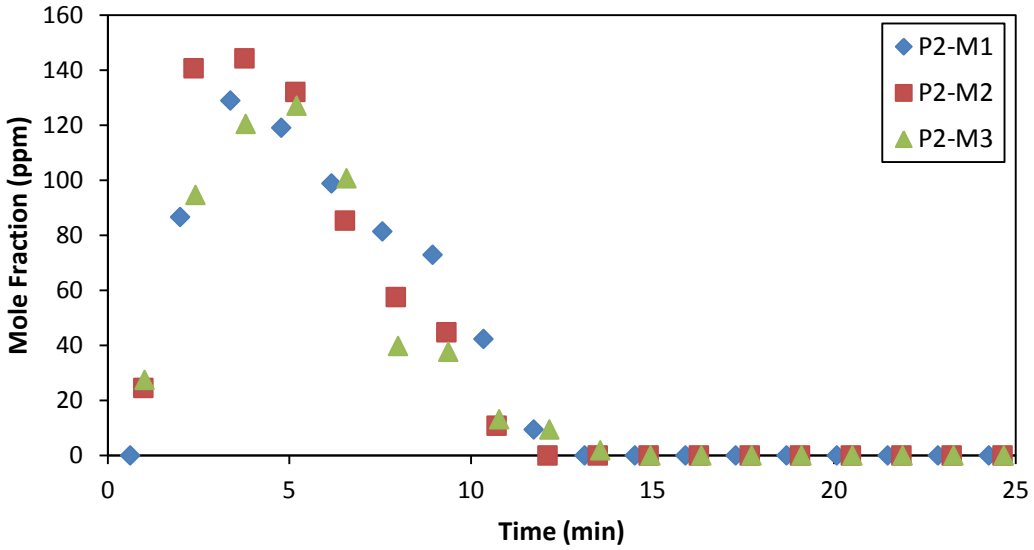

Figure 85. Experimental formaldehyde (HCHO) profiles for 3.8 cm wood sphere diameter with a medium final particle temperature (P2-M)

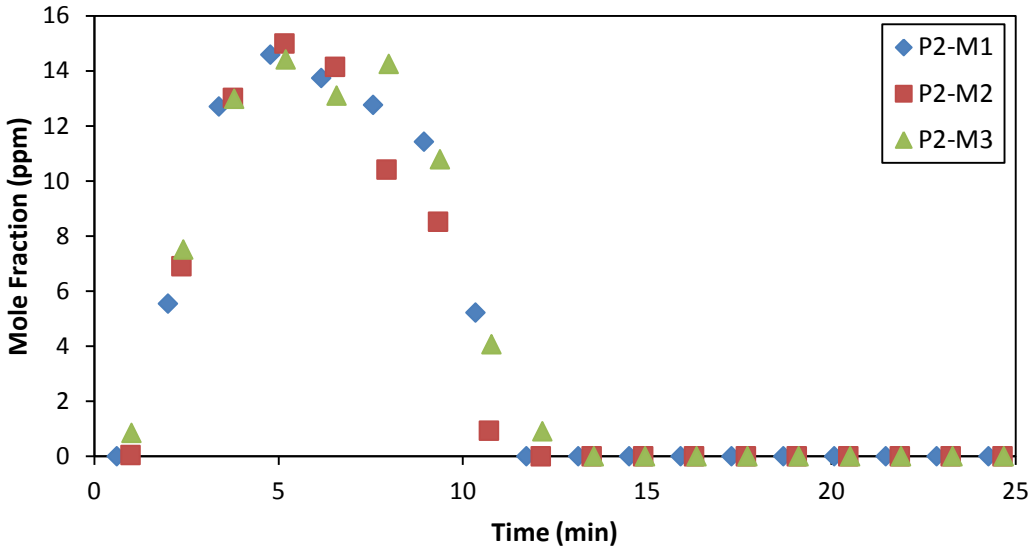

Figure 86. Experimental formic acid (HCOOH) profiles for 3.8 cm wood sphere diameter with a medium final particle temperature (P2-M)

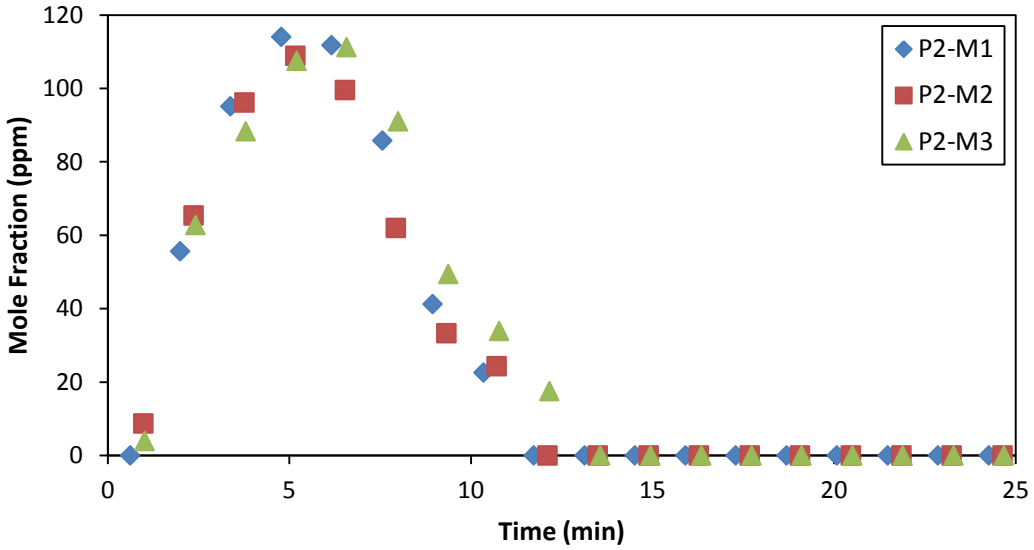

Figure 87. Experimental acetic acid (CH_3COOH) profiles for 3.8 cm wood sphere diameter with a medium final particle temperature (P2-M)

Experimental Data for 3.8 cm Wood Sphere Diameter with a High Final Particle Temperature (P2-H)

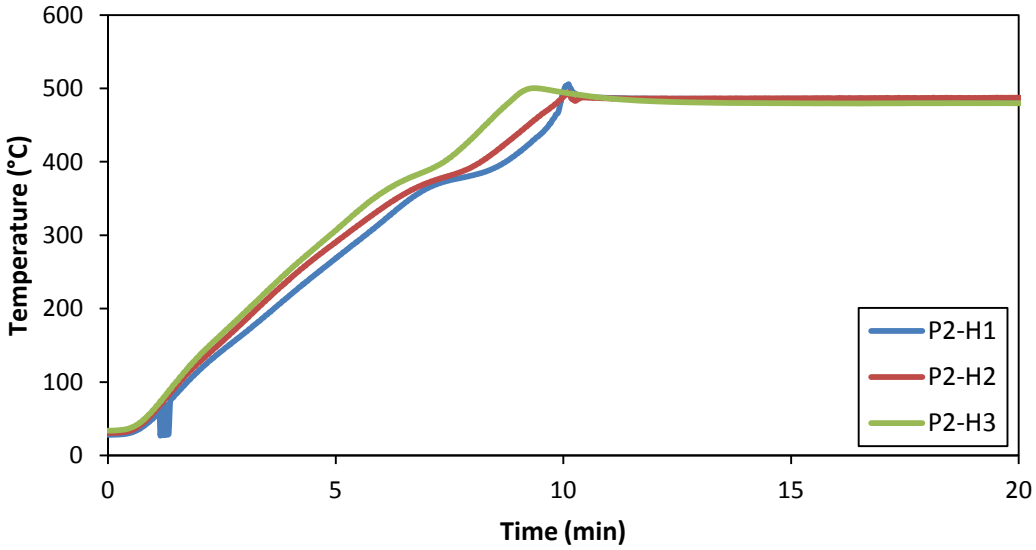

Figure 88. Experimental temperature profiles from the particle center for 3.8 cm wood sphere diameter with a high final particle temperature (P2-H)

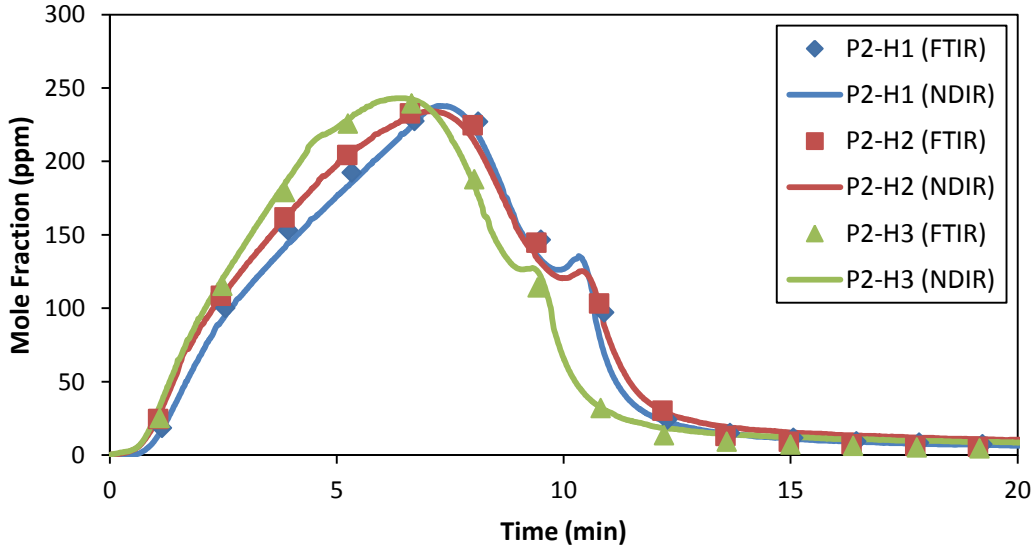

Figure 89. Experimental carbon monoxide (CO) profiles for 3.8 cm wood sphere diameter with a high final particle temperature (P2-H)

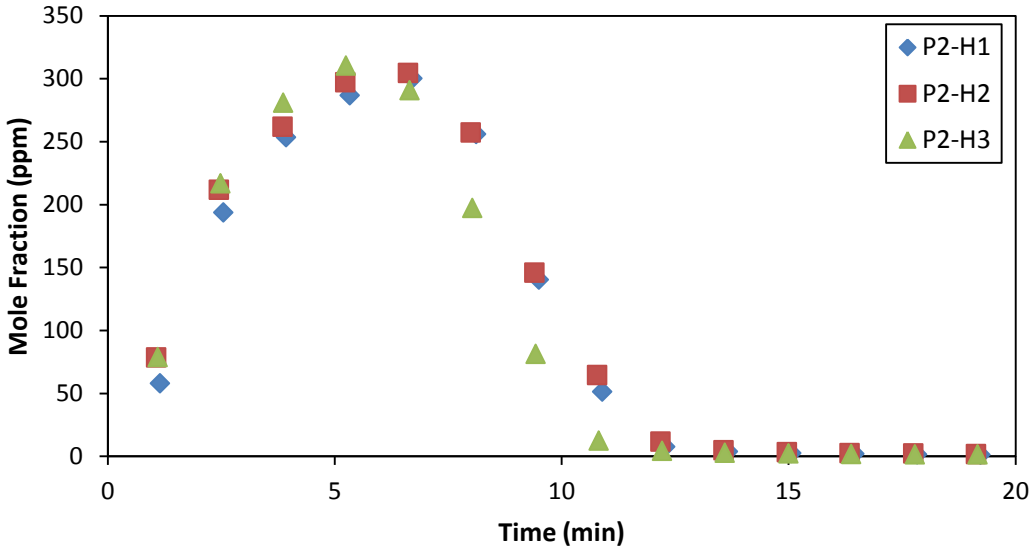

Figure 90. Experimental carbon dioxide (CO_2) profiles for 3.8 cm wood sphere diameter with a high final particle temperature (P2-H)

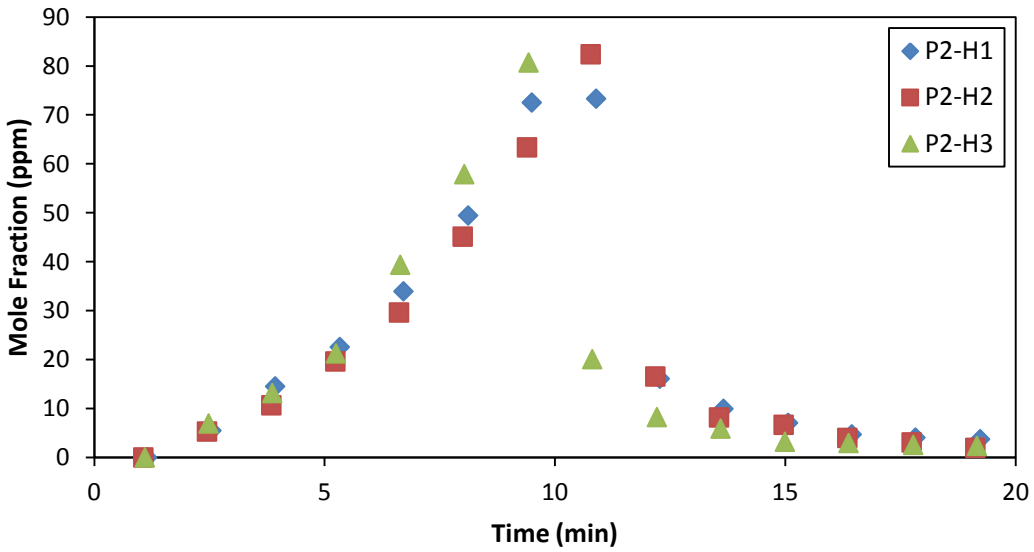

Figure 91. Experimental methane (CH_4) profiles for 3.8 cm wood sphere diameter with a high final particle temperature (P2-H)

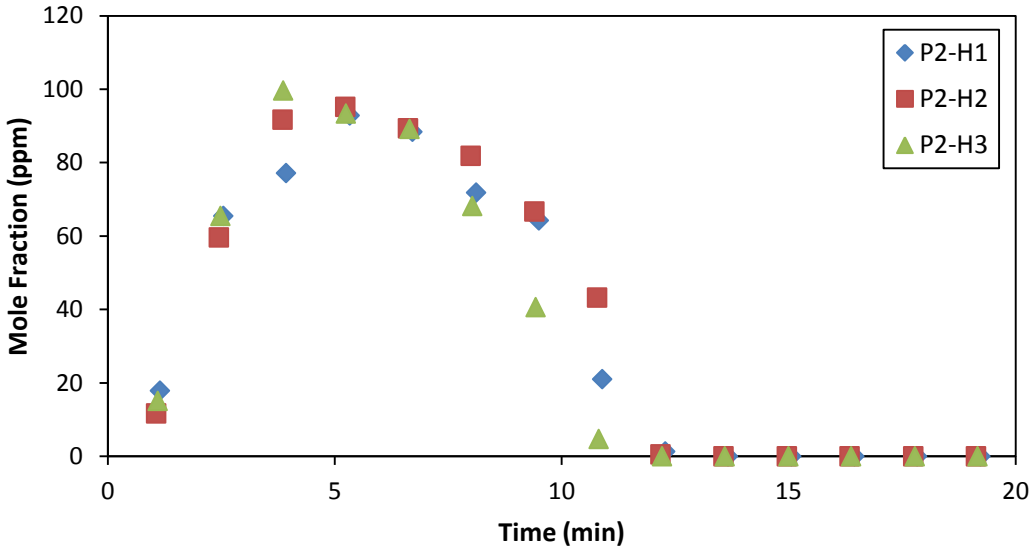

Figure 92. Experimental methanol (CH_3OH) profiles for 3.8 cm wood sphere diameter with a high final particle temperature (P2-H)

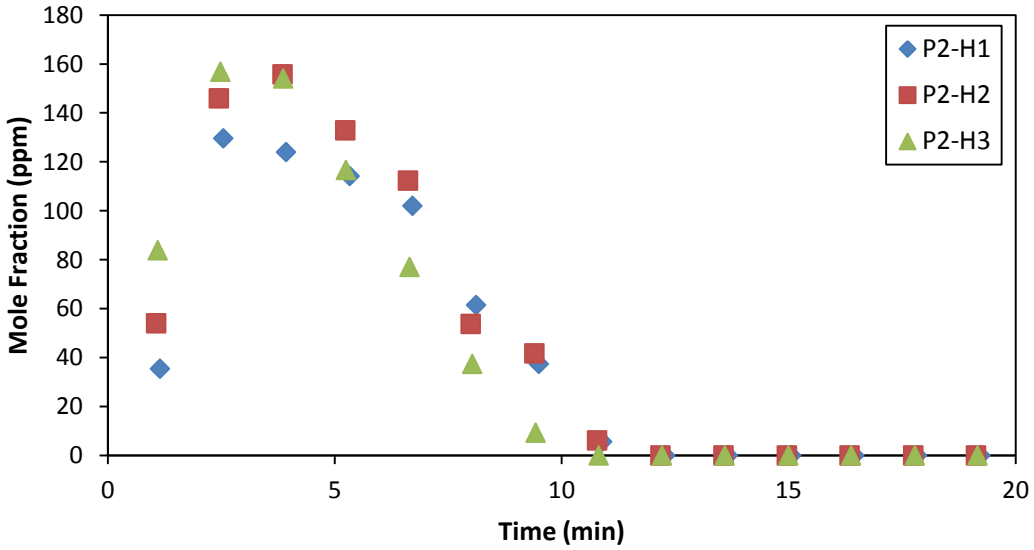

Figure 93. Experimental formaldehyde (HCHO) profiles for 3.8 cm wood sphere diameter with a high final particle temperature (P2-H)

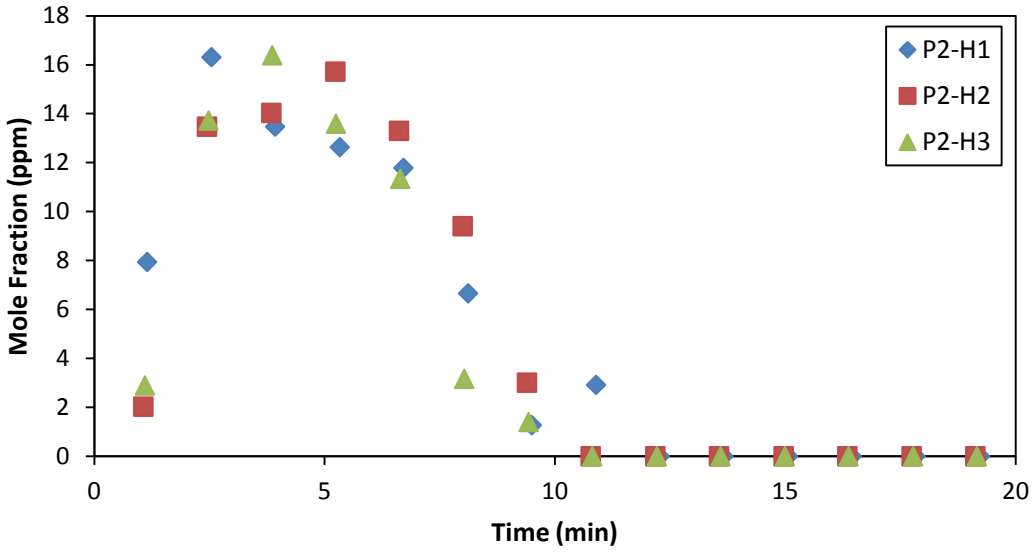

Figure 94. Experimental formic acid (HCOOH) profiles for 3.8 cm wood sphere diameter with a high final particle temperature (P2-H)

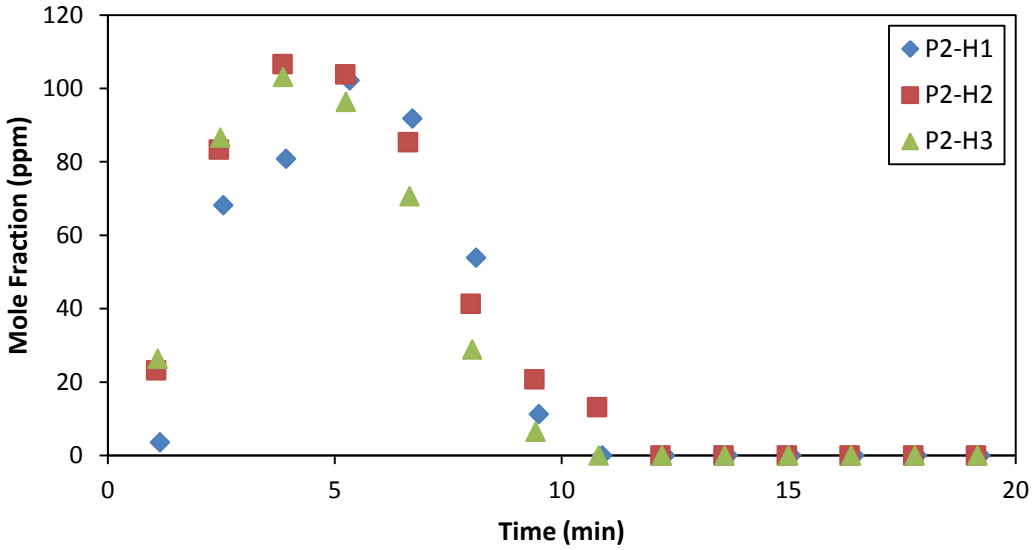

Figure 95. Experimental acetic acid (CH_3COOH) profiles for 3.8 cm wood sphere diameter with a high final particle temperature (P2-H)

APPENDIX B

Differential equations used to describe both the Park and Gauthier models are given in Table 57.

Table 57. Differential equations used to describe the Park and Gauthier models

	Park Model	**Gauthier Model**
Solid Species	$\frac{\partial \rho_a}{\partial t} = S_a = -(k_t + k_g + k_{is})\rho_a$ $\frac{\partial \rho_{is}}{\partial t} = S_{is} = k_{is}\rho_a - k_c\rho_{is}$ $\frac{\partial \rho_c}{\partial t} = S_c = k_c\rho_{is} + k_{c2}\rho_t$	$\frac{\partial \rho_i}{\partial t} = S_i$
Gas-Phase Species	$\frac{\partial(\varepsilon\rho_t)}{\partial t} + \frac{1}{r^2}\frac{\partial}{\partial r}(r^2 V\rho_t) = S_t$ $= k_t\rho_a - (k_{c2} + k_{g2})\varepsilon\rho_t$ $\frac{\partial(\varepsilon\rho_g)}{\partial t} + \frac{1}{r^2}\frac{\partial}{\partial r}(r^2 V\rho_g) = S_g$ $= k_g\rho_a + k_{g2}\varepsilon\rho_t$	$\frac{\partial(\varepsilon\rho_j)}{\partial t} + \frac{1}{r^2}\frac{\partial}{\partial r}(r^2 V\rho_j) = S_j$
Total Pressure	$\frac{\partial}{\partial t}\left(\frac{\varepsilon P}{T}\right) - \frac{1}{r^2}\frac{\partial}{\partial r}\left(r^2\frac{BP}{\mu T}\frac{\partial P}{\partial r}\right)$ $= \left(\frac{R}{M_t}S_t - \frac{R}{M_g}S_g\right)$	$\frac{\partial}{\partial t}\left(\frac{\varepsilon P}{T}\right) - \frac{1}{r^2}\frac{\partial}{\partial r}\left(r^2\frac{BP}{\mu T}\frac{\partial P}{\partial r}\right) = \sum_j \frac{R}{M_j}S_j$

<table>
<tr>
<td>Energy</td>
<td>$$\left(c_w\rho_a + c_w\rho_{is} + c_c\rho_c + \varepsilon c_{pt}\rho_t + \varepsilon c_{pg}\rho_g\right)\frac{\partial T}{\partial t} + \left(c_{pt}\rho_t + c_{pg}\rho_g\right)V\frac{\partial T}{\partial r} = \frac{1}{r^2}\frac{\partial T}{\partial r}\left(r^2\lambda\frac{\partial T}{\partial r}\right) + Q$$</td>
<td>$$\left(c_w\rho_a + c_w\rho_{is} + c_c\rho_c + \varepsilon c_{pt}\rho_t + \varepsilon c_{pg}\rho_g\right)\frac{\partial T}{\partial t} + \left(c_{pt}\rho_t + c_{pg}\rho_g\right)V\frac{\partial T}{\partial r} = \frac{1}{r^2}\frac{\partial T}{\partial r}\left(r^2\lambda\frac{\partial T}{\partial r}\right) + Q$$
where
$$\rho_a = \rho_{CELL} + \rho_{HCE} + \rho_{LIG-C} + \rho_{LIG-H} + \rho_{LIG-O}$$
$$\rho_{is} = \sum \rho_i - \rho_a - \rho_c$$
$$\rho_c = \rho_{Char}$$
$$\rho_t = \sum \rho_j - \rho_g$$
$$\rho_g = \rho_{C_2H_4} + \rho_{CH_4} + \rho_{CO} + \rho_{CO_2} + \rho_{H_2}$$</td>
</tr>
<tr>
<td>Kinetics</td>
<td> 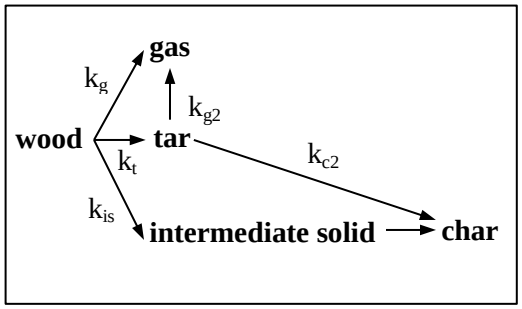
</td>
<td>CELL → Products
HCE → Products
LIG-C → Products
LIG-H → Products
LIG-O → Products
See Section 3.5 for details</td>
</tr>
</table>

APPENDIX C

Final parameter values used in the Park and Gauthier models for comparison to experimental data are presented in Tables 58 through 61.

Table 58. Final material properties used in both the Park and Gauthier models for comparison to experimental data

Property	Definition	Value	Units
ρ_w	Wood density	509.2[a]	kg/m^3
c_w	Wood specific heat	2375[a]	J/kg K
c_c	Char specific heat	2050[a]	J/kg K
c_{pt}	Tar specific heat	$-100 + 4.4T - 1.57 \times 10^{-3}T^2$	J/kg K
c_{pg}	Gas specific heat	$770 + 0.629T - 1.91 \times 10^{-4}T^2$	J/kg K
d_w	Wood pore diameter	5×10^{-6}[a]	m
d_c	Char pore diameter	1×10^{-5}[a]	m
d	Pore diameter	$(1-\eta)d_w + \eta d_c$	m
e	Pore emissivity	1	-
σ	Stefan-Boltzmann constant	5.67×10^{-8}	$W/m^2 K^4$
ε	Virgin wood porosity	0.4	-
λ_w	Wood thermal conductivity	0.4[a]	W/m K
λ_c	Char thermal conductivity	0.12[a]	W/m K
λ_v	Thermal conductivity of volatiles	0.0258	W/m K
B_w	Wood permeability	5×10^{-16}	m^2
B_c	Char permeability	1×10^{-13}	m^2
e_w	Wood emissivity	0.7	-
e_c	Char emissivity	0.92	-
μ	Viscosity of volatiles	3.0×10^{-5}	kg/m s
M_g	Gas molecular weight	0.038	kg/mol
M_t	Tar molecular weight	0.11	kg/mol
R	Gas constant	8.314	J/mol K

[a]Values were determined in this research. See Section 3.4.1.

Table 59. Final parameters used for the kinetic mechanism implemented in the Park model for comparison to experimental data

Reaction	t	g	is	c	c2	g2
A_i (s^{-1})	1.08×10^{10}	4.38×10^{9}	2.26×10^{6a}	9.0×10^{9a}	1.0×10^{5}	4.28×10^{6}
E_i (J/mol)	148,000	152,700	111,700	165,000[a]	108,000	108,000
Δh_i (kJ/kg)	80	80	80	-475[a]	-42	-42

[a]Values were determined in this research. See Section 3.4.2.

Table 60. Wood composition used in the Gauthier model for comparison to experimental data

Component	Wt %
CELL (cellulose)	46.98%[a]
HCE (hemicellulose)	25.52%[a]
LIG-C (lignin richer in carbon)	0.87%[a]
LIC-H (lignin richer in hydrogen)	26.3%[a]
LIG-O (lignin richer in oxygen)	0.34%[a]

[a]All numbers are presented on a dry, ash-free (DAF) basis

Table 61. Run parameters used in both the Park and Gauthier models for comparison to experimental data

Run #	D (cm)	Tinit (°C)	Tfinal (°C)	h (W/mK)
P1-L	2.54	29.1	371.2	56.15
P1-M	2.54	31.7	421.4	58.47
P1-H	2.54	33.4	474.1	60.89
P2-L	3.8	29.2	373.4	46.49
P2-M	3.8	31	417.8	48.18
P2-H	3.8	32.3	484.3	50.71

APPENDIX D

Table 62 presents details of the species used in the kinetic mechanism presented by Gauthier et al., 2013. The letter R indicates a bond which is left vacant as a consequence of the depolymerization and decomposition reactions.

Table 62. Details for the species used in the kinetic mechanism presented by Gauthier et al., 2013

Component Name	Formula	Structure	Phase at Room Temperature
CELL	$C_6H_{10}O_5$	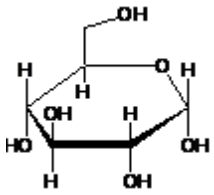	Solid
CELLA	$C_6H_{10}O_5$	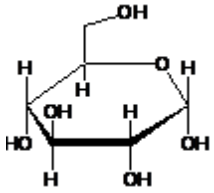	Solid
HCE	$C_5H_8O_4$	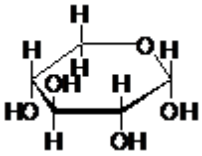	Solid
HCE1	$C_5H_8O_4$	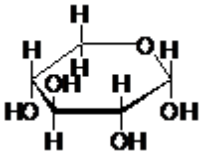	Solid
HCE2	$C_5H_8O_4$	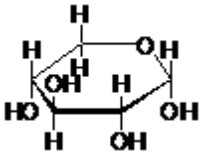	Solid

LIG-C	$C_{15}H_{14}O_4$	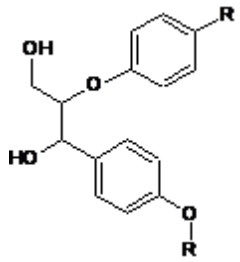	Solid
LIG-H	$C_{22}H_{28}O_9$	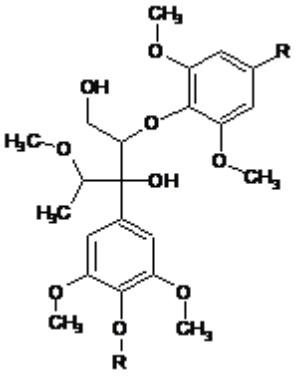	Solid
LIG-O	$C_{20}H_{22}O_{10}$	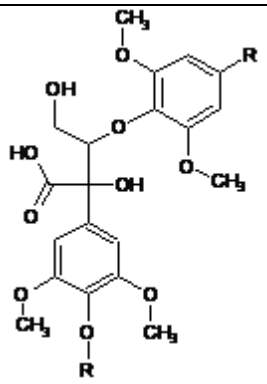	Solid
LIGCC	$C_{15}H_{14}O_4$	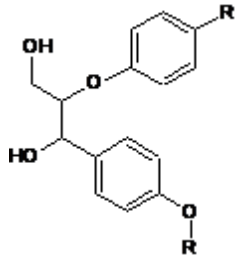	Solid
LIGOH	$C_{19}H_{22}O_8$	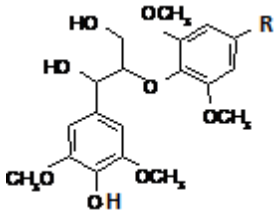	Solid

LIG	$C_{11}H_{12}O_4$	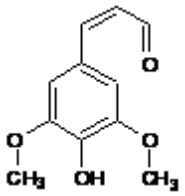	Solid
Char	C	C	Solid
G{H_2}	H_2		Chemisorbed
G{CO}	CO		Chemisorbed
G{CO_2}	CO_2	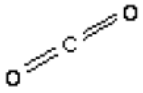	Chemisorbed
G{COH_2}	COH_2	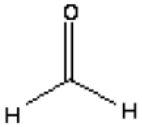	Chemisorbed
G{CH_4}	CH_4		Chemisorbed
G{C_2H_4}	C_2H_4	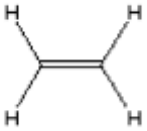	Chemisorbed
G{CH_3OH}	CH_4O	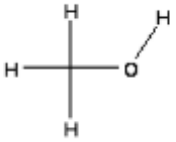	Chemisorbed
COUMARYL	$C_9H_{10}O_2$	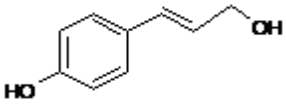	Vapor
FE2MACR	$C_{11}H_{12}O_4$	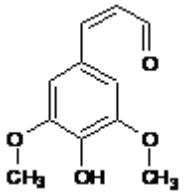	Vapor

Glyoxal	C_2H_2O	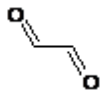	Vapor
HAA	$C_2H_4O_2$	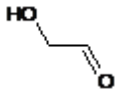	Vapor
HMFU	$C_6H_6O_3$		Vapor
LVG	$C_6H_{10}O_5$	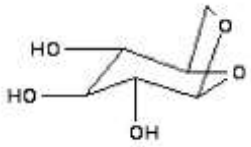	Vapor
PHENOL	C_6H_6O	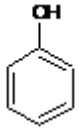	Vapor
XYLAN	$C_5H_8O_4$	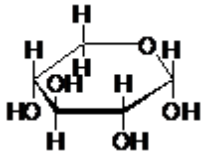	Vapor
H_2	H_2		Gas
H_2O	H_2O	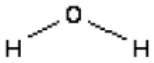	Vapor
CO	CO		Gas
CO_2	CO_2		Gas
CH_4	CH_4		Gas
CH_2O	CH_2O	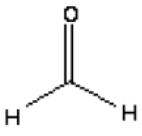	Vapor

CH_3OH	CH_4O	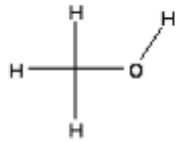	Vapor
HCOOH	CH_2O_2	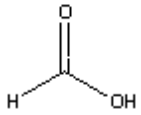	Vapor
C_2H_4	C_2H_4	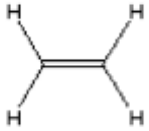	Gas
C_2H_5OH	C_2H_6O	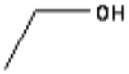	Vapor
C_2H_4O	C_2H_4O		Vapor
C_3H_6O	C_3H_6O		Vapor

APPENDIX E

Tables 63 through 67 present the details of implementing the pyrolysis model developed by Park et al., 2010 in COMSOL Multiphysics.

Table 63. Explanation of format used to describe differential equations presented by Park et al., 2010 in COMSOL Multiphysics

Conservation Equation	
COMSOL **Title of physical phenomena as it is presented in COMSOL** ***Additional information about the COMSOL equation*** The equation given in this location is the differential equation presented as it appears in COMSOL for the coordinate system chosen. Other equations presented here either define variables used in the COMSOL equation or transform the COMSOL equation into a form more suitable for comparison to that given by Park et al., 2010 (which can be found under the **Park** heading).	**Park** The equation given in this location is presented in Park et al., 2010. Modifications are then made to these equations to present them in a form similar to that found in COMSOL for determination of COMSOL variables.
Define COMSOL variables: Definitions of the variables given in this location are determined by matching the differential equation in the COMSOL part of the table to that presented in the Park location of the table. This provides a method for modeling the exact equations presented by Park et al., 2010 in COMSOL.	

Table 64. Details for implementing the conservation of solid species equations presented in Park et al., 2010 in COMSOL Multiphysics. For details on the table layout, see Table 63.

Conservation of Solid Species	
COMSOL **Transport of Diluted Species** ***1D Axisymmetric with No Diffusion*** $\frac{\partial c_i}{\partial t} + u\frac{\partial c_i}{\partial r} = R_i$	**Park** $\frac{\partial \rho_i}{\partial t} = S_i$
Define COMSOL variables: $c_i = \rho_i$ $u = 0$ $R_i = S_i$ $S_a = -(k_t + k_g + k_{is})\rho_a$ $S_{is} = k_{is}\rho_a - k_c\rho_{is}$ $S_c = k_c\rho_{is} + k_{c2}\varepsilon\rho_t$	

Table 65. Details for implementing the conservation of gaseous species equations presented in Park et al., 2010 in COMSOL Multiphysics. For details on the table layout, see Table 63.

Conservation of Gaseous Species

COMSOL

Transport of Concentrated Species
1D Axisymmetric with No Diffusion

$$\rho\frac{\partial\omega_i}{\partial t}+\rho u\frac{\partial\omega_i}{\partial r}=R_i$$

Park

$$\frac{\partial}{\partial t}(\varepsilon\rho_i)+\frac{1}{r^2}\frac{\partial}{\partial r}(r^2V\rho_i)=S_i$$

$$\frac{\partial}{\partial t}(\varepsilon\rho_v\omega_i)+\frac{1}{r^2}\frac{\partial}{\partial r}(r^2V\rho_v\omega_i)=S_i$$

$$\varepsilon\rho_v\frac{\partial\omega_i}{\partial t}+\omega_i\frac{\partial}{\partial t}(\varepsilon\rho_v)+\frac{1}{r^2}\left[r^2V\rho_v\frac{\partial\omega_i}{\partial r}+\omega_i\frac{\partial}{\partial r}(r^2V\rho_v)\right]=S_i$$

$$\varepsilon\rho_v\frac{\partial\omega_i}{\partial t}+\rho_vV\frac{\partial\omega_i}{\partial r}=S_i-\omega_i\frac{\partial}{\partial t}(\varepsilon\rho_v)-\omega_i\frac{1}{r^2}\frac{\partial}{\partial r}(r^2V\rho_v)$$

Define COMSOL variables:

$$\rho=\varepsilon\rho_v$$

$$u=\frac{V}{\varepsilon}$$

$$R_i=S_i-\omega_i\frac{\partial}{\partial t}(\varepsilon\rho_v)-\omega_i\frac{1}{r^2}\frac{\partial}{\partial r}(r^2V\rho_v)$$

$$S_t=k_t\rho_a-\left(k_{c2}+k_{g2}\right)\varepsilon\rho_t$$

$$S_g=k_g\rho_a+k_{g2}\varepsilon\rho_t$$

Table 66. Details for implementing the conservation of energy equation presented in Park et al., 2010 in COMSOL Multiphysics. For details on the table layout, see Table 63.

Conservation of Energy	
COMSOL **Heat Transfer in Porous Media** ***1D Axisymmetric*** $(\rho c_p)_{eq}\frac{\partial T}{\partial t}+\rho c_p u\frac{\partial T}{\partial r}=\frac{1}{r}\frac{\partial}{\partial r}\left(rk_{eq}\frac{\partial T}{\partial r}\right)+Q$ $\theta = volume\ fraction$ $\theta_p+\theta_L=1$ $k_{eq}=\theta_p k_p+\theta_L k$ $(\rho c_p)_{eq}=\theta_p\rho_p c_{p,p}+\theta_L\rho c_p$ $(\theta_p\rho_p c_{p,p}+\theta_L\rho c_p)\frac{\partial T}{\partial t}+\rho c_p u\frac{\partial T}{\partial r}$ $=\frac{1}{r}\frac{\partial}{\partial r}\left[r(\theta_p k_p+\theta_L k)\frac{\partial T}{\partial r}\right]+Q$	**Park** $(c_w\rho_a+c_w\rho_{is}+c_c\rho_c+\varepsilon c_{pt}\rho_t+\varepsilon c_{pg}\rho_g)\frac{\partial T}{\partial t}$ $+(c_{pt}\rho_t+c_{pg}\rho_g)V\frac{\partial T}{\partial r}=\frac{1}{r^2}\frac{\partial T}{\partial r}\left(r^2\lambda\frac{\partial T}{\partial r}\right)+Q$ Multiply both sides by r: $r(c_w\rho_a+c_w\rho_{is}+c_c\rho_c+\varepsilon c_{pt}\rho_t+\varepsilon c_{pg}\rho_g)\frac{\partial T}{\partial t}$ $+r(c_{pt}\rho_t+c_{pg}\rho_g)V\frac{\partial T}{\partial r}=\frac{1}{r}\frac{\partial T}{\partial r}\left(r^2\lambda\frac{\partial T}{\partial r}\right)+rQ$ $Q=-(k_t\Delta h_t+k_g\Delta h_g+k_{is}\Delta h_{is})\rho_a-k_c\Delta h_c\rho_{is}$ $-(k_{c2}\Delta h_{c2}+k_{g2}\Delta h_{g2})\rho_t$
Define COMSOL variables: $\theta_L=\varepsilon$ $\theta_p=1-\varepsilon$ $\rho_p=c_w\rho_a+c_w\rho_{is}+c_c\rho_c$ $c_{p,p}=\frac{r}{1-\varepsilon}$ $\rho=r\rho_v$ $c_p=c_{pt}\omega_t+c_{pg}\omega_g$ $k=0$ $k_p=\frac{r\lambda}{1-\varepsilon}$ $u=V$ $Q=r[-(k_t\Delta h_t+k_g\Delta h_g+k_{is}\Delta h_{is})\rho_a-k_c\Delta h_c\rho_{is}$ $-(k_{c2}\Delta h_{c2}+k_{g2}\Delta h_{g2})\rho_t]$	

Table 67. Details for implementing the Darcy Flow equation presented in Park et al., 2010 in COMSOL Multiphysics. For details on the table layout, see Table 63.

Darcy Flow	
COMSOL **Darcy's Law** ***1D Axisymmetric*** $\frac{\partial}{\partial t}(\rho\varepsilon_p) + \frac{1}{r}\frac{\partial}{\partial r}(r\rho u) = Q_m$ $u = -\frac{k}{\mu}\frac{\partial P}{\partial r}$ $\rho = \frac{PM_n}{R_u T}$ $\frac{\partial}{\partial t}\left(\frac{\varepsilon_p P M_n}{R_u T}\right) - \frac{1}{r}\frac{\partial}{\partial r}\left(\frac{rk\,PM_n}{\mu\ R_u T}\frac{\partial P}{\partial r}\right) = Q_m$ $\frac{1}{R_u}\frac{\partial}{\partial t}\left(\frac{\varepsilon_p P M_n}{T}\right) - \frac{1}{R_u}\frac{1}{r}\frac{\partial}{\partial r}\left(\frac{rk\,PM_n}{\mu\ \ T}\frac{\partial P}{\partial r}\right) = Q_m$ $\frac{\partial}{\partial t}\left(\frac{\varepsilon_p P M_n}{T}\right) - \frac{1}{r}\frac{\partial}{\partial r}\left(r\frac{kPM_n}{\mu T}\frac{\partial P}{\partial r}\right) = R_u Q_m$	**Park** $\frac{\partial}{\partial t}\left(\frac{\varepsilon P}{T}\right) - \frac{1}{r^2}\frac{\partial}{\partial r}\left(r^2\frac{BP}{\mu T}\frac{\partial P}{\partial r}\right) = Q$ $Q = \frac{R_u}{M_t}S_t + \frac{R_u}{M_g}S_g$ Multiply both sides by r: $r\frac{\partial}{\partial t}\left(\frac{\varepsilon P}{T}\right) - \frac{1}{r}\frac{\partial}{\partial r}\left(r^2\frac{BP}{\mu T}\frac{\partial P}{\partial r}\right) = rQ$ $\frac{\partial}{\partial t}\left(\frac{r\varepsilon P}{T}\right) - \frac{1}{r}\frac{\partial}{\partial r}\left(r^2\frac{BP}{\mu T}\frac{\partial P}{\partial r}\right) = rQ$
Define COMSOL variables: $\rho = \rho_v$ $\varepsilon_p = \frac{r\varepsilon}{M_n}$ $\mu = \mu$	$k = \frac{rB}{M_n}$ $Q_m = r\left(\frac{S_t}{M_t} + \frac{S_g}{M_g}\right)$

APPENDIX F

Report generated from COMSOL Multiphysics for the Park and Gauthier models. Reports were only created for cases with 2.54 cm sphere diameters at a low final particle temperature (P1-L). The report for the Park model is a complete report, while that for the Gauthier model only includes deviations from the Park model report.

Park Model

1 Global Definitions

1.1 Parameters 1

Parameters

Name	Expression	Description
D_sph	2.54/100	Cylinder diameter (m)
T_init	29.1 + 273	Initial temperature (K)
T_fn	371.2 + 273	Furnace temperature (K) (for radiative heat transfer)
T_N2	371.2 + 273	Nitrogen temperature (K)
rho_w	509.2	Wood density (kg/m^3)
e	1	Pore emissivity
sigma	5.67e-8	Stefan-Boltzmann constant (W/m^2 K^4)
k_v	0.0258	Vapor thermal conductivity (W/m K)

Name	Expression	Description
B_w	5e-16	Wood permeability (m^2)
B_c	1e-13	Char permeability (m^2)
e_w	0.7	Wood emissivity
e_c	0.92	Char emissivity
h_sph	56.15	Convection coefficient (W/m^2 K)
mu	3e-5	Vapor viscosity (kg/m s)
M_g	0.038	Gas molecular weight (kg/mol)
M_t	0.11	Tar molecular weight (kg/mol)
R	8.314	Gas constant (J/mol K)
phi_w	0.4	Virgin wood porosity
deltaH_t	80	Heat of reaction (kJ/kg)
deltaH_g	80	Heat of reaction (kJ/kg)
deltaH_is	80	Heat of reaction (kJ/kg)
deltaH_c	-300	Heat of reaction (kJ/kg)
deltaH_c2	-42	Heat of reaction (kJ/kg)
deltaH_g2	-42	Heat of reaction (kJ/kg)
m_w	pi*D_sph^3*rho_w/6	Mass of wood (kg)
k_w	0.4	Wood thermal conductivity (W/mK)
c_w	2375	Wood specific heat (J/kg K)
d_w	5e-6	Wood pore size (m)
k_c	0.12	Char thermal conductivity (W/mK)

Name	Expression	Description
c_c	2050	Char specific heat (J/kg K)
d_c	1e-5	Char pore size (m)

1.2 Functions

1.2.1 Analytic 1

Function name	e_s
Function type	Analytic

Function name

Name	Value
Function name	e_s

Parameters

Name	Value
Expression	(e_w + (T - 450)/(550 - 450)*(e_c - e_w)) + (-(T - 450)/(550 - 450)*(e_c - e_w))*(T<450) + (e_c - e_w - (T - 450)/(550 - 450)*(e_c - e_w))*(T>550)
Arguments	T

1.2.2 Analytic 2

Function name	k_t
Function type	Analytic

Function name

Name	Value
Function name	k_t

Parameters

Name	Value
Expression	1.08e10*exp(-148000/(R*T))
Arguments	T

1.2.3 Analytic 3

Function name	k_g
Function type	Analytic

Function name

Name	Value
Function name	k_g

Parameters

Name	Value
Expression	4.38e9*exp(-152700/(R*T))
Arguments	T

1.2.4 Analytic 4

Function name	k_is
Function type	Analytic

Function name

Name	Value
Function name	k_is

Parameters

Name	Value
Expression	2.26e6*exp(-111700/(R*T))
Arguments	T

1.2.5 Analytic 5

Function name	k_c
Function type	Analytic

Function name

Name	Value
Function name	k_c

Parameters

Name	Value
Expression	9e9*exp(-155000/(R*T))
Arguments	T

1.2.6 Analytic 6

Function name	k_c2
Function type	Analytic

Function name

Name	Value
Function name	k_c2

Parameters

Name	Value
Expression	1e5*exp(-108000/(R*T))
Arguments	T

1.2.7 Analytic 7

Function name	k_g2
Function type	Analytic

Function name

Name	Value
Function name	k_g2

Parameters

Name	Value
Expression	4.28e6*exp(-108000/(R*T))
Arguments	T

2 Model 1 (mod1)

2.1 Definitions

2.1.1 Variables

Variables 1

Selection

Geometric entity level	Entire model

Name	Expression	Description
cp_t	-100 + 4.4*T - 1.57e-3*T^2	Tar specific heat (J/kg K)
cp_g	770 + 0.629*T - 1.91e-4*T^2	Gas specific heat (J/kg K)
S_a	-(k_t(T) + k_g(T) + k_is(T))*rho_a	Wood source term
S_is	k_is(T)*rho_a - k_c(T)*rho_is	Intermediate solid source term
S_c	k_c(T)*rho_is + k_c2(T)*rho_v*wt*phi	Char source term
S_t	k_t(T)*rho_a - (k_c2(T) + k_g2(T))*rho_v*wt*phi	Tar source term
S_g	k_g(T)*rho_a + k_g2(T)*rho_v*wt*phi	Gas source term
rho_v_old	101325*chcs.M_wN2/(R*T_init)*(1/wN2)	Vapor density (kg/m^3)
rho_v	p*chcs.Mn/(R*T)	Vapor density (kg/m^3)
V	0 + - B/mu*pr*((-B/mu*pr)>0)	Vapor velocity (m/s)
eta	1 - (rho_a + rho_is)/rho_w	Degree of pyrolysis
d	d_w*(1 - eta) + d_c*eta	Pore diameter (m)
rho_s	rho_a + rho_is + rho_c	Density of solid (kg/m^3)

Name	Expression	Description
phi	1 - (rho_s/rho_w)*(1 - phi_w)	Porosity
B	(1 - eta)*B_w + eta*B_c	Permeability (m^2)
k_bms	(1 - eta)*k_w + eta*k_c + phi*k_v + (13.5*sigma*T^3*d)/e	Thermal conductivity (W/mK)
m_a	4*pi*intop1(rho_a*r^2)	Mass of wood (kg)
m_is	4*pi*intop1(rho_is*r^2)	Mass of intermediate solid (kg)
m_c	4*pi*intop1(rho_c*r^2)	Mass of char (kg)
m_t	4*pi*intop1(rho_v*wt*r^2)	Mass of tar (kg)
m_g	4*pi*intop1(rho_v*wg*r^2)	Mass of gas (kg)

2.1.2 Model Couplings

Integration 1

Coupling type	Integration
Operator name	intop1

Source selection

Geometric entity level	Domain
Selection	Domains 1–2

2.2 Geometry 1

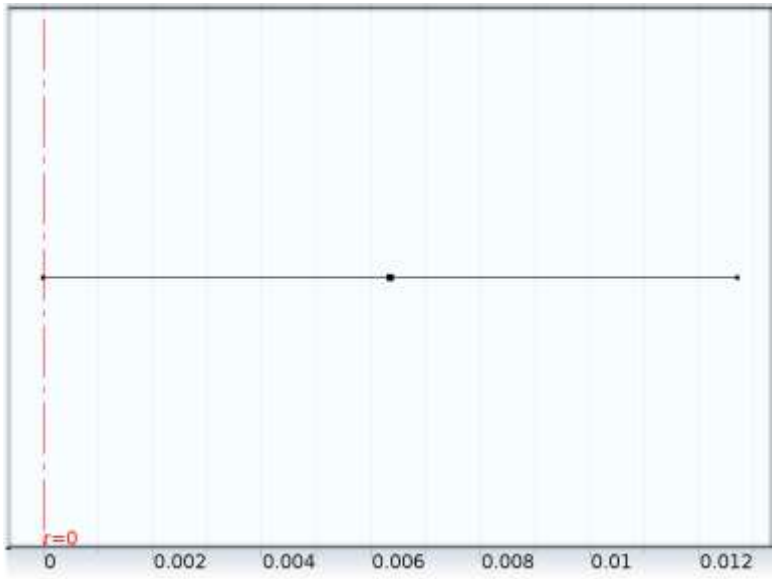

Geometry 1

units

Length unit	m
Angular unit	deg

Geometry statistics

Property	Value
Space dimension	1
Number of domains	2
Number of boundaries	3

2.2.1 Point 1 (pt1)

Selections of resulting entities

Name	Value
Point coordinate	D_sph/4

2.3 Heat Transfer in Porous Media (ht)

Heat Transfer in Porous Media

Selection

Geometric entity level	Domain
Selection	Domains 1–2

Equations

$$\rho C_p \frac{\partial T}{\partial t} + \rho C_p \mathbf{u} \cdot \nabla T = \nabla \cdot (k \nabla T) + Q$$

Settings

Description	Value
Value type when using splitting of complex variables	{Complex, Complex}
Heat transfer in porous media	On
Default model	Porous matrix
Show equation assuming	std1/time

2.3.1 Porous Matrix 1

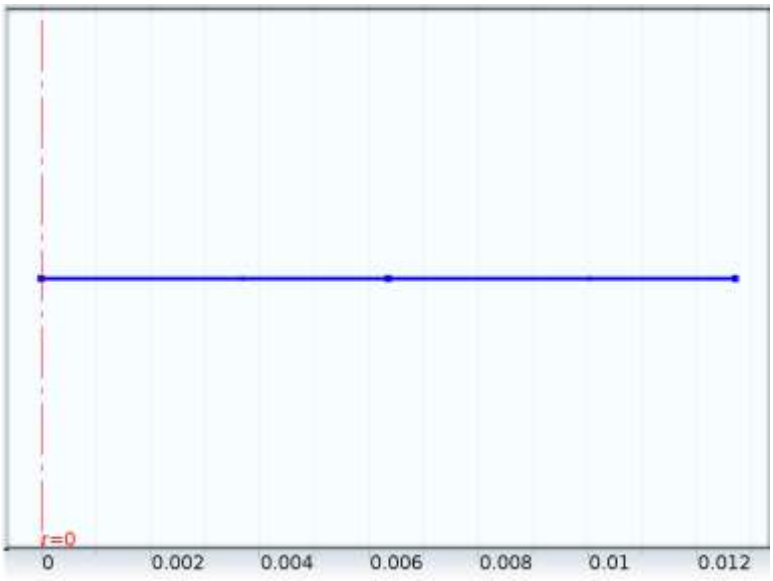

Porous Matrix 1

Selection

Geometric entity level	Domain
Selection	Domains 1–2

Equations

$$\rho C_p \frac{\partial T}{\partial t} + \rho C_p \mathbf{u} \cdot \nabla T = \nabla \cdot (k \nabla T) + Q$$
$$k = k_{eq}$$
$$k_{eq} = \theta_p k_p + (1 - \theta_p) k$$
$$\rho C_p = (\rho C_p)_{eq}$$
$$(\rho C_p)_{eq} = \theta_p \rho_p C_{p,p} + (1 - \theta_p) \rho C_p$$

Settings

Settings

Description	Value
Thermal conductivity	User defined

Description	Value
Thermal conductivity	{{r*k_bms/(1 - phi), 0, 0}, {0, r*k_bms/(1 - phi), 0}, {0, 0, r*k_bms/(1 - phi)}}
Density	User defined
Density	rho_a*c_w + rho_is*c_w + rho_c*c_c
Specific heat capacity	User defined
Specific heat capacity	r/(1 - phi)
Volume fraction	1 - phi

Variables

Name	Expression	Unit	Description	Selection
ht.k_prr	r*k_bms/(1 - phi)	W/(m*K)	Thermal conductivity, rr component	Domains 1–2
ht.k_pphir	0	W/(m*K)	Thermal conductivity, phir component	Domains 1–2
ht.k_pzr	0	W/(m*K)	Thermal conductivity, zr component	Domains 1–2
ht.k_prphi	0	W/(m*K)	Thermal conductivity,	Domains 1–2

Name	Expression	Unit	Description	Selection
			rphi component	
ht.k_pphiphi	r*k_bms/(1 - phi)	W/(m*K)	Thermal conductivity, phiphi component	Domains 1–2
ht.k_pzphi	0	W/(m*K)	Thermal conductivity, zphi component	Domains 1–2
ht.k_prz	0	W/(m*K)	Thermal conductivity, rz component	Domains 1–2
ht.k_pphiz	0	W/(m*K)	Thermal conductivity, phiz component	Domains 1–2
ht.k_pzz	r*k_bms/(1 - phi)	W/(m*K)	Thermal conductivity, zz component	Domains 1–2
ht.rho_p	rho_a*c_w + rho_is*c_w +	kg/m^3	Density	Domains 1–2

Name	Expression	Unit	Description	Selection
	rho_c*c_c			
ht.C_pp	r/(1 - phi)	J/(kg*K)	Specific heat capacity	Domains 1–2
ht.theta_p	1 - phi	1	Volume fraction	Domains 1–2
ht.k_eqrr	(1 - phi)*ht.k_prr + phi*ht.krr	W/(m*K)	Equivalent thermal conductivity, rr component	Domains 1–2
ht.k_eqphir	(1 - phi)*ht.k_pphir + phi*ht.kphir	W/(m*K)	Equivalent thermal conductivity, phir component	Domains 1–2
ht.k_eqzr	(1 - phi)*ht.k_pzr + phi*ht.kzr	W/(m*K)	Equivalent thermal conductivity, zr component	Domains 1–2
ht.k_eqrphi	(1 - phi)*ht.k_prphi + phi*ht.krphi	W/(m*K)	Equivalent thermal conductivity,	Domains 1–2

Name	Expression	Unit	Description	Selection
			rphi component	
ht.k_eqphiphi	(1 - phi)*ht.k_pphiphi + phi*ht.kphiphi	W/(m*K)	Equivalent thermal conductivity, phiphi component	Domains 1–2
ht.k_eqzphi	(1 - phi)*ht.k_pzphi + phi*ht.kzphi	W/(m*K)	Equivalent thermal conductivity, zphi component	Domains 1–2
ht.k_eqrz	(1 - phi)*ht.k_prz + phi*ht.krz	W/(m*K)	Equivalent thermal conductivity, rz component	Domains 1–2
ht.k_eqphiz	(1 - phi)*ht.k_pphiz + phi*ht.kphiz	W/(m*K)	Equivalent thermal conductivity, phiz component	Domains 1–2

Name	Expression	Unit	Description	Selection
ht.k_eqzz	(1 - phi)*ht.k_pzz + phi*ht.kzz	W/(m*K)	Equivalent thermal conductivity, zz component	Domains 1–2
ht.C_eq	(1 - phi)*ht.rho_p*ht.C_pp + phi*ht.rho*ht.Cp	J/(m^3*K)	Equivalent volumetric heat capacity	Domains 1–2

2.3.2 Heat Transfer in Fluids 1

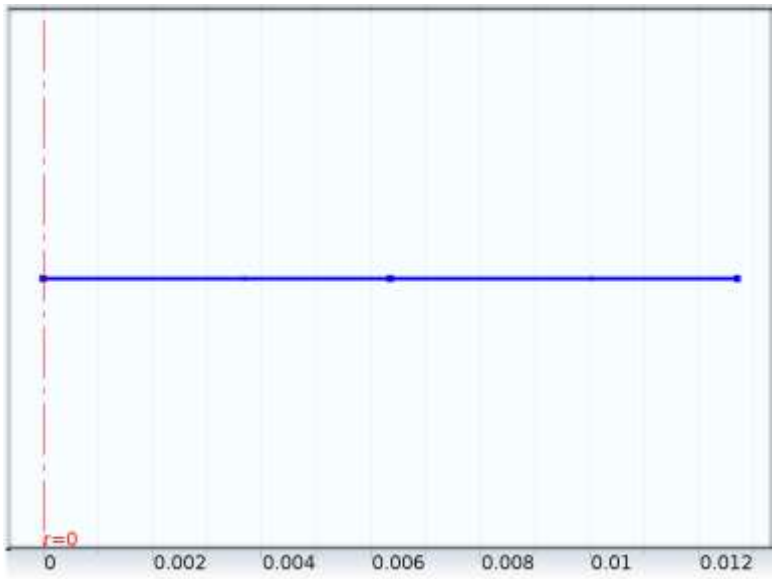

Heat Transfer in Fluids 1

Selection

Geometric entity level	Domain
Selection	Domains 1–2

Equations

$$\rho C_p \frac{\partial T}{\partial t} + \rho C_p \mathbf{u} \cdot \nabla T = \nabla \cdot (k \nabla T) + Q$$

Settings

Settings

Description	Value
Thermal conductivity	User defined
Thermal conductivity	{{0, 0, 0}, {0, 0, 0}, {0, 0, 0}}
Density	User defined
Density	r*rho_v
Heat capacity at constant pressure	User defined
Heat capacity at constant pressure	wt*cp_t + wg*cp_g
Ratio of specific heats	User defined

Variables

Name	Expression	Unit	Description	Selection
ht.alphap	-d(ht.rho, T)/(ht.rho + eps)	1/K	Isobaric compressibility coefficient	Domains 1–2
ht.pA	1[atm]	Pa	Absolute pressure	Domains 1–2
ht.ur	model.input.minput_velocity1	m/s	Velocity field, r component	Domains 1–2
ht.uphi	model.input.minput_ve	m/s	Velocity field, phi	Domains 1–

Name	Expression	Unit	Description	Selection
	locity2		component	2
ht.uz	model.input.minput_velocity3	m/s	Velocity field, z component	Domains 1–2
ht.gradTr	Tr	K/m	Temperature gradient, r component	Domains 1–2
ht.gradTphi	0	K/m	Temperature gradient, phi component	Domains 1–2
ht.gradTz	0	K/m	Temperature gradient, z component	Domains 1–2
ht.gradTmag	sqrt(ht.gradTr^2 + ht.gradTphi^2 + ht.gradTz^2)	K/m	Temperature gradient magnitude	Domains 1–2
ht.kmean	root.mod1.ht.k_eff_p1	W/(m*K)	Mean effective thermal conductivity	Domains 1–2
ht.dfluxr	-ht.k_effrr*Tr	W/m^2	Conductive heat flux, r component	Domains 1–2
ht.dfluxphi	-ht.k_effphir*Tr	W/m^2	Conductive heat	Domains 1–

Name	Expression	Unit	Description	Selection
			flux, phi component	2
ht.dfluxz	-ht.k_effzr*Tr	W/m^2	Conductive heat flux, z component	Domains 1–2
ht.dfluxMag	sqrt(ht.dfluxr^2 + ht.dfluxphi^2 + ht.dfluxz^2)	W/m^2	Conductive heat flux magnitude	Domains 1–2
ht.Q	0	W/m^3	Heat source	Domains 1–2
ht.qs	0	W/(m^3*K)	Production/absorption coefficient	Domains 1–2
ht.Qmet	0	W/m^3	Metabolic heat source	Domains 1–2
ht.Qtot	0	W/m^3	Total heat source	Domains 1–2
ht.rhoInt	ht.rho	kg/m^3	Density for integration	Domains 1–2
ht.CpInt	ht.Cp	J/(kg*K)	Specific heat capacity for integration	Domains 1–2
ht.gammaInt	ht.gamma	1	Ratio of specific heats for integration	Domains 1–2

Name	Expression	Unit	Description	Selection
ht.HRef	subst(subst(ht.CpInt, ht.pA, 1[atm]), T, 298.15[K])*298.15[K]/ subst(subst(ht.gammaInt, ht.pA, 1[atm]), T, 298.15[K]) + 1[atm]/subst(subst(ht.rhoInt, ht.pA, 1[atm]), T, 298.15[K])	J/kg	Reference enthalpy	Domains 1–2
ht.DeltaH	0.05*((subst(subst(ht.CpInt, ht.pA, 1[atm]), T, 298.15[K]) + 2*subst(subst(ht.CpInt, ht.pA, 1[atm]), T, 0.9*298.15[K] + 0.1*T) + 2*subst(subst(ht.CpInt, ht.pA, 1[atm]), T, 0.8*298.15[K] + 0.2*T) + 2*subst(subst(ht.CpInt,	J/kg	Sensible enthalpy	Domains 1–2

Name	Expression	Unit	Description	Selection
	ht.pA, 1[atm]), T, 0.7*298.15[K] + 0.3*T) + 2*subst(subst(ht.CpInt, ht.pA, 1[atm]), T, 0.6*298.15[K] + 0.4*T) + 2*subst(subst(ht.CpInt, ht.pA, 1[atm]), T, 0.5*(298.15[K] + T)) + 2*subst(subst(ht.CpInt, ht.pA, 1[atm]), T, 0.4*298.15[K] + 0.6*T) + 2*subst(subst(ht.CpInt, ht.pA, 1[atm]), T, 0.30000000000000004 *298.15[K] + 0.7*T) + 2*subst(subst(ht.CpInt, ht.pA, 1[atm]), T, 0.19999999999999996			

Name	Expression	Unit	Description	Selection
	*298.15[K] + 0.8*T) + 2*subst(subst(ht.CpInt, ht.pA, 1[atm]), T, 0.09999999999999998 *298.15[K] + 0.9*T) + subst(ht.CpInt, ht.pA, 1[atm]))*(T - 298.15[K]) + (subst((1 + T*d(ht.rhoInt, T)/ht.rhoInt)/ht.rhoInt, ht.pA, 1[atm]) + 2*subst((1 + T*d(ht.rhoInt, T)/ht.rhoInt)/ht.rhoInt, ht.pA, 0.9*1[atm] + 0.1*ht.pA) + 2*subst((1 + T*d(ht.rhoInt, T)/ht.rhoInt)/ht.rhoInt, ht.pA, 0.8*1[atm] + 0.2*ht.pA) +			

Name	Expression	Unit	Description	Selection
	2*subst((1 + T*d(ht.rhoInt, T)/ht.rhoInt)/ht.rhoInt, ht.pA, 0.7*1[atm] + 0.3*ht.pA) + 2*subst((1 + T*d(ht.rhoInt, T)/ht.rhoInt)/ht.rhoInt, ht.pA, 0.6*1[atm] + 0.4*ht.pA) + 2*subst((1 + T*d(ht.rhoInt, T)/ht.rhoInt)/ht.rhoInt, ht.pA, 0.5*(1[atm] + ht.pA)) + 2*subst((1 + T*d(ht.rhoInt, T)/ht.rhoInt)/ht.rhoInt, ht.pA, 0.4*1[atm] + 0.6*ht.pA) + 2*subst((1 + T*d(ht.rhoInt,			

Name	Expression	Unit	Description	Selection
	T)/ht.rhoInt)/ht.rhoInt, ht.pA, 0.30000000000000004 *1[atm] + 0.7*ht.pA) + 2*subst((1 + T*d(ht.rhoInt, T)/ht.rhoInt)/ht.rhoInt, ht.pA, 0.19999999999999996 *1[atm] + 0.8*ht.pA) + 2*subst((1 + T*d(ht.rhoInt, T)/ht.rhoInt)/ht.rhoInt, ht.pA, 0.09999999999999998 *1[atm] + 0.9*ht.pA) + (1 + T*d(ht.rhoInt, T)/ht.rhoInt)/ht.rhoInt) *(ht.pA - 1[atm]))			
ht.H	ht.HRef + ht.DeltaH	J/kg	Enthalpy	Domains 1–2

Name	Expression	Unit	Description	Selection
ht.H0	ht.H + 0.5*(ht.ur^2 + ht.uphi^2 + ht.uz^2)	J/kg	Total enthalpy	Domains 1–2
ht.Ei	ht.H - ht.pA/ht.rho	J/kg	Internal energy	Domains 1–2
ht.Ei0	ht.Ei + 0.5*(ht.ur^2 + ht.uphi^2 + ht.uz^2)	J/kg	Total internal energy	Domains 1–2
ht.trlfluxr	0	W/m^2	Translational heat flux, r component	Domains 1–2
ht.trlfluxphi	0	W/m^2	Translational heat flux, phi component	Domains 1–2
ht.trlfluxz	0	W/m^2	Translational heat flux, z component	Domains 1–2
ht.afluxr	ht.rho*ht.ur*ht.Ei	W/m^2	Convective heat flux, r component	Domains 1–2
ht.afluxphi	ht.rho*ht.uphi*ht.Ei	W/m^2	Convective heat flux, phi component	Domains 1–2
ht.afluxz	ht.rho*ht.uz*ht.Ei	W/m^2	Convective heat flux, z component	Domains 1–2
ht.tfluxr	ht.dfluxr + ht.trlfluxr + ht.afluxr	W/m^2	Total heat flux, r component	Domains 1–2
ht.tfluxphi	ht.dfluxphi +	W/m^2	Total heat flux, phi	Domains 1–

Name	Expression	Unit	Description	Selection
	ht.trlfluxphi + ht.afluxphi		component	2
ht.tfluxz	ht.dfluxz + ht.trlfluxz + ht.afluxz	W/m^2	Total heat flux, z component	Domains 1–2
ht.tfluxMag	sqrt(ht.tfluxr^2 + ht.tfluxphi^2 + ht.tfluxz^2)	W/m^2	Total heat flux magnitude	Domains 1–2
ht.tefluxr	ht.dfluxr + ht.rho*ht.ur*ht.H0	W/m^2	Total energy flux, r component	Domains 1–2
ht.tefluxphi	ht.dfluxphi + ht.rho*ht.uphi*ht.H0	W/m^2	Total energy flux, phi component	Domains 1–2
ht.tefluxz	ht.dfluxz + ht.rho*ht.uz*ht.H0	W/m^2	Total energy flux, z component	Domains 1–2
ht.tefluxMag	sqrt(ht.tefluxr^2 + ht.tefluxphi^2 + ht.tefluxz^2)	W/m^2	Total energy flux magnitude	Domains 1–2
ht.rflux	0	W/m^2	Radiative heat flux	Boundaries 2–3
ht.ccflux	0	W/m^2	Convective heat flux	Boundaries 2–3
ht.ntrlflux	mean(ht.trlfluxr)*ht.nr	W/m^2	Normal	Boundaries

Name	Expression	Unit	Description	Selection
	+ mean(ht.trlfluxphi)*ht.nphi + mean(ht.trlfluxz)*ht.nz		translational heat flux	2–3
ht.naflux	mean(ht.afluxr)*ht.nr + mean(ht.afluxphi)*ht.nphi + mean(ht.afluxz)*ht.nz	W/m^2	Normal convective heat flux	Boundaries 2–3
ht.ndflux	mean(ht.dfluxr)*ht.nr + mean(ht.dfluxphi)*ht.nphi + mean(ht.dfluxz)*ht.nz	W/m^2	Normal conductive heat flux	Boundaries 2–3
ht.ntflux	ht.ndflux + ht.ntrlflux + ht.naflux	W/m^2	Total normal heat flux	Boundaries 2–3
ht.nteflux	mean(ht.tefluxr)*ht.nr + mean(ht.tefluxphi)*ht.nphi + mean(ht.tefluxz)*ht.nz	W/m^2	Total normal energy flux	Boundaries 2–3
ht.Qbtot	0	W/m^2	Total boundary heat source	Boundaries 2–3

Name	Expression	Unit	Description	Selection
ht.Qltot	0	W/m	Total heat source	Domains 1–2
ht.res_T	2*(-ht.k_effrr*d(Tr, r) - ht.k_effphiphi*if(abs(r)<0.0010*h, d(Tr, r), Tr/r) - (ht.qs + ht.qs_oop)*T + ht.rho*ht.Cp*ht.ur*Tr - ht.Q - ht.Qoop)*pi*r	W/m^3	Equation residual	Domains 1–2
ht.cellPe	0.5*ht.rho*ht.Cp*h*sqrt(ht.ur^2 + ht.uphi^2 + ht.uz^2)/ht.kmean	1	Cell Péclet number	Domains 1–2
ht.afluxMag	sqrt((ht.rho*ht.ur*ht.Ei)^2 + (ht.rho*ht.uphi*ht.Ei)^2 + (ht.rho*ht.uz*ht.Ei)^2)	W/m^2	Convective heat flux magnitude	Domains 1–2
ht.krr	0	W/(m*K)	Thermal conductivity, rr component	Domains 1–2
ht.kphir	0	W/(m*K)	Thermal	Domains 1–

Name	Expression	Unit	Description	Selection
			conductivity, phir component	2
ht.kzr	0	W/(m*K)	Thermal conductivity, zr component	Domains 1–2
ht.krphi	0	W/(m*K)	Thermal conductivity, rphi component	Domains 1–2
ht.kphiphi	0	W/(m*K)	Thermal conductivity, phiphi component	Domains 1–2
ht.kzphi	0	W/(m*K)	Thermal conductivity, zphi component	Domains 1–2
ht.krz	0	W/(m*K)	Thermal conductivity, rz component	Domains 1–2
ht.kphiz	0	W/(m*K)	Thermal conductivity, phiz component	Domains 1–2
ht.kzz	0	W/(m*K)	Thermal	Domains 1–

Name	Expression	Unit	Description	Selection
			conductivity, zz component	2
ht.k_effrr	ht.k_eqrr	W/(m*K)	Effective thermal conductivity, rr component	Domains 1–2
ht.k_effphir	0	W/(m*K)	Effective thermal conductivity, phir component	Domains 1–2
ht.k_effzr	0	W/(m*K)	Effective thermal conductivity, zr component	Domains 1–2
ht.k_effrphi	0	W/(m*K)	Effective thermal conductivity, rphi component	Domains 1–2
ht.k_effphiphi	0	W/(m*K)	Effective thermal conductivity, phiphi component	Domains 1–2
ht.k_effzphi	0	W/(m*K)	Effective thermal conductivity, zphi component	Domains 1–2
ht.k_effrz	0	W/(m*K)	Effective thermal	Domains 1–

Name	Expression	Unit	Description	Selection
			conductivity, rz component	2
ht.k_effphiz	0	W/(m*K)	Effective thermal conductivity, phiz component	Domains 1–2
ht.k_effzz	0	W/(m*K)	Effective thermal conductivity, zz component	Domains 1–2
ht.C_eff	ht.C_eq	J/(m^3*K)	Effective volumetric heat capacity	Domains 1–2
ht.gamma	1	1	Ratio of specific heats	Domains 1–2
ht.rho	r*rho_v	kg/m^3	Density	Domains 1–2
ht.Cp	wt*cp_t + wg*cp_g	J/(kg*K)	Heat capacity at constant pressure	Domains 1–2

2.3.3 Axial Symmetry 1

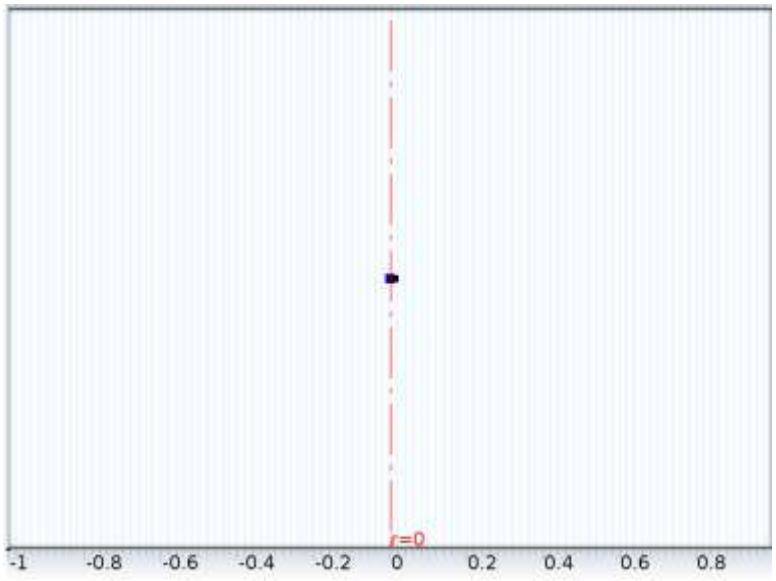

Axial Symmetry 1

Selection

Geometric entity level	Boundary
Selection	Boundary 1

2.3.4 Thermal Insulation 1

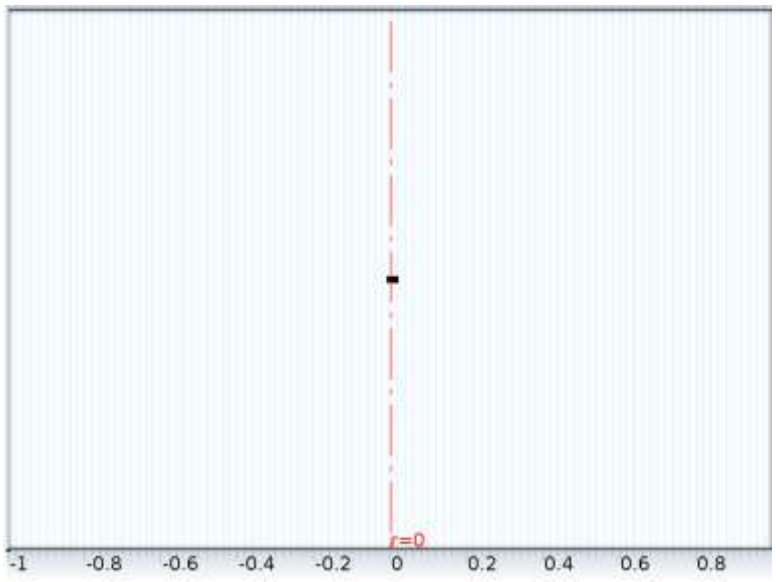

Thermal Insulation 1

Selection

Geometric entity level	Boundary
Selection	No boundaries

Equations

$$-\mathbf{n}\cdot(-k\nabla T)=0$$

2.3.5 Initial Values 1

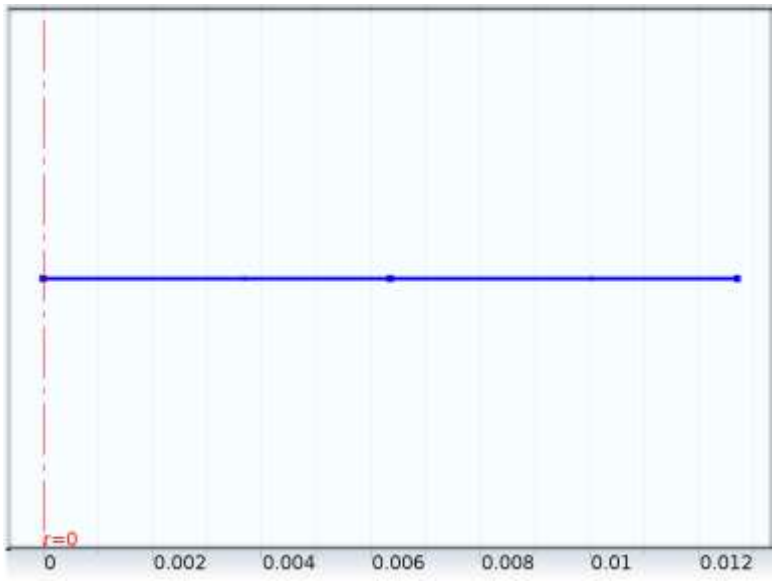

Initial Values 1

Selection

Geometric entity level	Domain
Selection	Domains 1–2

Settings

Settings

Description	Value
Temperature	T_init

2.3.6 Heat Flux 1

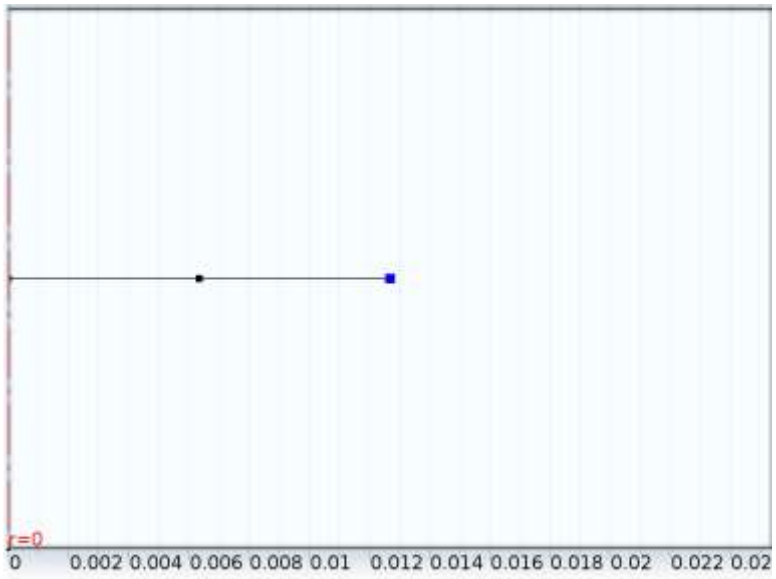

Heat Flux 1

Selection

Geometric entity level	Boundary
Selection	Boundary 3

Equations

$$-\mathbf{n}\cdot(-k\nabla T) = h\cdot(T_{ext} - T)$$

Settings

Settings

Description	**Value**
Heat flux	Inward heat flux
Heat transfer coefficient	h_sph*r
External temperature	T_N2

Variables

Name	Expression	Unit	Description	Selection
ht.q0	ht.q0_hf1	W/m^2	Inward heat flux	Boundary 3
ht.hf1.Text	T_N2	K	External temperature	Boundary 3
ht.hf1.h	h_sph*r	W/(m^2*K)	Heat transfer coefficient	Boundary 3
ht.q0_hf1	ht.hf1.h*(ht.hf1.Text - T)	W/m^2	Inward heat flux	Boundary 3

2.3.7 Heat Source 1

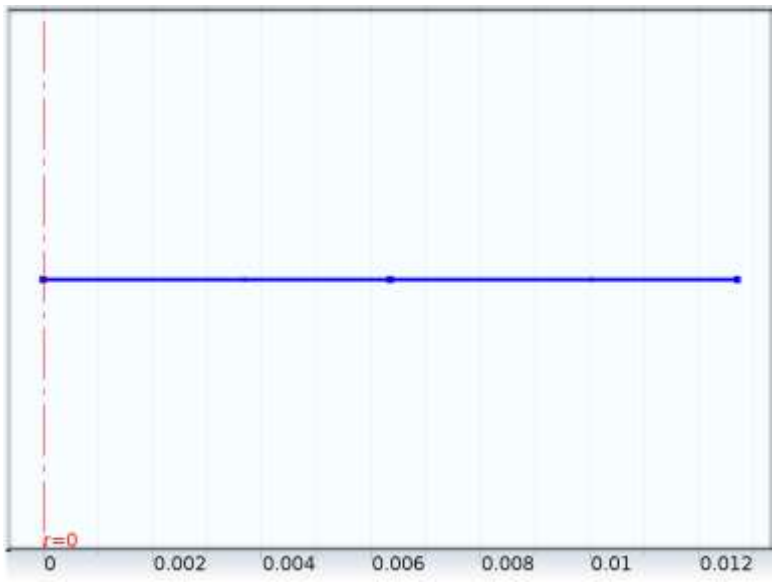

Heat Source 1

Selection

Geometric entity level	Domain
Selection	Domains 1–2

Equations

$$\rho C_p \frac{\partial T}{\partial t} + \rho C_p \mathbf{u} \cdot \nabla T = \nabla \cdot (k \nabla T) + Q$$

Settings

Settings

Description	Value
Heat source	r*(-1000*(k_t(T)*deltaH_t + k_g(T)*deltaH_g + k_is(T)*deltaH_is)*rho_a - 1000*k_c(T)*deltaH_c*rho_is - 1000*(k_c2(T)*deltaH_c2 + k_g2(T)*deltaH_g2)*rho_v*wt)

Variables

Name	Expression	Unit	Description	Selection
ht.Q	-1000*r*((k_t(T)*deltaH_t + k_g(T)*deltaH_g + k_is(T)*deltaH_is)*rho_a + k_c(T)*deltaH_c*rho_is + (k_c2(T)*deltaH_c2 + k_g2(T)*deltaH_g2)*rho_v*wt)	W/m^3	Heat source	Domains 1–2

Name	Expression	Unit	Description	Selection
ht.Qtot	-1000*r*((k_t(T)*deltaH_t + k_g(T)*deltaH_g + k_is(T)*deltaH_is)*rho_a + k_c(T)*deltaH_c*rho_is + (k_c2(T)*deltaH_c2 + k_g2(T)*deltaH_g2)*rho_v*wt)	W/m^3	Total heat source	Domains 1–2

2.4 Transport of Diluted Species (chds)

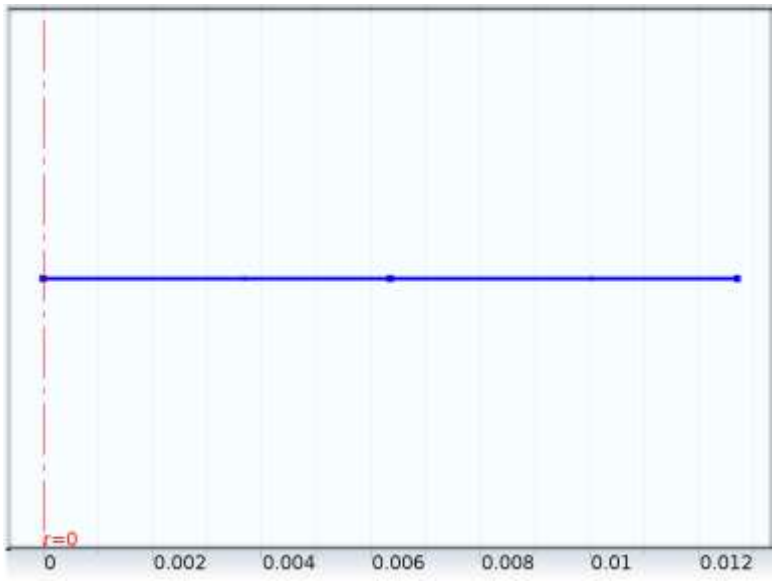

Transport of Diluted Species

Selection

Geometric entity level	Domain
Selection	Domains 1–2

Equations

$$\frac{\partial c_i}{\partial t} + \nabla \cdot \left(-D_i \nabla c_i\right) + \mathbf{u} \cdot \nabla c_i = R_i$$

$$\mathbf{N}_i = -D_i \nabla c_i + \mathbf{u} c_i$$

Settings

Description	Value
Value type when using splitting of complex variables	Complex
Show equation assuming	std1/time

2.4.1 Convection and Diffusion 1

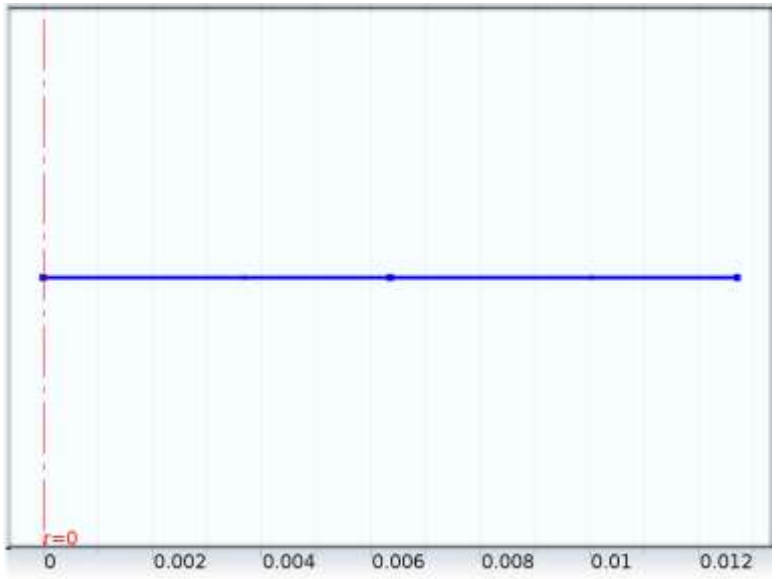

Convection and Diffusion 1

Selection

Geometric entity level	Domain
Selection	Domains 1–2

Equations

$$\frac{\partial c_i}{\partial t} + \nabla \cdot \left(-D_i \nabla c_i\right) + \mathbf{u} \cdot \nabla c_i = R_i$$

$$\mathbf{N}_i = -D_i \nabla c_i + \mathbf{u} c_i$$

Settings

Settings

Description	Value
Diffusion coefficient	{{0, 0, 0}, {0, 0, 0}, {0, 0, 0}}
Diffusion coefficient	{{0, 0, 0}, {0, 0, 0}, {0, 0, 0}}
Diffusion coefficient	{{0, 0, 0}, {0, 0, 0}, {0, 0, 0}}

Variables

Name	Expression	Unit	Description	Selection
chds.Drr_rho_a	0	m^2/s	Diffusion coefficient, rr component	Domains 1–2
chds.Dphir_rho_a	0	m^2/s	Diffusion coefficient, phir component	Domains 1–2
chds.Dzr_rho_a	0	m^2/s	Diffusion coefficient, zr component	Domains 1–2
chds.Drphi_rho_a	0	m^2/s	Diffusion coefficient, rphi component	Domains 1–2

Name	Expression	Unit	Description	Selection
chds.Dphiphi_rho_a	0	m^2/s	Diffusion coefficient, phiphi component	Domains 1–2
chds.Dzphi_rho_a	0	m^2/s	Diffusion coefficient, zphi component	Domains 1–2
chds.Drz_rho_a	0	m^2/s	Diffusion coefficient, rz component	Domains 1–2
chds.Dphiz_rho_a	0	m^2/s	Diffusion coefficient, phiz component	Domains 1–2
chds.Dzz_rho_a	0	m^2/s	Diffusion coefficient, zz component	Domains 1–2
chds.Dav_rho_a	chds.Drr_rho_a	m^2/s	Average diffusion coefficient	Domains 1–2

Name	Expression	Unit	Description	Selection
chds.tfluxr_rho_a	-chds.Drr_rho_a*rho_ar + chds.cfluxr_rho_a	mol/(m^2*s)	Total flux, r component	Domains 1–2
chds.tfluxphi_rho_a	-chds.Dphir_rho_a*rho_ar + chds.cfluxphi_rho_a	mol/(m^2*s)	Total flux, phi component	Domains 1–2
chds.tfluxz_rho_a	-chds.Dzr_rho_a*rho_ar + chds.cfluxz_rho_a	mol/(m^2*s)	Total flux, z component	Domains 1–2
chds.dfluxr_rho_a	-chds.Drr_rho_a*rho_ar	mol/(m^2*s)	Diffusive flux, r component	Domains 1–2
chds.dfluxphi_rho_a	-chds.Dphir_rho_a*rho_ar	mol/(m^2*s)	Diffusive flux, phi component	Domains 1–2
chds.dfluxz_rho_a	-chds.Dzr_rho_a*rho_ar	mol/(m^2*s)	Diffusive flux, z component	Domains 1–2
chds.gradr_rho_a	rho_ar	mol/m^4	Concentration gradient, r component	Domains 1–2
chds.gradphi_rho_a	0	mol/m^4	Concentration gradient, phi component	Domains 1–2
chds.gradz_rho_a	0	mol/m^4	Concentration gradient, z component	Domains 1–2

Name	Expression	Unit	Description	Selection
chds.ntflux_rho_a	chds.nr*chds.tfluxr_rho_a + chds.nphi*chds.tfluxphi_rho_a + chds.nz*chds.tfluxz_rho_a	mol/(m^2*s)	Normal total flux	Boundaries 1–3
chds.ndflux_rho_a	chds.nr*chds.dfluxr_rho_a + chds.nphi*chds.dfluxphi_rho_a + chds.nz*chds.dfluxz_rho_a	mol/(m^2*s)	Normal diffusive flux	Boundaries 1–3
chds.dfluxMag_rho_a	sqrt(chds.dfluxr_rho_a^2 + chds.dfluxphi_rho_a^2 + chds.dfluxz_rho_a^2)	mol/(m^2*s)	Diffusive flux magnitude	Domains 1–2
chds.tfluxMag_rho_a	sqrt(chds.tfluxr_rho_a^2 + chds.tfluxphi_rho_a^2 + chds.tfluxz_rho_a^2)	mol/(m^2*s)	Total flux magnitude	Domains 1–2
chds.Drr_rho_is	0	m^2/s	Diffusion coefficient, rr component	Domains 1–2
chds.Dphir_rho_is	0	m^2/s	Diffusion coefficient,	Domains 1–2

Name	Expression	Unit	Description	Selection
			phir component	
chds.Dzr_rho_is	0	m^2/s	Diffusion coefficient, zr component	Domains 1–2
chds.Drphi_rho_is	0	m^2/s	Diffusion coefficient, rphi component	Domains 1–2
chds.Dphiphi_rho_is	0	m^2/s	Diffusion coefficient, phiphi component	Domains 1–2
chds.Dzphi_rho_is	0	m^2/s	Diffusion coefficient, zphi component	Domains 1–2
chds.Drz_rho_is	0	m^2/s	Diffusion coefficient, rz component	Domains 1–2
chds.Dphiz_rh	0	m^2/s	Diffusion	Domains 1–

Name	Expression	Unit	Description	Selection
o_is			coefficient, phiz component	2
chds.Dzz_rho_is	0	m^2/s	Diffusion coefficient, zz component	Domains 1–2
chds.Dav_rho_is	chds.Drr_rho_is	m^2/s	Average diffusion coefficient	Domains 1–2
chds.tfluxr_rho_is	-chds.Drr_rho_is*rho_isr + chds.cfluxr_rho_is	mol/(m^2*s)	Total flux, r component	Domains 1–2
chds.tfluxphi_rho_is	-chds.Dphir_rho_is*rho_isr + chds.cfluxphi_rho_is	mol/(m^2*s)	Total flux, phi component	Domains 1–2
chds.tfluxz_rho_is	-chds.Dzr_rho_is*rho_isr + chds.cfluxz_rho_is	mol/(m^2*s)	Total flux, z component	Domains 1–2
chds.dfluxr_rho_is	-chds.Drr_rho_is*rho_isr	mol/(m^2*s)	Diffusive flux, r component	Domains 1–2
chds.dfluxphi_rho_is	-chds.Dphir_rho_is*rho_isr	mol/(m^2*s)	Diffusive flux, phi component	Domains 1–2
chds.dfluxz_rh	-chds.Dzr_rho_is*rho_isr	mol/(m^2*s)	Diffusive flux,	Domains 1–

Name	Expression	Unit	Description	Selection
o_is			z component	2
chds.gradr_rho_is	rho_isr	mol/m^4	Concentration gradient, r component	Domains 1–2
chds.gradphi_rho_is	0	mol/m^4	Concentration gradient, phi component	Domains 1–2
chds.gradz_rho_is	0	mol/m^4	Concentration gradient, z component	Domains 1–2
chds.ntflux_rho_is	chds.nr*chds.tfluxr_rho_is + chds.nphi*chds.tfluxphi_rho_is + chds.nz*chds.tfluxz_rho_is	mol/(m^2*s)	Normal total flux	Boundaries 1–3
chds.ndflux_rho_is	chds.nr*chds.dfluxr_rho_is + chds.nphi*chds.dfluxphi_rho_is + chds.nz*chds.dfluxz_rho_is	mol/(m^2*s)	Normal diffusive flux	Boundaries 1–3

Name	Expression	Unit	Description	Selection
chds.dfluxMag_rho_is	sqrt(chds.dfluxr_rho_is^2 + chds.dfluxphi_rho_is^2 + chds.dfluxz_rho_is^2)	mol/(m^2*s)	Diffusive flux magnitude	Domains 1–2
chds.tfluxMag_rho_is	sqrt(chds.tfluxr_rho_is^2 + chds.tfluxphi_rho_is^2 + chds.tfluxz_rho_is^2)	mol/(m^2*s)	Total flux magnitude	Domains 1–2
chds.Drr_rho_c	0	m^2/s	Diffusion coefficient, rr component	Domains 1–2
chds.Dphir_rho_c	0	m^2/s	Diffusion coefficient, phir component	Domains 1–2
chds.Dzr_rho_c	0	m^2/s	Diffusion coefficient, zr component	Domains 1–2
chds.Drphi_rho_c	0	m^2/s	Diffusion coefficient, rphi component	Domains 1–2
chds.Dphiphi_r	0	m^2/s	Diffusion	Domains 1–

Name	Expression	Unit	Description	Selection
ho_c			coefficient, phiphi component	2
chds.Dzphi_rho_c	0	m^2/s	Diffusion coefficient, zphi component	Domains 1–2
chds.Drz_rho_c	0	m^2/s	Diffusion coefficient, rz component	Domains 1–2
chds.Dphiz_rho_c	0	m^2/s	Diffusion coefficient, phiz component	Domains 1–2
chds.Dzz_rho_c	0	m^2/s	Diffusion coefficient, zz component	Domains 1–2
chds.Dav_rho_c	chds.Drr_rho_c	m^2/s	Average diffusion coefficient	Domains 1–2
chds.tfluxr_rho	-chds.Drr_rho_c*rho_cr +	mol/(m^2*s)	Total flux, r	Domains 1–

Name	Expression	Unit	Description	Selection
_c	chds.cfluxr_rho_c		component	2
chds.tfluxphi_rho_c	-chds.Dphir_rho_c*rho_cr + chds.cfluxphi_rho_c	mol/(m^2*s)	Total flux, phi component	Domains 1–2
chds.tfluxz_rho_c	-chds.Dzr_rho_c*rho_cr + chds.cfluxz_rho_c	mol/(m^2*s)	Total flux, z component	Domains 1–2
chds.dfluxr_rho_c	-chds.Drr_rho_c*rho_cr	mol/(m^2*s)	Diffusive flux, r component	Domains 1–2
chds.dfluxphi_rho_c	-chds.Dphir_rho_c*rho_cr	mol/(m^2*s)	Diffusive flux, phi component	Domains 1–2
chds.dfluxz_rho_c	-chds.Dzr_rho_c*rho_cr	mol/(m^2*s)	Diffusive flux, z component	Domains 1–2
chds.gradr_rho_c	rho_cr	mol/m^4	Concentration gradient, r component	Domains 1–2
chds.gradphi_rho_c	0	mol/m^4	Concentration gradient, phi component	Domains 1–2
chds.gradz_rho_c	0	mol/m^4	Concentration gradient, z component	Domains 1–2
chds.ntflux_rh	chds.nr*chds.tfluxr_rho_c	mol/(m^2*s)	Normal total	Boundaries

Name	Expression	Unit	Description	Selection
o_c	+ chds.nphi*chds.tfluxphi_rho_c + chds.nz*chds.tfluxz_rho_c		flux	1–3
chds.ndflux_rho_c	chds.nr*chds.dfluxr_rho_c + chds.nphi*chds.dfluxphi_rho_c + chds.nz*chds.dfluxz_rho_c	mol/(m^2*s)	Normal diffusive flux	Boundaries 1–3
chds.dfluxMag_rho_c	sqrt(chds.dfluxr_rho_c^2 + chds.dfluxphi_rho_c^2 + chds.dfluxz_rho_c^2)	mol/(m^2*s)	Diffusive flux magnitude	Domains 1–2
chds.tfluxMag_rho_c	sqrt(chds.tfluxr_rho_c^2 + chds.tfluxphi_rho_c^2 + chds.tfluxz_rho_c^2)	mol/(m^2*s)	Total flux magnitude	Domains 1–2
chds.u	model.input.u1	m/s	Velocity field, r component	Domains 1–2
chds.v	model.input.u2	m/s	Velocity field, phi component	Domains 1–2
chds.w	model.input.u3	m/s	Velocity field, z component	Domains 1–2

Name	Expression	Unit	Description	Selection
chds.cfluxr_rho_a	rho_a*model.input.u1	mol/(m^2*s)	Convective flux, r component	Domains 1–2
chds.cfluxphi_rho_a	rho_a*model.input.u2	mol/(m^2*s)	Convective flux, phi component	Domains 1–2
chds.cfluxz_rho_a	rho_a*model.input.u3	mol/(m^2*s)	Convective flux, z component	Domains 1–2
chds.cfluxMag_rho_a	sqrt(chds.cfluxr_rho_a^2 + chds.cfluxphi_rho_a^2 + chds.cfluxz_rho_a^2)	mol/(m^2*s)	Convective flux magnitude	Domains 1–2
chds.ncflux_rho_a	chds.nr*chds.cfluxr_rho_a + chds.nphi*chds.cfluxphi_rho_a + chds.nz*chds.cfluxz_rho_a	mol/(m^2*s)	Normal convective flux	Boundaries 1–3
chds.cbf_rho_a	0	mol/(m^2*s)	Convective boundary flux	Boundaries 1–3
chds.cfluxr_rho_is	rho_is*model.input.u1	mol/(m^2*s)	Convective flux, r	Domains 1–2

Name	Expression	Unit	Description	Selection
			component	
chds.cfluxphi_rho_is	rho_is*model.input.u2	mol/(m^2*s)	Convective flux, phi component	Domains 1–2
chds.cfluxz_rho_is	rho_is*model.input.u3	mol/(m^2*s)	Convective flux, z component	Domains 1–2
chds.cfluxMag_rho_is	sqrt(chds.cfluxr_rho_is^2 + chds.cfluxphi_rho_is^2 + chds.cfluxz_rho_is^2)	mol/(m^2*s)	Convective flux magnitude	Domains 1–2
chds.ncflux_rho_is	chds.nr*chds.cfluxr_rho_is + chds.nphi*chds.cfluxphi_rho_is + chds.nz*chds.cfluxz_rho_is	mol/(m^2*s)	Normal convective flux	Boundaries 1–3
chds.cbf_rho_is	0	mol/(m^2*s)	Convective boundary flux	Boundaries 1–3
chds.cfluxr_rho_c	rho_c*model.input.u1	mol/(m^2*s)	Convective flux, r component	Domains 1–2

Name	Expression	Unit	Description	Selection
chds.cfluxphi_rho_c	rho_c*model.input.u2	mol/(m^2*s)	Convective flux, phi component	Domains 1–2
chds.cfluxz_rho_c	rho_c*model.input.u3	mol/(m^2*s)	Convective flux, z component	Domains 1–2
chds.cfluxMag_rho_c	sqrt(chds.cfluxr_rho_c^2 + chds.cfluxphi_rho_c^2 + chds.cfluxz_rho_c^2)	mol/(m^2*s)	Convective flux magnitude	Domains 1–2
chds.ncflux_rho_c	chds.nr*chds.cfluxr_rho_c + chds.nphi*chds.cfluxphi_rho_c + chds.nz*chds.cfluxz_rho_c	mol/(m^2*s)	Normal convective flux	Boundaries 1–3
chds.cbf_rho_c	0	mol/(m^2*s)	Convective boundary flux	Boundaries 1–3
chds.helem	h	m	Element size	Domains 1–2
chds.glim	0.1[mol/m^3]/chds.helem	mol/m^4	Lower gradient limit	Domains 1–2
chds.Ck	0.5	1	Tuning	Domains 1–

Name	Expression	Unit	Description	Selection
			parameter	2
chds.Res_rho_a	chds.u*rho_ar - chds.R_rho_a	mol/(m^3*s)	Equation residual	Domains 1–2
chds.Res_rho_is	chds.u*rho_isr - chds.R_rho_is	mol/(m^3*s)	Equation residual	Domains 1–2
chds.Res_rho_c	chds.u*rho_cr - chds.R_rho_c	mol/(m^3*s)	Equation residual	Domains 1–2

2.4.2 Axial Symmetry 1

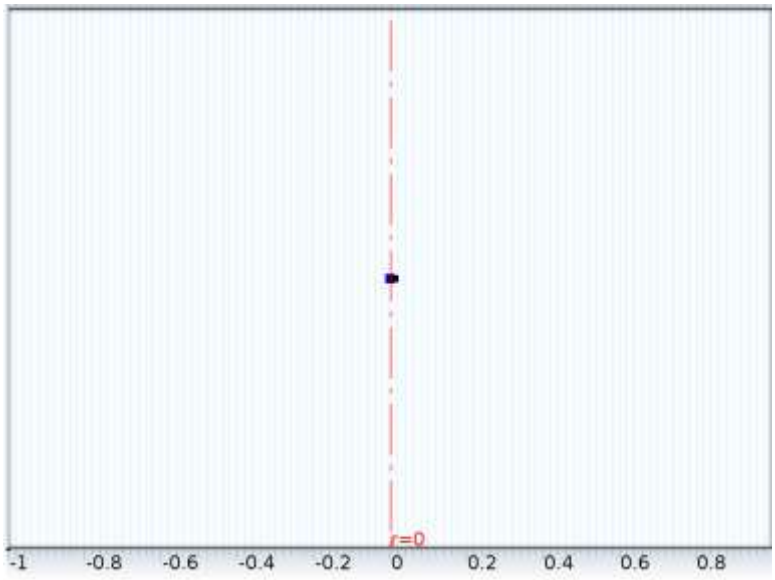

Axial Symmetry 1

Selection

Geometric entity level	Boundary
Selection	Boundary 1

2.4.3 No Flux 1

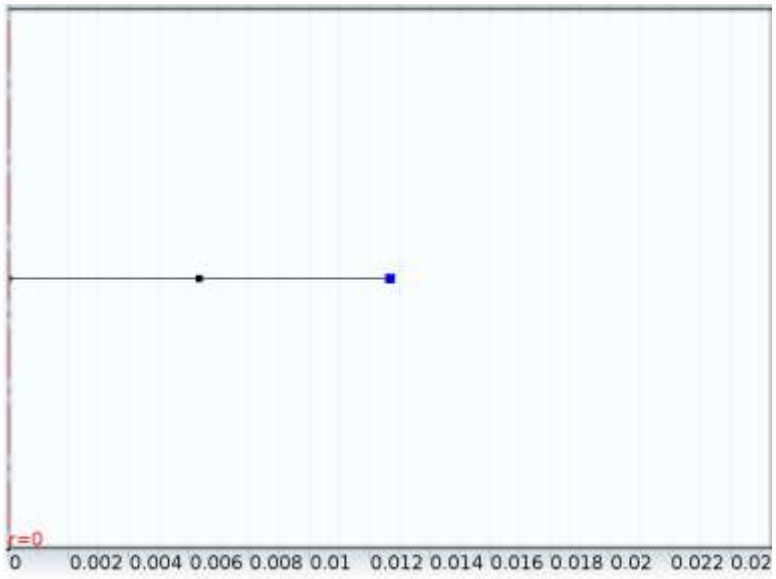

No Flux 1

Selection

Geometric entity level	Boundary
Selection	Boundary 3

Equations

$$-\mathbf{n} \cdot \mathbf{N}_i = 0$$

Variables

Name	Expression	Unit	Description	Selection
chds.cbf_rho_a	rho_a*(chds.u*chds.nr + chds.v*chds.nphi + chds.w*chds.nz)*test(rho_a)	mol/(m^2*s)	Convective boundary flux	Boundary 3
chds.cbf_rho_is	rho_is*(chds.u*chds.nr + chds.v*chds.nphi + chds.w*chds.nz)*test(rho_is)	mol/(m^2*s)	Convective boundary flux	Boundary 3

Name	Expression	Unit	Description	Selection
chds.cbf_rho_c	rho_c*(chds.u*chds.nr + chds.v*chds.nphi + chds.w*chds.nz)*test(rho_c)	mol/(m^2*s)	Convective boundary flux	Boundary 3

2.4.4 Initial Values 1

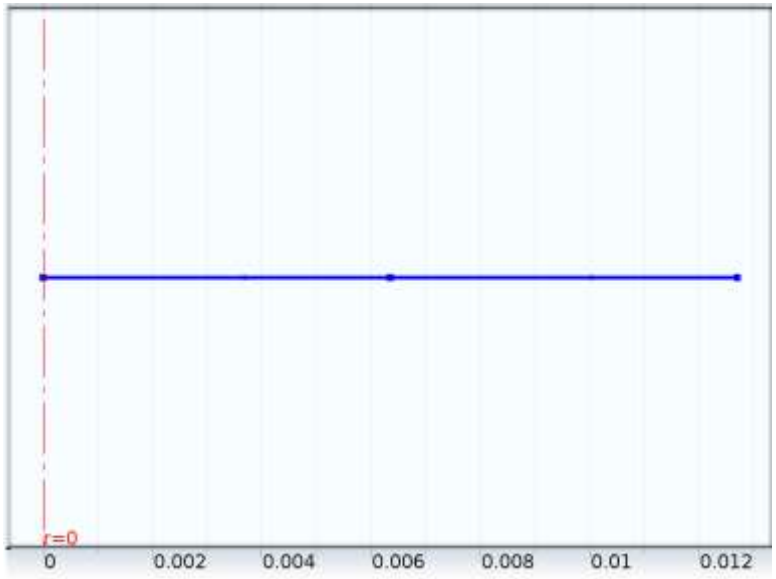

Initial Values 1

Selection

Geometric entity level	Domain
Selection	Domains 1–2

Settings

Settings

Description	Value
Concentration	rho_w

2.4.5 Reactions 1

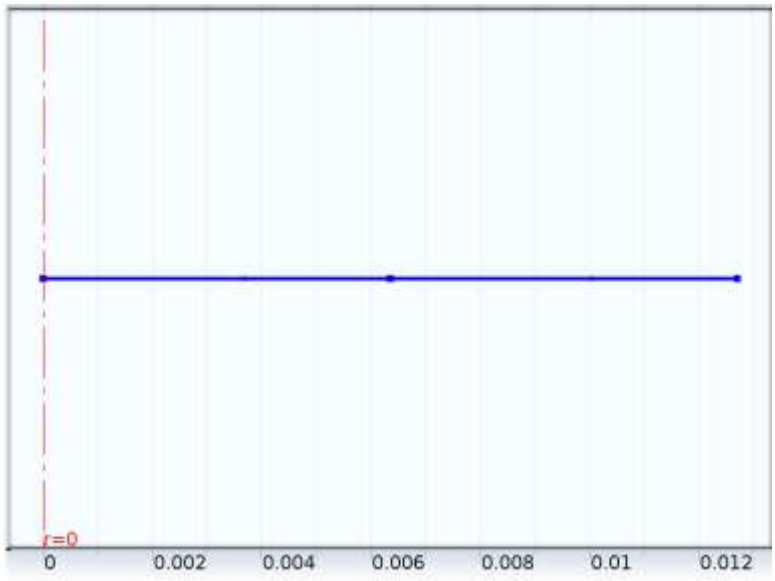

Reactions 1

Selection

Geometric entity level	Domain
Selection	Domains 1–2

Equations

$$\frac{\partial c_i}{\partial t} + \nabla \cdot \left(-D_i \nabla c_i\right) + \mathbf{u} \cdot \nabla c_i = R_i$$

Settings

Settings

Description	Value
Total rate expression	{S_a, S_is, S_c}

Variables

Name	Expression	Unit	Description	Selection
chds.R_rho_a	S_a	mol/(m^3*s)	Total rate expression	Domains 1–2

Name	Expression	Unit	Description	Selection
chds.R_rho_is	S_is	mol/(m^3*s)	Total rate expression	Domains 1–2
chds.R_rho_c	S_c	mol/(m^3*s)	Total rate expression	Domains 1–2

2.5 Transport of Concentrated Species (chcs)

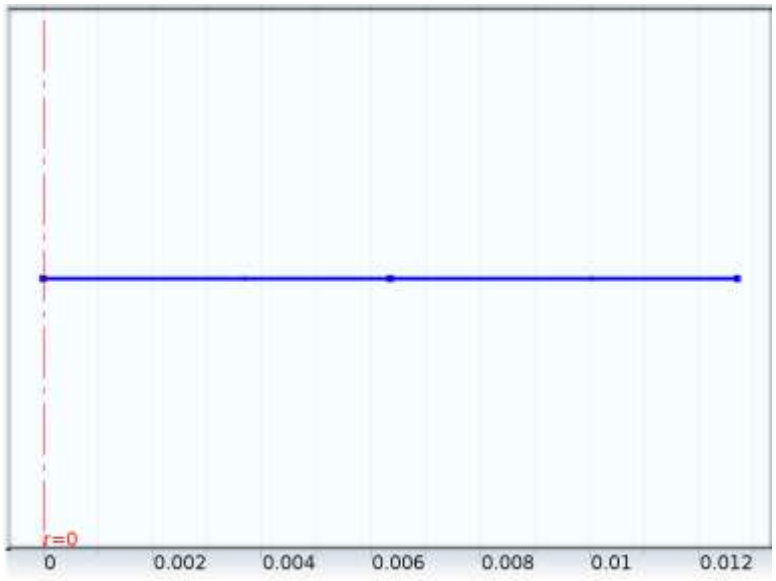

Transport of Concentrated Species

Selection

Geometric entity level	Domain
Selection	Domains 1–2

Equations

$$\rho\frac{\partial \omega_i}{\partial t} + \nabla \cdot \mathbf{j}_i + \rho(\mathbf{u} \cdot \nabla)\omega_i = R_i$$

$$\mathbf{N}_i = \mathbf{j}_i + \rho\mathbf{u}\omega_i$$

$$\mathbf{j}_i = -\left(\rho D_i^f \nabla\omega_i + \rho\omega_i D_i^f \frac{\nabla M_n}{M_n} + D_i^T \frac{\nabla T}{T}\right)$$

$$M_n = \left(\sum_i \frac{\omega_i}{M_i}\right)^{-1}$$

Settings

Description	Value
Value type when using splitting of complex variables	Complex
Diffusion model	Fick's law
From mass constraint	wg
Show equation assuming	std1/time

2.5.1 Convection and Diffusion

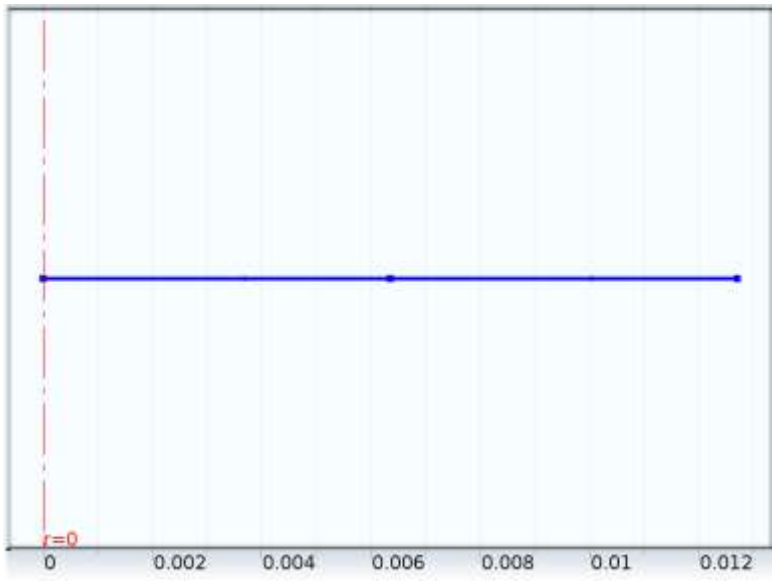

Convection and Diffusion

Selection

Geometric entity level	Domain
Selection	Domains 1–2

Equations

$$\rho\frac{\partial\omega_i}{\partial t}+\nabla\cdot\mathbf{j}_i+\rho(\mathbf{u}\cdot\nabla)\omega_i=R_i$$

$$\mathbf{N}_i=\mathbf{j}_i+\rho\mathbf{u}\omega_i$$

$$\mathbf{j}_i=-\left(\rho D_i^f\nabla\omega_i+\rho\omega_i D_i^f\frac{\nabla M_n}{M_n}+D_i^T\frac{\nabla T}{T}\right)$$

$$M_n = \left(\sum_i \frac{\omega_i}{M_i} \right)^{-1}$$

Settings

Settings

Description	Value
Velocity field	{V/phi + eps, 0, 0}
Molar mass	{28.0134[g/mol], M_g, M_t}
Density	phi*rho_v
Mixture density	User defined
Maxwell-Stefan diffusivity matrix	{{1e-5[m^2/s], 1e-5[m^2/s], 1e-5[m^2/s]}, {1e-5[m^2/s], 1e-5[m^2/s], 1e-5[m^2/s]}, {1e-5[m^2/s], 1e-5[m^2/s], 1e-5[m^2/s]}}
Diffusion coefficient	{{{eps, 0, 0}, {0, eps, 0}, {0, 0, eps}}, {{eps, 0, 0}, {0, eps, 0}, {0, 0, eps}}, {{eps, 0, 0}, {0, eps, 0}, {0, 0, eps}}}

Variables

Name	Expression	Unit	Description	Selection
wg	1 - wN2 - wt	1	Mass fraction	Domains 1–2
chcs.M_wN2	28.0134[g/mol]	kg/mol	Molar mass	Domains 1–2
chcs.M_wg	M_g	kg/mol	Molar mass	Domains 1–

Name	Expression	Unit	Description	Selection
				2
chcs.M_wt	M_t	kg/mol	Molar mass	Domains 1–2
chcs.rho	phi*rho_v	kg/m^3	Density	Domains 1–2
chcs.Mn	1/(chcs.wrwN2/chcs.M_wN2 + chcs.wrwg/chcs.M_wg + chcs.wrwt/chcs.M_wt)	kg/mol	Mean molar mass	Domains 1–2
chcs.tfluxr_wN2	chcs.dfluxr_wN2 + chcs.cfluxr_wN2	kg/(m^2*s)	Total flux, r component	Domains 1–2
chcs.tfluxphi_wN2	chcs.dfluxphi_wN2 + chcs.cfluxphi_wN2	kg/(m^2*s)	Total flux, phi component	Domains 1–2
chcs.tfluxz_wN2	chcs.dfluxz_wN2 + chcs.cfluxz_wN2	kg/(m^2*s)	Total flux, z component	Domains 1–2
chcs.x_wN2	chcs.wrwN2*chcs.Mn/chcs.M_wN2	1	Mole fraction	Domains 1–2
chcs.ndflux_wN2	chcs.nr*chcs.dfluxr_wN2 + chcs.nphi*chcs.dfluxphi_wN2 +	kg/(m^2*s)	Normal diffusive flux	Boundaries 1–3

Name	Expression	Unit	Description	Selection
	chcs.nz*chcs.dfluxz_wN2			
chcs.ntflux_wN2	chcs.nr*chcs.tfluxr_wN2 + chcs.nphi*chcs.tfluxphi_wN2 + chcs.nz*chcs.tfluxz_wN2	kg/(m^2*s)	Normal total flux	Boundaries 1–3
chcs.Vdr_wN2	chcs.dfluxr_wN2/(chcs.rho*chcs.wrwN2)	m/s	Diffusion velocity, r component	Domains 1–2
chcs.Vdphi_wN2	chcs.dfluxphi_wN2/(chcs.rho*chcs.wrwN2)	m/s	Diffusion velocity, phi component	Domains 1–2
chcs.Vdz_wN2	chcs.dfluxz_wN2/(chcs.rho*chcs.wrwN2)	m/s	Diffusion velocity, z component	Domains 1–2
chcs.dfluxMag_wN2	sqrt(chcs.dfluxr_wN2^2 + chcs.dfluxphi_wN2^2 + chcs.dfluxz_wN2^2)	kg/(m^2*s)	Diffusive flux magnitude	Domains 1–2
chcs.tfluxMag_wN2	sqrt(chcs.tfluxr_wN2^2 + chcs.tfluxphi_wN2^2 + chcs.tfluxz_wN2^2)	kg/(m^2*s)	Total flux magnitude	Domains 1–2
chcs.TfluxMag_	sqrt(chcs.Tflux_r_wN2^2	kg/(m^2*s)	Thermal	Domains 1–

Name	Expression	Unit	Description	Selection
wN2	+ chcs.Tflux_phi_wN2^2 + chcs.Tflux_z_wN2^2)		diffusion flux magnitude	2
chcs.vTr_wN2	chcs.Tflux_r_wN2/(chcs.rho*chcs.wrwN2)	m/s	Thermal drift velocity, r component	Domains 1–2
chcs.vTphi_wN2	chcs.Tflux_phi_wN2/(chcs.rho*chcs.wrwN2)	m/s	Thermal drift velocity, phi component	Domains 1–2
chcs.vTz_wN2	chcs.Tflux_z_wN2/(chcs.rho*chcs.wrwN2)	m/s	Thermal drift velocity, z component	Domains 1–2
chcs.gradr_wN2	d(chcs.wrwN2, r)	1/m	Concentration gradient, r component	Domains 1–2
chcs.gradphi_wN2	0	1/m	Concentration gradient, phi component	Domains 1–2
chcs.gradz_wN2	0	1/m	Concentration gradient, z component	Domains 1–2
chcs.c_wN2	chcs.wrwN2*chcs.rho/chcs	mol/m^3	Molar	Domains 1–

Name	Expression	Unit	Description	Selection
	.M_wN2		concentration	2
chcs.n_wN2	chcs.wrwN2*N_A_const*chcs.rho/chcs.M_wN2	1/m^3	Number density	Domains 1–2
chcs.mdfluxMag_wN2	sqrt(chcs.mdfluxr_wN2^2 + chcs.mdfluxphi_wN2^2 + chcs.mdfluxz_wN2^2)	kg/(m^2*s)	Molecular diffusive flux magnitude	Domains 1–2
chcs.tfluxr_wg	chcs.dfluxr_wg + chcs.cfluxr_wg	kg/(m^2*s)	Total flux, r component	Domains 1–2
chcs.tfluxphi_wg	chcs.dfluxphi_wg + chcs.cfluxphi_wg	kg/(m^2*s)	Total flux, phi component	Domains 1–2
chcs.tfluxz_wg	chcs.dfluxz_wg + chcs.cfluxz_wg	kg/(m^2*s)	Total flux, z component	Domains 1–2
chcs.x_wg	chcs.wrwg*chcs.Mn/chcs.M_wg	1	Mole fraction	Domains 1–2
chcs.ndflux_wg	chcs.nr*chcs.dfluxr_wg + chcs.nphi*chcs.dfluxphi_wg + chcs.nz*chcs.dfluxz_wg	kg/(m^2*s)	Normal diffusive flux	Boundaries 1–3
chcs.ntflux_wg	chcs.nr*chcs.tfluxr_wg + chcs.nphi*chcs.tfluxphi_wg +	kg/(m^2*s)	Normal total flux	Boundaries 1–3

Name	Expression	Unit	Description	Selection
	chcs.nz*chcs.tfluxz_wg			
chcs.Vdr_wg	chcs.dfluxr_wg/(chcs.rho*chcs.wrwg)	m/s	Diffusion velocity, r component	Domains 1–2
chcs.Vdphi_wg	chcs.dfluxphi_wg/(chcs.rho*chcs.wrwg)	m/s	Diffusion velocity, phi component	Domains 1–2
chcs.Vdz_wg	chcs.dfluxz_wg/(chcs.rho*chcs.wrwg)	m/s	Diffusion velocity, z component	Domains 1–2
chcs.dfluxMag_wg	sqrt(chcs.dfluxr_wg^2 + chcs.dfluxphi_wg^2 + chcs.dfluxz_wg^2)	kg/(m^2*s)	Diffusive flux magnitude	Domains 1–2
chcs.tfluxMag_wg	sqrt(chcs.tfluxr_wg^2 + chcs.tfluxphi_wg^2 + chcs.tfluxz_wg^2)	kg/(m^2*s)	Total flux magnitude	Domains 1–2
chcs.TfluxMag_wg	sqrt(chcs.Tflux_r_wg^2 + chcs.Tflux_phi_wg^2 + chcs.Tflux_z_wg^2)	kg/(m^2*s)	Thermal diffusion flux magnitude	Domains 1–2
chcs.vTr_wg	chcs.Tflux_r_wg/(chcs.rho*chcs.wrwg)	m/s	Thermal drift velocity, r	Domains 1–2

Name	Expression	Unit	Description	Selection
			component	
chcs.vTphi_wg	chcs.Tflux_phi_wg/(chcs.rho*chcs.wrwg)	m/s	Thermal drift velocity, phi component	Domains 1–2
chcs.vTz_wg	chcs.Tflux_z_wg/(chcs.rho*chcs.wrwg)	m/s	Thermal drift velocity, z component	Domains 1–2
chcs.gradr_wg	d(chcs.wrwg, r)	1/m	Concentration gradient, r component	Domains 1–2
chcs.gradphi_wg	0	1/m	Concentration gradient, phi component	Domains 1–2
chcs.gradz_wg	0	1/m	Concentration gradient, z component	Domains 1–2
chcs.c_wg	chcs.wrwg*chcs.rho/chcs.M_wg	mol/m^3	Molar concentration	Domains 1–2
chcs.n_wg	chcs.wrwg*N_A_const*chcs.rho/chcs.M_wg	1/m^3	Number density	Domains 1–2
chcs.mdfluxMa	sqrt(chcs.mdfluxr_wg^2 +	kg/(m^2*s)	Molecular	Domains 1–

Name	Expression	Unit	Description	Selection
g_wg	chcs.mdfluxphi_wg^2 + chcs.mdfluxz_wg^2)		diffusive flux magnitude	2
chcs.tfluxr_wt	chcs.dfluxr_wt + chcs.cfluxr_wt	kg/(m^2*s)	Total flux, r component	Domains 1–2
chcs.tfluxphi_wt	chcs.dfluxphi_wt + chcs.cfluxphi_wt	kg/(m^2*s)	Total flux, phi component	Domains 1–2
chcs.tfluxz_wt	chcs.dfluxz_wt + chcs.cfluxz_wt	kg/(m^2*s)	Total flux, z component	Domains 1–2
chcs.x_wt	chcs.wrwt*chcs.Mn/chcs.M_wt	1	Mole fraction	Domains 1–2
chcs.ndflux_wt	chcs.nr*chcs.dfluxr_wt + chcs.nphi*chcs.dfluxphi_wt + chcs.nz*chcs.dfluxz_wt	kg/(m^2*s)	Normal diffusive flux	Boundaries 1–3
chcs.ntflux_wt	chcs.nr*chcs.tfluxr_wt + chcs.nphi*chcs.tfluxphi_wt + chcs.nz*chcs.tfluxz_wt	kg/(m^2*s)	Normal total flux	Boundaries 1–3
chcs.Vdr_wt	chcs.dfluxr_wt/(chcs.rho*chcs.wrwt)	m/s	Diffusion velocity, r component	Domains 1–2
chcs.Vdphi_wt	chcs.dfluxphi_wt/(chcs.rho*chcs.wrwt)	m/s	Diffusion velocity, phi	Domains 1–2

Name	Expression	Unit	Description	Selection
			component	
chcs.Vdz_wt	chcs.dfluxz_wt/(chcs.rho*chcs.wrwt)	m/s	Diffusion velocity, z component	Domains 1–2
chcs.dfluxMag_wt	sqrt(chcs.dfluxr_wt^2 + chcs.dfluxphi_wt^2 + chcs.dfluxz_wt^2)	kg/(m^2*s)	Diffusive flux magnitude	Domains 1–2
chcs.tfluxMag_wt	sqrt(chcs.tfluxr_wt^2 + chcs.tfluxphi_wt^2 + chcs.tfluxz_wt^2)	kg/(m^2*s)	Total flux magnitude	Domains 1–2
chcs.TfluxMag_wt	sqrt(chcs.Tflux_r_wt^2 + chcs.Tflux_phi_wt^2 + chcs.Tflux_z_wt^2)	kg/(m^2*s)	Thermal diffusion flux magnitude	Domains 1–2
chcs.vTr_wt	chcs.Tflux_r_wt/(chcs.rho*chcs.wrwt)	m/s	Thermal drift velocity, r component	Domains 1–2
chcs.vTphi_wt	chcs.Tflux_phi_wt/(chcs.rho*chcs.wrwt)	m/s	Thermal drift velocity, phi component	Domains 1–2
chcs.vTz_wt	chcs.Tflux_z_wt/(chcs.rho*chcs.wrwt)	m/s	Thermal drift velocity, z	Domains 1–2

Name	Expression	Unit	Description	Selection
			component	
chcs.gradr_wt	d(chcs.wrwt, r)	1/m	Concentration gradient, r component	Domains 1–2
chcs.gradphi_wt	0	1/m	Concentration gradient, phi component	Domains 1–2
chcs.gradz_wt	0	1/m	Concentration gradient, z component	Domains 1–2
chcs.c_wt	chcs.wrwt*chcs.rho/chcs.M_wt	mol/m^3	Molar concentration	Domains 1–2
chcs.n_wt	chcs.wrwt*N_A_const*chcs.rho/chcs.M_wt	1/m^3	Number density	Domains 1–2
chcs.mdfluxMag_wt	sqrt(chcs.mdfluxr_wt^2 + chcs.mdfluxphi_wt^2 + chcs.mdfluxz_wt^2)	kg/(m^2*s)	Molecular diffusive flux magnitude	Domains 1–2
chcs.u	model.input.u1	m/s	Velocity field, r component	Domains 1–2
chcs.v	model.input.u2	m/s	Velocity field, phi component	Domains 1–2

Name	Expression	Unit	Description	Selection
chcs.w	model.input.u3	m/s	Velocity field, z component	Domains 1–2
chcs.cfluxr_wN2	chcs.rho*model.input.u1*chcs.wrwN2	kg/(m^2*s)	Convective flux, r component	Domains 1–2
chcs.cfluxphi_wN2	chcs.rho*model.input.u2*chcs.wrwN2	kg/(m^2*s)	Convective flux, phi component	Domains 1–2
chcs.cfluxz_wN2	chcs.rho*model.input.u3*chcs.wrwN2	kg/(m^2*s)	Convective flux, z component	Domains 1–2
chcs.ncflux_wN2	chcs.nr*chcs.cfluxr_wN2 + chcs.nphi*chcs.cfluxphi_wN2 + chcs.nz*chcs.cfluxz_wN2	kg/(m^2*s)	Normal convective flux	Boundaries 1–3
chcs.cfluxMag_wN2	sqrt(chcs.cfluxr_wN2^2 + chcs.cfluxphi_wN2^2 + chcs.cfluxz_wN2^2)	kg/(m^2*s)	Convective flux magnitude	Domains 1–2
chcs.cbf_wN2	0	kg/(m^2*s)	Convective boundary flux	Boundaries 1–3
chcs.cfluxr_wg	chcs.rho*model.input.u1*c	kg/(m^2*s)	Convective	Domains 1–

Name	Expression	Unit	Description	Selection
	hcs.wrwg		flux, r component	2
chcs.cfluxphi_wg	chcs.rho*model.input.u2*chcs.wrwg	kg/(m^2*s)	Convective flux, phi component	Domains 1–2
chcs.cfluxz_wg	chcs.rho*model.input.u3*chcs.wrwg	kg/(m^2*s)	Convective flux, z component	Domains 1–2
chcs.ncflux_wg	chcs.nr*chcs.cfluxr_wg + chcs.nphi*chcs.cfluxphi_wg + chcs.nz*chcs.cfluxz_wg	kg/(m^2*s)	Normal convective flux	Boundaries 1–3
chcs.cfluxMag_wg	sqrt(chcs.cfluxr_wg^2 + chcs.cfluxphi_wg^2 + chcs.cfluxz_wg^2)	kg/(m^2*s)	Convective flux magnitude	Domains 1–2
chcs.cbf_wg	0	kg/(m^2*s)	Convective boundary flux	Boundaries 1–3
chcs.cfluxr_wt	chcs.rho*model.input.u1*chcs.wrwt	kg/(m^2*s)	Convective flux, r component	Domains 1–2
chcs.cfluxphi_w	chcs.rho*model.input.u2*c	kg/(m^2*s)	Convective	Domains 1–

Name	Expression	Unit	Description	Selection
t	hcs.wrwt		flux, phi component	2
chcs.cfluxz_wt	chcs.rho*model.input.u3*chcs.wrwt	kg/(m^2*s)	Convective flux, z component	Domains 1–2
chcs.ncflux_wt	chcs.nr*chcs.cfluxr_wt + chcs.nphi*chcs.cfluxphi_wt + chcs.nz*chcs.cfluxz_wt	kg/(m^2*s)	Normal convective flux	Boundaries 1–3
chcs.cfluxMag_wt	sqrt(chcs.cfluxr_wt^2 + chcs.cfluxphi_wt^2 + chcs.cfluxz_wt^2)	kg/(m^2*s)	Convective flux magnitude	Domains 1–2
chcs.cbf_wt	0	kg/(m^2*s)	Convective boundary flux	Boundaries 1–3
chcs.T	model.input.minput_temperature	K	Temperature	Domains 1–2
chcs.Dfrr_wN2	eps	m^2/s	Diffusion coefficient, rr component	Domains 1–2
chcs.Dfphir_wN2	0	m^2/s	Diffusion coefficient, phir	Domains 1–2

Name	Expression	Unit	Description	Selection
			component	
chcs.Dfzr_wN2	0	m^2/s	Diffusion coefficient, zr component	Domains 1–2
chcs.Dfrphi_wN2	0	m^2/s	Diffusion coefficient, rphi component	Domains 1–2
chcs.Dfphiphi_wN2	eps	m^2/s	Diffusion coefficient, phiphi component	Domains 1–2
chcs.Dfzphi_wN2	0	m^2/s	Diffusion coefficient, zphi component	Domains 1–2
chcs.Dfrz_wN2	0	m^2/s	Diffusion coefficient, rz component	Domains 1–2
chcs.Dfphiz_wN2	0	m^2/s	Diffusion coefficient,	Domains 1–2

Name	Expression	Unit	Description	Selection
			phiz component	
chcs.Dfzz_wN2	eps	m^2/s	Diffusion coefficient, zz component	Domains 1–2
chcs.Dav_wN2	chcs.Dfrr_wN2	m^2/s	Average diffusion coefficient	Domains 1–2
chcs.DT_wN2	0	kg/(m*s)	Thermal diffusion coefficient	Domains 1–2
chcs.jr_wN2	-chcs.rho*chcs.Dfrr_wN2*wN2r - chcs.rho*wN2*chcs.Dfrr_wN2*d(chcs.Mn, r)/chcs.Mn - chcs.DT_wN2*d(model.input.minput_temperature, r)/model.input.minput_temperature	kg/(m^2*s)	Diffusive flux vector, r component	Domains 1–2

Name	Expression	Unit	Description	Selection
chcs.jphi_wN2	chcs.rho*chcs.Dfphir_wN2*(-wN2r - wN2*d(chcs.Mn, r)/chcs.Mn)	kg/(m^2*s)	Diffusive flux vector, phi component	Domains 1–2
chcs.jz_wN2	chcs.rho*chcs.Dfzr_wN2*(-wN2r - wN2*d(chcs.Mn, r)/chcs.Mn)	kg/(m^2*s)	Diffusive flux vector, z component	Domains 1–2
chcs.dfluxr_wN2	-chcs.rho*chcs.Dfrr_wN2*wN2r - chcs.rho*wN2*chcs.Dfrr_wN2*d(chcs.Mn, r)/chcs.Mn - chcs.DT_wN2*d(model.input.minput_temperature, r)/model.input.minput_temperature	kg/(m^2*s)	Diffusive flux, r component	Domains 1–2
chcs.dfluxphi_wN2	chcs.rho*chcs.Dfphir_wN2*(-wN2r - wN2*d(chcs.Mn, r)/chcs.Mn)	kg/(m^2*s)	Diffusive flux, phi component	Domains 1–2

Name	Expression	Unit	Description	Selection
chcs.dfluxz_wN2	chcs.rho*chcs.Dfzr_wN2*(-wN2r - wN2*d(chcs.Mn, r)/chcs.Mn)	kg/(m^2*s)	Diffusive flux, z component	Domains 1–2
chcs.mdfluxr_wN2	chcs.rho*chcs.Dfrr_wN2*(wN2r + wN2*d(chcs.Mn, r)/chcs.Mn)	kg/(m^2*s)	Molecular diffusive flux, r component	Domains 1–2
chcs.mdfluxphi_wN2	chcs.rho*chcs.Dfphir_wN2*(wN2r + wN2*d(chcs.Mn, r)/chcs.Mn)	kg/(m^2*s)	Molecular diffusive flux, phi component	Domains 1–2
chcs.mdfluxz_wN2	chcs.rho*chcs.Dfzr_wN2*(wN2r + wN2*d(chcs.Mn, r)/chcs.Mn)	kg/(m^2*s)	Molecular diffusive flux, z component	Domains 1–2
chcs.Tflux_r_wN2	-chcs.DT_wN2*d(model.input.minput_temperature, r)/model.input.minput_temperature	kg/(m^2*s)	Thermal diffusion flux, r component	Domains 1–2
chcs.Tflux_phi_wN2	0	kg/(m^2*s)	Thermal diffusion flux, phi component	Domains 1–2

Name	Expression	Unit	Description	Selection
chcs.Tflux_z_wN2	0	kg/(m^2*s)	Thermal diffusion flux, z component	Domains 1–2
chcs.Dfrr_wg	eps	m^2/s	Diffusion coefficient, rr component	Domains 1–2
chcs.Dfphir_wg	0	m^2/s	Diffusion coefficient, phir component	Domains 1–2
chcs.Dfzr_wg	0	m^2/s	Diffusion coefficient, zr component	Domains 1–2
chcs.Dfrphi_wg	0	m^2/s	Diffusion coefficient, rphi component	Domains 1–2
chcs.Dfphiphi_wg	eps	m^2/s	Diffusion coefficient, phiphi component	Domains 1–2

Name	Expression	Unit	Description	Selection
chcs.Dfzphi_wg	0	m^2/s	Diffusion coefficient, zphi component	Domains 1–2
chcs.Dfrz_wg	0	m^2/s	Diffusion coefficient, rz component	Domains 1–2
chcs.Dfphiz_wg	0	m^2/s	Diffusion coefficient, phiz component	Domains 1–2
chcs.Dfzz_wg	eps	m^2/s	Diffusion coefficient, zz component	Domains 1–2
chcs.Dav_wg	chcs.Dfrr_wg	m^2/s	Average diffusion coefficient	Domains 1–2
chcs.DT_wg	0	kg/(m*s)	Thermal diffusion coefficient	Domains 1–2
chcs.jr_wg	-	kg/(m^2*s)	Diffusive flux	Domains 1–

Name	Expression	Unit	Description	Selection
	chcs.rho*chcs.Dfrr_wg*d(wg, r) - chcs.rho*wg*chcs.Dfrr_wg*d(chcs.Mn, r)/chcs.Mn - chcs.DT_wg*d(model.input.minput_temperature, r)/model.input.minput_temperature		vector, r component	2
chcs.jphi_wg	chcs.rho*chcs.Dfphir_wg*(-d(wg, r) - wg*d(chcs.Mn, r)/chcs.Mn)	kg/(m^2*s)	Diffusive flux vector, phi component	Domains 1–2
chcs.jz_wg	chcs.rho*chcs.Dfzr_wg*(-d(wg, r) - wg*d(chcs.Mn, r)/chcs.Mn)	kg/(m^2*s)	Diffusive flux vector, z component	Domains 1–2
chcs.dfluxr_wg	- chcs.rho*chcs.Dfrr_wg*d(wg, r) - chcs.rho*wg*chcs.Dfrr_wg*d(chcs.Mn, r)/chcs.Mn - chcs.DT_wg*d(model.input.minput_temperature,	kg/(m^2*s)	Diffusive flux, r component	Domains 1–2

Name	Expression	Unit	Description	Selection
	r)/model.input.minput_temperature			
chcs.dfluxphi_wg	chcs.rho*chcs.Dfphir_wg*(-d(wg, r) - wg*d(chcs.Mn, r)/chcs.Mn)	kg/(m^2*s)	Diffusive flux, phi component	Domains 1–2
chcs.dfluxz_wg	chcs.rho*chcs.Dfzr_wg*(-d(wg, r) - wg*d(chcs.Mn, r)/chcs.Mn)	kg/(m^2*s)	Diffusive flux, z component	Domains 1–2
chcs.mdfluxr_wg	chcs.rho*chcs.Dfrr_wg*(d(wg, r) + wg*d(chcs.Mn, r)/chcs.Mn)	kg/(m^2*s)	Molecular diffusive flux, r component	Domains 1–2
chcs.mdfluxphi_wg	chcs.rho*chcs.Dfphir_wg*(d(wg, r) + wg*d(chcs.Mn, r)/chcs.Mn)	kg/(m^2*s)	Molecular diffusive flux, phi component	Domains 1–2
chcs.mdfluxz_wg	chcs.rho*chcs.Dfzr_wg*(d(wg, r) + wg*d(chcs.Mn, r)/chcs.Mn)	kg/(m^2*s)	Molecular diffusive flux, z component	Domains 1–2
chcs.Tflux_r_wg	-chcs.DT_wg*d(model.input.minput_temperature, r)/model.input.minput_tem	kg/(m^2*s)	Thermal diffusion flux, r component	Domains 1–2

Name	Expression	Unit	Description	Selection
	perature			
chcs.Tflux_phi_wg	0	kg/(m^2*s)	Thermal diffusion flux, phi component	Domains 1–2
chcs.Tflux_z_wg	0	kg/(m^2*s)	Thermal diffusion flux, z component	Domains 1–2
chcs.Dfrr_wt	eps	m^2/s	Diffusion coefficient, rr component	Domains 1–2
chcs.Dfphir_wt	0	m^2/s	Diffusion coefficient, phir component	Domains 1–2
chcs.Dfzr_wt	0	m^2/s	Diffusion coefficient, zr component	Domains 1–2
chcs.Dfrphi_wt	0	m^2/s	Diffusion coefficient, rphi component	Domains 1–2

Name	Expression	Unit	Description	Selection
chcs.Dfphiphi_wt	eps	m^2/s	Diffusion coefficient, phiphi component	Domains 1–2
chcs.Dfzphi_wt	0	m^2/s	Diffusion coefficient, zphi component	Domains 1–2
chcs.Dfrz_wt	0	m^2/s	Diffusion coefficient, rz component	Domains 1–2
chcs.Dfphiz_wt	0	m^2/s	Diffusion coefficient, phiz component	Domains 1–2
chcs.Dfzz_wt	eps	m^2/s	Diffusion coefficient, zz component	Domains 1–2
chcs.Dav_wt	chcs.Dfrr_wt	m^2/s	Average diffusion coefficient	Domains 1–2

Name	Expression	Unit	Description	Selection
chcs.DT_wt	0	kg/(m*s)	Thermal diffusion coefficient	Domains 1–2
chcs.jr_wt	-chcs.rho*chcs.Dfrr_wt*wtr-chcs.rho*wt*chcs.Dfrr_wt*d(chcs.Mn, r)/chcs.Mn - chcs.DT_wt*d(model.input.minput_temperature, r)/model.input.minput_temperature	kg/(m^2*s)	Diffusive flux vector, r component	Domains 1–2
chcs.jphi_wt	chcs.rho*chcs.Dfphir_wt*(-wtr - wt*d(chcs.Mn, r)/chcs.Mn)	kg/(m^2*s)	Diffusive flux vector, phi component	Domains 1–2
chcs.jz_wt	chcs.rho*chcs.Dfzr_wt*(-wtr - wt*d(chcs.Mn, r)/chcs.Mn)	kg/(m^2*s)	Diffusive flux vector, z component	Domains 1–2
chcs.dfluxr_wt	-chcs.rho*chcs.Dfrr_wt*wtr-	kg/(m^2*s)	Diffusive flux, r component	Domains 1–2

Name	Expression	Unit	Description	Selection
	chcs.rho*wt*chcs.Dfrr_wt*d(chcs.Mn, r)/chcs.Mn - chcs.DT_wt*d(model.input.minput_temperature, r)/model.input.minput_temperature			
chcs.dfluxphi_wt	chcs.rho*chcs.Dfphir_wt*(-wtr - wt*d(chcs.Mn, r)/chcs.Mn)	kg/(m^2*s)	Diffusive flux, phi component	Domains 1–2
chcs.dfluxz_wt	chcs.rho*chcs.Dfzr_wt*(-wtr - wt*d(chcs.Mn, r)/chcs.Mn)	kg/(m^2*s)	Diffusive flux, z component	Domains 1–2
chcs.mdfluxr_wt	chcs.rho*chcs.Dfrr_wt*(wtr + wt*d(chcs.Mn, r)/chcs.Mn)	kg/(m^2*s)	Molecular diffusive flux, r component	Domains 1–2
chcs.mdfluxphi_wt	chcs.rho*chcs.Dfphir_wt*(wtr + wt*d(chcs.Mn, r)/chcs.Mn)	kg/(m^2*s)	Molecular diffusive flux, phi component	Domains 1–2
chcs.mdfluxz_wt	chcs.rho*chcs.Dfzr_wt*(wtr + wt*d(chcs.Mn, r)/chcs.Mn)	kg/(m^2*s)	Molecular diffusive flux, z component	Domains 1–2

Name	Expression	Unit	Description	Selection
chcs.Tflux_r_wt	-chcs.DT_wt*d(model.input.minput_temperature, r)/model.input.minput_temperature	kg/(m^2*s)	Thermal diffusion flux, r component	Domains 1–2
chcs.Tflux_phi_wt	0	kg/(m^2*s)	Thermal diffusion flux, phi component	Domains 1–2
chcs.Tflux_z_wt	0	kg/(m^2*s)	Thermal diffusion flux, z component	Domains 1–2
chcs.V	model.input.V	V	Electric potential	Domains 1–2
chcs.helem	h	m	Element size	Domains 1–2
chcs.glim	1.0E-6/chcs.helem	mol/m^4	Lower gradient limit	Domains 1–2
chcs.Ck	0.5	1	Tuning parameter	Domains 1–2
chcs.Res_wN2	d(-wN2*chcs.rho*chcs.Dfrr_	kg/(m^3*s)	Equation residual	Domains 1–2

Name	Expression	Unit	Description	Selection
	wN2*d(chcs.Mn, r)/chcs.Mn, r) + if(abs(r)<0.0010*h, d(-wN2*chcs.rho*chcs.Dfrr_wN2*d(chcs.Mn, r)/chcs.Mn, r), -wN2*chcs.rho*chcs.Dfrr_wN2*d(chcs.Mn, r)/(chcs.Mn*r)) + chcs.rho*chcs.u*wN2r + d(-chcs.DT_wN2*d(chcs.T, r)/chcs.T, r) + if(abs(r)<0.0010*h, d(-chcs.DT_wN2*d(chcs.T, r)/chcs.T, r), -chcs.DT_wN2*d(chcs.T, r)/(chcs.T*r)) - chcs.R_wN2			
chcs.Res_wt	d(-wt*chcs.rho*chcs.Dfrr_wt	kg/(m^3*s)	Equation residual	Domains 1–2

Name	Expression	Unit	Description	Selection
	*d(chcs.Mn, r)/chcs.Mn, r) + if(abs(r)<0.0010*h, d(-wt*chcs.rho*chcs.Dfrr_wt *d(chcs.Mn, r)/chcs.Mn, r), - wt*chcs.rho*chcs.Dfrr_wt *d(chcs.Mn, r)/(chcs.Mn*r)) + chcs.rho*chcs.u*wtr + d(-chcs.DT_wt*d(chcs.T, r)/chcs.T, r) + if(abs(r)<0.0010*h, d(-chcs.DT_wt*d(chcs.T, r)/chcs.T, r), - chcs.DT_wt*d(chcs.T, r)/(chcs.T*r)) - chcs.R_wt			

2.5.2 Axial Symmetry 1

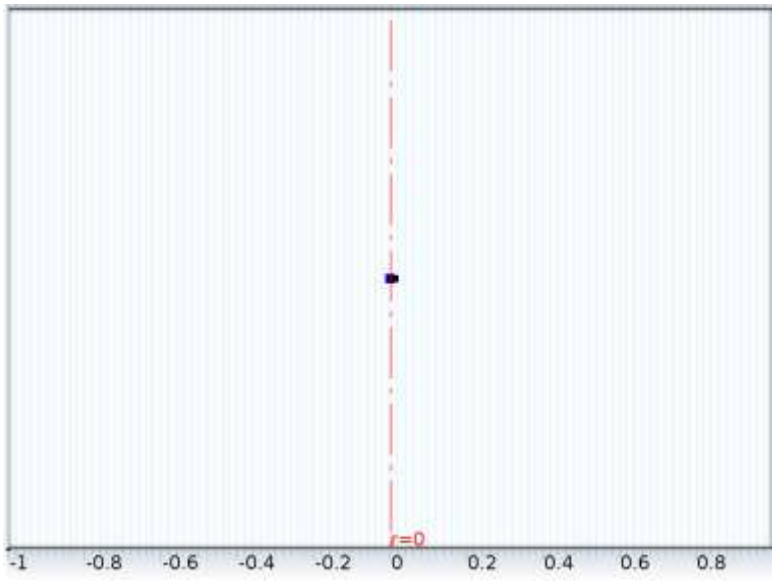

Axial Symmetry 1

Selection

Geometric entity level	Boundary
Selection	Boundary 1

2.5.3 No Flux 1

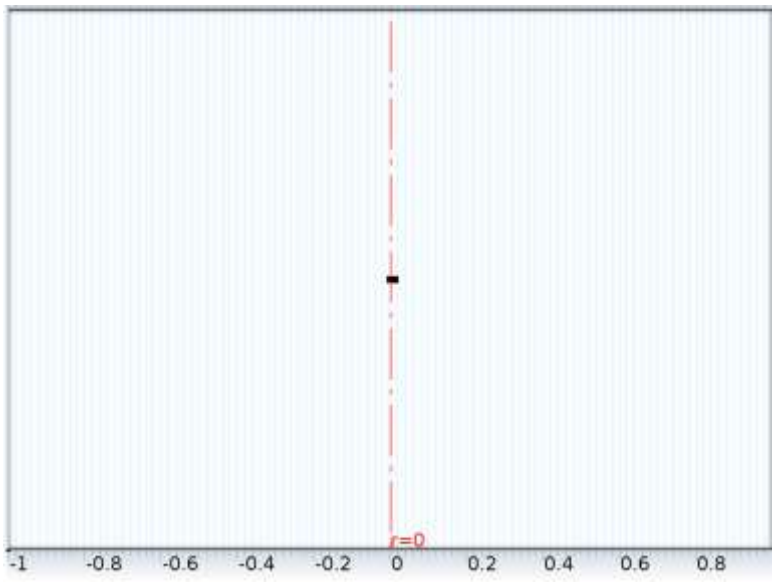

No Flux 1

Selection

Geometric entity level	Boundary
Selection	No boundaries

Equations

$$-\mathbf{n} \cdot \mathbf{N}_i = 0$$

2.5.4 Initial Values 1

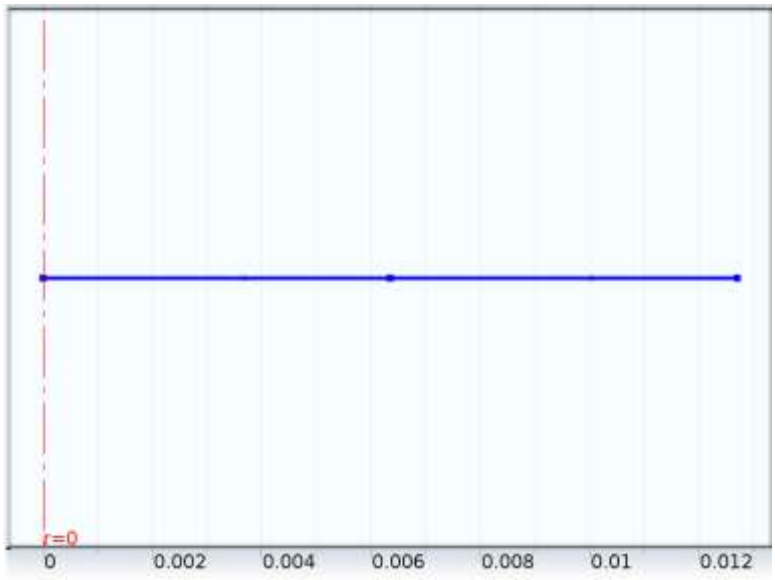

Initial Values 1

Selection

Geometric entity level	Domain
Selection	Domains 1–2

Settings

Settings

Description	Value
Mass fraction	0

Description	Value
Mass fraction	1

2.5.5 Reactions 1

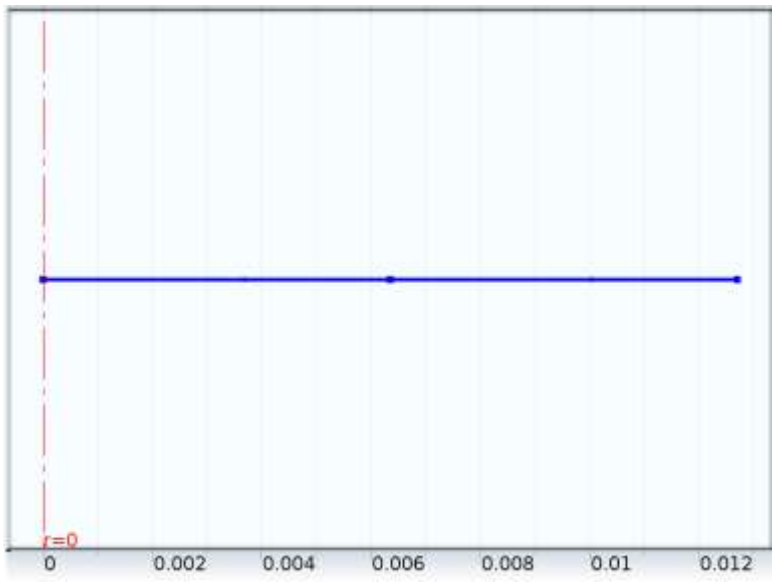

Reactions 1

Selection

Geometric entity level	Domain
Selection	Domains 1–2

Equations

Settings

Settings

Description	Value
Total rate expression	{-wN2*d(rho_v*phi, t) - (wN2/(r^2))*d((r^2)*V*rho_v, r), S_g - wg*d(rho_v*phi, t) - (wg/(r^2))*d((r^2)*V*rho_v, r), S_t - wt*d(rho_v*phi, t)

Description	Value
	- (wt/(r^2))*d((r^2)*V*rho_v, r)}
Mass transfer to other phases	1

Variables

Name	Expression	Unit	Description	Selection
chcs.R_wN2	wN2*(-d(rho_v*phi, t) - d(r^2*V*rho_v, r)/r^2)	kg/(m^3*s)	Total rate expression	Domains 1–2
chcs.R_wt	S_t - wt*d(rho_v*phi, t) - wt*d(r^2*V*rho_v, r)/r^2	kg/(m^3*s)	Total rate expression	Domains 1–2
chcs.R_wg	S_g - wg*d(rho_v*phi, t) - wg*d(r^2*V*rho_v, r)/r^2	kg/(m^3*s)	Total rate expression	Domains 1–2

2.5.6 Open Boundary 1

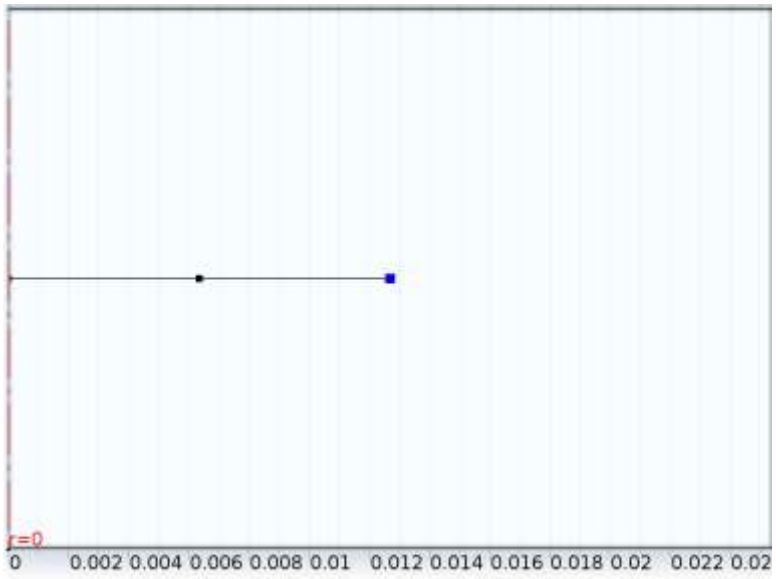

Open Boundary 1

Selection

Geometric entity level	Boundary
Selection	Boundary 3

Equations

$$\begin{cases} -\mathbf{n} \cdot \rho D_i^f \nabla \omega = 0 & \text{if } \mathbf{n} \cdot \mathbf{u} \geq 0 \\ \omega_i = \omega_{0,i} & \text{if } \mathbf{n} \cdot \mathbf{u} < 0 \end{cases}$$

Settings

Settings

Description	Value
Mass fraction	{1, 0, 0}

Variables

Name	Expression	Unit	Description	Selection
chcs.cjump_wN2	wN2 - chcs.w0_wN2	1	Concentration jump	Boundary 3
chcs.jump_pen_wN2	4*root.mod1.chcs.open1.Dphere_wN21/h	kg/(m^2*s)	Boundary condition jump penalty term	Boundary 3
chcs.Dgradcn_wN2	chcs.nrmesh*chcs.rho*chcs.Dfrr_wN2*wN2r	kg/(m^2*s)	Boundary condition help variable	Boundary 3
chcs.DTestgradcn_wN2	chcs.nrmesh*chcs.rho*chcs.Dfrr_wN2*test(wN2r)	kg/(m^2*s)	Boundary condition help variable	Boundary 3
chcs.upwind_wN2	chcs.nrmesh*chcs.rho*(chcs.u*chcs.cjump_wN2 + chcs.w0_wN2*chcs.Dfrr_wN2*d(chcs.Mn, r)/chcs.Mn)	kg/(m^2*s)	Boundary condition upwinding term	Boundary 3
chcs.cjump_wt	wt - chcs.w0_wt	1	Concentration jump	Boundary 3

Name	Expression	Unit	Description	Selection
chcs.jump_pen_wt	4*root.mod1.chcs.open1.Dphere_wt1/h	kg/(m^2*s)	Boundary condition jump penalty term	Boundary 3
chcs.Dgradcn_wt	chcs.nrmesh*chcs.rho*chcs.Dfrr_wt*wtr	kg/(m^2*s)	Boundary condition help variable	Boundary 3
chcs.DTestgradcn_wt	chcs.nrmesh*chcs.rho*chcs.Dfrr_wt*test(wtr)	kg/(m^2*s)	Boundary condition help variable	Boundary 3
chcs.upwind_wt	chcs.nrmesh*chcs.rho*(chcs.u*chcs.cjump_wt + chcs.w0_wt*chcs.Dfrr_wt*d(chcs.Mn, r)/chcs.Mn)	kg/(m^2*s)	Boundary condition upwinding term	Boundary 3
chcs.w0_wN2	1	1	Mass fraction	Boundary 3
chcs.w0_wt	0	1	Mass fraction	Boundary 3

2.6 Darcy's Law (dl)

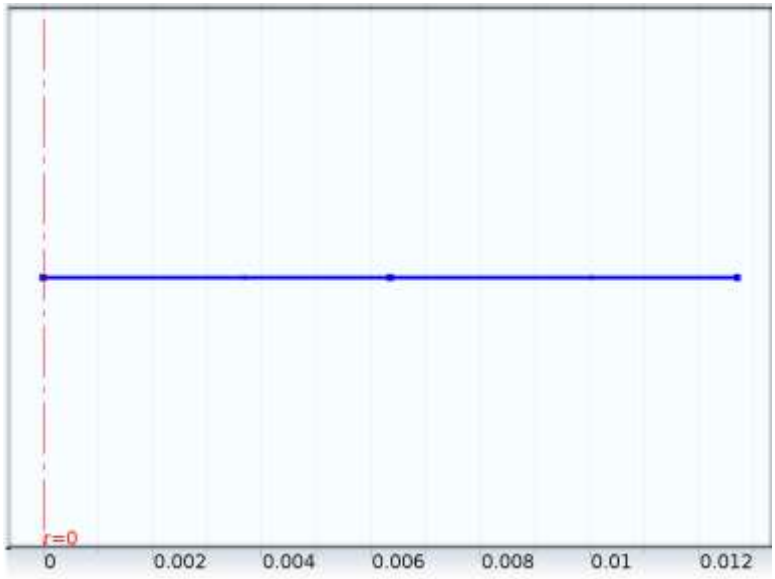

Darcy's Law

Selection

Geometric entity level	Domain
Selection	Domains 1–2

Equations

$$\frac{\partial}{\partial t}(\rho \epsilon_p) + \nabla \cdot (\rho \mathbf{u}) = Q_m$$

$$\mathbf{u} = -\frac{\kappa}{\mu}\nabla p$$

Settings

Description	Value
Value type when using splitting of complex variables	Complex
Show equation assuming	std1/time

2.6.1 Fluid and Matrix Properties 1

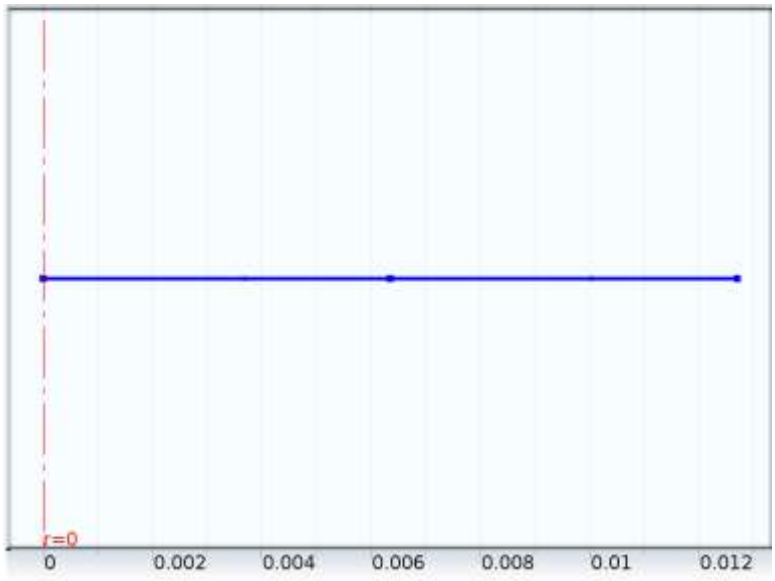

Fluid and Matrix Properties 1

Selection

Geometric entity level	Domain
Selection	Domains 1–2

Equations

$$\frac{\partial}{\partial t}(\rho\epsilon_p) + \nabla \cdot (\rho \mathbf{u}) = Q_m$$

$$\mathbf{u} = -\frac{\kappa}{\mu}\nabla p$$

Settings

Settings

Description	**Value**
Density	User defined
Density	rho_v
Dynamic viscosity	User defined

Description	Value
Dynamic viscosity	mu
Permeability	User defined
Permeability	{{B/chcs.Mn, 0, 0}, {0, B/chcs.Mn, 0}, {0, 0, B/chcs.Mn}}
Porosity	User defined
Porosity	phi/chcs.Mn

Variables

Name	Expression	Unit	Description	Selection
dl.rho	rho_v	kg/m^3	Density	Domains 1–2
dl.mu	mu	Pa*s	Dynamic viscosity	Domains 1–2
dl.u	-dl.kapparr*pr/dl.mu	m/s	Darcy's velocity field, r component	Domains 1–2
dl.v	-dl.kappaphir*pr/dl.mu	m/s	Darcy's velocity field, phi component	Domains 1–2
dl.w	-dl.kappazr*pr/dl.mu	m/s	Darcy's velocity field, z component	Domains 1–2
dl.U	sqrt(dl.u^2 + dl.v^2 + dl.w^2)	m/s	Darcy's	Domains 1–2

Name	Expression	Unit	Description	Selection
			velocity magnitude	
dl.Krr	2.94E-4[m/s]	m/s	Hydraulic conductivity, rr component	Domains 1–2
dl.Kphir	0	m/s	Hydraulic conductivity, phir component	Domains 1–2
dl.Kzr	0	m/s	Hydraulic conductivity, zr component	Domains 1–2
dl.Krphi	0	m/s	Hydraulic conductivity, rphi component	Domains 1–2
dl.Kphiphi	2.94E-4[m/s]	m/s	Hydraulic conductivity, phiphi component	Domains 1–2
dl.Kzphi	0	m/s	Hydraulic	Domains 1–2

Name	Expression	Unit	Description	Selection
			conductivity, zphi component	
dl.Krz	0	m/s	Hydraulic conductivity, rz component	Domains 1–2
dl.Kphiz	0	m/s	Hydraulic conductivity, phiz component	Domains 1–2
dl.Kzz	2.94E-4[m/s]	m/s	Hydraulic conductivity, zz component	Domains 1–2
dl.kapparr	B/chcs.Mn	m^2	Permeability, rr component	Domains 1–2
dl.kappaphir	0	m^2	Permeability, phir component	Domains 1–2
dl.kappazr	0	m^2	Permeability, zr component	Domains 1–2
dl.kapparphi	0	m^2	Permeability,	Domains 1–2

Name	Expression	Unit	Description	Selection
			rphi component	
dl.kappaphiphi	B/chcs.Mn	m^2	Permeability, phiphi component	Domains 1–2
dl.kappazphi	0	m^2	Permeability, zphi component	Domains 1–2
dl.kapparz	0	m^2	Permeability, rz component	Domains 1–2
dl.kappaphiz	0	m^2	Permeability, phiz component	Domains 1–2
dl.kappazz	B/chcs.Mn	m^2	Permeability, zz component	Domains 1–2
dl.epsilon	phi/chcs.Mn	1	Porosity	Domains 1–2

2.6.2 Axial Symmetry 1

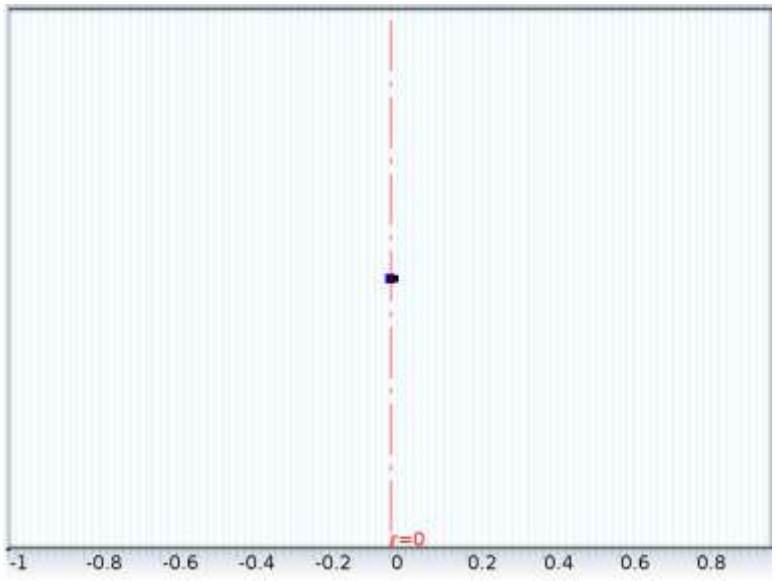

Axial Symmetry 1

Selection

Geometric entity level	Boundary
Selection	Boundary 1

2.6.3 No Flow 1

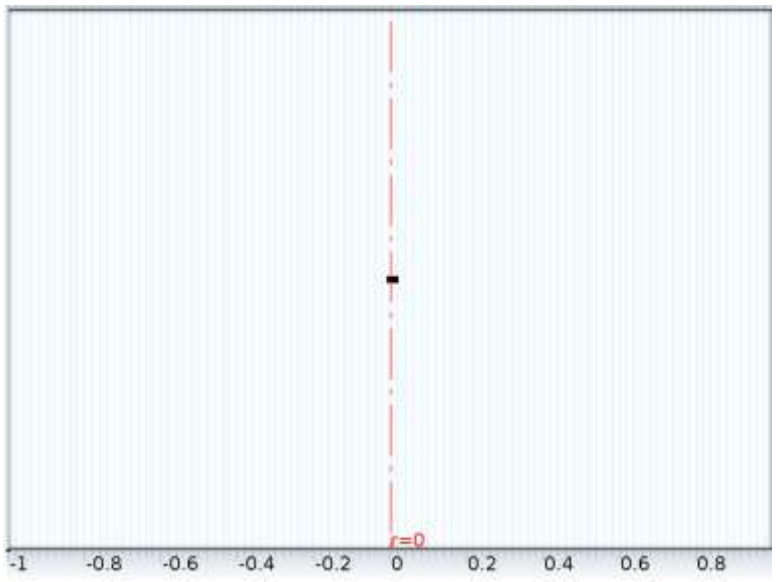

No Flow 1

Selection

Geometric entity level	Boundary
Selection	No boundaries

Equations

$$-\mathbf{n} \cdot \rho\mathbf{u} = 0$$

2.6.4 Initial Values 1

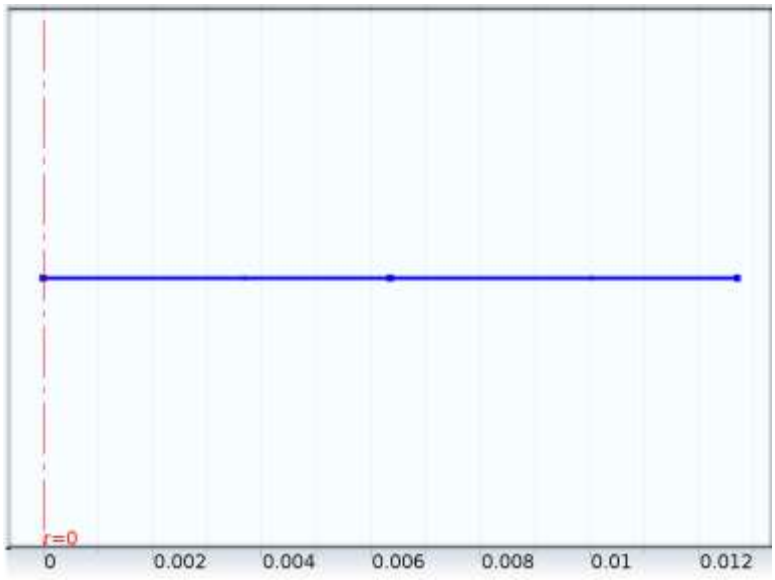

Initial Values 1

Selection

Geometric entity level	Domain
Selection	Domains 1–2

Settings

Settings

Description	Value
Pressure	101325

2.6.5 Pressure 1

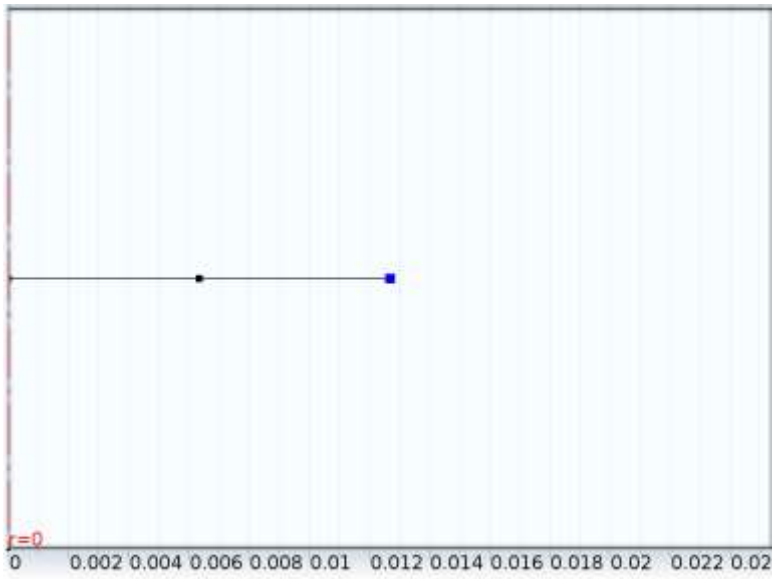

Pressure 1

Selection

Geometric entity level	Boundary
Selection	Boundary 3

Equations

$p = p_0$

Settings

Settings

Description	Value
Pressure	101325

Variables

Name	Expression	Unit	Description	Selection
dl.p0	101325	Pa	Pressure	Boundary 3

2.6.6 Mass Source 1

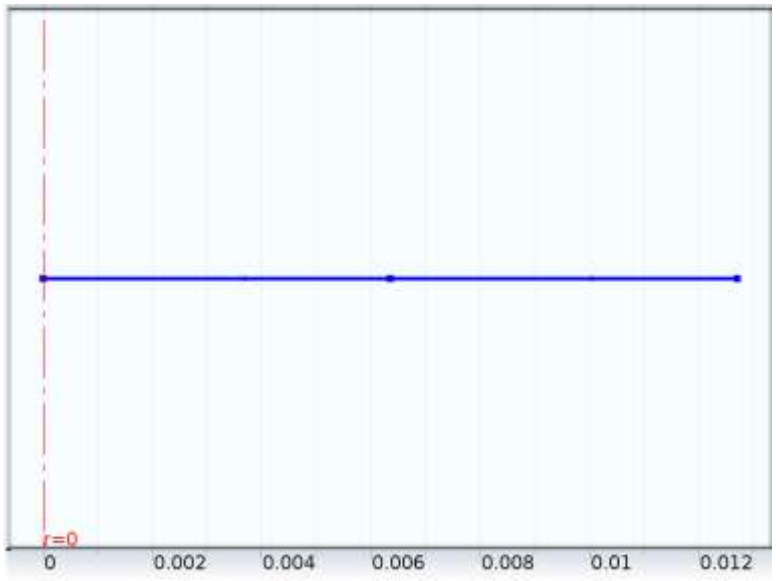

Mass Source 1

Selection

Geometric entity level	Domain
Selection	Domains 1–2

Equations

$$\frac{\partial}{\partial t}(\rho\epsilon_p) + \nabla \cdot (\rho \mathbf{u}) = \underbrace{Q_m}$$

Settings

Settings

Description	Value
Mass source	S_t/chcs.M_wt + S_g/chcs.M_wg + B*p/(r*mu*R*T)*pr

2.7 Mesh 1

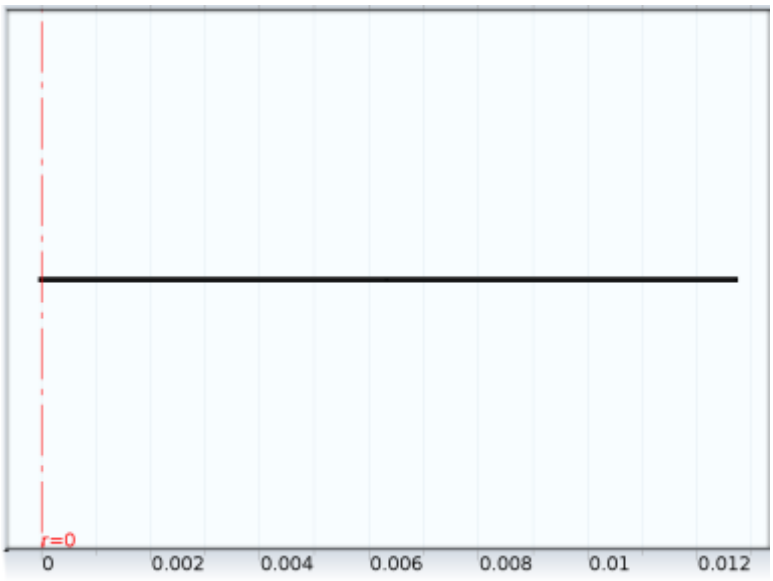

Mesh 1

2.7.1 Size (size)

Settings

Name	Value
Maximum element size	1.27E-4
Minimum element size	2.54E-7
Resolution of curvature	0.2
Predefined size	Extremely fine

3 Study 1

3.1 Time Dependent

Times: range(0,1,1600)

Mesh selection

Geometry	Mesh
Geometry 1 (geom1)	mesh1

Physics selection

Physics	Discretization
Heat Transfer in Porous Media (ht)	physics
Transport of Diluted Species (chds)	physics
Transport of Concentrated Species (chcs)	physics
Darcy's Law (dl)	physics

3.2 Solver Configurations

3.2.1 Solver 1

Compile Equations: Time Dependent (st1)

Study and step

Name	Value
Use study	Study 1
Use study step	Time Dependent

Dependent Variables 1 (v1)

General

Name	Value
Defined by study step	Time Dependent

Initial values of variables solved for

Name	Value
Solution	Zero

Values of variables not solved for

Name	Value
Solution	Zero

mod1.wN2 (mod1_wN2)

General

Name	Value
Field components	mod1.wN2
Field name	mod1_wt

mod1.wt (mod1_wt)

General

Name	Value
Field components	mod1.wt
Field name	mod1_wg

mod1.p (mod1_p)

General

Name	Value
Field components	mod1.p

mod1.T (mod1_T)

General

Name	Value
Field components	mod1.T

mod1.rho_a (mod1_rho_a)

General

Name	Value
Field components	mod1.rho_a
Field name	mod1_c

mod1.rho_c (mod1_rho_c)

General

Name	Value
Field components	mod1.rho_c
Field name	mod1_c3

mod1.rho_is (mod1_rho_is)

General

Name	Value
Field components	mod1.rho_is
Field name	mod1_c2

Time-Dependent Solver 1 (t1)

General

Name	Value
Defined by study step	Time Dependent
Time	{0, 1, 2, 3, 4, 5, 6, 7, 8, 9, 10, 11, 12, 13, 14, 15, 16, 17, 18, 19, 20, 21, 22, 23, 24, 25, 26, 27, 28, 29, 30, 31, 32, 33, 34, 35, 36, 37, 38, 39, 40, 41, 42, 43, 44, 45, 46, 47, 48, 49, 50, 51, 52, 53, 54, 55, 56, 57, 58, 59, 60, 61, 62, 63, 64, 65, 66, 67, 68, 69, 70, 71, 72, 73, 74, 75, 76, 77, 78, 79, 80, 81, 82, 83, 84, 85, 86, 87, 88, 89, 90, 91, 92, 93, 94, 95, 96, 97, 98, 99, 100, 101, 102, 103, 104, 105, 106, 107, 108, 109, 110, 111, 112, 113, 114, 115, 116, 117, 118, 119, 120, 121, 122, 123, 124, 125, 126, 127, 128, 129, 130, 131, 132, 133, 134, 135, 136, 137, 138, 139, 140, 141, 142, 143, 144, 145, 146, 147, 148, 149, 150, 151, 152, 153, 154, 155, 156, 157, 158, 159, 160, 161, 162, 163, 164, 165, 166, 167, 168, 169, 170, 171, 172, 173, 174, 175, 176, 177, 178, 179, 180, 181, 182, 183, 184, 185, 186, 187, 188, 189, 190, 191, 192, 193, 194, 195, 196, 197, 198, 199, 200, 201, 202, 203, 204, 205, 206, 207, 208, 209, 210, 211, 212, 213, 214, 215, 216, 217, 218, 219, 220, 221, 222, 223, 224, 225, 226, 227, 228, 229, 230, 231, 232, 233, 234, 235, 236, 237, 238, 239, 240, 241, 242, 243, 244, 245, 246, 247, 248, 249, 250, 251, 252, 253, 254, 255, 256, 257, 258, 259, 260, 261, 262, 263, 264, 265, 266, 267, 268, 269, 270, 271, 272, 273, 274, 275, 276, 277, 278, 279, 280, 281, 282, 283, 284, 285,

Name	Value
	286, 287, 288, 289, 290, 291, 292, 293, 294, 295, 296, 297, 298, 299, 300, 301, 302, 303, 304, 305, 306, 307, 308, 309, 310, 311, 312, 313, 314, 315, 316, 317, 318, 319, 320, 321, 322, 323, 324, 325, 326, 327, 328, 329, 330, 331, 332, 333, 334, 335, 336, 337, 338, 339, 340, 341, 342, 343, 344, 345, 346, 347, 348, 349, 350, 351, 352, 353, 354, 355, 356, 357, 358, 359, 360, 361, 362, 363, 364, 365, 366, 367, 368, 369, 370, 371, 372, 373, 374, 375, 376, 377, 378, 379, 380, 381, 382, 383, 384, 385, 386, 387, 388, 389, 390, 391, 392, 393, 394, 395, 396, 397, 398, 399, 400, 401, 402, 403, 404, 405, 406, 407, 408, 409, 410, 411, 412, 413, 414, 415, 416, 417, 418, 419, 420, 421, 422, 423, 424, 425, 426, 427, 428, 429, 430, 431, 432, 433, 434, 435, 436, 437, 438, 439, 440, 441, 442, 443, 444, 445, 446, 447, 448, 449, 450, 451, 452, 453, 454, 455, 456, 457, 458, 459, 460, 461, 462, 463, 464, 465, 466, 467, 468, 469, 470, 471, 472, 473, 474, 475, 476, 477, 478, 479, 480, 481, 482, 483, 484, 485, 486, 487, 488, 489, 490, 491, 492, 493, 494, 495, 496, 497, 498, 499, 500, 501, 502, 503, 504, 505, 506, 507, 508, 509, 510, 511, 512, 513, 514, 515, 516, 517, 518, 519, 520, 521, 522, 523, 524, 525, 526, 527, 528, 529, 530, 531, 532, 533, 534, 535, 536, 537, 538, 539, 540, 541, 542, 543, 544, 545, 546, 547, 548, 549, 550, 551, 552, 553, 554, 555, 556, 557, 558,

Name	Value
	559, 560, 561, 562, 563, 564, 565, 566, 567, 568, 569, 570, 571, 572, 573, 574, 575, 576, 577, 578, 579, 580, 581, 582, 583, 584, 585, 586, 587, 588, 589, 590, 591, 592, 593, 594, 595, 596, 597, 598, 599, 600, 601, 602, 603, 604, 605, 606, 607, 608, 609, 610, 611, 612, 613, 614, 615, 616, 617, 618, 619, 620, 621, 622, 623, 624, 625, 626, 627, 628, 629, 630, 631, 632, 633, 634, 635, 636, 637, 638, 639, 640, 641, 642, 643, 644, 645, 646, 647, 648, 649, 650, 651, 652, 653, 654, 655, 656, 657, 658, 659, 660, 661, 662, 663, 664, 665, 666, 667, 668, 669, 670, 671, 672, 673, 674, 675, 676, 677, 678, 679, 680, 681, 682, 683, 684, 685, 686, 687, 688, 689, 690, 691, 692, 693, 694, 695, 696, 697, 698, 699, 700, 701, 702, 703, 704, 705, 706, 707, 708, 709, 710, 711, 712, 713, 714, 715, 716, 717, 718, 719, 720, 721, 722, 723, 724, 725, 726, 727, 728, 729, 730, 731, 732, 733, 734, 735, 736, 737, 738, 739, 740, 741, 742, 743, 744, 745, 746, 747, 748, 749, 750, 751, 752, 753, 754, 755, 756, 757, 758, 759, 760, 761, 762, 763, 764, 765, 766, 767, 768, 769, 770, 771, 772, 773, 774, 775, 776, 777, 778, 779, 780, 781, 782, 783, 784, 785, 786, 787, 788, 789, 790, 791, 792, 793, 794, 795, 796, 797, 798, 799, 800, 801, 802, 803, 804, 805, 806, 807, 808, 809, 810, 811, 812, 813, 814, 815, 816, 817, 818, 819, 820, 821, 822, 823, 824, 825, 826, 827, 828, 829, 830, 831,

Name	Value
	832, 833, 834, 835, 836, 837, 838, 839, 840, 841, 842, 843, 844, 845, 846, 847, 848, 849, 850, 851, 852, 853, 854, 855, 856, 857, 858, 859, 860, 861, 862, 863, 864, 865, 866, 867, 868, 869, 870, 871, 872, 873, 874, 875, 876, 877, 878, 879, 880, 881, 882, 883, 884, 885, 886, 887, 888, 889, 890, 891, 892, 893, 894, 895, 896, 897, 898, 899, 900, 901, 902, 903, 904, 905, 906, 907, 908, 909, 910, 911, 912, 913, 914, 915, 916, 917, 918, 919, 920, 921, 922, 923, 924, 925, 926, 927, 928, 929, 930, 931, 932, 933, 934, 935, 936, 937, 938, 939, 940, 941, 942, 943, 944, 945, 946, 947, 948, 949, 950, 951, 952, 953, 954, 955, 956, 957, 958, 959, 960, 961, 962, 963, 964, 965, 966, 967, 968, 969, 970, 971, 972, 973, 974, 975, 976, 977, 978, 979, 980, 981, 982, 983, 984, 985, 986, 987, 988, 989, 990, 991, 992, 993, 994, 995, 996, 997, 998, 999, 1000, 1001, 1002, 1003, 1004, 1005, 1006, 1007, 1008, 1009, 1010, 1011, 1012, 1013, 1014, 1015, 1016, 1017, 1018, 1019, 1020, 1021, 1022, 1023, 1024, 1025, 1026, 1027, 1028, 1029, 1030, 1031, 1032, 1033, 1034, 1035, 1036, 1037, 1038, 1039, 1040, 1041, 1042, 1043, 1044, 1045, 1046, 1047, 1048, 1049, 1050, 1051, 1052, 1053, 1054, 1055, 1056, 1057, 1058, 1059, 1060, 1061, 1062, 1063, 1064, 1065, 1066, 1067, 1068, 1069, 1070, 1071, 1072, 1073, 1074, 1075, 1076, 1077, 1078, 1079, 1080,

Name	Value
	1081, 1082, 1083, 1084, 1085, 1086, 1087, 1088, 1089, 1090, 1091, 1092, 1093, 1094, 1095, 1096, 1097, 1098, 1099, 1100, 1101, 1102, 1103, 1104, 1105, 1106, 1107, 1108, 1109, 1110, 1111, 1112, 1113, 1114, 1115, 1116, 1117, 1118, 1119, 1120, 1121, 1122, 1123, 1124, 1125, 1126, 1127, 1128, 1129, 1130, 1131, 1132, 1133, 1134, 1135, 1136, 1137, 1138, 1139, 1140, 1141, 1142, 1143, 1144, 1145, 1146, 1147, 1148, 1149, 1150, 1151, 1152, 1153, 1154, 1155, 1156, 1157, 1158, 1159, 1160, 1161, 1162, 1163, 1164, 1165, 1166, 1167, 1168, 1169, 1170, 1171, 1172, 1173, 1174, 1175, 1176, 1177, 1178, 1179, 1180, 1181, 1182, 1183, 1184, 1185, 1186, 1187, 1188, 1189, 1190, 1191, 1192, 1193, 1194, 1195, 1196, 1197, 1198, 1199, 1200, 1201, 1202, 1203, 1204, 1205, 1206, 1207, 1208, 1209, 1210, 1211, 1212, 1213, 1214, 1215, 1216, 1217, 1218, 1219, 1220, 1221, 1222, 1223, 1224, 1225, 1226, 1227, 1228, 1229, 1230, 1231, 1232, 1233, 1234, 1235, 1236, 1237, 1238, 1239, 1240, 1241, 1242, 1243, 1244, 1245, 1246, 1247, 1248, 1249, 1250, 1251, 1252, 1253, 1254, 1255, 1256, 1257, 1258, 1259, 1260, 1261, 1262, 1263, 1264, 1265, 1266, 1267, 1268, 1269, 1270, 1271, 1272, 1273, 1274, 1275, 1276, 1277, 1278, 1279, 1280, 1281, 1282, 1283, 1284, 1285, 1286, 1287, 1288, 1289, 1290,

Name	Value
	1291, 1292, 1293, 1294, 1295, 1296, 1297, 1298, 1299, 1300, 1301, 1302, 1303, 1304, 1305, 1306, 1307, 1308, 1309, 1310, 1311, 1312, 1313, 1314, 1315, 1316, 1317, 1318, 1319, 1320, 1321, 1322, 1323, 1324, 1325, 1326, 1327, 1328, 1329, 1330, 1331, 1332, 1333, 1334, 1335, 1336, 1337, 1338, 1339, 1340, 1341, 1342, 1343, 1344, 1345, 1346, 1347, 1348, 1349, 1350, 1351, 1352, 1353, 1354, 1355, 1356, 1357, 1358, 1359, 1360, 1361, 1362, 1363, 1364, 1365, 1366, 1367, 1368, 1369, 1370, 1371, 1372, 1373, 1374, 1375, 1376, 1377, 1378, 1379, 1380, 1381, 1382, 1383, 1384, 1385, 1386, 1387, 1388, 1389, 1390, 1391, 1392, 1393, 1394, 1395, 1396, 1397, 1398, 1399, 1400, 1401, 1402, 1403, 1404, 1405, 1406, 1407, 1408, 1409, 1410, 1411, 1412, 1413, 1414, 1415, 1416, 1417, 1418, 1419, 1420, 1421, 1422, 1423, 1424, 1425, 1426, 1427, 1428, 1429, 1430, 1431, 1432, 1433, 1434, 1435, 1436, 1437, 1438, 1439, 1440, 1441, 1442, 1443, 1444, 1445, 1446, 1447, 1448, 1449, 1450, 1451, 1452, 1453, 1454, 1455, 1456, 1457, 1458, 1459, 1460, 1461, 1462, 1463, 1464, 1465, 1466, 1467, 1468, 1469, 1470, 1471, 1472, 1473, 1474, 1475, 1476, 1477, 1478, 1479, 1480, 1481, 1482, 1483, 1484, 1485, 1486, 1487, 1488, 1489, 1490, 1491, 1492, 1493, 1494, 1495, 1496, 1497, 1498, 1499, 1500,

Name	Value
	1501, 1502, 1503, 1504, 1505, 1506, 1507, 1508, 1509, 1510, 1511, 1512, 1513, 1514, 1515, 1516, 1517, 1518, 1519, 1520, 1521, 1522, 1523, 1524, 1525, 1526, 1527, 1528, 1529, 1530, 1531, 1532, 1533, 1534, 1535, 1536, 1537, 1538, 1539, 1540, 1541, 1542, 1543, 1544, 1545, 1546, 1547, 1548, 1549, 1550, 1551, 1552, 1553, 1554, 1555, 1556, 1557, 1558, 1559, 1560, 1561, 1562, 1563, 1564, 1565, 1566, 1567, 1568, 1569, 1570, 1571, 1572, 1573, 1574, 1575, 1576, 1577, 1578, 1579, 1580, 1581, 1582, 1583, 1584, 1585, 1586, 1587, 1588, 1589, 1590, 1591, 1592, 1593, 1594, 1595, 1596, 1597, 1598, 1599, 1600}
Relative tolerance	0.000001

Fully Coupled 1 (fc1)

General

Name	Value
Linear solver	Direct 1

Direct 1 (d1)

General

Name	Value
Solver	PARDISO

3.2.2 Solver 3

Compile Equations: Time Dependent (st1)

Study and step

Name	Value
Use study	Study 1
Use study step	Time Dependent

Dependent Variables 1 (v1)

General

Name	Value
Defined by study step	Time Dependent

Initial values of variables solved for

Name	Value
Method	Solution
Solution	Solver 1

Values of variables not solved for

Name	Value
Solution	Zero

mod1.T (mod1_T)

General

Name	Value
Field components	mod1.T

mod1.rho_is (mod1_rho_is)

General

Name	Value
Field components	mod1.rho_is

mod1.p (mod1_p)

General

Name	Value
Field components	mod1.p

mod1.wN2 (mod1_wN2)

General

Name	Value
Field components	mod1.wN2
Field name	mod1_wAr

mod1.rho_a (mod1_rho_a)

General

Name	Value
Field components	mod1.rho_a

mod1.wt (mod1_wt)

General

Name	Value
Field components	mod1.wt
Field name	mod1_wg

mod1.rho_c (mod1_rho_c)

General

Name	Value
Field components	mod1.rho_c

Time-Dependent Solver 1 (t1)

General

Name	Value
Defined by study step	Time Dependent
Time	{0, 1, 2, 3, 4, 5, 6, 7, 8, 9, 10, 11, 12, 13, 14, 15, 16, 17, 18, 19, 20, 21, 22, 23, 24, 25, 26, 27, 28, 29, 30, 31, 32, 33, 34, 35, 36, 37, 38, 39, 40, 41, 42, 43, 44, 45, 46, 47, 48, 49, 50, 51, 52, 53, 54, 55, 56, 57, 58, 59, 60, 61, 62, 63, 64, 65, 66, 67, 68, 69, 70, 71, 72, 73, 74, 75, 76, 77, 78, 79, 80, 81, 82, 83, 84, 85, 86, 87, 88, 89, 90, 91, 92, 93, 94, 95, 96, 97, 98, 99, 100, 101, 102, 103, 104, 105, 106, 107, 108, 109, 110, 111, 112, 113, 114, 115, 116, 117, 118, 119, 120, 121, 122, 123, 124, 125, 126, 127, 128, 129, 130, 131, 132, 133, 134, 135, 136, 137, 138, 139, 140, 141, 142, 143, 144, 145, 146, 147, 148, 149, 150, 151, 152, 153, 154, 155, 156, 157, 158, 159, 160, 161, 162, 163, 164, 165, 166, 167, 168, 169, 170, 171, 172, 173, 174, 175, 176, 177, 178, 179, 180, 181, 182, 183, 184, 185, 186, 187, 188, 189, 190, 191, 192, 193, 194, 195, 196, 197, 198, 199, 200, 201, 202, 203, 204, 205, 206, 207, 208, 209, 210, 211, 212, 213, 214, 215, 216, 217, 218, 219, 220,

Name	Value
	221, 222, 223, 224, 225, 226, 227, 228, 229, 230, 231, 232, 233, 234, 235, 236, 237, 238, 239, 240, 241, 242, 243, 244, 245, 246, 247, 248, 249, 250, 251, 252, 253, 254, 255, 256, 257, 258, 259, 260, 261, 262, 263, 264, 265, 266, 267, 268, 269, 270, 271, 272, 273, 274, 275, 276, 277, 278, 279, 280, 281, 282, 283, 284, 285, 286, 287, 288, 289, 290, 291, 292, 293, 294, 295, 296, 297, 298, 299, 300, 301, 302, 303, 304, 305, 306, 307, 308, 309, 310, 311, 312, 313, 314, 315, 316, 317, 318, 319, 320, 321, 322, 323, 324, 325, 326, 327, 328, 329, 330, 331, 332, 333, 334, 335, 336, 337, 338, 339, 340, 341, 342, 343, 344, 345, 346, 347, 348, 349, 350, 351, 352, 353, 354, 355, 356, 357, 358, 359, 360, 361, 362, 363, 364, 365, 366, 367, 368, 369, 370, 371, 372, 373, 374, 375, 376, 377, 378, 379, 380, 381, 382, 383, 384, 385, 386, 387, 388, 389, 390, 391, 392, 393, 394, 395, 396, 397, 398, 399, 400, 401, 402, 403, 404, 405, 406, 407, 408, 409, 410, 411, 412, 413, 414, 415, 416, 417, 418, 419, 420, 421, 422, 423, 424, 425, 426, 427, 428, 429, 430, 431, 432, 433, 434, 435, 436, 437, 438, 439, 440, 441, 442, 443, 444, 445, 446, 447, 448, 449, 450, 451, 452, 453, 454, 455, 456, 457, 458, 459, 460, 461, 462, 463, 464, 465, 466, 467, 468, 469, 470, 471, 472, 473, 474, 475, 476, 477, 478, 479, 480, 481, 482, 483, 484, 485, 486, 487, 488, 489, 490, 491, 492, 493,

Name	Value
	494, 495, 496, 497, 498, 499, 500, 501, 502, 503, 504, 505, 506, 507, 508, 509, 510, 511, 512, 513, 514, 515, 516, 517, 518, 519, 520, 521, 522, 523, 524, 525, 526, 527, 528, 529, 530, 531, 532, 533, 534, 535, 536, 537, 538, 539, 540, 541, 542, 543, 544, 545, 546, 547, 548, 549, 550, 551, 552, 553, 554, 555, 556, 557, 558, 559, 560, 561, 562, 563, 564, 565, 566, 567, 568, 569, 570, 571, 572, 573, 574, 575, 576, 577, 578, 579, 580, 581, 582, 583, 584, 585, 586, 587, 588, 589, 590, 591, 592, 593, 594, 595, 596, 597, 598, 599, 600, 601, 602, 603, 604, 605, 606, 607, 608, 609, 610, 611, 612, 613, 614, 615, 616, 617, 618, 619, 620, 621, 622, 623, 624, 625, 626, 627, 628, 629, 630, 631, 632, 633, 634, 635, 636, 637, 638, 639, 640, 641, 642, 643, 644, 645, 646, 647, 648, 649, 650, 651, 652, 653, 654, 655, 656, 657, 658, 659, 660, 661, 662, 663, 664, 665, 666, 667, 668, 669, 670, 671, 672, 673, 674, 675, 676, 677, 678, 679, 680, 681, 682, 683, 684, 685, 686, 687, 688, 689, 690, 691, 692, 693, 694, 695, 696, 697, 698, 699, 700, 701, 702, 703, 704, 705, 706, 707, 708, 709, 710, 711, 712, 713, 714, 715, 716, 717, 718, 719, 720, 721, 722, 723, 724, 725, 726, 727, 728, 729, 730, 731, 732, 733, 734, 735, 736, 737, 738, 739, 740, 741, 742, 743, 744, 745, 746, 747, 748, 749, 750, 751, 752, 753, 754, 755, 756, 757, 758, 759, 760, 761, 762, 763, 764, 765, 766,

Name	Value
	767, 768, 769, 770, 771, 772, 773, 774, 775, 776, 777, 778, 779, 780, 781, 782, 783, 784, 785, 786, 787, 788, 789, 790, 791, 792, 793, 794, 795, 796, 797, 798, 799, 800, 801, 802, 803, 804, 805, 806, 807, 808, 809, 810, 811, 812, 813, 814, 815, 816, 817, 818, 819, 820, 821, 822, 823, 824, 825, 826, 827, 828, 829, 830, 831, 832, 833, 834, 835, 836, 837, 838, 839, 840, 841, 842, 843, 844, 845, 846, 847, 848, 849, 850, 851, 852, 853, 854, 855, 856, 857, 858, 859, 860, 861, 862, 863, 864, 865, 866, 867, 868, 869, 870, 871, 872, 873, 874, 875, 876, 877, 878, 879, 880, 881, 882, 883, 884, 885, 886, 887, 888, 889, 890, 891, 892, 893, 894, 895, 896, 897, 898, 899, 900, 901, 902, 903, 904, 905, 906, 907, 908, 909, 910, 911, 912, 913, 914, 915, 916, 917, 918, 919, 920, 921, 922, 923, 924, 925, 926, 927, 928, 929, 930, 931, 932, 933, 934, 935, 936, 937, 938, 939, 940, 941, 942, 943, 944, 945, 946, 947, 948, 949, 950, 951, 952, 953, 954, 955, 956, 957, 958, 959, 960, 961, 962, 963, 964, 965, 966, 967, 968, 969, 970, 971, 972, 973, 974, 975, 976, 977, 978, 979, 980, 981, 982, 983, 984, 985, 986, 987, 988, 989, 990, 991, 992, 993, 994, 995, 996, 997, 998, 999, 1000, 1001, 1002, 1003, 1004, 1005, 1006, 1007, 1008, 1009, 1010, 1011, 1012, 1013, 1014, 1015, 1016, 1017, 1018, 1019, 1020, 1021, 1022, 1023, 1024, 1025, 1026, 1027, 1028, 1029, 1030,

Name	Value
	1031, 1032, 1033, 1034, 1035, 1036, 1037, 1038, 1039, 1040, 1041, 1042, 1043, 1044, 1045, 1046, 1047, 1048, 1049, 1050, 1051, 1052, 1053, 1054, 1055, 1056, 1057, 1058, 1059, 1060, 1061, 1062, 1063, 1064, 1065, 1066, 1067, 1068, 1069, 1070, 1071, 1072, 1073, 1074, 1075, 1076, 1077, 1078, 1079, 1080, 1081, 1082, 1083, 1084, 1085, 1086, 1087, 1088, 1089, 1090, 1091, 1092, 1093, 1094, 1095, 1096, 1097, 1098, 1099, 1100, 1101, 1102, 1103, 1104, 1105, 1106, 1107, 1108, 1109, 1110, 1111, 1112, 1113, 1114, 1115, 1116, 1117, 1118, 1119, 1120, 1121, 1122, 1123, 1124, 1125, 1126, 1127, 1128, 1129, 1130, 1131, 1132, 1133, 1134, 1135, 1136, 1137, 1138, 1139, 1140, 1141, 1142, 1143, 1144, 1145, 1146, 1147, 1148, 1149, 1150, 1151, 1152, 1153, 1154, 1155, 1156, 1157, 1158, 1159, 1160, 1161, 1162, 1163, 1164, 1165, 1166, 1167, 1168, 1169, 1170, 1171, 1172, 1173, 1174, 1175, 1176, 1177, 1178, 1179, 1180, 1181, 1182, 1183, 1184, 1185, 1186, 1187, 1188, 1189, 1190, 1191, 1192, 1193, 1194, 1195, 1196, 1197, 1198, 1199, 1200, 1201, 1202, 1203, 1204, 1205, 1206, 1207, 1208, 1209, 1210, 1211, 1212, 1213, 1214, 1215, 1216, 1217, 1218, 1219, 1220, 1221, 1222, 1223, 1224, 1225, 1226, 1227, 1228, 1229, 1230, 1231, 1232, 1233, 1234, 1235, 1236, 1237, 1238, 1239, 1240,

Name	Value
	1241, 1242, 1243, 1244, 1245, 1246, 1247, 1248, 1249, 1250, 1251, 1252, 1253, 1254, 1255, 1256, 1257, 1258, 1259, 1260, 1261, 1262, 1263, 1264, 1265, 1266, 1267, 1268, 1269, 1270, 1271, 1272, 1273, 1274, 1275, 1276, 1277, 1278, 1279, 1280, 1281, 1282, 1283, 1284, 1285, 1286, 1287, 1288, 1289, 1290, 1291, 1292, 1293, 1294, 1295, 1296, 1297, 1298, 1299, 1300, 1301, 1302, 1303, 1304, 1305, 1306, 1307, 1308, 1309, 1310, 1311, 1312, 1313, 1314, 1315, 1316, 1317, 1318, 1319, 1320, 1321, 1322, 1323, 1324, 1325, 1326, 1327, 1328, 1329, 1330, 1331, 1332, 1333, 1334, 1335, 1336, 1337, 1338, 1339, 1340, 1341, 1342, 1343, 1344, 1345, 1346, 1347, 1348, 1349, 1350, 1351, 1352, 1353, 1354, 1355, 1356, 1357, 1358, 1359, 1360, 1361, 1362, 1363, 1364, 1365, 1366, 1367, 1368, 1369, 1370, 1371, 1372, 1373, 1374, 1375, 1376, 1377, 1378, 1379, 1380, 1381, 1382, 1383, 1384, 1385, 1386, 1387, 1388, 1389, 1390, 1391, 1392, 1393, 1394, 1395, 1396, 1397, 1398, 1399, 1400, 1401, 1402, 1403, 1404, 1405, 1406, 1407, 1408, 1409, 1410, 1411, 1412, 1413, 1414, 1415, 1416, 1417, 1418, 1419, 1420, 1421, 1422, 1423, 1424, 1425, 1426, 1427, 1428, 1429, 1430, 1431, 1432, 1433, 1434, 1435, 1436, 1437, 1438, 1439, 1440, 1441, 1442, 1443, 1444, 1445, 1446, 1447, 1448, 1449, 1450,

Name	Value
	1451, 1452, 1453, 1454, 1455, 1456, 1457, 1458, 1459, 1460, 1461, 1462, 1463, 1464, 1465, 1466, 1467, 1468, 1469, 1470, 1471, 1472, 1473, 1474, 1475, 1476, 1477, 1478, 1479, 1480, 1481, 1482, 1483, 1484, 1485, 1486, 1487, 1488, 1489, 1490, 1491, 1492, 1493, 1494, 1495, 1496, 1497, 1498, 1499, 1500, 1501, 1502, 1503, 1504, 1505, 1506, 1507, 1508, 1509, 1510, 1511, 1512, 1513, 1514, 1515, 1516, 1517, 1518, 1519, 1520, 1521, 1522, 1523, 1524, 1525, 1526, 1527, 1528, 1529, 1530, 1531, 1532, 1533, 1534, 1535, 1536, 1537, 1538, 1539, 1540, 1541, 1542, 1543, 1544, 1545, 1546, 1547, 1548, 1549, 1550, 1551, 1552, 1553, 1554, 1555, 1556, 1557, 1558, 1559, 1560, 1561, 1562, 1563, 1564, 1565, 1566, 1567, 1568, 1569, 1570, 1571, 1572, 1573, 1574, 1575, 1576, 1577, 1578, 1579, 1580, 1581, 1582, 1583, 1584, 1585, 1586, 1587, 1588, 1589, 1590, 1591, 1592, 1593, 1594, 1595, 1596, 1597, 1598, 1599, 1600}
Relative tolerance	0.000001

Fully Coupled 1 (fc1)

General

Name	Value
Linear solver	Direct 1

Gauthier Model

1 Global Definitions

1.1 Parameters 1

Parameters

Name	Expression	Description
cell_init	0.4698	Initial cellulose mass percent
hemi_init	0.2552	Initial hemicellulose mass percent
ligC_init	0.0087	Initial ligC mass percent
ligH_init	0.263	Initial ligH mass percent
ligO_init	0.0034	Initial ligO mass percent
deltaH_1	0	Heat of reaction (J/mol)
deltaH_2	1.053E5	Heat of reaction (J/mol)
deltaH_3	7.938E4	Heat of reaction (J/mol)
deltaH_4	-2.916E5	Heat of reaction (J/mol)
deltaH_5	1.32e4	Heat of reaction (J/mol)
deltaH_6	2.904E3	Heat of reaction (J/mol)
deltaH_7	-1.848E5	Heat of reaction (J/mol)
deltaH_8	7.788e4	Heat of reaction (J/mol)
deltaH_9	-4.356E4	Heat of reaction (J/mol)
deltaH_10	-2.58E4	Heat of reaction (J/mol)
deltaH_11	5.668E4	Heat of reaction (J/mol)
deltaH_12	1.0972E5	Heat of reaction (J/mol)

Name	Expression	Description
deltaH_13	-1.161E5	Heat of reaction (J/mol)
deltaH_14	2.646E4	Heat of reaction (J/mol)
deltaH_15	-4.914E5	Heat of reaction (J/mol)
deltaH_16	1.8512E5	Heat of reaction (J/mol)
deltaH_17	-6.24e4	Heat of reaction (J/mol)
deltaH_18	-3.6816E5	Heat of reaction (J/mol)
deltaH_19	-3.784E4	Heat of reaction (J/mol)
deltaH_20	-4.2e4	Heat of reaction (J/mol)
deltaH_21	2.04e5	Heat of reaction (J/mol)
deltaH_22	0	Heat of reaction (J/mol)
deltaH_23	0	Heat of reaction (J/mol)
deltaH_24	0	Heat of reaction (J/mol)
deltaH_25	0	Heat of reaction (J/mol)
MW_cell	162.1413	Molecular weight of cellulose (g/mol)
MW_hemi	132.1152	Molecular weight of hemicellulose (g/mol)
MW_ligC	258.2707	Molecular weight of ligC (g/mol)
MW_ligH	436.4545	Molecular weight of ligH (g/mol)
MW_ligO	422.3847	Molecular weight of ligO (g/mol)
MW_Char	12.0108	Char molecular weight (g/mol)
MW_CELLA	162.1413	Molecular weight of CELLA (g/mol)
MW_GC2H4	28.0534	Molecular weight of GC2H4 (g/mol)

Name	Expression	Description
MW_GCH3OH	32.042	Molecular weight of GCH3OH (g/mol)
MW_GCH4	16.0426	Molecular weight of GCH4 (g/mol)
MW_GCO	28.0102	Molecular weight of GCO (g/mol)
MW_GCO2	44.0096	Molecular weight of GCO2 (g/mol)
MW_GCOH2	30.0261	Molecular weight of GCOH2 (g/mol)
MW_GH2	2.0159	Molecular weight of GH2 (g/mol)
MW_HCE1	132.1152	Molecular weight of HCE1 (g/mol)
MW_HCE2	132.1152	Molecular weight of HCE2 (g/mol)
MW_LIG	208.2117	Molecular weight of LIG (g/mol)
MW_LIGCC	258.2707	Molecular weight of LIGCC (g/mol)
MW_LIGOH	378.3751	Molecular weight of LIGOH (g/mol)

1.2 Functions

1.2.1 Analytic 1

Function name	k_1
Function type	Analytic

Function name

Name	Value
Function name	k_1

Parameters

Name	Value
Expression	8e13*exp(-45000/(R*T))

Name	Value
Arguments	T

1.2.2 Analytic 2

Function name	k_2
Function type	Analytic

Function name

Name	Value
Function name	k_2

Parameters

Name	Value
Expression	1e9*exp(-30000/(R*T))
Arguments	T

1.2.3 Analytic 3

Function name	k_3
Function type	Analytic

Function name

Name	Value
Function name	k_3

Parameters

Name	Value
Expression	4*T*exp(-10000/(R*T))
Arguments	T

1.2.4 Analytic 4

Function name	k_4
Function type	Analytic

Function name

Name	Value
Function name	k_4

Parameters

Name	Value
Expression	8e7*exp(-31000/(R*T))
Arguments	T

1.2.5 Analytic 5

Function name	k_5
Function type	Analytic

Function name

Name	Value
Function name	k_5

Parameters

Name	Value
Expression	1e10*exp(-31000/(R*T))
Arguments	T

1.2.6 Analytic 6

Function name	k_6
Function type	Analytic

Function name

Name	Value
Function name	k_6

Parameters

Name	Value
Expression	3e9*exp(-32000/(R*T))
Arguments	T

1.2.7 Analytic 7

Function name	k_7
Function type	Analytic

Function name

Name	Value
Function name	k_7

Parameters

Name	Value
Expression	0.15*T*exp(-8000/(R*T))
Arguments	T

1.2.8 Analytic 8

Function name	k_8
Function type	Analytic

Function name

Name	Value
Function name	k_8

Parameters

Name	Value
Expression	3*T*exp(-11000/(R*T))
Arguments	T

1.2.9 Analytic 9

Function name	k_9
Function type	Analytic

Function name

Name	Value
Function name	k_9

Parameters

Name	Value
Expression	1e10*exp(-33000/(R*T))
Arguments	T

1.2.10 Analytic 10

Function name	k_10
Function type	Analytic

Function name

Name	Value
Function name	k_10

Parameters

Name	Value
Expression	4e15*exp(-48500/(R*T))

Name	Value
Arguments	T

1.2.11 Analytic 11

Function name	k_11
Function type	Analytic

Function name

Name	Value
Function name	k_11

Parameters

Name	Value
Expression	2e13*exp(-37500/(R*T))
Arguments	T

1.2.12 Analytic 12

Function name	k_12
Function type	Analytic

Function name

Name	Value
Function name	k_12

Parameters

Name	Value
Expression	1e9*exp(-25500/(R*T))
Arguments	T

1.2.13 Analytic 13

Function name	k_13
Function type	Analytic

Function name

Name	Value
Function name	k_13

Parameters

Name	Value
Expression	5e6*exp(-31500/(R*T))
Arguments	T

1.2.14 Analytic 14

Function name	k_14
Function type	Analytic

Function name

Name	Value
Function name	k_14

Parameters

Name	Value
Expression	3e8*exp(-30000/(R*T))
Arguments	T

1.2.15 Analytic 15

Function name	k_15
Function type	Analytic

Function name

Name	Value
Function name	k_15

Parameters

Name	Value
Expression	100*exp(-15000/(R*T))
Arguments	T

1.2.16 Analytic 16

Function name	k_16
Function type	Analytic

Function name

Name	Value
Function name	k_16

Parameters

Name	Value
Expression	8*T*exp(-12000/(R*T))
Arguments	T

1.2.17 Analytic 17

Function name	k_17
Function type	Analytic

Function name

Name	Value
Function name	k_17

Parameters

Name	Value
Expression	1.2e9*exp(-30000/(R*T))
Arguments	T

1.2.18 Analytic 18

Function name	k_18
Function type	Analytic

Function name

Name	Value
Function name	k_18

Parameters

Name	Value
Expression	0.25*T*exp(-8000/(R*T))
Arguments	T

1.2.19 Analytic 19

Function name	k_19
Function type	Analytic

Function name

Name	Value
Function name	k_19

Parameters

Name	Value
Expression	6e5*exp(-24000/(R*T))

Name	Value
Arguments	T

1.2.20 Analytic 20

Function name	k_20
Function type	Analytic

Function name

Name	Value
Function name	k_20

Parameters

Name	Value
Expression	5E11*exp(-50000/(R*T))
Arguments	T

1.2.21 Analytic 21

Function name	k_21
Function type	Analytic

Function name

Name	Value
Function name	k_21

Parameters

Name	Value
Expression	5e11*exp(-71000/(R*T))
Arguments	T

1.2.22 Analytic 22

Function name	k_22
Function type	Analytic

Function name

Name	Value
Function name	k_22

Parameters

Name	Value
Expression	5e11*exp(-75000/(R*T))
Arguments	T

1.2.23 Analytic 23

Function name	k_23
Function type	Analytic

Function name

Name	Value
Function name	k_23

Parameters

Name	Value
Expression	0.5e13*exp(-50000/(R*T))
Arguments	T

1.2.24 Analytic 24

Function name	k_24
Function type	Analytic

Function name

Name	Value
Function name	k_24

Parameters

Name	Value
Expression	0.5e13*exp(-50000/(R*T))
Arguments	T

1.2.25 Analytic 25

Function name	k_25
Function type	Analytic

Function name

Name	Value
Function name	k_25

Parameters

Name	Value
Expression	0.5e13*exp(-50000/(R*T))
Arguments	T

2 Model 1 (mod1)

2.1 Definitions

2.1.1 Variables

Variables 2a

Selection

Geometric entity level	Entire model

Name	Expression	Description
rho_a	cCELL*MW_cell/1000 + cHCE*MW_hemi/1000 + cLIGC*MW_ligC/1000 + cLIGH*MW_ligH/1000 + cLIGO*MW_ligO/1000	Density of initial wood constituents (kg/m^3)
rho_is	cCELLA*MW_CELLA/1000 + cGC2H4*MW_GC2H4/1000 + cGCH3OH*MW_GCH3OH/1000 + cGCH4*MW_GCH4/1000 + cGCO*MW_GCO/1000 + cGCO2*MW_GCO2/1000 + cGCOH2*MW_GCOH2/1000 + cGH2*MW_GH2/1000 + cHCE1*MW_HCE1/1000 + cHCE2*MW_HCE2/1000 +	Density of intermediate solids (kg/m^3)

Name	Expression	Description
	cLIG*MW_LIG/1000 + cLIGCC*MW_LIGCC/1000 + cLIGOH*MW_LIGOH/1000	
rho_c	cChar*MW_Char/1000	Density of char (kg/m^3)
wg	wC2H4 + wCH4 + wCO + wCO2 + wH2	Mass fraction of "gas"
wt	wC2H4O + wC3H6O + wCH2O + wCH3OH + wCOU + wF2M + wFEN + wGLY + wH2O + wHAA + wHCOOH + wHMFU + wEtOH + wLVG + wXYL	Mass fraction of "tar"

Variables 3a

Selection

Geometric entity level	Entire model

Name	Expression	Description
R_C2H4	chcs.M_wC2H4*(0.25*k_6(T)*cHCE1 + 0.41*k_10(T)*cLIGC + 0.7*k_15(T)*cLIGOH + 1*k_25(T)*cGC2H4)	Reaction rate for C2H4 (kg/m^3 s)
R_C2H4O	chcs.M_wC2H4O*(0.2*k_2(T)*cCELLA + 0.2*k_17(T)*cLIG)	Reaction rate for C3H4O2 (kg/m^3 s)
R_C3H6O	chcs.M_wC3H6O*(0.1*k_2(T)*cCELLA + 1*k_11(T)*cLIGH +	Reaction rate for C3H6O (kg/m^3 s)

Name	Expression	Description
	0.2*k_17(T)*cLIG)	
R_CH2O	chcs.M_wCH2O*(0.1*k_2(T)*cCELLA + 0.3*k_6(T)*cHCE1 + 0.3*k_7(T)*cHCE1 + 0.4*k_9(T)*cHCE2 + 0.3*k_10(T)*cLIGC + 0.3*k_13(T)*cLIGCC + 0.2*k_14(T)*cLIGOH + 0.2*k_17(T)*cLIG + 0.3*k_18(T)*cLIG)	Reaction rate for CH2O (kg/m^3 s)
R_CH3OH	chcs.M_wCH3OH*(0.3*k_14(T)*cLIGOH + 0.4*k_17(T)*cLIG + 1*k_24(T)*cGCH3OH)	Reaction rate for CH3OH (kg/m^3 s)
R_CH4	chcs.M_wCH4*(0.1*k_2(T)*cCELLA + 0.625*k_6(T)*cHCE1 + 0.495*k_10(T)*cLIGC + 1*k_23(T)*cGCH4)	Reaction rate for CH4 (kg/m^3 s)
R_CO	chcs.M_wCO*(0.16*k_2(T)*cCELLA + 1.1*k_6(T)*cHCE1 + 0.7*k_7(T)*cHCE1 + 0.2*k_9(T)*cHCE2 +	Reaction rate for CO (kg/m^3 s)

Name	Expression	Description
	0.32*k_10(T)*cLIGC + 0.4*k_13(T)*cLIGCC + 0.3*k_14(T)*cLIGOH + 1*k_17(T)*cLIG + 0.4*k_18(T)*cLIG + 1*k_20(T)*cGCO + 1*k_21(T)*cGCOH2)	
R_CO2	chcs.M_wCO2*(0.22*k_2(T)*cCELLA + 1.075*k_6(T)*cHCE1 + 0.75*k_7(T)*cHCE1 + 0.425*k_9(T)*cHCE2 + 1*k_12(T)*cLIGO + 0.05*k_14(T)*cLIGOH + 0.5*k_15(T)*cLIGOH + 0.4*k_18(T)*cLIG + 1*k_19(T)*cGCO2)	Reaction rate for CO2 (kg/m^3 s)
R_COU	chcs.M_wCOU*(0.1*k_10(T)*cLIGC + 0.3*k_13(T)*cLIGCC)	Reaction rate for COU (kg/m^3 s)
R_EtOH	chcs.M_wEtOH*(0.125*k_6(T)*cHCE1 + 0.1*k_9(T)*cHCE2)	Reaction rate for EtOH (kg/m^3 s)
R_F2M	chcs.M_wF2M*(1*k_16(T)*cLIG)	Reaction rate for F2M (kg/m^3 s)
R_FEN	chcs.M_wFEN*(0.08*k_10(T)*cLIGC	Reaction rate for FEN (kg/m^3 s)

Name	Expression	Description
	+ 0.2*k_13(T)*cLIGCC)	
R_GLY	chcs.M_wGLY*(0.2*k_2(T)*cCELLA)	Reaction rate for GLY (kg/m^3 s)
R_H2	chcs.M_wH2*(1*k_21(T)*cGCOH2 + 1*k_22(T)*cGH2)	Reaction rate for H2 (kg/m^3 s)
R_H2O	chcs.M_wH2O*(0.83*k_2(T)*cCELLA + 5*k_4(T)*cCELL + 0.025*k_6(T)*cHCE1 + 0.25*k_7(T)*cHCE1 + 0.2*k_9(T)*cHCE2 + 1*k_10(T)*cLIGC + 0.7*k_13(T)*cLIGCC + 0.9*k_14(T)*cLIGOH + 1.5*k_15(T)*cLIGOH + 0.95*k_17(T)*cLIG + 0.6*k_18(T)*cLIG)	Reaction rate for H2O (kg/m^3 s)
R_HAA	chcs.M_wHAA*(1*k_2(T)*cCELLA + 0.2*k_9(T)*cHCE2 + 0.35*k_13(T)*cLIGCC)	Reaction rate for HAA (kg/m^3 s)
R_HCOOH	chcs.M_wHCOOH*(0.01*k_2(T)*cCELLA + 0.025*k_6(T)*cHCE1 + 0.05*k_7(T)*cHCE1 +	

Name	Expression	Description
	0.025*k_9(T)*cHCE2 + 0.05*k_14(T)*cLIGOH + 0.05*k_17(T)*cLIG)	
R_HMFU	chcs.M_wHMFU*(0.25*k_2(T)*cCELLA)	Reaction rate for HMFU (kg/m^3 s)
R_LVG	chcs.M_wLVG*(1*k_3(T)*cCELLA)	Reaction rate for LVG (kg/m^3 s)
R_XYL	chcs.M_wXYL*(1*k_8(T)*cHCE1)	Reaction rate for XYL (kg/m^3 s)
mass_src	R_C2H4/chcs.M_wC2H4 + R_C2H4O/chcs.M_wC2H4O + R_C3H6O/chcs.M_wC3H6O + R_CH2O/chcs.M_wCH2O + R_CH3OH/chcs.M_wCH3OH + R_CH4/chcs.M_wCH4 + R_CO/chcs.M_wCO + R_CO2/chcs.M_wCO2 + R_COU/chcs.M_wCOU + R_EtOH/chcs.M_wEtOH + R_F2M/chcs.M_wF2M + R_FEN/chcs.M_wFEN + R_GLY/chcs.M_wGLY +R_H2/chcs.M_wH2 +	Gas phase mass source

Name	Expression	Description
	R_H2O/chcs.M_wH2O + R_HAA/chcs.M_wHAA + R_HCOOH/chcs.M_wHCOOH + R_HMFU/chcs.M_wHMFU + R_LVG/chcs.M_wLVG + R_XYL/chcs.M_wXYL	

2.1.2 Model Couplings

Integration 1

Coupling type	Integration
Operator name	intop1

Source selection

Geometric entity level	Domain
Selection	Domain 1

2.2 Geometry 1

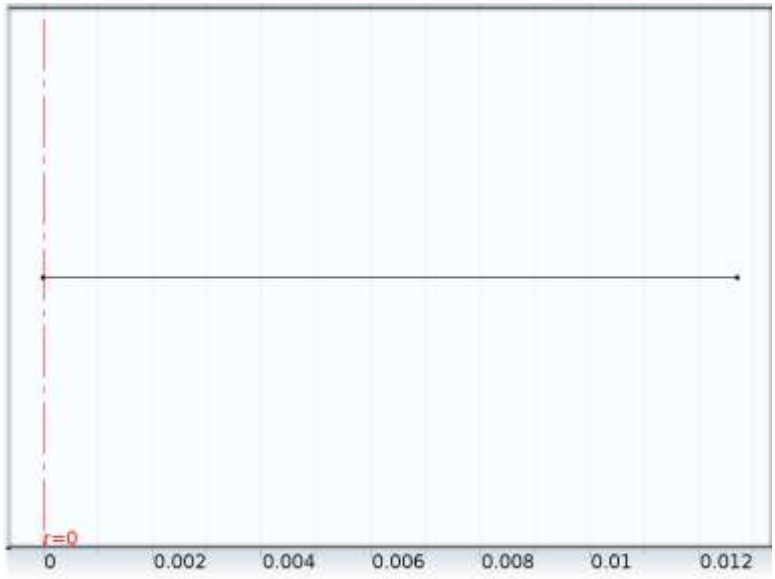

Geometry 1

units

Length unit	m
Angular unit	deg

Geometry statistics

Property	Value
Space dimension	1
Number of domains	1
Number of boundaries	2

2.3 Heat Transfer in Porous Media (ht)

2.3.1 Heat Source 1

Heat Source 1

Selection

Geometric entity level	Domain
Selection	Domain 1

Equations

$$\rho C_p \frac{\partial T}{\partial t} + \rho C_p \mathbf{u} \cdot \nabla T = \nabla \cdot (k \nabla T) + Q$$

Settings

Settings

Description	Value
Heat source	r*(-1*(k_1(T)*deltaH_1*cCELL + k_2(T)*deltaH_2*cCELLA + k_3(T)*deltaH_3*cCELLA + k_4(T)*deltaH_4*cCELL + k_5(T)*deltaH_5*cHCE+k_6(T)*deltaH_6*cHCE1 +

Description	Value
	k_7(T)*deltaH_7*cHCE1 + k_8(T)*deltaH_8*cHCE1 + k_9(T)*deltaH_9*cHCE2 + k_10(T)*deltaH_10*cLIGC + k_11(T)*deltaH_11*cLIGH + k_12(T)*deltaH_12*cLIGO + k_13(T)*deltaH_13*cLIGCC + k_14(T)*deltaH_14*cLIGOH + k_15(T)*deltaH_15*cLIGOH + k_16(T)*deltaH_16*cLIG + k_17(T)*deltaH_17*cLIG + k_18(T)*deltaH_18*cLIG + k_19(T)*deltaH_19*cGCO2 + k_20(T)*deltaH_20*cGCO + k_21(T)*deltaH_21*cGCOH2 + k_22(T)*deltaH_22*cGH2 + k_23(T)*deltaH_23*cGCH4 + k_24(T)*deltaH_24*cGCH3OH + k_25(T)*deltaH_25*cGC2H4))

Variables

Name	Expression	Unit	Description	Selection
ht.Q	-r*(k_1(T)*deltaH_1*cCELL + k_2(T)*deltaH_2*cCELLA + k_3(T)*deltaH_3*cCELLA + k_4(T)*deltaH_4*cCELL + k_5(T)*deltaH_5*cHCE+k	W/m^3	Heat source	Domain 1

Name	Expression	Unit	Description	Selection
	_6(T)*deltaH_6*cHCE1 + k_7(T)*deltaH_7*cHCE1 + k_8(T)*deltaH_8*cHCE1 + k_9(T)*deltaH_9*cHCE2 + k_10(T)*deltaH_10*cLIGC + k_11(T)*deltaH_11*cLIGH + k_12(T)*deltaH_12*cLIGO + k_13(T)*deltaH_13*cLIGCC + k_14(T)*deltaH_14*cLIGOH + k_15(T)*deltaH_15*cLIGOH + k_16(T)*deltaH_16*cLIG + k_17(T)*deltaH_17*cLIG + k_18(T)*deltaH_18*cLIG			

Name	Expression	Unit	Description	Selection
	+ k_19(T)*deltaH_19*cGCO2 + k_20(T)*deltaH_20*cGCO + k_21(T)*deltaH_21*cGCOH2 + k_22(T)*deltaH_22*cGH2 + k_23(T)*deltaH_23*cGCH4 + k_24(T)*deltaH_24*cGCH3OH + k_25(T)*deltaH_25*cGC2H4)			
ht.Qtot	- r*(k_1(T)*deltaH_1*cCELL + k_2(T)*deltaH_2*cCELLA + k_3(T)*deltaH_3*cCELLA	W/m^3	Total heat source	Domain 1

Name	Expression	Unit	Description	Selection
	+ k_4(T)*deltaH_4*cCELL + k_5(T)*deltaH_5*cHCE+k_6(T)*deltaH_6*cHCE1 + k_7(T)*deltaH_7*cHCE1 + k_8(T)*deltaH_8*cHCE1 + k_9(T)*deltaH_9*cHCE2 + k_10(T)*deltaH_10*cLIGC + k_11(T)*deltaH_11*cLIGH + k_12(T)*deltaH_12*cLIGO + k_13(T)*deltaH_13*cLIGCC + k_14(T)*deltaH_14*cLIGOH + k_15(T)*deltaH_15*cLIGOH + k_16(T)*deltaH_16*cLIG +			

Name	Expression	Unit	Description	Selection
	k_17(T)*deltaH_17*cLIG + k_18(T)*deltaH_18*cLIG + k_19(T)*deltaH_19*cGCO2 + k_20(T)*deltaH_20*cGCO + k_21(T)*deltaH_21*cGCOH2 + k_22(T)*deltaH_22*cGH2 + k_23(T)*deltaH_23*cGCH4 + k_24(T)*deltaH_24*cGCH3OH + k_25(T)*deltaH_25*cGC2H4)			

2.4 Transport of Diluted Species (chds)

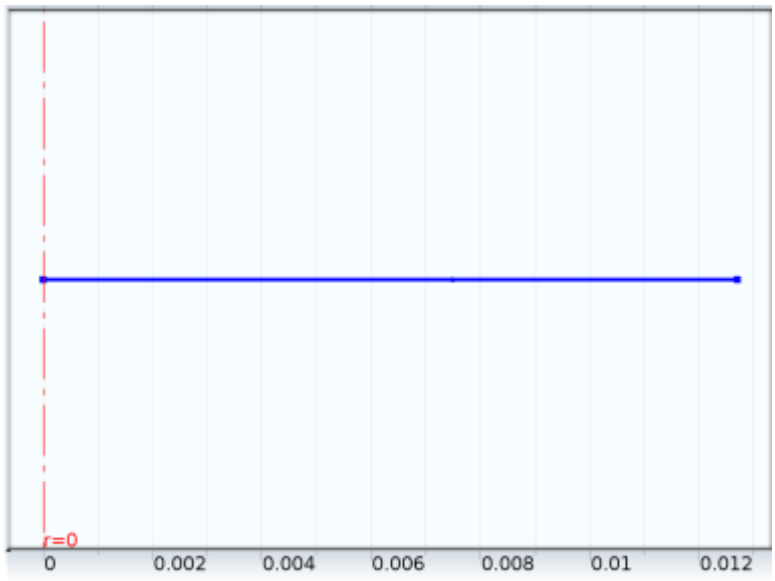

Transport of Diluted Species

Selection

Geometric entity level	Domain
Selection	Domain 1

Equations

$$\frac{\partial c_i}{\partial t} + \nabla \cdot \left(-D_i \nabla c_i\right) + \mathbf{u} \cdot \nabla c_i = R_i$$

$$\mathbf{N}_i = -D_i \nabla c_i + \mathbf{u} c_i$$

Settings

Description	Value
Value type when using splitting of complex variables	Complex
Show equation assuming	std3/time

2.4.1 Initial Values 1

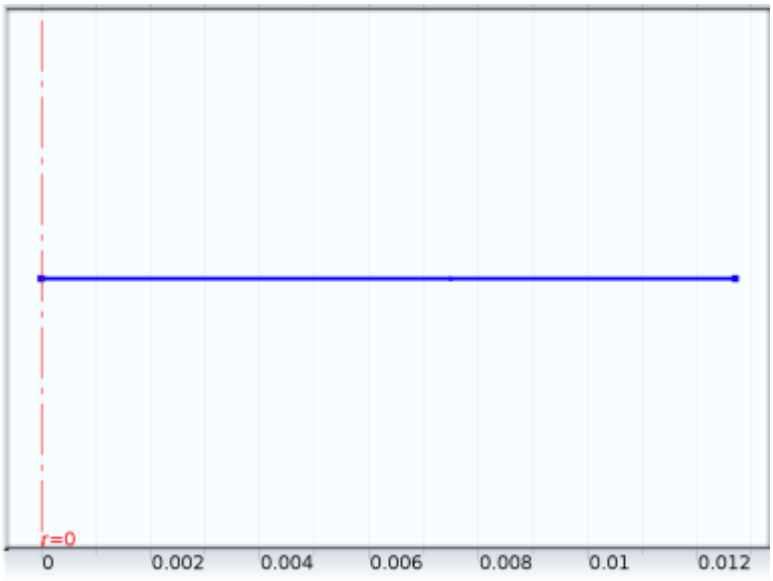

Initial Values 1

Selection

Geometric entity level	Domain
Selection	Domain 1

Settings

Settings

Description	Value
Concentration	rho_w*cell_init*1000/MW_cell
Concentration	rho_w*hemi_init*1000/MW_hemi
Concentration	rho_w*ligC_init*1000/MW_ligC
Concentration	rho_w*ligH_init*1000/MW_ligH
Concentration	rho_w*ligO_init*1000/MW_ligO

2.4.2 Reactions 1

Reactions 1

Selection

Geometric entity level	Domain
Selection	Domain 1

Equations

$$\frac{\partial c_i}{\partial t} + \nabla \cdot \left(-D_i \nabla c_i\right) + \mathbf{u} \cdot \nabla c_i = R_i$$

Variables

Name	Expression	Unit	Description	Selection
chds.R_cCELL	cCELL*(-k_1(T) - k_4(T))	mol/(m^3*s)	Total rate expression	Domain 1
chds.R_cCELLA	k_1(T)*cCELL - k_2(T)*cCELLA - k_3(T)*cCELLA	mol/(m^3*s)	Total rate expression	Domain 1

Name	Expression	Unit	Description	Selection
chds.R_cChar	0.61*k_2(T)*cCELLA + 6*k_4(T)*cCELL + 0.875*k_6(T)*cHCE1 + 0.675*k_7(T)*cHCE1 + k_9(T)*cHCE2 + 5.735*k_10(T)*cLIGC + 6.75*k_13(T)*cLIGCC + 4.15*k_14(T)*cLIGOH + 10.15*k_15(T)*cLIGOH + 5.5*k_17(T)*cLIG + 6*k_18(T)*cLIG	mol/(m^3*s)	Total rate expression	Domain 1
chds.R_cGC2H4	0.1*k_2(T)*cCELLA + 0.375*k_7(T)*cHCE1 +	mol/(m^3*s)	Total rate expression	Domain 1

Name	Expression	Unit	Description	Selection
	0.275*k_9(T)*cHCE2 + 0.6*k_13(T)*cLIGCC + 0.2*k_14(T)*cLIGOH + 0.65*k_17(T)*cLIG + 0.5*k_18(T)*cLIG - k_25(T)*cGC2H4			
chds.R_cGCH3OH	0.25*k_6(T)*cHCE1 + 0.5*k_14(T)*cLIGOH + 0.2*k_18(T)*cLIG - k_24(T)*cGCH3OH	mol/(m^3*s)	Total rate expression	Domain 1
chds.R_cGCH4	0.625*k_7(T)*cHCE1 + 0.55*k_9(T)*cHCE2 + 0.65*k_13(T)*cLIGCC +	mol/(m^3*s)	Total rate expression	Domain 1

Name	Expression	Unit	Description	Selection
	0.45*k_14(T)*cLIGOH + 1.45*k_15(T)*cLIGOH + 0.6*k_17(T)*cLIG + k_18(T)*cLIG - k_23(T)*cGCH4			
chds.R_cGCO	0.15*k_7(T)*cHCE1 + 0.4*k_13(T)*cLIGCC + k_14(T)*cLIGOH + 1.6*k_15(T)*cLIGOH + 0.45*k_17(T)*cLIG + 0.2*k_18(T)*cLIG - k_20(T)*cGCO	mol/(m^3*s)	Total rate expression	Domain 1
chds.R_cGCO2	0.55*k_9(T)*cHCE2 - k_19(T)*cGCO2	mol/(m^3*s)	Total rate expression	Domain 1
chds.R_cGCOH2	k_7(T)*cHCE1 + 0.7*k_9(T)*cHCE2 + 0.7*k_10(T)*cLIGC	mol/(m^3*s)	Total rate expression	Domain 1

Name	Expression	Unit	Description	Selection
	+ 0.7*k_13(T)*cLIGCC + 0.6*k_14(T)*cLIGOH + 3.9*k_15(T)*cLIGOH + 0.5*k_17(T)*cLIG + 1.5*k_18(T)*cLIG - k_21(T)*cGCOH2			
chds.R_cGH2	0.01*k_2(T)*cCELLA + 1.025*k_6(T)*cHCE1 + 0.4*k_7(T)*cHCE1 + 0.325*k_9(T)*cHCE2 + 0.35*k_14(T)*cLIGOH + 1.3*k_15(T)*cLIGOH +	mol/(m^3*s)	Total rate expression	Domain 1

Name	Expression	Unit	Description	Selection
	0.2*k_18(T)*cLIG - k_22(T)*cGH2			
chds.R_cHCE	-k_5(T)*cHCE	mol/(m^3*s)	Total rate expression	Domain 1
chds.R_cHCE1	0.4*k_5(T)*cHCE- k_6(T)*cHCE1 - k_7(T)*cHCE1 - k_8(T)*cHCE1	mol/(m^3*s)	Total rate expression	Domain 1
chds.R_cHCE2	0.6*k_5(T)*cHCE- k_9(T)*cHCE2	mol/(m^3*s)	Total rate expression	Domain 1
chds.R_cLIG	k_14(T)*cLIGOH - k_16(T)*cLIG - k_17(T)*cLIG - k_18(T)*cLIG	mol/(m^3*s)	Total rate expression	Domain 1
chds.R_cLIGC	-k_10(T)*cLIGC	mol/(m^3*s)	Total rate expression	Domain 1
chds.R_cLIGCC	0.35*k_10(T)*cLIGC - k_13(T)*cLIGCC	mol/(m^3*s)	Total rate expression	Domain 1
chds.R_cLIGH	-k_11(T)*cLIGH	mol/(m^3*s)	Total rate expression	Domain 1
chds.R_cLIGO	-k_12(T)*cLIGO	mol/(m^3*s)	Total rate	Domain 1

Name	Expression	Unit	Description	Selection
			expression	
chds.R_cLIGOH	k_11(T)*cLIGH + k_12(T)*cLIGO - k_14(T)*cLIGOH - k_15(T)*cLIGOH	mol/(m^3*s)	Total rate expression	Domain 1

2.5 Transport of Concentrated Species (chcs)

Transport of Concentrated Species

Selection

Geometric entity level	Domain
Selection	Domain 1

Equations

$$\rho\frac{\partial\omega_i}{\partial t}+\nabla\cdot\mathbf{j}_i+\rho(\mathbf{u}\cdot\nabla)\omega_i=R_i$$
$$\mathbf{N}_i=\mathbf{j}_i+\rho\mathbf{u}\omega_i$$

$$\mathbf{j}_i = -\left(\rho D_i^f \nabla \omega_i + \rho \omega_i D_i^f \frac{\nabla M_n}{M_n} + D_i^T \frac{\nabla T}{T}\right)$$

$$M_n = \left(\sum_i \frac{\omega_i}{M_i}\right)^{-1}$$

Settings

Description	Value
Value type when using splitting of complex variables	Complex
Diffusion model	Fick's law
From mass constraint	wN2
Show equation assuming	std3/time

2.5.1 Convection and Diffusion

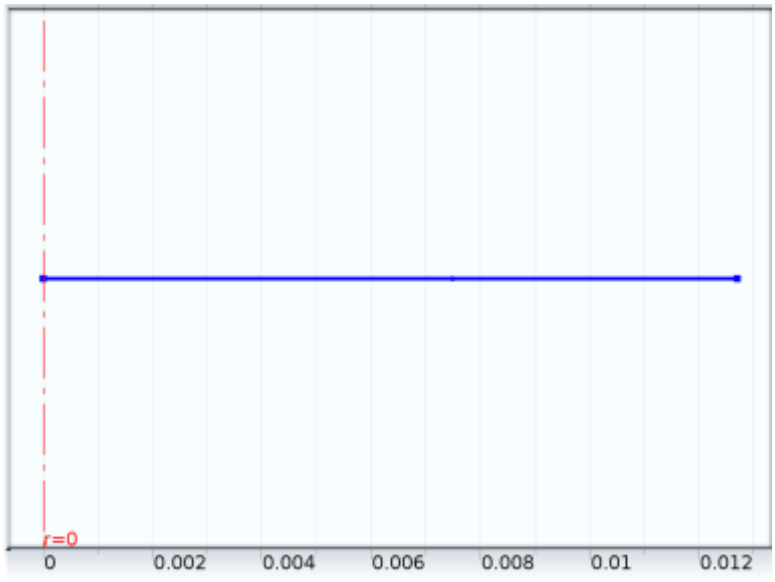

Convection and Diffusion

Selection

Geometric entity level	Domain
Selection	Domain 1

Equations

$$\rho\frac{\partial\omega_i}{\partial t}+\nabla\cdot\mathbf{j}_i+\rho(\mathbf{u}\cdot\nabla)\omega_i=R_i$$

$$\mathbf{N}_i=\mathbf{j}_i+\rho\mathbf{u}\omega_i$$

$$\mathbf{j}_i=-\left(\rho D_i^F\nabla\omega_i+\rho\omega_i D_i^F\frac{\nabla M_n}{M_n}+D_i^T\frac{\nabla T}{T}\right)$$

$$M_n=\left(\sum_i\frac{\omega_i}{M_i}\right)^{-1}$$

Variables

Name	Expression	Unit	Description	Selection
wN2	1 - wC2H4 - wC2H4O - wC3H6O - wCH2O - wCH3OH - wCH4 - wCO - wCO2 - wCOU - wEtOH - wF2M - wFEN - wGLY - wH2 - wH2O - wHAA - wHCOOH - wHMFU - wLVG - wXYL	1	Mass fraction	Domain 1
chcs.M_wC2H4	28.0533[g/mol]	kg/mol	Molar mass	Domain 1
chcs.M_wC2H4O	44.0528[g/mol]	kg/mol	Molar mass	Domain 1
chcs.M_wC3H6O	58.0795[g/mol]	kg/mol	Molar mass	Domain 1
chcs.M_wCH2O	30.0261[g/mol]	kg/mol	Molar mass	Domain 1

Name	Expression	Unit	Description	Selection
chcs.M_wCH3OH	32.042[g/mol]	kg/mol	Molar mass	Domain 1
chcs.M_wCH4	16.0426[g/mol]	kg/mol	Molar mass	Domain 1
chcs.M_wCO	28.0102[g/mol]	kg/mol	Molar mass	Domain 1
chcs.M_wCO2	44.0096[g/mol]	kg/mol	Molar mass	Domain 1
chcs.M_wCOU	150.1754[g/mol]	kg/mol	Molar mass	Domain 1
chcs.M_wEtOH	46.0687[g/mol]	kg/mol	Molar mass	Domain 1
chcs.M_wF2M	208.2117[g/mol]	kg/mol	Molar mass	Domain 1
chcs.M_wFEN	94.1118[g/mol]	kg/mol	Molar mass	Domain 1
chcs.M_wGLY	58.0363[g/mol]	kg/mol	Molar mass	Domain 1
chcs.M_wH2	2.0159[g/mol]	kg/mol	Molar mass	Domain 1
chcs.M_wH2O	18.0153[g/mol]	kg/mol	Molar mass	Domain 1
chcs.M_wHAA	60.0522[g/mol]	kg/mol	Molar mass	Domain 1
chcs.M_wHCOOH	46.0255[g/mol]	kg/mol	Molar mass	Domain 1
chcs.M_wHMFU	126.1107[g/mol]	kg/mol	Molar mass	Domain 1
chcs.M_wLVG	162.1413[g/mol]	kg/mol	Molar mass	Domain 1
chcs.M_wXYL	132.1152[g/mol]	kg/mol	Molar mass	Domain 1
chcs.M_wN2	28.0134[g/mol]	kg/mol	Molar mass	Domain 1

2.5.2 Reactions 1

Reactions 1

Selection

Geometric entity level	Domain
Selection	Domain 1

Equations

Variables

Name	Expression	Unit	Description	Selection
chcs.R_wC2H4	R_C2H4 - wC2H4*d(rho_v*phi, t) - wC2H4*d(r^(2)*V*rho_v, r)/r^2	kg/(m^3*s)	Total rate expression	Domain 1
chcs.R_wC2H4	R_C2H4O -	kg/(m^3*s)	Total rate expression	Domain 1

Name	Expression	Unit	Description	Selection
O	wC2H4O*d(rho_v*phi, t) - wC2H4O*d(r^2*V*rho_v, r)/r^2			
chcs.R_wC3H6O	R_C3H6O - wC3H6O*d(rho_v*phi, t) - wC3H6O*d(r^2*V*rho_v, r)/r^2	kg/(m^3*s)	Total rate expression	Domain 1
chcs.R_wCH2O	R_CH2O - wCH2O*d(rho_v*phi, t) - wCH2O*d(r^2*V*rho_v, r)/r^2	kg/(m^3*s)	Total rate expression	Domain 1
chcs.R_wCH3OH	R_CH3OH - wCH3OH*d(rho_v*phi, t) - wCH3OH*d(r^2*V*rho_v, r)/r^2	kg/(m^3*s)	Total rate expression	Domain 1
chcs.R_wCH4	R_CH4 - wCH4*d(rho_v*phi, t)	kg/(m^3*s)	Total rate expression	Domain 1

Name	Expression	Unit	Description	Selection
	- wCH4*d(r^2*V*rho_ v, r)/r^2			
chcs.R_wCO	R_CO - wCO*d(rho_v*phi, t) - wCO*d(r^2*V*rho_v, r)/r^2	kg/(m^3*s)	Total rate expression	Domain 1
chcs.R_wCO2	R_CO2 - wCO2*d(rho_v*phi, t) - wCO2*d(r^2*V*rho_ v, r)/r^2	kg/(m^3*s)	Total rate expression	Domain 1
chcs.R_wCOU	R_COU - wCOU*d(rho_v*phi, t) - wCOU*d(r^2*V*rho_ v, r)/r^2	kg/(m^3*s)	Total rate expression	Domain 1
chcs.R_wEtOH	R_EtOH - wEtOH*d(rho_v*phi, t) - wEtOH*d(r^2*V*rho_	kg/(m^3*s)	Total rate expression	Domain 1

Name	Expression	Unit	Description	Selection
	v, r)/r^2			
chcs.R_wF2M	R_F2M - wF2M*d(rho_v*phi, t) - wF2M*d(r^2*V*rho_ v, r)/r^2	kg/(m^3*s)	Total rate expression	Domain 1
chcs.R_wFEN	R_FEN - wFEN*d(rho_v*phi, t) - wFEN*d(r^2*V*rho_ v, r)/r^2	kg/(m^3*s)	Total rate expression	Domain 1
chcs.R_wGLY	R_GLY - wGLY*d(rho_v*phi, t) - wGLY*d(r^2*V*rho_ v, r)/r^2	kg/(m^3*s)	Total rate expression	Domain 1
chcs.R_wH2	R_H2 - wH2*d(rho_v*phi, t) - wH2*d(r^2*V*rho_v, r)/r^2	kg/(m^3*s)	Total rate expression	Domain 1
chcs.R_wH2O	R_H2O -	kg/(m^3*s)	Total rate expression	Domain 1

Name	Expression	Unit	Description	Selection
	wH2O*d(rho_v*phi, t) - wH2O*d(r^2*V*rho_v, r)/r^2			
chcs.R_wHAA	R_HAA - wHAA*d(rho_v*phi, t) - wHAA*d(r^2*V*rho_v, r)/r^2	kg/(m^3*s)	Total rate expression	Domain 1
chcs.R_wHCOOH	R_HCOOH - wHCOOH*d(rho_v*phi, t) - wHCOOH*d(r^2*V*rho_v, r)/r^2	kg/(m^3*s)	Total rate expression	Domain 1
chcs.R_wHMFU	R_HMFU - wHMFU*d(rho_v*phi, t) - wHMFU*d(r^2*V*rho_v, r)/r^2	kg/(m^3*s)	Total rate expression	Domain 1
chcs.R_wLVG	R_LVG - wLVG*d(rho_v*phi,	kg/(m^3*s)	Total rate expression	Domain 1

Name	Expression	Unit	Description	Selection
	t) - wLVG*d(r^2*V*rho_v, r)/r^2			
chcs.R_wXYL	R_XYL - wXYL*d(rho_v*phi, t) - wXYL*d(r^2*V*rho_v, r)/r^2	kg/(m^3*s)	Total rate expression	Domain 1
chcs.R_wN2	wN2*(-d(rho_v*phi, t) - d(r^2*V*rho_v, r)/r^2	kg/(m^3*s)	Total rate expression	Domain 1

2.6 Darcy's Law (dl)

Darcy's Law

Selection

Geometric entity level	Domain
Selection	Domain 1

Equations

$$\frac{\partial}{\partial t}(\rho\varepsilon_p)+\nabla\cdot(\rho\mathbf{u})=Q_m$$

$$\mathbf{u}=-\frac{\kappa}{\mu}\nabla p$$

Settings

Description	Value
Value type when using splitting of complex variables	Complex
Show equation assuming	std3/time

2.6.1 Mass Source 1

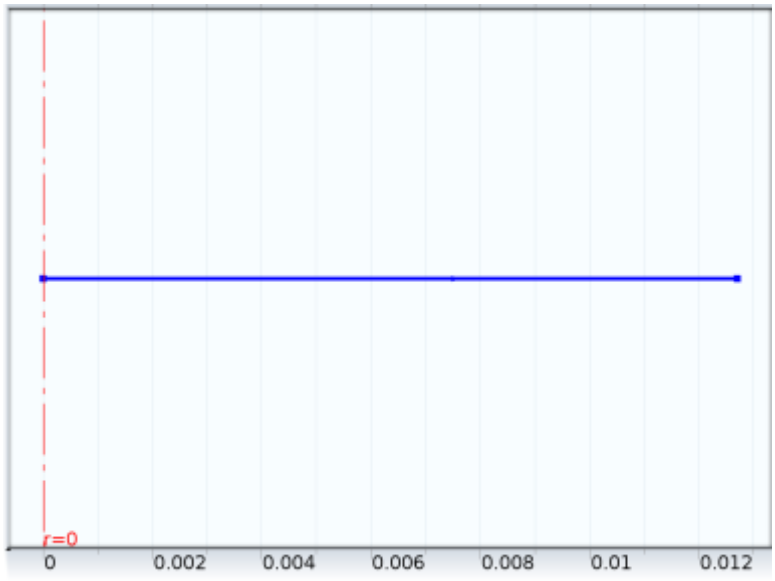

Mass Source 1

Selection

Geometric entity level	Domain
Selection	Domain 1

Equations

$$\frac{\partial}{\partial t}(\rho \epsilon_p) + \nabla \cdot (\rho \mathbf{u}) = Q_m$$

Settings

Settings

Description	Value
Mass source	mass_src*r

BIBLIOGRAPHY

Aiman, S.; Stubington, J.F. The pyrolysis kinetics of bagasse at low heating rates. *Biomass and Bioenergy* **1993,** *5* (2), 113-120.

Antal, M.J.; Mochidzuki, K.; Paredes, L.S. Flash carbonization of biomass. *Industrial & Engineering Chemistry Research* **2003**, *42* (16), 3690-3699.

Bennadji, H.; Smith, K.; Shabangu, S.; Fisher, E.M. Low-temperature pyrolysis of woody biomass in the thermally thick regime. *Energy & Fuels* **2013,** *27* (3), 1453-1459.

Boroson, M.L; Howard, J.B.; Longwell, J.P.; Peters, W.A. Products yields and kinetics from the vapour phase cracking of wood pyrolysis tars. *AIChE Journal* **1989,** *35* (1), 120-128.

Bradbury, A.G.; Sakal, Y.; Shafizadeh, F. Kinetic model for pyrolysis of cellulose. *Journal of Applied Polymer Science* **1979,** *23,* 3271-3280.

Bridgwater, A.V. Principles and practice of biomass fast pyrolysis processes for liquids. *Journal of Analytical and Applied Pyrolysis* **1999,** *51,* 3-22.

Bridgwater, A.V. Renewable fuels and chemicals by thermal processing of biomass. *Chemical Engineering Journal* **2003,** *91,* 87-102.

Bryden, K.M.; Ragland, K.W.; Rutland, C.J. Modeling thermally thick pyrolysis of wood. *Biomass Bioenergy* **2002,** *22,* 41-53.

Calonaci, M.; Grana, R.; Hemings, E.B.; Bozzano, G.; Dente, M.; Ranzi, E. Comprehensive Kinetic Modeling study of bio-oil formation from fast pyrolysis of biomass. *Energy & Fuels* **2010,** *24* (10), 5727-5734.

Chan, W.C.R.; Kelbon, M.; Krieger, B.B. Modelling and experimental verification of physical and chemical processes during pyrolysis of a large biomass particle. *Fuel* **1985,** *64* (11), 1505-1513.

Czernik, S.; Bridgwater, A.V. Overview of application of biomass fast pyrolysis oil. *Energy and Fuels* **2004,** *18,* 590-598.

Di Blasi, C. Analysis of convection and secondary reaction effects within porous solid fuels undergoing pyrolysis. *Combustion Science and Technology* **1993a,** *90,* 315-340.

Di Blasi, C. Modeling and simulation of combustion processes of charring and non-charring solid fuels. *Progress in Energy and Combustion Science* **1993b,** *19,* 71-104.

Di Blasi, C. Heat, momentum and mass transport through a shrinking biomass particle exposed to thermal radiation. *Chemical Engineering Science* **1996a,** *51* (7), 1121-1132.

Di Blasi, C. Kinetic and heat transfer control in the slow and flash pyrolysis of solids. *Industrial & Engineering Chemistry Research* **1996b,** *35,* 37-47.

Di Blasi, C. Comparison of semi-global mechanisms for primary pyrolysis of lignocellulosic fuels. *Journal of Analytical and Applied Pyrolysis* **1998a,** *47,* 43-64.

Di Blasi, C. Physico-chemical processes occurring inside a degrading two-dimensional anisotropic porous medium. *International Journal of Heat and Mass Transfer* **1998b,** *41,* 4139-4150.

Di Blasi, C. Modeling intra- and extra-particle processes of wood fast pyrolysis, *AIChE Journal* **2002,** *48* (10), 2386-2397.

Di Blasi, C. Modeling chemical and physical processes of wood and biomass pyrolysis. *Progress in Energy and Combustion Science* **2008,** *34,* 47-90.
Encinar, J.M.; Beltran, F.J.; Bernalte, A.; Ramiro, A.; Gonzalez, J.F. Pyrolysis of two agricultural residues: olive and grape bagasse. Influence of particle size and temperature. *Biomass and Bioenergy* **1996,** *11* (5), 397-409.
Fagbemi, L.; Khezami, L.; Carpat, L. Pyrolysis products from different biomasses: application to the thermal cracking of tar. *Applied Energy* **2001,** *69,* 293-306.
Font, R.; Marcilla, A.; Verdu, E.; Devesa, J. Kinetics of the pyrolysis of almond shells and almond shells impregnated with CoCl2 in a fluidized bed reactor and in a Pyroprobe 100. *Industrial and Engineering Chemistry Research* **1990,** *29,* 1846-1855.
Gauthier, G.; Melkior, T.; Salvador, S.; Corbetta, M.; Frassoldati, A.; Pierucci, S.; Ranzi, E.; Bennadji, H.; Fisher, E.M. Pyrolysis of thick biomass particles: experimental and kinetic modeling. In *Chemical Engineering Transactions*; De Rademaeker, E., Fabiano, B., Buratti, S.S.; 2013; Volume 32, p 601.
Ghabi, C.; Benticha, H.; Sassi, M. Two-dimensional computational modeling and simulation of wood particles pyrolysis in a fixed bed reactor. *Combustion Science and Technology* **2008,** *180* (5), 833-853.
Grieco, E.; Baldi, G. Analysis and modeling of wood pyrolysis. *Chemical Engineering Science* **2011,** *66,* 650-660.
Gronli, M.G. A theoretical and experimental study of the thermal degradation of biomass. PhD Dissertation, Norwegian University of Science and Technology, Trondheim, Norway, 1996.
Hankalin, V.; Ahonen, T.; Raiko, R. On thermal properties of a pyrolysing wood particle. Proceedings of the Finnish-Swedish Flame Days, Naantali, Finland, 2009.
Howell, J.R. *A Catalog of Radiation Configuration Factors*; McGraw-Hill: New York, 1982.
Huber, G.W. *Breaking the Chemical and Engineering Barriers to Lignocellulosic Biofuels: Next Generation Hydrocarbon Biorefineries*; National Science Foundation, Chemical, Bioengineering, Environmental and Transport Systems Division: Washington, DC, 2008; p 180.
Incropera, F.P.; DeWitt, D.P. *Fundamentals of Heat and Mass Transfer*, fifth edition; John Wiley and Sons: New York, 2001.
Janse, A.M.C.; Westerhout, R.W.J.; Prins, W. Modelling of flash pyrolysis of a single wood particle. *Chemical Engineering and Processing* **2000,** *39,* 239-252.
Kays, W.M.; Crawford, M.E. *Convective Heat and Mass Transfer*, second edition; McGraw-Hill: New York, 1980; p 220.
Koufopanos, C.A.; Maschio, G.; Lucchesi, A. Kinetic modeling of the pyrolysis of biomass and biomass components. *Canadian Journal of Chemical Engineering* **1989,** *67,* 75-84.
Kung, H.C.; Kalelkar, A.S. On the heat of reaction in wood pyrolysis. *Combustion and Flame* **1973,** *20,* 91-103.
Larfeldt, J.; Leckner, B.; Melaaen, M.C. Modeling and measurements of the pyrolysis of large wood particles. *Fuel* **2000,** *70,* 1637-1643.
Lehmann, J.; Joseph, S. *Biochar for Environmental Management: Science and Technology*; Earthscan: 2009.
Li, S.; Xu, S.; Liu, S.; Yang, C.; Lu, Q. Fast pyrolysis of biomass in free-fall reactor for hydrogen-rich gas. *Fuel Processing Technology* **2004,** *85,* 1201-1211.

Liden, A.G.; Berruti, F.; Scott, D.S. A kinetic model for the production of liquids from the flash pyrolysis of biomass. *Chemical Engineering Communications* **1988,** *65,* 207-221.
Manya, J.J. Pyrolysis for biochar purposes: a review to establish current knowledge gaps and research needs. *Environmental Science & Technology* **2012,** *46* (15), 7939-7954.
Mazumdar, B.K.; Chatterjee, N.N. Mechanism of coal pyrolysis in relation to industrial practice. *Fuel* **1973,** *52* (1), 11-19.
Miller, R.S.; Bellan, J. A generalized biomass pyrolysis model based on superimposed cellulose, hemicellulose and lignin kinetics. *Combustion Science and Technology* **1997,** *126,* 97-137.
Mok, L.K.; Bergougnou, M.A.; de Lasa, H.J. Fast pyrolysis of biomass for the production of chemicals and fuels from wood. 4th Bioenergy R and D Seminar, Winnipeg, March 1980.
Ozisik, M.N. *Heat Conduction,* first edition; John Wiley and Sons: New York, 1980; p 631-632.
Park, W.C.; Atreya, A.; Baum, H.R. Experimental and theoretical investigation of heat and mass transfer processes during wood pyrolysis. *Combustion and Flame* **2010,** *157,* 481-494.
Ranzi, E.; Cuoci, A.; Faravelli, T.; Frassoldati, A.; Migliavacca, G.; Pierucci, S.; Sommariva, S. Chemical kinetics of biomass pyrolysis. *Energy & Fuels* **2008,** *22,* 4292-4300.
Shafizadeh, F.; Bradbury, A.G. Thermal degradation of cellulose in air and nitrogen at low temperatures. *Journal of Applied Polymer Science* **1979,** *23* (5), 1431-1442.
Sharypov, V.I.; Marin, N.; Beregovtsova, N.G.; Baryshnikov, S.V.; Kuznetsov, B.N.; Cebolla, V.N.; Weber, J.W. Co-pyrolysis of wood biomass and synthetic polymer mixtures. Part I influence of the experimental conditions on the evolution of solids, liquids, and gases. *Journal of Analytical and Applied Pyrolysis* **2002,** *64,* 15-28.
Soltes, E.J.; Elder, T.S. Pyrolysis. In *Organic Chemical from Biomass*; Goldstein, I.S.; CRC Press: Boca Raton, FL, 1981.
Tabatabaie-Raissi, A.; Mok, W.S.L.; Antal, M.J. Cellulose pyrolysis kinetics in a simulated solar environment. *Industrial & Engineering Chemistry Research* **1989,** *28* (6), 856-865.
Tang, W.K. Effect of inorganic salts on pyrolysis of wood. *US Forest service research paper FPL* **1967,** 71.
Thurner, F.; Mann, U. Kinetic investigation of wood pyrolysis. *Industrial & Engineering Chemistry Process Design and Development* **1981,** *20* (3), 482-488.
Vamvuka, D.; Kakaras, E.; Kastanaki, E.; Grammelis, P. Pyrolysis characteristics and kinetics of biomass residuals mixtures with lignite. *Fuel* **2003,** *82,* 1949-1960.
Williams, P.T.; Besler, S. Influence of temperature and heating rate on the slow pyrolysis of biomass. *Renewable Energy* **1996,** *7* (3), 233-250.
Whitaker, S. Forced Convection heat transfer correlations for flow in pipes, past flat plates, single cylinders, single spheres, and for flow in packed beds and tube bundles. *AIChE Journal* **1972,** *18* (2), 361-371.
Yang, H.; Yan, R.; Chen, H.; Lee, D.H.; Zheng, C. Characteristics of hemicellulose, cellulose and lignin pyrolysis. *Fuel* **2007,** *86,* 1781-1788.
Zaror, C.A.; Hutchings, I.S.; Pyle, D.L.; Stiles, H.N.; Kandiyoti, R. Secondary char formation in the catalytic pyrolysis of biomass. *Fuel* **1985,** *64* (7), 990-994.